MAX PLANCK INSTITUTE
OF MOLECULAR PHYSIOLOGY
CHEMICAL GENOMICS CENTRE
OF THE MAX PLANCK SOCIETY

technische universität
dortmund

Design, synthesis, and evaluation of small molecules and associated bifunctional conjugates targeting the Protein–RNA interaction of LIN28 and *let-7*

Dissertation

For the achievement of the academic degree of the

Doctor in Natural Sciences

(Dr. rer. Nat.)

Submitted to

The Faculty of Chemistry and Chemical Biology

Technical University Dortmund

by

Pascal Hommen, M.Sc.

Dortmund 2022

The work presented in this thesis was performed during the period from October 2018 to November 2022 under the supervision of Dr. Peng Wu at the Chemical Genomics Centre, the Max Planck Institute for Molecular Physiology, Dortmund, and the Faculty of Chemistry and Chemical Biology at the Technical University Dortmund.

Dekan:	Prof. Dr. Stefan M. Kast
1st Examiner:	Prof. Dr. Dr. h.c. Herbert Waldmann
2nd Examiner:	Prof. Dr. Andreas Brunschweiger
Supervisor:	Dr. Peng Wu

Results displayed in this dissertation contributed to the following publications:

P. Hommen, F. Huang, J. Hwang, L. Borgelt, L. Hohnen and P. Wu, "Chromenopyrazole-peptide conjugates as small-molecule-based inhibitors disrupting the protein-RNA interaction of Lin28-*let-7*", *to be submitted*.

G. L. Goebel[*], L. Hohnen[*], L. Borgelt, P. Hommen, X. Qiu, H. Lightfoot, P. Wu, "Small molecules with tetrahydroquinoline-containing Povarov Scaffolds as inhibitors disrupting the Protein-RNA interaction of LIN28-*let-7*", *European Journal of Medicinal Chemistry* **2022**, 114014, 228, DOI: https://doi.org/10.1016/j.ejmech.2021.114014.

L. Borgelt[*], F. Li[*], P. Hommen[*], P. Lampe[*], J. Hwang, G. L. Goebel, S. Sievers, and P. Wu, "Trisubstituted Pyrrolinones as Small-Molecule Inhibitors Disrupting the Protein–RNA Interaction of LIN28 and *Let-7*", *ACS Medicinal Chemistry Letters* **2021** 12 (6), 893-898, DOI: 10.1021/acsmedchemlett.0c00546.

Results displayed in this dissertation can also be found in the following bachelor/master thesis:

L. Hohnen, "Assay development and biological evaluation of small-molecule inhibitors targeting the protein-RNA interaction of LIN28 and *let-7*", Master Thesis, **2021**

G. Goebel, "Synthesis of Small-Molecule Modulators Targeting the Protein-RNA Interaction of Lin28 and *Let-7*", Master Thesis, **2021**

R. Walter, "Synthesis of chromeno[4,3-*c*]pyrazole derivatives as RNA-binding protein LIN28 inhibitors", Bachelor Thesis, **2020**

Für Meine Eltern

Acknowledgment

I had a great and enriching time at the Chemical Genomics Centre. While the pursuit of a Dr. rer. nat. is a taxing journey; it was made all the more memorable by the environment and people present in both the CGC and the MPI. I am very thankful to everyone, who contributed to this important phase of my life.

First, I would like to thank Prof. Dr. Herbert Waldmann for not only taking over the duty as the first examiner but probably more importantly establishing a third round of funding for the CGC project. Without these efforts, my whole endeavor would not have been possible.

Second, I would like to thank Prof. Dr. Andreas Brunschweiger for taking over the duty as the second examiner.

Third, I need to thank Dr. Peng Wu for giving me the opportunity to work on these interesting and challenging projects. It was an exciting experience to start the lab with you. I learned a whole lot beyond the limits of going through several research projects and am convinced this experience will be very valuable in my future endeavors. Thank you for the intensive and constructive discussions and the opportunity to work in such a high-end equipped scientific environment.

Fourth, I want to thank all the people who enabled my different projects. I would like to thank Jimin Hwang and Dr. Fubao Huang for their contributions to the main scaffold of my work and the many discussions about chemistry and non-chemistry-related topics. Furthermore, I would like to thank Georg Goebel. It was a pleasure to supervise you during your master thesis and all the best for your future projects. For the assistance concerning the peptide part of my work, I would like to thank Jen-Yao Chang, Adrian Krzyzanowski, and Joseph Openy for the great discussions and exchange of protocols. Since all this chemistry also required quite a bit of evaluation, I would like to highlight the efforts of Lydia Borgelt, Lisa Hohnen, and Neele Haacke. I appreciated the fruitful collaboration, the enriching discussions, and your patience in teaching me the required methods to further progress my projects.

Next, I would like to thank both, NMR and Chromatography Teams located in MPI and the TU Dortmund. The efficient and reliable processing of samples greatly improved the smooth workflow of my projects. A special thanks here goes to Jens Warmers, who not only kept everything running at the MPI but also assisted me in maintaining and repairing our LC systems at the CGC.

Acknowledgment

To finalize the work-related part of this appreciation thread a big thanks goes out to all the brave proofreaders. I would like to thank Dr. Caitlin Davies, Jimin Hwang, and Regine Siedentop for the efficient and extremely helpful corrections.

I would like to thank the collaborative and pleasant environment both in the CGC and Dept. 4. The breaks during incubation times and column runs were always well spent; either with coffee, ice cream, or cake but always with great conversation. Beyond the work life, I also want to appreciate the social events “off the clock” with brewery tours, Taco Fridays, beer breaks, and the annual thanksgiving. Lastly, I need to thank my partner in crime, Stefan Schmeing, it was a pleasure to transform the Mettwoch into such a long-lasting tradition to enrich the environment in CGC every single week.

First of all, I would like to express my sincere thanks to Fabian Horn and Philipp Heynen. The never-ending contrast between profound and less profound conversations across everyday relevant and absolutely irrelevant topics has always improved my mood. I would like to express my sincere thanks for the constant support, absolute quality time whenever we found time, and constant loyalty despite the not insignificant physical distance.

Also, to be mentioned here are Dr. Andreas Hermann and Simon Herrmann. Since the first semester, we have stuck together at the university and tried to help each other as much as we could. Even if acoustic input was the Achilles' heel most of the time. In the same breath, I would also like to thank the entire "Herrenrunde" for the golden years of study. Lastly I would like to thank Verena Kunig, Carina Seitz, Kirujan Jeyakumar, Felix Otte, Jana Flegel and Simon Kotnig for the quality lunch times throughout my time in Dortmund.

A very special thanks goes to my parents, Marion and Christoph. Thank you for the unconditional support, the open ear, and the relentless encouragement throughout the years. On the same note, I would also like to thank Horst Hein and the Taylors, Kathy, Ken, George, and Ricky, for their significant contributions to where I am today. I would also like to thank my entire family for their constant support and aid whenever I required it. Without all of you, I would neither be the person nor be in the spot where I am today.

And lastly, I would like to thank my partner Jimin yet another time. Thank you for your patience, help, endurance, and constant support throughout this very busy time. Thank you so much, that I can always count on you!

Table of Contents

Abstract

RNAs have evolved as prominent targets to tackle challenging topics in the field of chemical biology and medicinal chemistry. Concomitantly, RNA binding proteins (RBPs) are emerging as a new class of drug targets given the essential regulatory functions of RBPs in deciding cell fates. Despite the increasing understanding of the importance of RBPs, limited chemical tools are available to probe the biological functions of RBPs, which raises the need for the development of effective and selective tool compounds targeting RBPs.

The LIN28–*let-7* interaction is one of the most well-investigated protein–RNA interactions to date. Due to its association with a poor cancer prognosis, LIN28 is a potential new anticancer target. Among the current collection of reported LIN28 inhibitors, potent molecules with clear mechanisms of inhibition are lacking. Additionally, most reported LIN28 inhibitors were identified via high throughput screening of different formats against molecular libraries that were not tailored to target RBPs. Therefore, there is a need to diversify the discovery approaches for RBP-targeting molecules.

In this context, small-molecule-based approaches were adopted to engage the challenging topic of targeting the miRNA-binding protein LIN28. Furthermore, we designed an intriguing bifunctional molecule in which an affinity-enhancing moiety was linked to a known LIN28 small-molecule inhibitor to build bifunctional molecules to improve efficacy. Inspired by a rationale, first established in targeting protein–protein interactions, hotspot amino acids were identified through an analysis of LIN28–*let-7* crystal structure and a virtual alanine scan to design the corresponding affinity-enhancing moieties consisting of peptides. Conjugation between the designed peptides and the known LIN28 inhibitors led to enhanced binding affinity. In other approaches, we investigated compounds of three chemical scaffolds intending to study the structural features required for LIN28 inhibition, as well as identifying suitable small molecules to be used in the bifunctional molecule approach. After the initial investigation, chromeno[4,3-*c*]pyrazoles were used as the small molecule components to be conjugated to a peptide moiety through CuAAC chemistry. After screening for optimal linker length and the amino acid composition of the peptide, compound **111** was identified as a potent bifunctional molecule disrupting the LIN28–*let-7* interaction. The resulting novel class of chromenopyrazole–peptide conjugates showed improved properties in comparison with peptide-based probes. Therefore, proving the design strategy of the study and underlining the advantageous properties of conjugated entities over nonconjugated inhibitors.

Zusammenfassung

Ribonukleinsäuren haben sich zu einem bedeutsamen und anspruchsvollen Forschungsgebiet entwickelt, um Fragestellungen im Bereich der chemischen Biologie und der medizinischen Chemie besser zu verstehen. Gleichzeitig entwickeln sich RNA-bindende Proteine (RBPs) zu einer neuen Klasse von Arzneimittelzielen, da RBPs wesentliche regulatorische Funktionen in der Zelle beeinflussen. Trotz des zunehmenden Verständnisses der Bedeutung von RBPs stehen nur begrenzte chemische Hilfsmittel zur Verfügung, um die biologischen Funktionen von RBPs zu untersuchen, was die Notwendigkeit der Entwicklung wirksamer und selektiver Modulatoren rechtfertigt, die auf RBPs abzielen.

Die LIN28–*let*-*7*-Interaktion ist eine der bisher am besten untersuchten Protein-RNA-Interaktionen. Da sie mit einer schlechten Krebsprognose in Verbindung gebracht wird, ist LIN28 ein potenzielles neues Ziel für die Krebsforschung. Unter den derzeit bekannten LIN28-Inhibitoren fehlen potente Inhibitoren mit aufgeklärtem Wirkmechanismus. Darüber hinaus wurden die meisten publizierten LIN28-Inhibitoren durch Hochdurchsatz-Screening verschiedener Formate gegen Molekülbibliotheken identifiziert, die nicht auf RBPs ausgerichtet waren. Daher müssen die Entdeckungsansätze für RBP-modulierende Moleküle diversifiziert werden.

In diesem Zusammenhang wurden in dieser Studie Ansätze auf der Basis niedermolekularer Strukturen gewählt, um das anspruchsvolle Gebiet der Modulation des miRNA-bindenden Proteins LIN28 zu ergänzen. Bei unserem Ansatz haben wir eine affinitätssteigernde Struktur an einen bekannten niedermolekularen LIN28-Inhibitor angehängt, um bifunktionelle Moleküle mit einer verbesserten Wirksamkeit zu entwickeln. Nach einer Analyse der LIN28-*let*-*7*-Kristallstruktur und einem virtuellen Alanin-Scan wurden Hotspot-Aminosäuren identifiziert, um die entsprechende affinitätssteigernde Komponente rational auf Basis von Peptiden zu entwerfen. Das Design war inspiriert von etablierten Design Kriterien für Protein-Protein-Wechselwirkungen. Die Konjugation zwischen den entworfenen Peptiden und den bekannten LIN28-Inhibitoren führte zu einer erhöhten Bindungsaffinität. Ebenso untersuchten wir Verbindungen aus drei chemischen Grundstrukturen mit dem Ziel, die für die LIN28-Inhibition erforderlichen strukturellen Merkmale zu identifizieren und geeignete niedermolekulare Strukturen für den bifunktionellen Molekülansatz zu identifizieren. Chromeno[4,3-*c*]pyrazole wurden als niedermolekulare Strukturkomponenten verwendet, die mittels CuAAC-Chemie an eine Peptideinheit konjugiert werden sollten. Nach einem Screening und der Optimierung der

Linker Länge und der Aminosäurezusammensetzung des Peptids wurde **111** als ein wirksames bifunktionelles Molekül identifiziert, das die LIN28-*let-7*-Interaktion inhibiert. Die daraus resultierende neue Klasse von Chromenopyrazol-Peptid-Konjugaten zeigte vorteilhafte Eigenschaften im Vergleich zu rein peptidbasierten Strukturen. Dies bestätigt die Designstrategie der Studie und unterstreicht die vorteilhaften Eigenschaften konjugierter Moleküle in diesem Kontext gegenüber nicht konjugierten Inhibitoren.

1. Introduction

1.1 Significance of RNA Biology

RNAs (Ribonucleic acids) have drawn increasing attention in recent years. It has become clear, that only ~1–2% of the human genome encodes proteins (Figure 1).[1] Therefore, the potential druggable space goes far beyond the initially proposed central dogma of molecular biology proposed in 1970.[2] The remaining portion of genes encodes a variety of non-coding RNAs (ncRNA) that take part in many different processes inside the cell.[3] RNAs interact with protein partners, so-called RNA-binding proteins (RBPs), to form ribonucleoprotein complexes (RNP).[4] RNPs are heavily involved in posttranscriptional processes. The regulatory effect of these complexes depends on which type of RNA and which protein are associated with the respective complex.[5] Hence, structural elucidation and selective perturbation to better understand each RNP complex is a growing field of research.

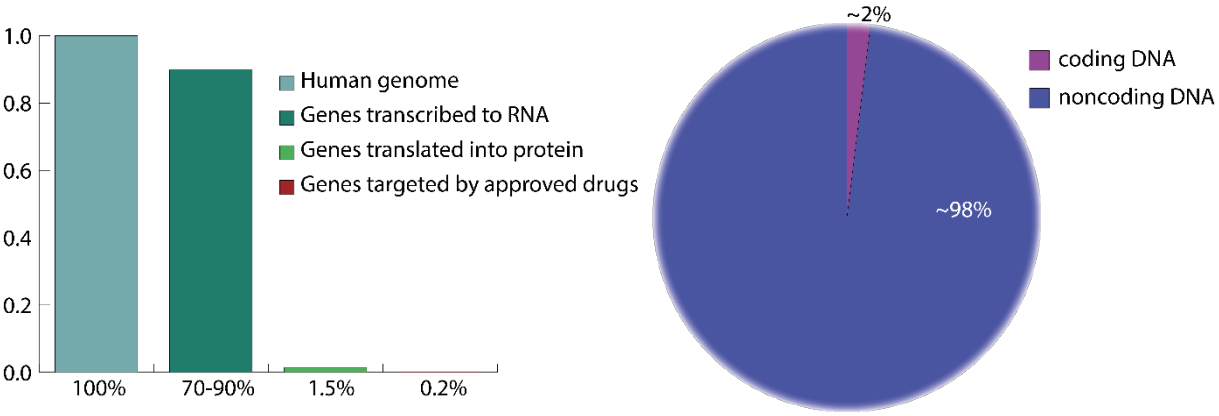

Figure 1: Bar chart to showcase the abundance of genetic information present in the human genome and its respective expression pattern. Additionally, the percentage of genes targeted by approved drugs is included to point out the vast space, and the possibility of still being available for future treatments.[6] Pie chart illustrating the ratio between coding and noncoding genomic information in the human genome.

Coding RNAs are usually messenger RNAs (mRNAs) and follow posttranscriptional processing by respective ribonucleases (RNases). Hence, mRNAs are considered key players in protein synthesis.[7] The field of ncRNA is more diverse. Ribosomal RNA (rRNA) makes up ~50–60% of the ribosome and is responsible for translating mRNA into the respective protein.[8] Another key player has to be mentioned, while on the topic of protein synthesis. Transfer RNA (tRNA) brings respective amino acid building blocks to the ribosome to enable the translation of the mRNA into a protein.[9] Small nuclear RNA (snRNA) is a key building block of the spliceosome and essential for mRNA maturation.[9] Other small non-coding RNAs (small

ncRNAs) are small interfering RNA (siRNA)[10] and micro RNA (miRNA)[11], which differ in origin but are essentially regulating mRNA translation and processing. Small nucleolar RNAs (snoRNA) are localized primarily in the nucleus where they mainly perform the necessary posttranslational modifications on rRNA, but they have also been associated with splicing or miRNAs.[12]

Complementary to small ncRNA, there is another category of ncRNA involved in gene expression, called the long non-coding RNA (lncRNA). By definition, a lncRNA is longer than 200 nucleotides and mostly lacks the ability to be translated into a protein.[13] It can have diverse functionalities, which are crucial for cell fate decisions, and has been associated with many diseases.[14] They can function as a scaffold to assemble numerous complexes of proteins or affect proteins through their interaction and change the proteins' confirmation to the active or inactive state.[15] An example for the importance of lncRNA complex formation is the selective degradation of DExH-box helicase 9 (DHX9) through murine double minute 2 (MDM2) by lnc cervical cancer DExH-box helicase 9 suppressive transcript (CCDST) to suppress cervical cancer.[7] The opposite can be observed in castration-resistant prostate cancer, where upregulation of lncRNA Hox transcript antisense RNA (HOTAIR) causes androgen-independent androgen receptor activation and activates the androgen-dependent transcriptional pathway, causing cancer cell growth and tissue invasion (Figure 2).[16]

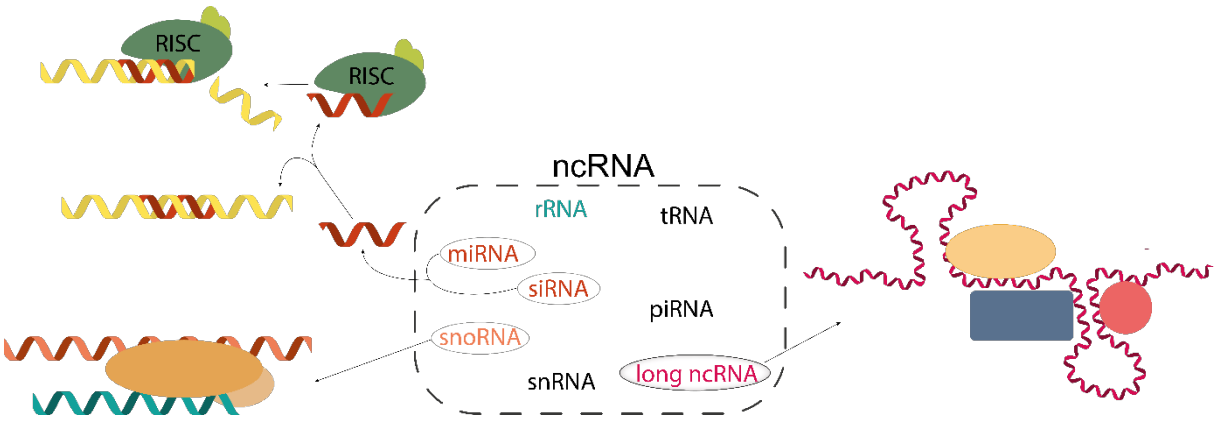

Figure 2: Illustration and overview of different types of non-coding RNAs. miRNA and siRNA are intracellular regulation points to inhibit and regulate most processes involved in protein expression. snoRNAs are involved in the chemical modification of other RNAs. Long ncRNA can take on numerous tasks and mostly function as a core scaffold to assemble several proteins.

1.2 MicroRNAs and the Function of *let-7*

An interesting subclass of ncRNA is the miRNA. Their best-known function is the regulation of gene expression.[17] miRNAs are single-stranded RNA fragments, consisting of 23–29 nucleotides (nt).[18] They function as a guiding fragment in RNA silencing complexes and can guide the silencing of specific mRNAs.[18] miRNA is transcribed in the nucleus as primary-miRNA (pri-miRNA) by RNA polymerase II & III.[17] pri-miRNAs are several kilobases long and contain several hairpin structures. The stem-loop structure of the pri-miRNA is recognized and cleaved by the RNase III Drosha within the nucleus to release the precursor-miRNA (pre-miRNA) fragment.[19] Although there are many different pri-miRNA sequences, the RNP formed around Drosha seems to selectively process the majority into pre-miRNA fragments. It is hypothesized that the tertiary structure of the pri-miRNA is mainly responsible for substrate specificity instead of its respective sequence.[20] The pre-miRNA is then recognized by the nuclear membrane transporter protein Exportin 5 and transported into the cytosol.[21] The exported pre-miRNA is then processed by another RNase, Dicer, into 18–24 nt double-stranded oligonucleotides. These strands will then be incorporated into the RNA-induced silencing complex (RISC) which degrades the complementary mRNA in the cytoplasm (Figure 3).[11][22] This expression regulation mechanism is involved in many different diseases, e.g. cancer, retinitis pigmentosa, autism, Charcot-Marie-Tooth Disease, or susceptibility to diabetes mellitus.[23][24] Due to these findings, miRNAs and their respective protein-RNA interactions (PRIs) have gained more attention from the scientific community to further understand their involvement in cellular- and disease-related processes. To better understand and explore the pathways around miRNAs, novel tools must be developed to enable uncovering interaction partners, understanding their mode of binding, and their involvement in the many different types of diseases.

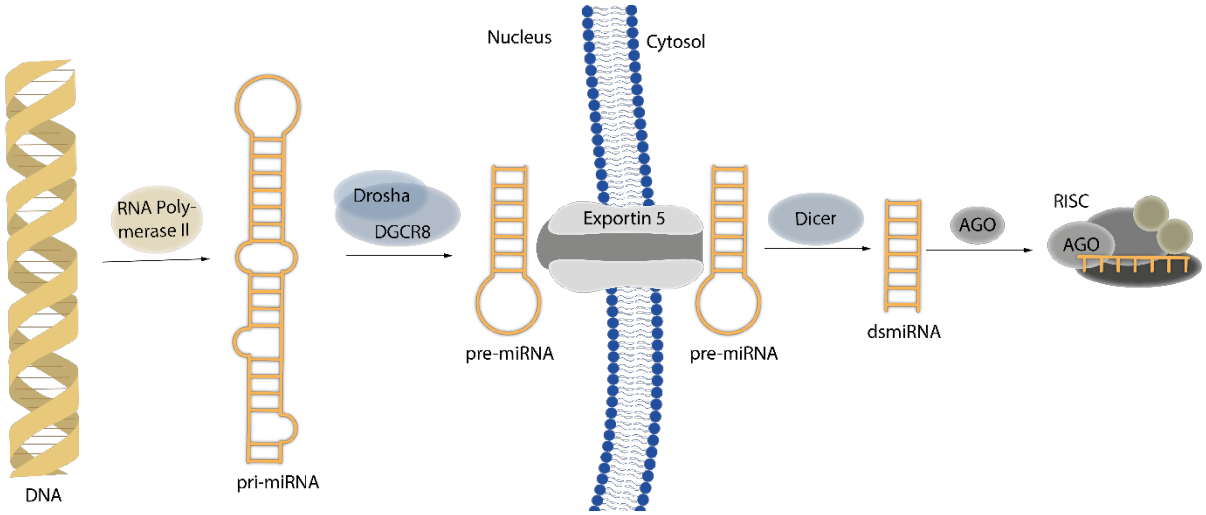

Figure 3: Schematic showing miRNA biogenesis. Primary transcripts of miRNA, pri-miRNAs are transcribed in the nucleus from DNA by RNA Polymerase apparatus. Pri-miRNA is then processed through Drosha/Dicer complex into pre-miRNA. Pre-miRNA is then exported into the cytosol by Exportin 5 transport channel and further processed into double-stranded miRNA by dicer. AGO protein then recruits double-stranded RNA into the RISC complex to regulate numerous processes in the cell by recognizing and degrading respective RNA segments.

Pri-miRNA *let-7* is transcribed in the nucleus by RNA Polymerase II. The pri-miRNA is then processed by the protein complex Drosha/DGCR8. This microprocessor complex releases 60–70 nt fragments defined as pre-miRNA. The pre-*let-7* miRNA is then exported from the nucleus into the cytosol, where it is further processed by dicer. After the dicer processing, the final miRNA gets recruited into the RISC complex, where it regulates many factors involved in cell-fate decisions, including the oncogenes c-Myc, Ras, and HMGA-2.[25][26] Besides oncogenes, *let-7* miRNAs also regulate cell fate decisions directly by regulating cyclin and cdk proteins.[27,28] It has also been found that *let-7* miRNAs are involved in the regulatory mechanisms of the immune system, as it has been associated with the regulation of Blimp-1. Also, *let-7* misregulation has been correlated with elevated IL-6 levels.[29,30] Lastly, an important function of the *let-7* miRNA is to inhibit LIN28 mRNA to stabilize the differentiated cell state (Figure 4).[31]

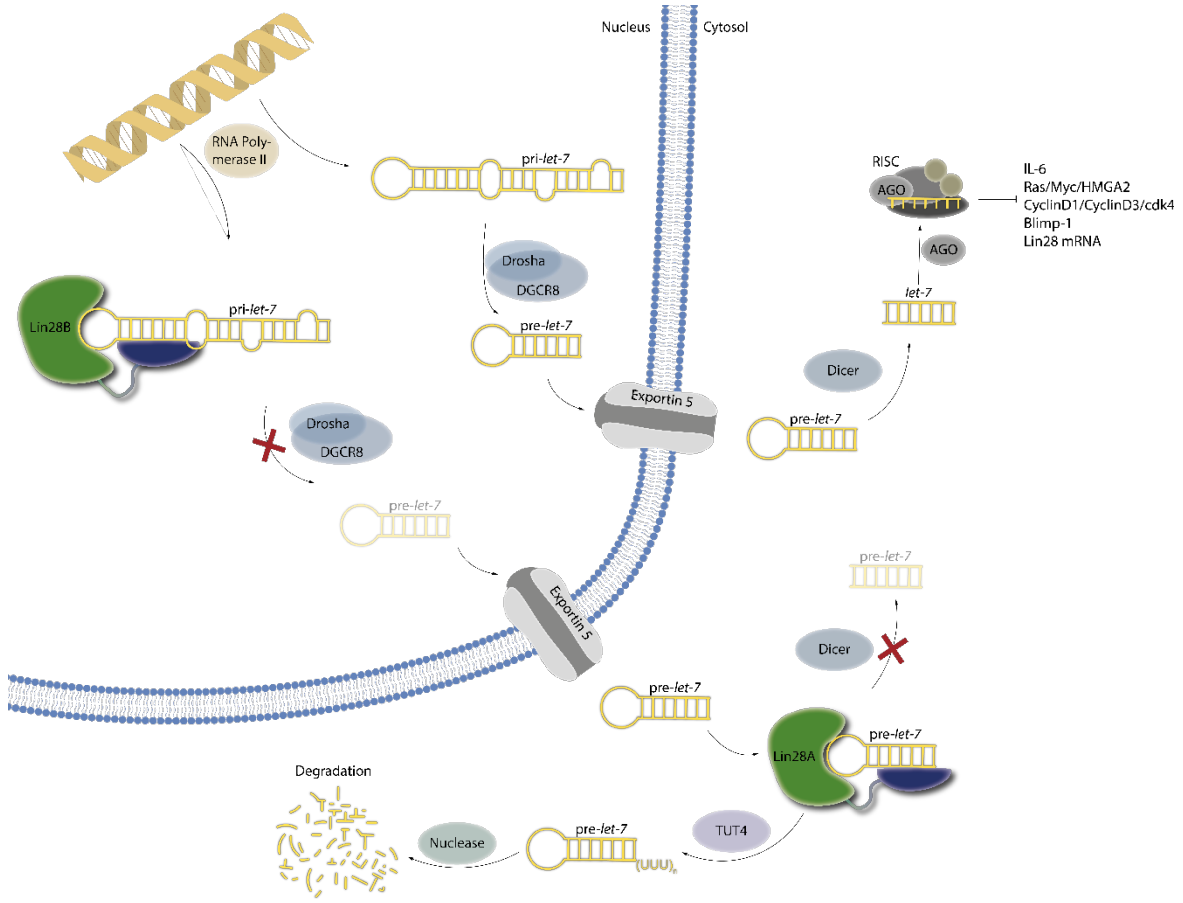

Figure 4: Cellular maturation pathway of *let-7* miRNAs, with and without LIN28 presence. Following the upper arrow pathway, pri-*let-7* is transcribed in the nucleus, processed by Drosha, and transported to the cytosol by Exportin 5. Here it is further processed by Dicer and then finally recruited in the RISC complex to regulate a list of oncogenes and other cell fate regulators. Following the bottom arrow, LIN28 is present to interfere with *let-7* maturation. Firstly, LIN28B binds to pri-*let-7* in the nucleus to prevent Drosha activity. The second point of interference is in the cytosol by LIN28A binding to pre-*let-7* and preventing processing by Dicer. Additionally, LIN28A also recruits TUT4 to cause degradation of the pre-*let-7* fragment.

1.3 RNA Binding Proteins (RBPs) and the Relevance of LIN28

Understanding RNA biology and uncovering more targets to tackle diseases, uncovered through tremendous efforts in the RNA field, are to elucidate PRIs. RNPs usually consist of one or several RBPs and one or more RNA components.[32] RBPs can contain several RNA binding domains (RBDs) that influence the proteins' selectivity by their respective arrangement.[33] Besides the modular combination of already characterized RBDs, a growing number of unorthodox RBPs without these RBDs was found during the increasing elucidation of the many RNPs in past years.[34] The arrangement of known RBDs (e. g. RNA-recognition motif (RRM)[35], K-homology domain (KH domain))[33] or the double-stranded RBD ((ds)RBD)[36]) and yet unknown RNA binding regions (e.g. multifunctional domains[37], protein regions of

unknown function[38] or protein regions of unknown fold[39]) on a protein is relevant for target binding. The complexity of RNP formation also increases, as protein-protein interactions between RBPs affect complex assembly as well.[40] The final factor known to influence RNP formation is the linker fragment connecting different RBP components. Either by additional binding to the RNA or tethering the respective components, the linker can have a significant impact on selectivity and binding strength for the respective RNP complex[41]. Several ways exist for RBPs to find their respective binding partner. The first known way is a very specific interaction pocket that forms strong interaction with its target RNA. Iron regulatory protein 1 (IRP1) binds to the iron responsive element (IRE) with a strong picomolar affinity.[42] Another mechanism is the interaction and recognition of specific modifications at the 3' or 5' end of RNAs to initiate the binding thereof. eIF4E is one example of such a scaffold protein, leading to the assembly of a protein complex that is thought to keep the 5' end from rehybridizing and therefore free for ribosomal attachment.[43] The last mode of binding is to simply not exhibiting any high specificity or selectivity but regulates these interactions through abundance. RBPs contain certain domains(e.g. ZKD, CSD, RRM, and KH)[44] that can bind numerous different sequences, but selectivity and strengthening of the interaction are then produced by additional domains or only side chains in specific positions.[45] The diversity and different processes in which RBPs are involved are vast (Figure 5). Most RBPs require complex formation to exert their respective function. A complex combination of PRIs and PPIs is required to selectively perform the required modification, alteration, or regulation for the majority of RNAs. The current knowledge about the precise mechanism and function of RBPs is constantly growing. Nevertheless, much more is to be found out and due to the rapidly expanding field, a new set of molecular tools for the respective research is urgently required.[46]

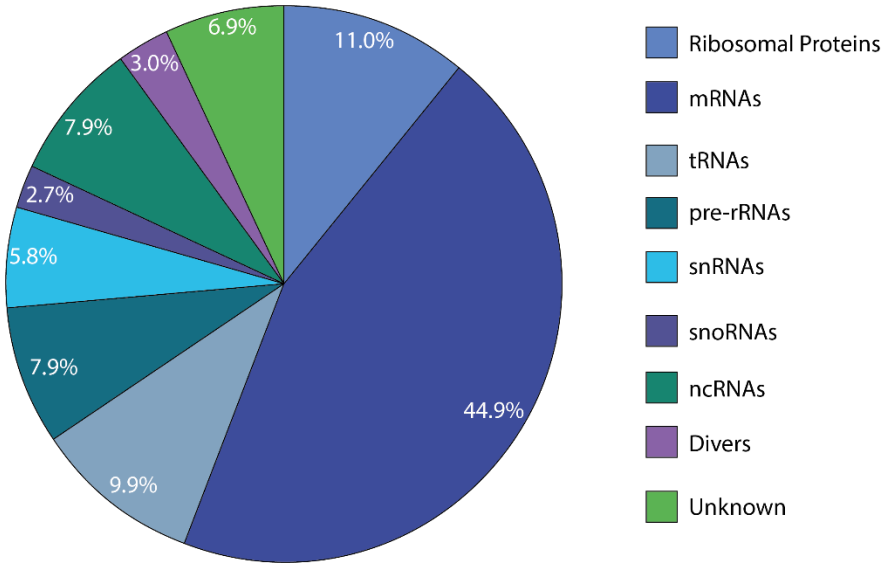

Figure 5: RNA-binding proteins and RBP families grouped by their respective targets. Overview of 1542 RBPs categorized by the respective target they bind in the cell. RBPs are involved in all regulatory processes of the cell. Adapted from *Gerstberger et. al*.[47]

LIN28 protein consists of two RNA binding domains. The cold-shock domain (CSD) and the zinc-knuckle domain (ZKD).[48] LIN28 is involved in regulating the maturation of *let-7* miRNA. During cellular differentiation, *let-7* levels rise and simultaneously also downregulate LIN28 levels in the cell through a direct inhibitory mechanism (Figure 6). LIN28 protein occurs in two isoforms in the mammalian cell; LIN28A and LIN28B.[49] A high degree of homology is found between these two isoforms. The main difference between the two proteins is, that LIN28B also contains a nuclear localization sequence. Both isoforms bind *let-7* precursors through a distinct mechanism. LIN28A is mostly located in the cytoplasm and binds the conserved terminal loop of pre-*let-7* to recruit TUTase Zcchc11 (TUT4) to block pre-*let-7* processing through dicer by polyuridylating the RNA.[50] Additionally, LIN28A has also been identified as a stem cell pluripotency factor and has successfully been used to reprogram adult human fibroblasts into pluripotent stem cells.[51] For LIN28B, no clear subcellular localization has been discovered yet. Although a nuclear localization sequence is present within the protein chain, it is not clear if the protein permeates from the cytoplasm into the nucleus in a cycle or stays there to interact with pri-*let-7* as initially believed. The exact inhibitory mechanism of how LIN28B prevents *let-7* maturation remains unclear (Figure 4).[50]

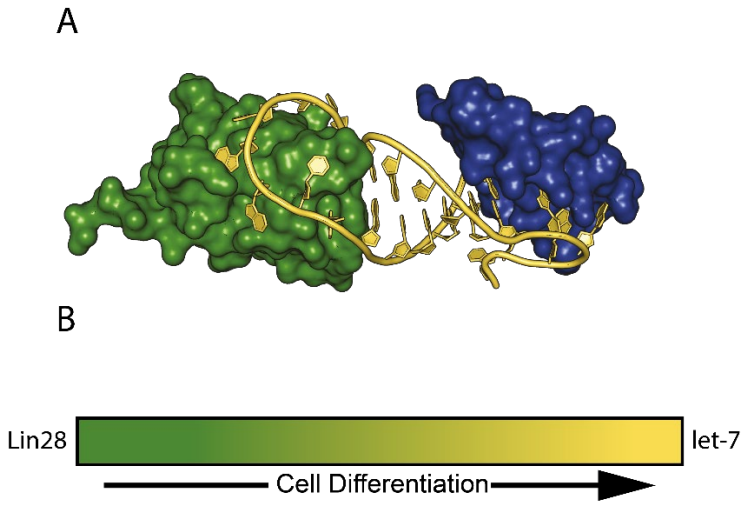

Figure 6: A: Crystal structure (PDB: 5UDZ) of LIN28A (green/blue) in complex with *let-7f-1* (yellow). B: Illustration of LIN28–*let-7* equilibrium during cell maturation. The further cells progress towards fully differentiated cells, the less LIN28 is present in the cells and the more *let-7* miRNA will be present.

Since its discovery in 1984 by Prof. H. Robert Horvitz, the LIN28–*let-7* interaction has become one of the best-characterized interactions between a miRNA and its posttranscriptional regulator.[52] This development holds also true for the view of LIN28 as a therapeutic target as it has been shown that *LIN28*$^{+}$ tumors make up 15% of all human tumor cell lines.[53]

1.4 RBP Targeting Focusing on the LIN28–*let-7* Interaction

One way to tackle the challenge of uncovering the interactome of certain RNAs or RBPs is the development of selective inhibitors. One method of targeting RNAs within the cellular system is to introduce a complementary oligonucleotide. This will bind the corresponding RNA strain within the cell and block it from exerting its original biological function. This approach is straightforward, highly selective, and an established and proven technique.[54] Oligonucleotide-based approaches suffer from low *in vivo* stability and narrow bioavailability.[55] Medicinal chemistries' favorite probe, the small molecule, has managed to make major advances toward the targeting of RBPs in recent years. There are five general approaches to consider when targeting PRIs. A PRI usually consists of one or more RNA and one or more protein components. The most straightforward way to target a PRI is selective targeting of the protein binding partner to induce conformational changes and inhibit RNA binding. Another apparent method is direct competition with the RNA for the binding site on the protein. A more challenging method to perturb PRIs would be the targeting of PTMs of the respective protein binding partner. Through PTM targeting, the protein can either be destabilized or kept in the inactive form to prevent PRI formation. A comparable method would be the indirect targeting

of the PRI through perturbation of required PPIs stabilizing the PRI complex. For both approaches, a solid understanding of the PRI complex and the respective protein target is required. The final approach would be the complete removal of the target RBP. A targeted degradation approach can be successful in perturbing PRIs but can also lead to severe off-target effects, as many of RBPs are involved in complex networks, binding different RNA targets or whole RNA families (Figure 7).[56]

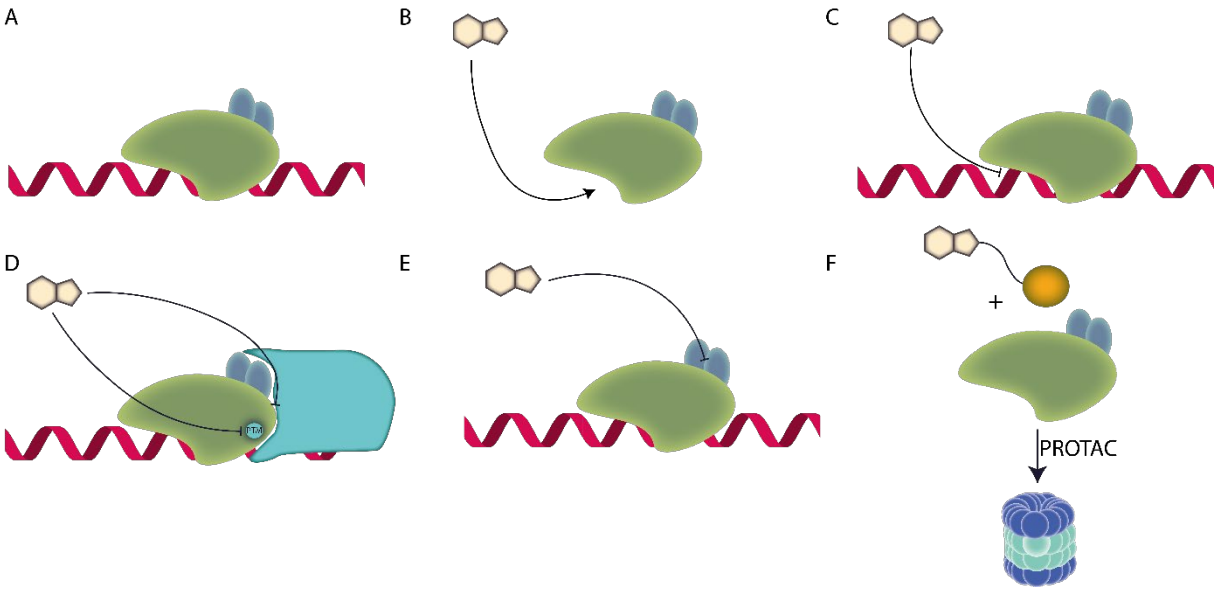

Figure 7: Five strategies that should be considered when planning to selectively target an RBP through a small molecule-based strategy. **A**: regular RNP consisting of RNA (red), RBP of interest (green), and other protein components of the RNP complex (blue). **B**: Targeting of the binding site of the RBP stabilizing any sort of inactive conformation. **C**: Direct competition with the RNA for the binding pocket on the RBP. **D**: Targeting of the posttranslational modification of the RBP to thereby stabilize the inactive confirmation. **E**: Direct targeting of the PPI with other proteins in the RNP to thereby perturb the complex formation. **F**: Targeted degradation through a proximity-induced mechanism that selectively targets the RBP of interest.

Topotecan was discovered through a screening campaign involving a TR-FRET assay in a high-throughput screen (HTS) campaign. A library of 10,173 bioactive compounds was selected and evaluated in a single dose at 15 µM concentration. Following validation revealed a modulator of the interaction between NHP2L1 and U4, influencing the interaction of two key regulators of the spliceosome.[57] The small molecule KH-3 inhibits the interaction between HuR RRM1/2. It also destabilizes HuR target genes and inhibits breast cancer cell growth *in vitro* and *in vivo*.[58] Ro 08-2750 was previously discovered in a fluorescence polarization (FP)-based screening campaign. Biochemical, structural, and cellular validation classified and characterized the compound as a selective MSI inhibitor. This chemical probe will be useful to

push for treatment in myeloid leukemia.[59] The natural product Hippuristanol was found to be an inhibitor selective for eIF4A, by disturbing its RNA-binding activity as its primary mechanism of action. It binds the carboxy-terminal domain of the protein and thereby stabilizes its closed formation and inhibits all helicase activity.[60] Ellipticine was discovered through AlphaScreen assay but does not yet have an elucidated mechanism of action. Ellipticine exposure increases the expression of *BDNF* genes in HEK293 cells. Since the upregulation of the respective mRNA was significantly higher it is hypothesized that Ellipticine is somehow involved in that pathway.[61] The most prominent example from this list is Risdiplam, the first orally available treatment for spinal muscular atrophy. It is a selective splicing modifier and is believed to interact with specific primary or secondary RNA structures in the SMN2 pre-mRNA complex (Figure 8).[62]

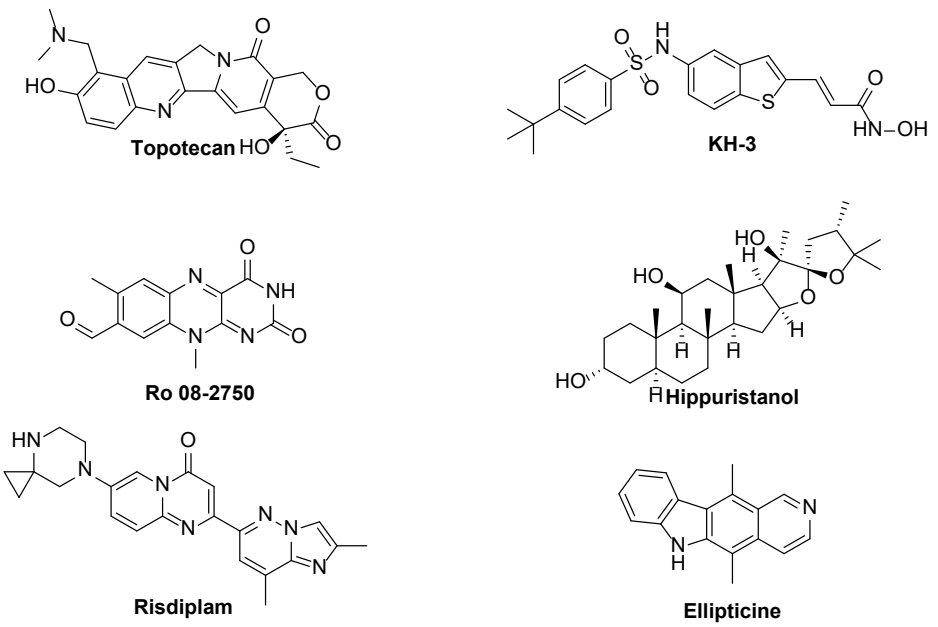

Figure 8: Overview of compounds representing different efforts to perturb protein RNA interactions with small molecules. Topotecan disrupts the interaction between NHP2LI and U4 and therefore inhibits RNA splicing.[57] KH-3 as an inhibitor of the HuR-FOXQ1 PRI as a therapeutic in cancer therapy.[58] Ro 08-2750 is a direct competitor for the RNA binding domain on MSI2 as a potential therapeutic for leukemia.[59] Hippuristanol binds the carboxy-terminal domain of elF4A and thereby stabilizing its closed formation, blocking any RNA interaction.[63] Risdiplam is a selective SMN2 splicing modifier that was approved for patients.[62] Ellipticine upregulates *BDNF* gene expression in HEK293 cells.[61]

Alternative strategies have been discovered as well. While alternative protein degradation strategies, like proteolysis targeting chimeras (PROTAC), have been developed, traditional approaches through small molecule targeting have also been investigated more thoroughly.[64] Nevertheless, initial bifunctional approaches have been made to target RBPs as small molecules

usually suffer from the limitation of affinities in the low micromolar range. A 7-nt PS-MOE oligonucleotide analog was designed to bring a VHL ligand into proximity of the LIN28 protein, degrading it and restoring *let-7* levels within the target cells.[65] Upregulated LIN28 levels are in general associated with a poor prognosis in cancer patients.

Due to its biological function and its association with poor prognosis in cancer, LIN28–*let-7* has become a well-researched target in cancer research. It has become one of the most well-characterized PRIs. Surprisingly, few inhibitors and tool compounds are available for the elaborate effort that has been invested into this interaction. In addition, the best affinities these compounds can manage is a low micromolar range. CCG-233094 was discovered through the adaption of the cat-ELCCA for the LIN28–*let-7* interaction to enable further HTS screening on the LIN28 protein. After a brief structural investigation, the best-performing compound was found to have an IC_{50} of 2.3 µM, but further investigation into the exact mode of action is necessary.[66] An FP-assay investigation into the LIN28–*let-7* interaction uncovered LI71 and TPEN. Through follow-up investigation, it was discovered that TPEN interferes with the Zn^{2+} from the ZKD, while LI71 selectively binds the CSD to interfere with binding. Both compounds showed IC50 values of 2.5 and 7 µM, respectively. KCB170522 was discovered through a fluorescence intensity-based assay and verified through electrophoretic mobility shift assay (EMSA). IC_{50} was determined to be 9.6 µM in fluorescence intensity-based assay and 12.8 µM through a dose-response EMSA.[67] Through the efforts of this work, the trisubstituted pyrrolinone C902/PH-31 was discovered through a HTS screen employing FP-assay. The compound was further investigated through FP-assay and dose-response EMSA to determine the IC_{50} 5 µM.[68] Lastly, SB1301 was discovered in a HTS FRET screen and investigated further with FP-assay and a dose-response EMSA to exhibit an IC_{50} of 10 µM. Additionally, SPR experiments were performed to validate, that SB1301 is selectively binding to the CSD domain (Figure 9).[69]

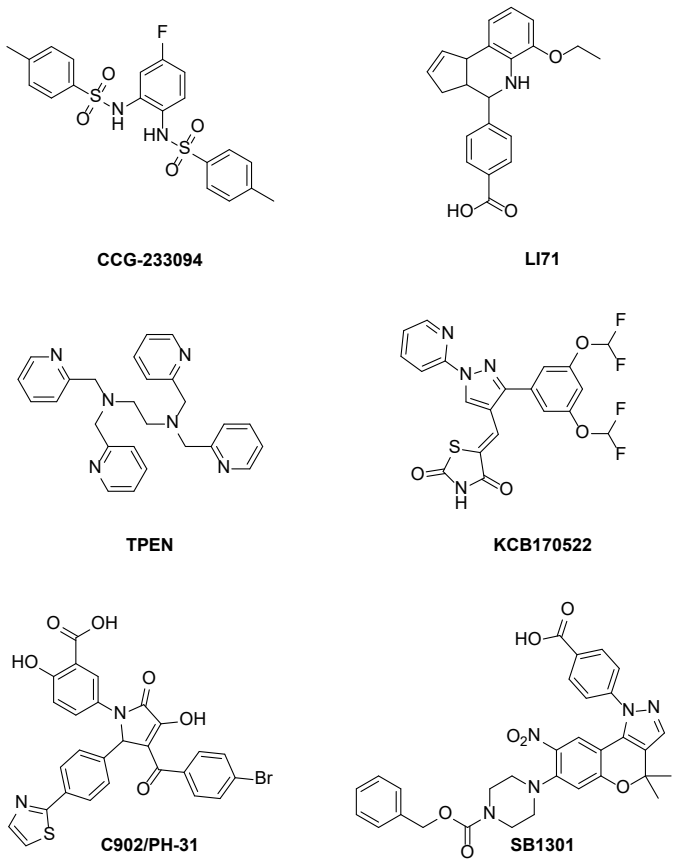

Figure 9: Overview of published LIN28–*let-7* inhibitors. CCG-233094 was discovered through cat-ELCCA and inhibits the interaction by binding to LIN28, but also requires more cellular investigation.[66] LI71 and TPEN were discovered through FP-assay and LI71 seems to be CSD selective while TPEN needs further cellular investigation.[70] KCB170522 was discovered through fluorescence intensity-based assay, inhibits by LIN28 binding, and increases levels of *let-7* in JAR cells.[67] C902/PH-31 was discovered through HTS screen and validated through FP-assay and EMSA.[68] Lastly, SB1301 was discovered in an HTS campaign and proven to bind to the LIN28 CSD.[69]

The inhibitors presented above are mostly well-investigated potential tool compounds to further understand the LIN28–*let-7* interaction.[6] Nevertheless, there is a demand for more potent and selective compounds to find out more about this interaction. One reason for the lack of affinity might be, that a small molecule is limited in its size. On the contrary, this molecule has to compete with a significantly larger RNA structure for interaction sites that are usually more flat surface areas instead of traditional targetable pockets. A change in strategy to address this problem for certain PRIs from small molecules to hybrid molecules, macrocycles, or bifunctional molecules might be a solution to resolve the current lack of selectivity and affinity for many PRIs.

1.5 NEC Strategy

Oligonucleotide therapeutics often suffer from toxicity or delivery issues which have been discussed in the previous chapter (1.4). Small molecule probes do not have the same issues as oligonucleotides but suffer from selectivity or potency issues in terms of targeting either 3D RNA structures or the corresponding RBP. To overcome this issue, peptide-small molecule conjugates have previously been synthesized to improve these flaws. Peptides on their own are powerful tools in medicinal chemistry, while, similar to oligonucleotides, showing great affinity, but having poor pharmacokinetic and pharmacodynamic properties.[71] Due to their high affinity, narrow pharmacokinetic distribution, short half-life, and synthetic accessibility, peptides have received attention as conjugation candidates in drug discovery.[72] Especially in the field of PPI inhibition, the usage of these hybrid macrocycles has been successful.[73] A proof of concept is the peptide-drug conjugate targeting the 6HB formation of HIV.[74] The additive effect of combining a small molecule and peptide binding to different positions on the same binding interface produced a low nanomolar inhibitor through a synergistic effect.[75]

Capitalization upon this synergistic effect gave the inspiration for the negatively charged moiety (NEC) strategy to selectively target PRIs. As most reported small-molecule probes targeting RBPs suffer from the limited potency to reliably modulate the PRI in the desired manner, we envision that the attachment of a NEC to a small-molecule RBP binder will enhance the disruptive efficacy against PRI. The NEC conjugate will bind via the electric charge attraction between NEC and the positively charged RNA-binding domains that are usually found on RBPs.[76–78] Additionally, negative charges from the RNA backbone and NEC will also repel each other. This additive electrostatic interaction can increase the overall potency of the probe to reliably inhibit the interaction in a non-covalent manner. For further binding enhancement, it is also required to introduce several aromatic amino acids into the NEC peptides. Besides electrostatic interactions, π-stacking interactions are also a major contributor to PRI formation.

To further understand the structure disruptive activity relationship surrounding the NEC molecules, linkers of different lengths were screened to investigate the effect on perturbing the desired interaction.[79] After the successful identification of an amenable linker attachment site on the small molecule scaffold, NEC moieties of varied sizes were evaluated. By perturbing the interaction, rather than degrading either component, we envision a more precise influence on cellular regulatory processes and fewer side effects (Figure 10). The majority of RBPs not only interact with a single type of RNA but are involved in complex networks.[80] Therefore, the

degradation through PROTAC or ribonuclease targeting chimeras (RIBOTAC) of respective components from these networks could cause undesired side effects through the removal of whole nodes in the complex network of protein-RNA interactions.[81] With the NEC strategy, we hope to not only overcome the lack of sub-micromolar inhibitors for the LIN28–*let-7* interaction but also present a platform tool to enhance known or novel inhibitors to perturb this interaction.

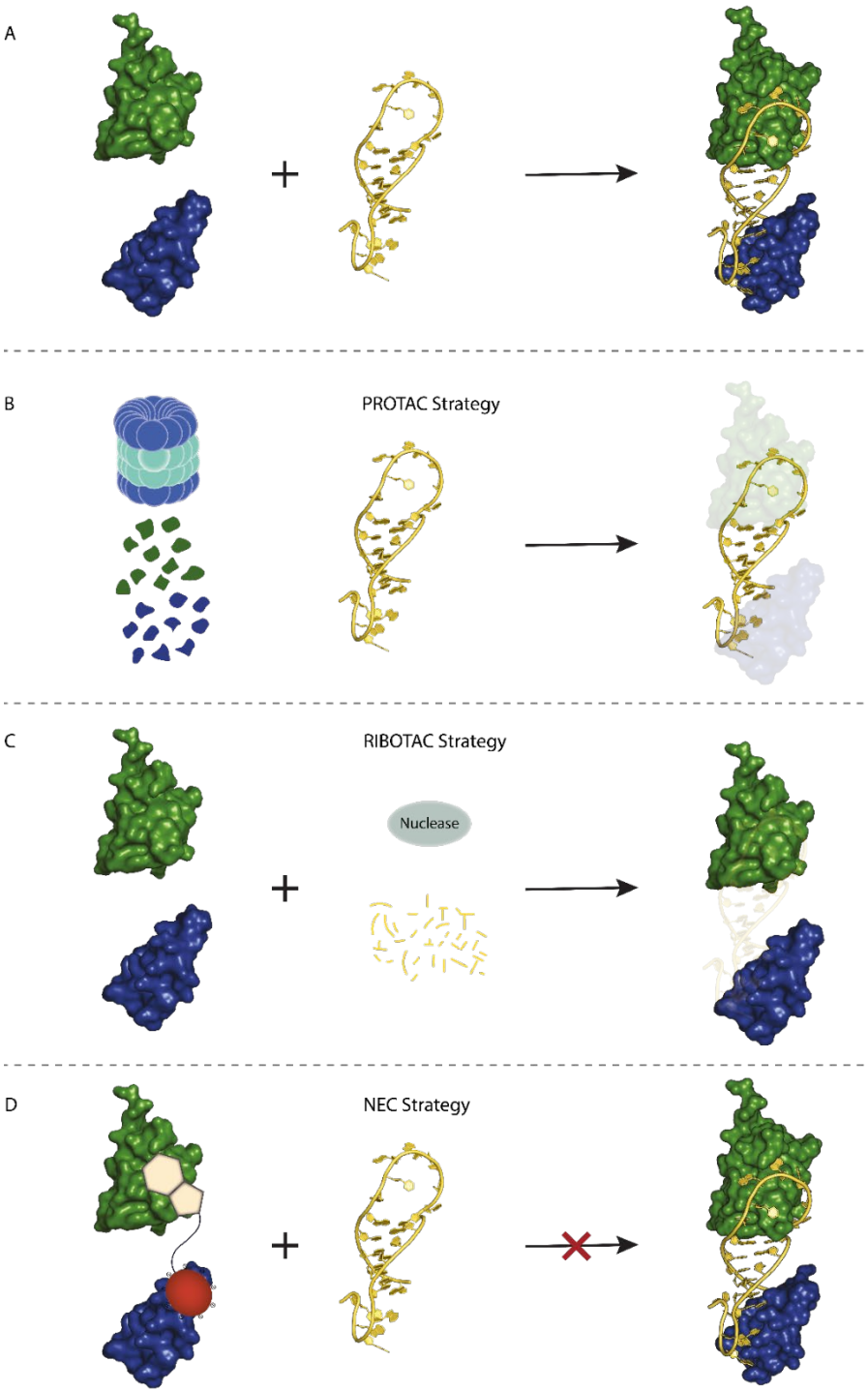

Figure 10: Comparison of the NEC strategy with PROTAC and RIBOTAC strategies.[81] A: Depiction of the LIN28–*let-7* interaction. B: Depiction of the result of a PROTAC approach targeting LIN28 and removing it through proteasomal degradation. C: Schematic representation of the RIBOTAC approach removing *let 7* from the equation. D: Introduction of the NEC strategy. While PROTAC and RIBOTAC strategies attach to the protein or RNA of interest and cause its respective degradation, the NEC strategy functions as an occupancy-driven interaction, that will keep both protein and RNA intact but selectively perturb the desired interaction

2. Aim of the Thesis

One research field at the forefront of chemical biology has been the targeting of RBPs which are closely involved in various regulatory processes. Therefore, targeting RBPs has been proposed as a new strategy to treat human diseases and to expand understanding of cellular networks involving protein–RNA interactions.[44] With the characterization of new RBPs and the identification of associated proteins required for RNA regulation, an increasing need to develop precise tool compounds to facilitate the investigation of RBPs and interacting RNAs has surfaced. The miRNA-binding protein LIN28 is involved in the regulation of the *let-7* miRNA family and is generally associated with a poor prognosis if upregulated in different cancers. As one of the most studied RBPs, although small molecule LIN28 inhibitors of different structures have been reported, no effective inhibitor with high binding affinity has been revealed yet. The need is urgent for high-affinity compounds that can either be used to further investigate the LIN28–*let-7* interaction and can potentially be studied as drug candidates for the reliable treatment of *LIN28*$^{+}$ tumors.

The first aim of this thesis is to investigate small molecules as LIN28 inhibitors. This includes the exploration of structural moieties that can be functionalized to enhance the LIN28-binding affinity and exploiting suitable appendage positions for linker attachment to form small molecule–peptide conjugates. For this purpose, an initial series of structural modifications performed on the selected chromenopyrazole and tetrahydroquinoline scaffolds are evaluated. In parallel, a screening campaign against a local small molecule library is also performed to retrieve new chemical entities as LIN28 inhibitors, followed by linker appendage.

The second aim of the thesis is to evaluate and provide proof-of-concept for the small molecule–peptide conjugate rationale to target RBPs. The NEC strategy is intended to be tested as a general concept to provide a rational design approach for RBP targeting with selective high-affinity probes. For this, a set of peptides is rationally designed based on available crystal structure data of the LIN28–*let-7* complex. After the identification of the best binders, the peptides are conjugated with the above-mentioned small molecule probes appendaged with linkers, resulting in the formation of novel bifunctional molecule probes. The goal is to validate the NEC strategy as a generally applicable approach to improve RBP binding and expand the overall toolkit for the investigation of RBPs.

3. Results and Discussion

3.1 Chromeno[4,3-*c*]pyrazoles as Potential NEC component

3.1.1 Chromeno[4,3-*c*]pyrazole Synthetic Investigation

*Compounds **8-10**, **15**, **26-30,** and **32-38** were provided by J. Hwang. Compounds **12**, **17**, **19-21** were provided by Dr. F. Huang. EMSA evaluation was performed by L. Hohnen and L. Borgelt.*

Chromeno[4,3-*c*]pyrazoles, also known as benzopyranylpyrazoles, are known as LIN28 inhibitors.[82] The core scaffold contains four potential handles to introduce new modifications and is therefore of high interest for the NEC strategy. In the presence of pyrrolidine, commercially available acetophenone **1** was cyclized with acetone to form 7-fluoro-chroman-4-one **2** through a Kabbe condensation.[83] A nitration was then performed to introduce a nitro group in the 6-positon to yield chromanone **3**. The benzyl carbamate (Cbz) protected piperazine moiety (R_1) was introduced to the scaffold through nucleophilic aromatic substitution on the 7-position to yield substituted chromanone **4**. Treatment with triethyl orthoformate gave diethoxy methyl chromanone **5**.[84] The catalytic deprotection of the acetal group with molecular iodine yielded enone **6**.[85] Chromeno[4,3-*c*]pyrazole **7** was formed by the formation of the pyrazole ring through a cyclization condensation reaction of **6** and 4-hydrazinobenzoic acid (Scheme 1).[82]

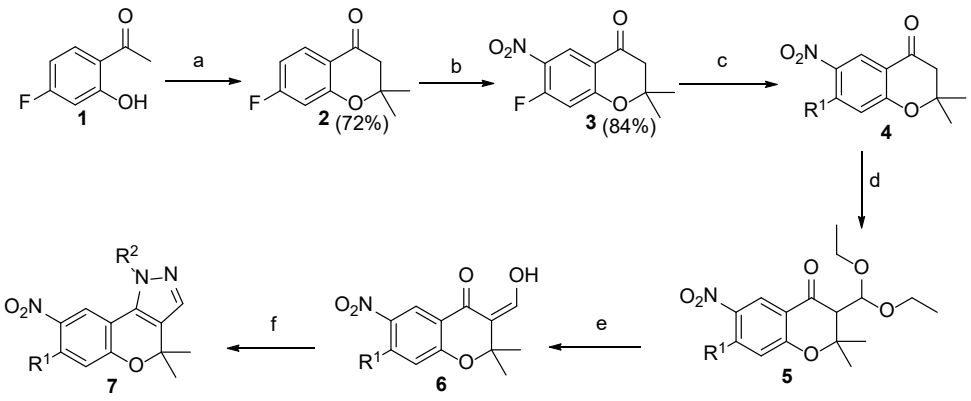

Scheme 1: General synthetic route for chromeno[4,3-*c*]pyrazoles to explore R^1 and R^2 handles.[82] (a) acetone, pyrrolidine, EtOH, room temperature, 16 h. (b) 70% nitric acid, conc. H_2SO_4, 0 °C, 2 h. (c) 1-((benzyloxy)carbonyl) piperazine, K_2CO_3, ACN, 40 °C, 16 h. (d) $BF_3{\cdot}Et_2O$, triethyl orthoformate, DCM, -5 °C to 0 °C, then -78 °C and then warm to room temperature for 2 h. (e) I_2, acetone, 35 °C, 16 h. (f) 4-hydrazinobenzoic acid, acetic acid, 35 °C, 2 h.

Following this route, eighteen derivatives were synthesized to explore the structure-activity relationship of the chromeno[4,3-*c*]pyrazoles. To explore the importance of the carboxylic acid

moiety of the initial LIN28 hit, SB1301 was resynthesized in-house as **7**; seven derivatives were synthesized. Compounds **8** and **9** were formed through the condensation with 6-hydrazineylbenzenesulfonic acid and 6-hydrazineylnicotinic acid respectively to explore the potential substitution of the carboxylic acid with a comparable acidic group and the tolerance of heteroatoms in the aromatic moiety. Synthesized as a negative control, **10** was used to investigate the complete removal of the R^2 moiety. It was also of interest to observe the change in the position of the carboxylic acid moiety. Therefore, **11** and **12** were synthesized by employing 3- and 2-hydrazineylbenzoic acid as well. Both phenyl- and benzyl hydrazine were employed in the cyclization reaction with **6** to yield chromeno[4,3-*c*]pyrazoles **13** and **14** as additional controls (Scheme 1 and Scheme 2).

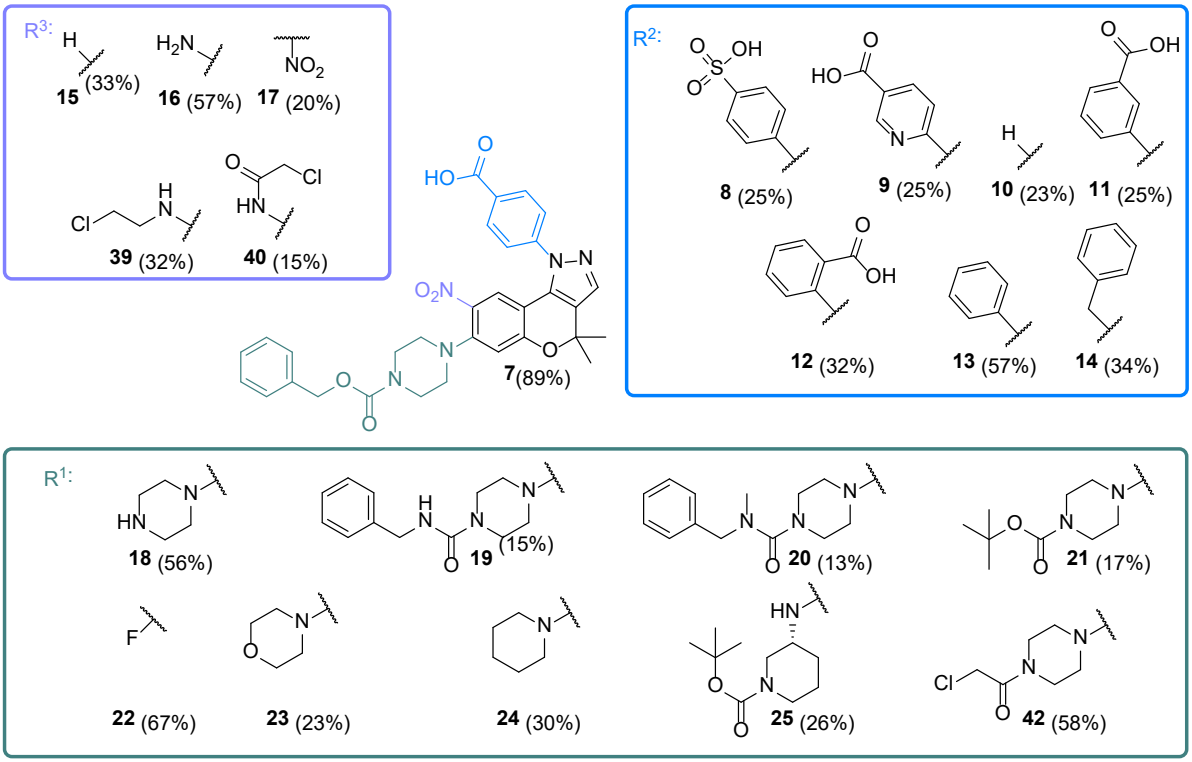

Scheme 2: Overview of all synthesized chromeno[4,3-*c*]pyrazoles. The different orientation for the substituent of compound **17** indicates the change in the nitro group position from 8- to the 6-position.

The next point of interest in this scaffold was the nitro group. As a result, **15** was synthesized without any modification in the 8-position of the original scaffold. To obtain **15,** the initial route had to be altered. Due to the missing nitro-group in the para-position to the fluoride, a much higher activation energy was necessary to favor the desired aromatic substitution. An elevated reaction temperature and a different solvent led to a successful synthesis (Scheme 3). Reduction of the 8-position provided primary amine **16**, to evaluate the effect on the compounds in their

reduced form, which will be occurring naturally in cells due to respective cellular pathways.[86] The last alternation to the nitro moiety was its position on the chromenone ring. 6-nitrochromanone instead of 8-nitrochromanone was obtained as a minor side product during the nitration reaction and followed the same chemistry as shown above to obtain **17**(Scheme 2).

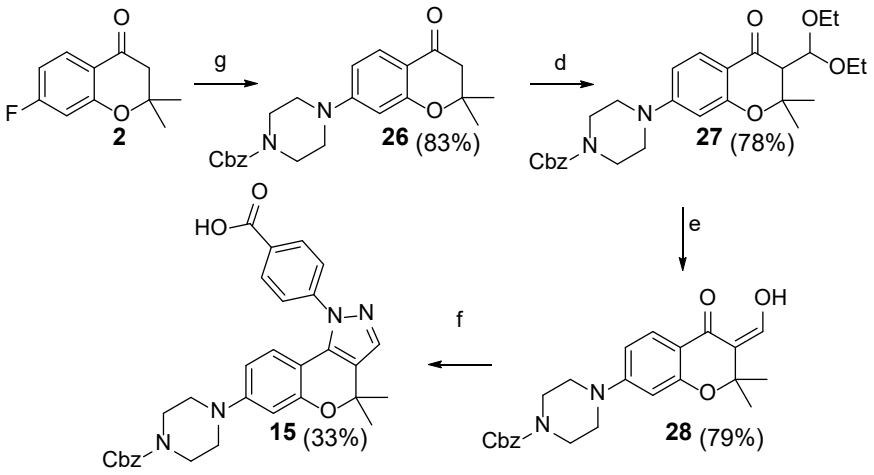

Scheme 3: Synthesis of **15**. (d) $BF_3{\cdot}Et_2O$, triethyl orthoformate, DCM, -5 °C to 0 °C, then -78 °C and then warm to room temperature for 2 h. (e) I_2, acetone, 35 °C, 16 h. (f) 4-hydrazinobenzoic acid, acetic acid, 35 °C, 2 h. (g) 1-((benzyloxy)carbonyl) piperazine, K_2CO_3, DMSO, 100 °C, 16 h. (h) $SnCl_2$, EtOH, 70 °C, 16 h.

The last position to be investigated from the original hit compound was the Cbz-piperazine moiety. The removal of the Cbz moiety was performed first with **18** to evaluate the necessity of the aromatic carbamate residue (Scheme 4). The substitution of the carbamate moiety for a carbamoyl moiety either free with **19** or in its methylated form **20** was also synthesized. Lastly, the Cbz group was exchanged for a Boc group to evaluate the exchange from an aromatic hydrophobic residue to an aliphatic hydrophobic residue with **21**. In addition to these derivatives of the original scaffold, the original fluoride substituent was left unsubstituted to give **22**. This was later substituted with morpholine or an unsubstituted piperidine residue to give **23** and **24** respectively and evaluate the necessity of the hydrophobic aromatic moiety (Scheme 1). Additionally, the introduction of a stereocenter and more flexibility through the substitution of the original R^1 moiety with a *tert*-butyl(R)-3-aminopiperidine-1-carboxylate was employed in **25**.

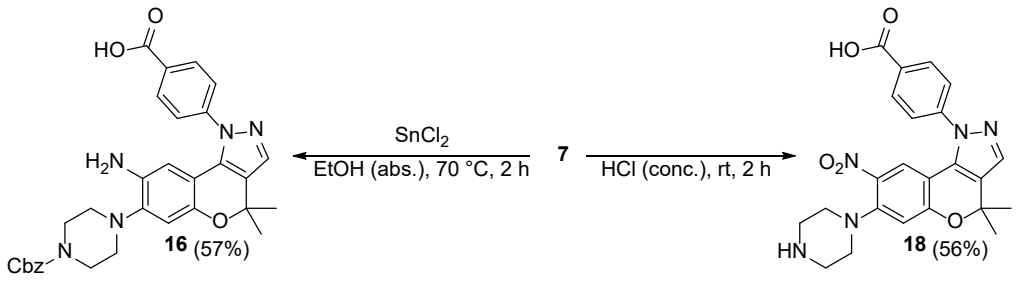

Scheme 4: Selective functionalization of potential linker attachment points on chromeno[4,3-*c*]pyrazole scaffold.

The fourth and final handle to investigate was the 1-position of the core scaffold. Exchanging the oxygen within the ring into a nitrogen would change the core scaffold from a chromanone into a quinoline. Since tetrahydroquinolines are known inhibitors for LIN28 protein, an effort to combine two known scaffolds could lead to a desirable improvement in affinity. To generate the quinoline molecule, the initial Kabbe condensation was exchanged for a Sonogashira coupling of 5-fluoro-2-iodoaniline with 2-methylbut-3-yn-2-ol to give **29**. Subsequent acid-catalyzed hydration of the alkyne introduced the ketone functionality, which was followed by a condensation cyclization to yield a quinolinone core structure **30**. After successfully obtaining the core structure, further steps were followed as described above to generate the quinolino[4,3-*c*]pyrazoles **36**–**38** (Scheme 5).

To prepare the chromeno[4,3-*c*]pyrazole scaffold for potential linker attachment, **16** and **18** were selected as starting points. Deprotection of the Cbz group was achieved under acidic conditions in concentrated HCl. The selective reduction of the aromatic nitro group was performed with $SnCl_2$, to leave the Cbz group intact (Scheme 4).

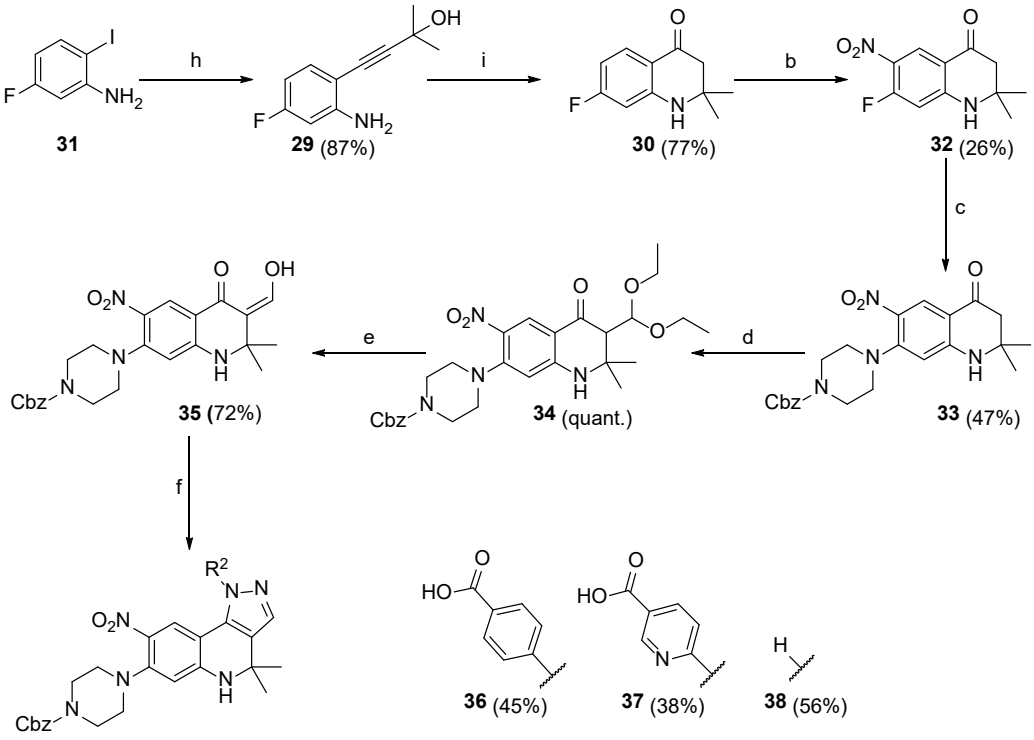

Scheme 5: Synthetic strategy to generate quinolino[4,3-*c*]pyrazoles**.** (b) 70% nitric acid, conc. H_2SO_4, 0 °C, 2 h. (c) 1-((benzyloxy)carbonyl) piperazine , K_2CO_3, MeCN, 40 °C, 16 h. (d) $BF_3{\cdot}Et_2O$, triethyl orthoformate, DCM, -5 °C to 0 °C, then -78 °C and then warm to room temperature for 2 h. (e) I_2, acetone, 35 °C, 16 h. (f) hydrazine derivative, acetic acid, 35 °C, 2 h. (h) 2-methylbut-3-yn-2-ol, $Pd(PPh_3)Cl_2$, CuI, Et_3N, 50 °C, ACN, 1.5h. (i) PTSA, EtOH, reflux, 10 h.

From **16**, **39,** and **40** were synthesized by nucleophilic substitution on the primary amine. Substitution with 1-bromo-2-chloroethane gave **39** and **40** was produced using 2-chloroacetyl chloride. Through the alkyl- and acyl products, a potential conclusion about the importance of the carbonyl group on the general interaction can be investigated. Similarly, the secondary amine of the piperazine moiety of **18** was also substituted with **12** and **13**. While **41** was not obtained successfully, **42** could be synthesized in moderate yield. This was the first step to further investigate the potential SAR of this position in the core scaffold. Additionally, it can be considered to exchange the piperazine moiety altogether as this moiety was chosen by the authors for its beneficial pharmacological properties (Scheme 6).[82]

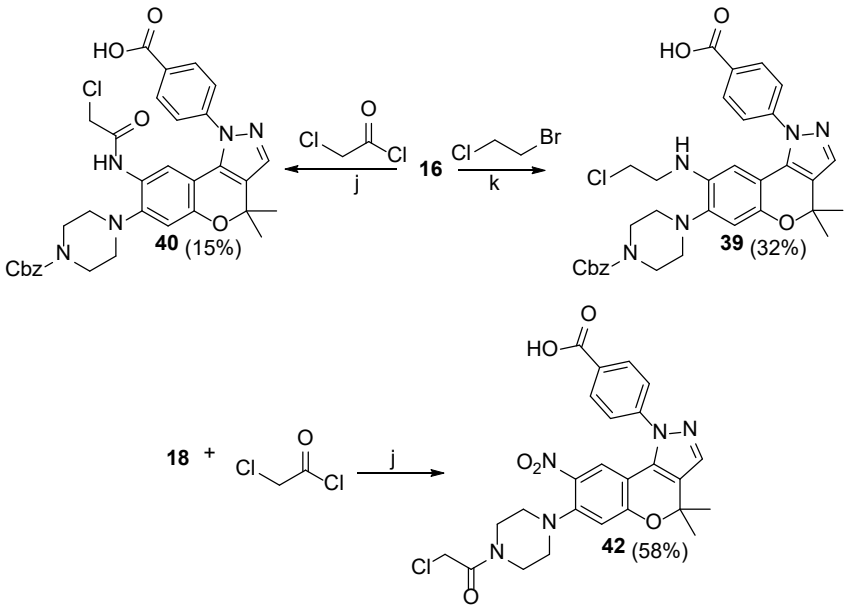

Scheme 6: Synthesis of test compounds to validate potential linker attachment point on the chromeno[4,3-*c*]pyrazole scaffold. j) TEA, dry THF, rt, 1 h. k) K_2CO_3, ACN, 80 °C, on.

3.1.2 Biological Evaluation through Single Dose EMSA

Biological evaluation of the compounds was performed using electrophoretic mobility shift assay (EMSA). The aim of the chromeno[4,3-*c*]pyrazole library was to improve the compounds' ability to perturb the LIN28–*let-7* interaction and identify potential linker attachment sites on the scaffold. The first step was to optimize the potency of the compound *in vitro*. To obtain a general overview of the synthesized compounds, a single dose EMSA was performed at 75 µM compound concentration. LIN28 protein and preE-*let-7-1f*-Cy3 were selected to obtain a fluorescent readout. For positive controls, an excess of unlabeled preE-*let-7-1f* and known inhibitors SB1301 were used for comparison.[69] In case a compound was comparably potent as selected positive controls to disrupt the LIN28–*let-7* interaction, a band in the lower part of the gel will develop, indicating free preE-*let-7-1f*-Cy3. If the compound does not possess an inhibitory character, only a band at the bottom of the gel will be visible, indicating the intact LIN28–*let-7* complex.

Table 1: Summary of the SAR of the synthesized chromeno[4,3-*c*]pyrazoles selected for biological evaluation and their respective relative inhibition values determined from single dose EMSA at 75 µM.

Compound ID	R^1	R^2	R^3	% Inhibition
SB1301/7	4-((benzyloxy)carbonyl) piperazin-1-yl	4-carboxyphenyl	nitro	100
13	4-((benzyloxy)carbonyl) piperazin-1-yl	phenyl	nitro	0
14	4-((benzyloxy)carbonyl) piperazin-1-yl	benzyl	nitro	0
25	1-(*tert*-butoxycarbonyl) piperidin-3-yl)amino	4-carboxyphenyl	nitro	0
11	4-((benzyloxy)carbonyl) piperazin-1-yl	3-carboxyphenyl	nitro	93
12	4-((benzyloxy)carbonyl) piperazin-1-yl	2-carboxyphenyl	nitro	36
8	4-((benzyloxy)carbonyl) piperazin-1-yl	4-sulfoxyphenyl	nitro	98
9	4-((benzyloxy)carbonyl) piperazin-1-yl	4-carboxypyridin-2-yl	nitro	57
10	4-((benzyloxy)carbonyl) piperazin-1-yl	H	nitro	0
18	piperazin-1-yl	4-carboxyphenyl	nitro	0
23	4-morpholino	4-carboxyphenyl	nitro	0
24	piperidin-1-yl	4-carboxyphenyl	nitro	95
21	4-(*tert*-butoxycarbonyl) piperazin-1-yl	4-carboxyphenyl	nitro	0
19	4-(benzylcarbamoyl) piperazin-1-yl	4-carboxyphenyl	nitro	98
20	4-(benzyl(methyl) carbamoyl)piperazin-1-yl	4-carboxyphenyl	nitro	0
15	4-((benzyloxy)carbonyl) piperazin-1-yl	4-carboxyphenyl	H	0
16	4-((benzyloxy)carbonyl) piperazin-1-yl	4-carboxyphenyl	NH_2	25
17	4-((benzyloxy)carbonyl) piperazin-1-yl	4-carboxyphenyl	nitro[a]	79
22	fluoride	4-carboxyphenyl	nitro	0
42	4-(2-chloroacetyl) piperazin-1-yl	4-carboxyphenyl	nitro	60
39	4-((benzyloxy)carbonyl) piperazin-1-yl	4-carboxyphenyl	(2-chloroethyl)amino	0
40	4-((benzyloxy)carbonyl) piperazin-1-yl	4-carboxyphenyl	2-chloroacetamido	100

[a]nitro group at 6-position, instead of 8-position of chromeno[4,3-*c*]pyrazole

The library of chromeno[4,3-*c*]pyrazoles was tested in a single dose EMSA. In this assay, the original literature compound SB1301 was used as a positive control to compare the derivatives to the original hit (Table 1). The initially attempted alterations to the R^1 residue were moderately tolerated. Removal of the Cbz-group **18** or substitution to a more polar morpholine **23** was not tolerated and resulted in a complete loss of activity. The substitution of the piperazine moiety for a chiral center, including a nonaromatic hydrophobic group in **25,** also showed no activity. Similarly, keeping the piperazine moiety but with a *tert*-butoxycarbonyl group **21** instead of the Cbz group also entirely lost the activity to perturb the interaction. Retaining the initial fluoride substituent throughout the synthesis, as in **22**, also did not improve targeting this interaction. Substituting the original carbamate region into a carbamoyl **19** retained activity comparable to the literature compound at 98% inhibition. Methylating the free amino group of the newly introduced carbamoyl (**20**) led to a complete loss of activity. The most promising substituent for this position was piperidine **24** with a relative inhibition of 95%. Thus, the R^1 derivatives, **24** and **19** were selected for the dose-response EMSA to determine their respective IC_{50} values (Figure 11). The initial investigation suggested that a hydrophobic patch on the protein surface is targeted by the R^1 residue. In addition, aromatic stacking interactions are likely to be involved, as indicated by the loss of activity in **21**.

Substituents on the R^2 position were introduced to explore any flexibility of the carboxylic acid moiety. A shift in the carboxylic acid to the meta position **11** was well tolerated with a relative inhibition of 93%. Whereas the para position **12**, observed 36% relative inhibition. Substituting the carboxylic acid to a sulfonic acid **8** retained activity with 98% but the introduction of a pyridine ring instead of a phenyl ring **9** significantly decreased the observed activity to 57%. Removing the carboxylic acid and leaving either a phenyl **13** or a benzyl **14** moiety lost the entire activity. The complete removal of the R^2 residue **10** also led to a complete loss of activity. Therefore, sulfonic acid **8** was selected for dose dependent EMSA (Figure 11).

Removal of nitro group **15** led to a complete loss of activity, whereas the aniline **16** reduced activity significantly but still showed 25% inhibition. Change in the nitro position **17** was tolerated well, retaining 79% relative inhibition. As a result, **17** were chosen for a dose dependency investigation (Figure 11).

Lastly, the quinolino[4,3-*c*]pyrazoles were investigated. The analog with the same substitution pattern as SB1301, **36**, demonstrated 21% inhibition. Substitution of the original oxygen atom seems to be more favored than a secondary amine in the 1-position. As expected from this initial

data, **37** as a quinoline analog of **9** and **38** as a quinoline analog of **10** showed no inhibition (Table 2). Therefore, none of the quinoline derivatives were selected for further dose-response investigation.

Table 2: Summary of the SAR of the synthesized quinonlino[4,3-*c*]pyrazole, selected for biological evaluation and their respective relative inhibition values determined from single dose EMSA at 75 µM compound concentration.

Compound ID	R^1	R^2	R^3	% Inhibition
36	4-((benzyloxy)carbonyl) piperazin-1-yl	4-carboxyphenyl	nitro	21
37	4-((benzyloxy)carbonyl) piperazin-1-yl	4-carboxypyridin-2-yl	nitro	0
38	4-((benzyloxy)carbonyl) piperazin-1-yl	H	nitro	0

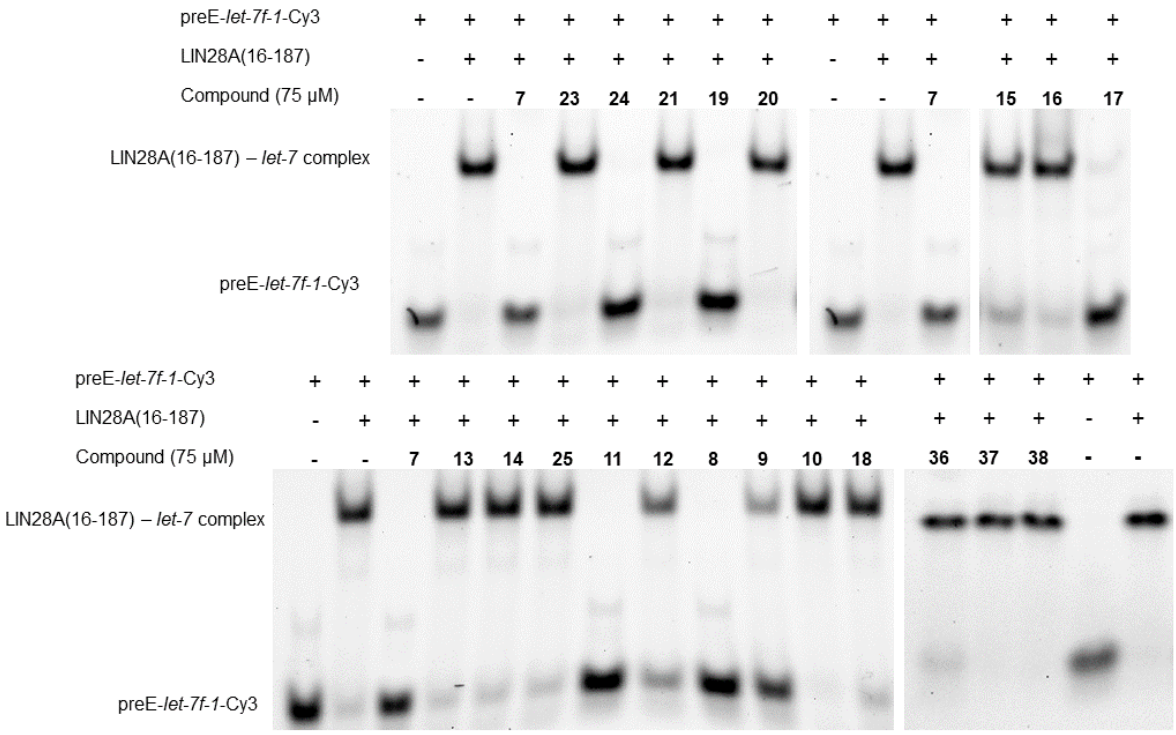

Figure 11: Screening EMSAs of various chromeno[4,3-*c*]pyrazole-based small-molecules (representative).

3.1.3 Biological Evaluation Dose Response EMSA

Following up on the most active compounds and elucidating the potential effects of LIN28 affinity in more detail, dose-response EMSAs were performed. Determination of IC_{50} values required the compounds to be applied in a dilution series ranging from 75–5 µM or for more potent inhibitors from 45–0.18 µM. Compound **7** was used as a positive control in the assay.

To establish a measure for the effect of the selected modifications of the chromeno[4,3-*c*]pyrazole scaffold, the IC_{50} value of **7** was determined. EMSA band evaluation resulted in an IC_{50} of 10.1 µM (Figure 12). While a shift in the nitro group from the 8- to the 6-position on the scaffold seemed comparable in the single dose measurement as **17** showed an IC_{50} of 40.1 µM in the dose-response EMSA (Figure 12). Similarly, the substitution of the 4-carboxyphenyl residue on the R^2 position into a 4-sulfoxyphenyl residue **8** resulted in an IC_{50} of 28.1 µM (Figure 12). The shift in the carboxylic acid around the aromatic moiety of the R^2 residue introduced in **11**, resulted in a worse affinity than the original literature compound once it was analyzed in more detail. Compound **11** showed an IC_{50} of 50.5 µM (Figure 12). Both substitutions decreased the activity from **7** and suggested an unfavorable substitution pattern. Substitution of the Cbz-piperazine group into piperidine on **24** resulted in an IC_{50} of 67.8 µM (Figure 12). On the contrary, the unmethylated carbamoyl moiety on **19** needed to be re-evaluated as the concentration range from 75–5 µM did not allow for IC_{50} determination (Figure 12 and Scheme 7). Re-evaluation of **19** in the range from 45–0.18 µM resulted in an IC_{50} of 3.95 µM (Figure 31).

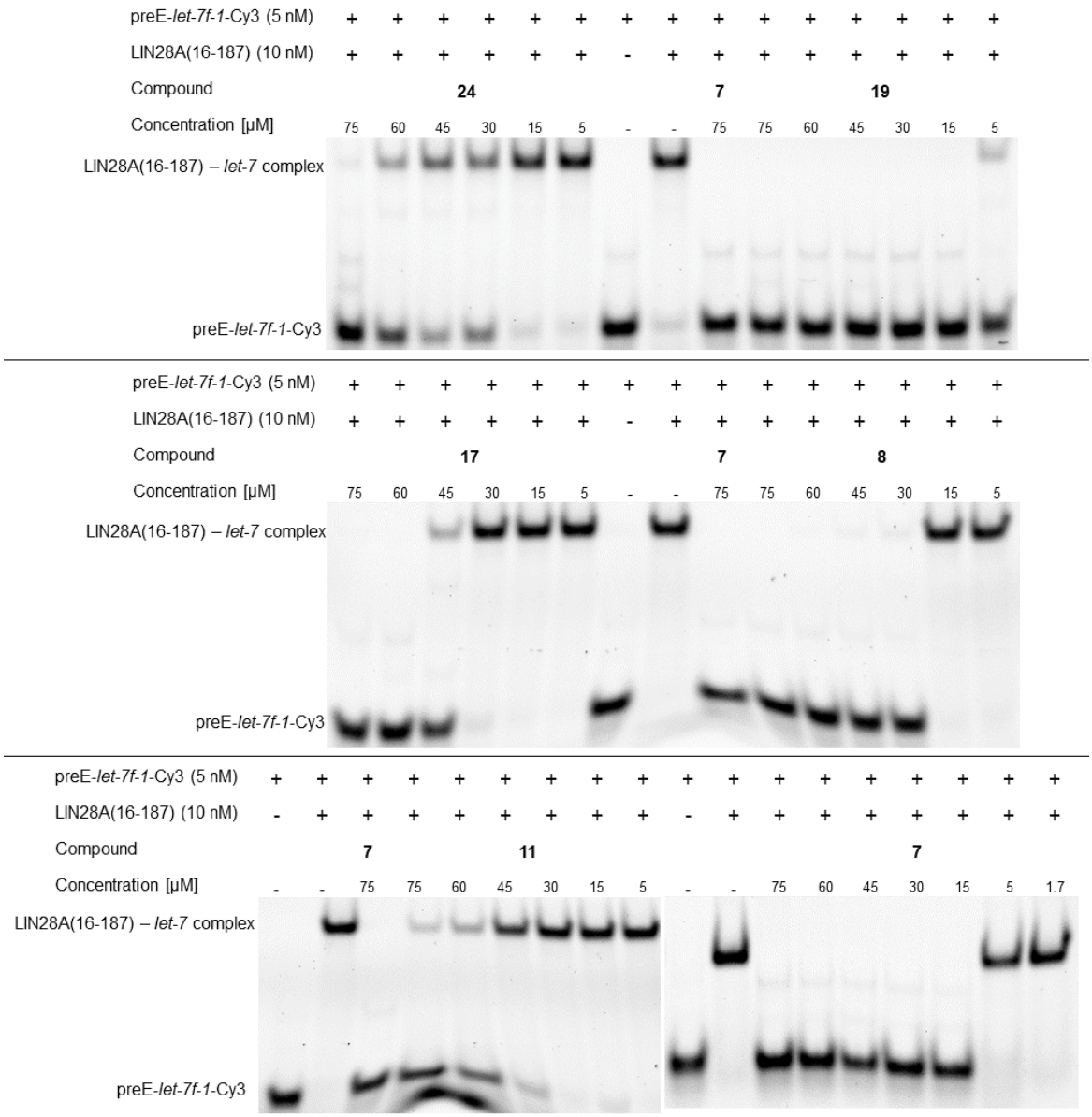

Figure 12: Dose-response EMSAs of most active chromeno[4,3-*c*]pyrazole inhibitors. **24**, **19**, **17**, **8**, **11,** and **7** were investigated in the concentration range from 75 to 5 µM (representative).

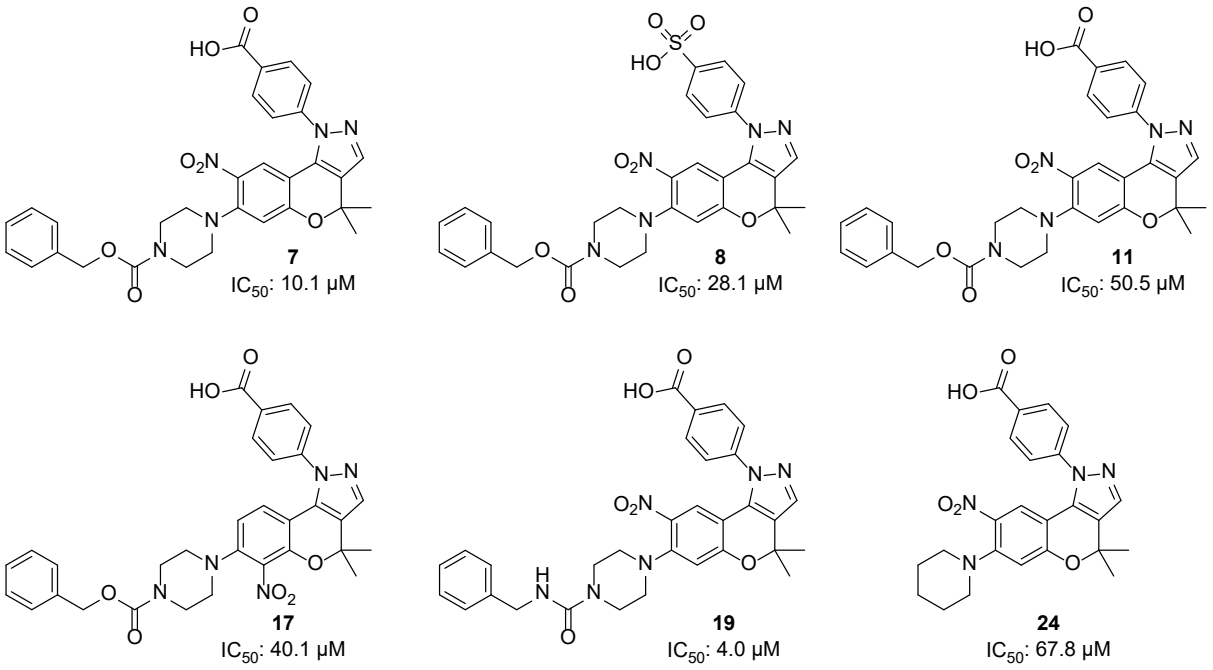

Scheme 7: Structure and determined corresponding IC_{50} values for all selected candidates with the Chromeno[4,3-*c*]pyrazole core scaffold.

3.1.4 Evaluation of Chromeno[4,3-*c*]pyrazole Scaffold for the NEC Strategy

Lastly, the linker probes were further evaluated. As both **18** and **16** showed a complete loss of activity by removing the Cbz group or reducing the nitro group, further modifications should be performed to evaluate the linker attachment points. To enable this evaluation, **42**, **39,** and **40** were synthesized. The idea was to investigate if the missing oxygen atom, in the form of the nitro group or in form of the carbamate, has an essential effect on the interaction or if the increase in polarity, by removal of the previously mentioned groups caused the loss of activity. The alkyl amino **39** showed no inhibitory activity, suggesting that a 2-chloroethyl amino moiety is not sufficient to recover the compound's affinity. Next, amide **40** was tested and showed full recovery of the LIN28 inhibitory effect at 75 µM in the single dose EMSA. This result suggests that the interaction of an oxygen atom in this position of the molecule is essential for the interaction with the LIN28 protein. Therefore, this position is feasible to introduce potential linker moieties through an amide bond. Based on this result, **39** was synthesized to observe, if retaining the carbonyl group but substituting the aromatic ring will be tolerated. Through single-dose EMSA, a drop to 60% inhibition was observed (Figure 11).

The reported chromeno[4,3-*c*]pyrazole scaffold qualifies as a starting point for small molecule-peptide conjugate to target the RBP LIN28. The proven selectivity for the CSD and the limited SAR around this scaffold qualified it as a potential starting point for the design of NEC probes.

During our investigation into the potential of this scaffold, we were able to identify two suitable positions to introduce the linker for the creation of a bifunctional molecule. Both the R^1 and the R^3 handles retained activity or showed improvements towards LIN28–*let-7* RNP complex perturbation. The limitation for R^1 and R^3 allows for the introduction of the respective linkage through an amide bond or a substituted piperidine. This qualifies the chromeno[4,3-*c*]pyrazole scaffold as the designated small molecule component for the NEC strategy due to the scaffold's selectivity and potential for biofunctionalization.

3.2 Assembly and Construction of Bifunctional NEC Molecules

3.2.1 Design of NEC Moieties

The ability to disrupt PRIs selectively has gained a significant increase in attention from the drug discovery community. Since RNA has become of increasing interest to the community, it is in urgent need to find tool compounds to further understand the mechanisms and pathways through which RNA and proteins determine the fate of the cell. Because PRIs share several features with protein-protein interaction inhibitors, targeting PRI interactions with a beyond "Rule of 5" mindset may lead to comparable successes.[87] Both interactions are area driven, meaning that a certain amount of hotspots need to be covered with a specific secondary structure to initiate the interaction.[88,89] A hotspot is defined as an area or amino acid on the protein surface that contributes significantly more to the respective binding than other areas or amino acids.[90] Through this main criteria, a traditional small molecule will, in most cases, not achieve a high potency to inhibit this interaction, because it cannot cover enough hotspots. Therefore, the approach of a bifunctional molecule combining a selectivity-inducing and a potency-improving segment into one molecular entity could be a solution to this problem. In terms of the potency improving moiety, a molecule mimicking RNA features could not only lead to similar affinities when interacting with the protein surface but also repel the RNA by incorporating negatively charged moieties. To start the design for a LIN28 binding enhancing probe, a virtual alanine scan was performed to identify potential hotspot amino acids (Table 3). PRI HotScore was used to perform the virtual alanine scan.[91]

Table 3: Excerpt of the numerical results from PRI HotScore virtual alanine scan.[91] Results show the interaction score for the crystal structure of LIN28–*let*-7 (PDB: 5UDZ). Scores are classified into hotspots with values >2 (red), warm spots with values ≥1 and ≤2 (orange), and irrelevant amino acids with values ≤1 (white). For the full table see Table 17.

#Res-ID	AA	Chain	Interaction Score	#Res-ID	AA	Chain	Interaction Score
46	W	A	1.141	**46**	W	B	1.403
48	N	A	0.933	**48**	N	B	1.186
50	R	A	2.926	**50**	R	B	3.387
51	M	A	1.291	**51**	M	B	0.790
53	F	A	2.231	**53**	F	B	2.498
55	F	A	2.169	**55**	F	B	1.563
73	F	A	2.332	**73**	F	B	2.125
75	H	A	2.020	**75**	H	B	1.891
84	F	A	2.507	**84**	F	B	1.865
102	K	A	1.270	**102**	K	B	1.288
122	R	A	1.415	**122**	R	B	1.332
140	Y	A	3.504	**140**	Y	B	3.158
148	H	A	1.140	**148**	H	B	1.860
159	K	A	1.911	**159**	K	B	1.845
162	H	A	3.000	**162**	H	B	3.462
170	M	A	1.063	**170**	M	B	0.912
177	K	A	1.920	**177**	K	B	2.057

The authors of the web tool defined two different key interactors for the PRI. Amino acid residues that generate an interaction score between 1 and 2 are considered warmspots. These residues do not have an unproportionally high contribution to the interaction but are beneficial for binding, nonetheless. Hotspots were defined as any amino acid that scores a value above 2.[91] The number of warmspots is generally higher than the number of hotspots on the analyzed protein RNA interactions.[91] This ratio was also observed in the analysis of LIN28–*let*-7 crystal structure (Table 3). In detail, we obtained a total of 9 aromatic, 5 positively charged, and 3 neutral amino acid side chains that seem to have a significant contribution to the interaction. While N48, M51, and M170 can barely be considered warmspots, a clear difference between charged and aromatic side chains was observed. Positively charged amino acid side chains were represented for only 20% in the hotspot category, while 80% were ranked as warmspots. For the aromatic side chains, 56% contribute as hotspots while 44% score as warmspots. From this analysis, it can be observed that aromatic interactions seem to contribute significantly more toward the interaction between RNA and protein (Figure 13).

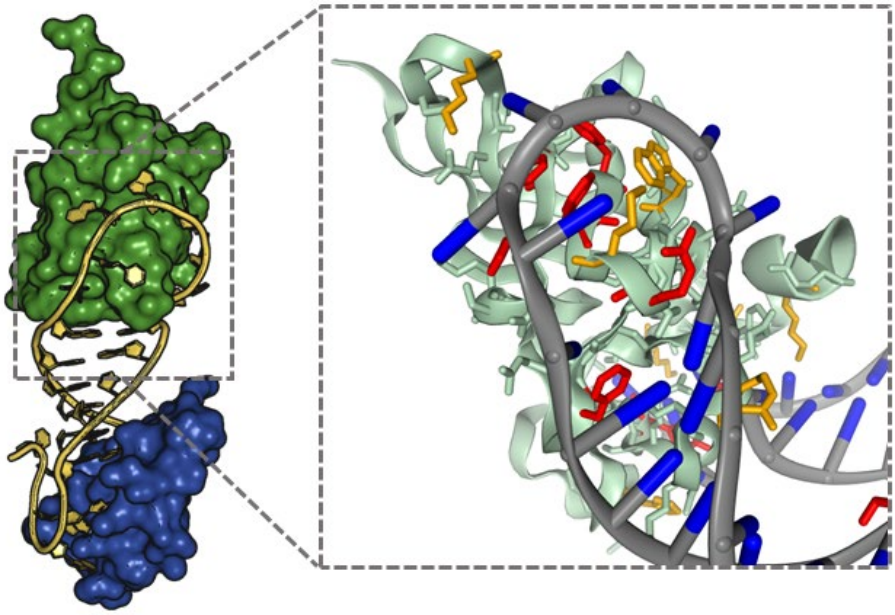

Figure 13: LIN28–*let-7* crystal structure (PDB: 5UDZ) and a zoom-in excerpt from the result generated by PRI HotScore. Hotspot amino acids (red) and warmspot (yellow) show the essential amino acids for the interaction of LIN28 (green) with *let-7f-1* (grey) according to the virtual alanine scan performed on LIN28–*let-7* crystal structure (PDB: 5UDZ).[91] Representation generated by NGL Viewer.[92]

With this initial analysis, the design of the improved inhibitor for this interaction was started. As a crystal structure only depicts a specific snapshot of the protein in solution and does not cover all the conformations, a broader approach needed to be considered. The reason is that most RBPs interact with several RNA partners instead of one specific RNA. The proteins achieve this by their specific combination of RNA binding domains and a flexible linker fragment connecting them.[44] Due to this inherent characteristic which also applies to LIN28, a surface area correlated approach was not considered. This was mainly caused by a lack of crystallographic data with a small molecule inhibitor, that would have confirmed any changes in the protein surface in comparison with the RNA-bound crystal structure. Instead, the hypothesis was created that an RNA mimetic, in terms of charge per molecular volume, could yield the desired improved affinity. Fortunately, research has already measured the average volume occupied by a respective RNA base or their respective nucleotide (Table 4).[93]

Table 4: Molecular volumes determined for the individual RNA bases and their respective nucleotides.[93]

	Base Volume [Å³]	Nucleotide Volume [Å³]
GUA	145.9	322.6
ADE	139.2	315.0
CYT	115.0	290.7
URI	110.8	285.5
SUG	176.1	-

The respective RNA fragments were then analyzed with the average occupied volumes from the literature to generate the volume/charge ratio (Table 5). As both, the overall fragment as well as the selected RNA segment, seem to result in a very comparable volume/charge ratio, a value of ~300 Å³ was chosen for the future design.

Table 5: Analysis of *let-7-1f* fragment from the employed crystal structure (PDB: 5UDZ). The upper fragment is the full sequence of the crystalized RNA, lower entry is the selected sequence that is occupying the surface area with most hot- and warmspots from the PRI HotScore analysis.

	Total Volume [Å³]	Total Charge	Volume/Charge
GGGGUAGUGAUUUUACCCUGGAGA	7349.0	24.0	306.2
AGUGAUUUUAC	3308.4	11.0	300.8

With a guide for the future design in place, the next step was an analysis of the amino acids available for the design. Volume determination for amino acids in solution has already been investigated as well. Additionally, it was also concluded that a protein is usually found to be bigger than the added sums of each amino acids individual volume (Table 6).[94]

Table 6: Values for the molecular volume occupied by individual amino acids.[94]

Amino Acid	Molecular Volume [Å³]	Amino Acid	Molecular Volume [Å³]
Alanine	88.6	**Leucine**	166.7
Arginine	173.4	**Lysine**	168.6
Asparagine	114.1	**Methionine**	162.9
Aspartic Acid	111.1	**Phenylalanine**	69.9
Cysteine	108.5	**Proline**	112.7
Glutamine	143.8	**Serine**	89.0
Glutamic Acid	138.4	**Threonine**	116.1
Glycine	60.1	**Tryptophane**	227.8
Histidine	153.2	**Tyrosine**	193.6
Isoleucine	166.7	**Valine**	140.0

The last necessary parameter for the design of the NEC peptides was obtained and attention was then focused on the actual design of the probes.

Table 7: Set of designed NEC peptides according to the previously determined design criteria to function as potential inhibition enhancers through the NEC strategy. X represents Isoleucine.

Sequence	Molecular Weight [g/mol]	Molecular Volume approximation [Å³]	Charge	Volume/Charge
DFEWDY (43)	873.32	971.9	-4	242.98
DIEMDY (44)	839.33	883.8	-4	220.95
EWDY (45)	611.22	670.9	-3	223.63
EMDY (46)	556.18	606.0	-3	202.00
QWNY (47)	609.25	679.3	-1	679.30
QMNY (48)	554.22	614.4	-1	614.40
QMNS (49)	478.18	509.8	-1	509.80
NFQWNY (50)	960.00	983.3	0	-
QWNY (51)	663.00	679.3	0	-
AAAA (52)	356.00	354.4	0	-
AAAAAA (53)	534.00	531.6	0	-
QXNS (54)	514.00	513.6	0	-
DIEXDS (55)	780.00	783.0	-4	195.75
EXDS (56)	516.00	505.2	-3	168.40

In summary, the design of the NEC probes should explore the impact of negative charges in our peptides on the inhibitory character of the bifunctional probes. It is also of high interest to observe the impact of different variations of aromatic side chains because the PRI HotScore analysis showed that these contribute significantly to the interaction between RNA and RBP. Furthermore, a rough guideline for the molecular volume-to-charge ratio was designed by following a closer analysis of the crystal structure. And lastly, it is of interest to vary the length of the respective peptide probes to determine the smallest necessary fragment size for the peptidic moiety. Peptides **43**–**49**, **55,** and **56** were synthesized on 2-chlorotrityl chloride resin. Therefore, all C-termini were free carboxylic acids, resulting in one additional negative charge. Peptides **50**–**54** were synthesized with rink amide resin and possessed an amide at the C-terminus.

For easier purification, most of the designed peptides (**43**, **44**, **45**, **46**, **47**, **48**, **50**, **51**) include a C-terminal Y. Since the inclusion of a Y not only improves the detection of the peptide in a UV detector during purification but also fits the design criteria of increasing the peptides aromaticity, this was an obvious choice. For the evaluation of the Y contribution to LIN28

inhibition, this amino acid was substituted for a S (**49**, **54**, **55**, **56**). Two control peptides as pure alanine multimers were synthesized (**52**, **53**) as negative controls. As a starting point for the design of NEC probes, **43** was designed. The sequence DFEWDY was chosen due to the design criteria mentioned above. Probe **43** contains four negative charges and has a volume-to-charge ratio of 242.98 Å³. The peptide was constructed exclusively from negatively charged or aromatic amino acids. To further investigate the effect of the aromatic side chains, two substitutions were performed to exchange the F to I and the W to M. For the F to I exchange, we hypothesized that a potential hydrophobic patch would still maintain an interaction, while a more π-stacking focused interaction might lose affinity. The W to M exchange was based on the PRI HotScore results which showed that in general, M can also have a beneficial effect on the respective interactions, and it is the largest non-aromatic amino acid capable of forming hydrogen bond interactions available for the design for **44**. For **44**, the four negative charges were retained, but due to the exchange of large aromatic amino acids, the volume-to-charge ratio decreased to 223.63 Å³. To shorten the peptide, two amino acids were removed from the N-terminus. This included the negatively charged D and either the F or I. Probe **45** contained the shortened sequence of **43** with only four amino acids EWDY. Therefore, **45** only contained three negative charges and has a volume-to-charge ratio of 223.63 Å³. Probe **46** contained the sequence EMDY and was the shortened sequence of **44**. With three negative charges, **46** had a volume-to-charge ratio of 202.00 Å³. Following this, peptides with fewer negative charges were designed. For example, **47** was designed with a sequence of QWNY and only contained the negative charge from the resin. Due to the low number of negative charges, the volume-to-charge ratio increased to 679.30 Å³. Similarly, **48** was designed with a sequence of QMNY to retain one negative charge, but also to evaluate the effect of the W to M substitution. Due to this substitution, there was a decrease in volume to charge ratio leading to a value of 614.40 Å³. As a control to evaluate the effect of the C-terminal Y, **49** was designed with a sequence of QMNS, containing one negative charge and a volume-to-charge ratio of 509.80 Å³. To validate if the charge of the C-terminus can also impact the interaction, several peptides were synthesized on rink amide resin to incorporate an amide instead of a charged carboxylic acid. Probe **50** was designed to evaluate the sole effect of aromatic moieties. With a sequence of NFQWNY, no charge was present in the peptide. Similarly, charge-free derivative **47**, was synthesized with **51**, where the only difference was the amide at the C-terminus. Besides the two polyalanine negative controls, **52** and **53**, an additional negative control containing no charge, no aromatic moiety, and no M was synthesized. In **54,** M was substituted for X which

represents Nle (since this amino acid has no predefined single-letter code). And finally, both **44** and **46** were designed as aromaticity and M-free derivatives. Derivative **55** contained a sequence of DIEXDS. The four negative charges provide a volume-to-charge ratio of 195.75 Å³. Whereas **56** contained a shorter sequence of EXDS with three negative charges and a volume-to-charge ratio of 168.40 Å³ (Table 7). With these 14 peptides, sufficient variations of the initial four design criteria were synthesized to establish a first proof of concept and understanding of the NEC strategy.

3.2.2 Synthesis of NEC Probes

Synthesis of the designed probes was performed in two batches. One batch of peptides was acetylated on the N-terminus to prevent any further reaction or positive charge formation. This was performed to evaluate the binding of the peptides only and later compare them to the fully conjugated NEC probes. The second batch of peptides was functionalized with three different polyethylene glycol linkers. These linkers were functionalized with the respective functional group to allow conjugation to the corresponding small molecule. Synthesis of the respective peptides was performed via established solid-phase peptide synthesis protocols following the Fmoc strategy (Scheme 8).[95]

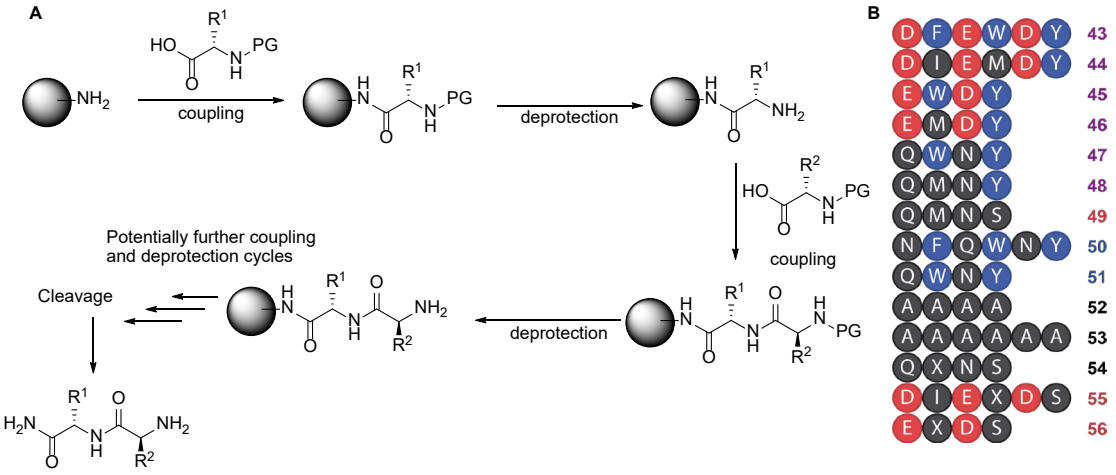

Scheme 8: A: Schematic depiction of the cycles generally performed in SPPS to obtain desired peptides. R represents potential amino acid side chains. PG represents the respective protection group. In the course of this work, Fmoc was used exclusively.[95] Grey ball represents attachment to solid phase resin. B: Synthesized peptides in the course of this work. Red balls indicate a negatively charged side chain. Blue balls represent amino acids containing aromatic side chains. Black balls contain neither aromatic side chains nor negative charges. Peptide identifiers are colored purple, red, blue, and black. Purple indicates the presence of aromatic and negatively charged amino acids, red indicates only negative charges are present. Blue represents peptides that only contain

aromatic side chains, but no negative charges, and black identifiers contain neither aromatic side chains nor negative charges.

Since the peptide component of the NEC probes posed no problem, the next step was the selection of a suitable linker. It was noted that linker selection and design in several bifunctional molecules play an essential role to determine the affinity of the probe.[79] In addition, the lack of structural data about the interaction and the knowledge of the inherent flexibility of LIN28 to bind several different pri- and pre-miRNAs required an investigation into the appropriate linker length. Because NECs need to cover a certain surface area to inhibit the interaction rather than stabilize a certain protein complex, the idea of short rigid linkers was disregarded as the NEC strategy is fundamentally different than PROTACs.[96] The most established linker employed in the design of bifunctional probes is the polyethylene glycol (PEG) linker. Therefore, owing to its accessibility and proven functionality, the core linker fragment was decided to be PEG based. For the easy combination of fragments of different linker lengths and the incorporation of an additional aromatic fragment, copper-catalyzed azide-alkyne cycloaddition chemistry was chosen to conjugate the peptide and small molecule entities.

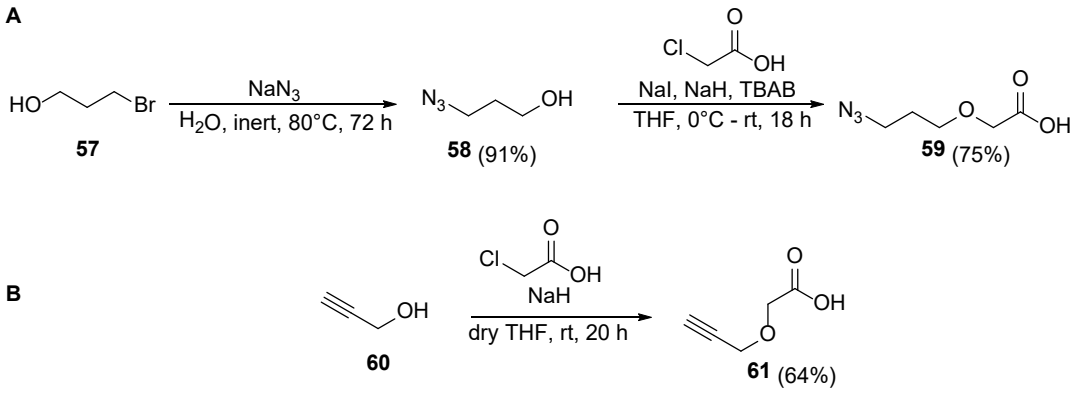

Scheme 9: Synthetic route to obtain functionalized click chemistry compatible linkers. Route A generates 2-(3-azidopropoxy)acetic acid, which can then later be combined with the product of route B, 2-(prop-2-yn-1-yloxy)acetic acid in a CuAAC type reaction.

Starting from alkyl bromide **57**, substitution in an aqueous environment with sodium azide generated **58** in 91% yield. Formation of linker fragment **59** occurred through the substitution of 2-chloroacetic acid with an alcohol in good yield (75%) (Scheme 9 A). The complementary linker fragment **61** could be obtained in a single step by substituting 2-chloroacetic acid with **60** in moderate yield (64%) (Scheme 9 B).

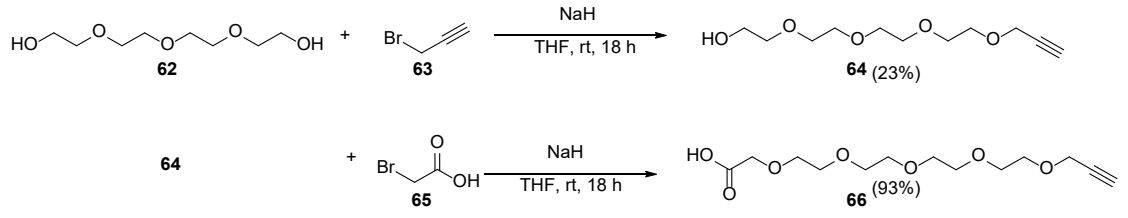

Scheme 10: Two-step synthetic route to obtain long alkyne functionalized PEG linker for the incorporation into the conjugation of the NEC probes.

After the synthesis of the short linker fragments, the next step was to generate longer PEG linkers, so that in total 4 combinations of NEC probes can be synthesized. Firstly, the alkyne moiety was introduced through the substitution of the bromide on **65** with the alcohol **62** to obtain **64** in a yield of 23%. The carboxylic acid moiety was introduced through a substitution reaction of **64** with **65** to generate **66** in good yield (93%) (Scheme 10).

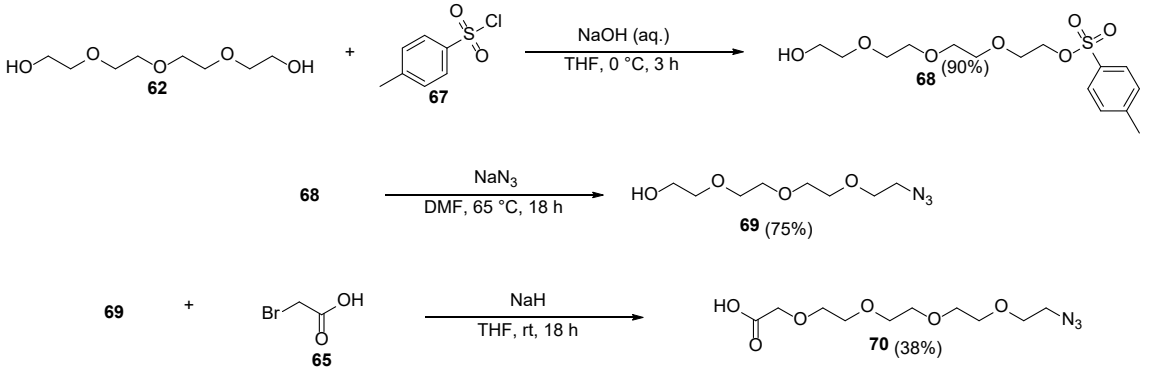

Scheme 11: Three-step synthetic route to obtain long azide functionalized PEG linker for incorporation into the conjugation of the NEC probes.

Lastly, the final fourth linker was synthesized over three steps. Starting from PEG linker **62**, mono-activation of the hydroxy group was performed through the introduction of a tosyl group using **67** to generate **68** in excellent yield (90%). The tosylated PEG **68** then underwent a substitution reaction with sodium azide to obtain **69** in good yield (75%). The carboxylic acid moiety was again introduced through the substitution with **65** to yield the final functionalized PEG linker **70** in moderate yield (38%) (Scheme 11).

With the completion of the four different linker fragments, the small molecule was the last remaining piece to be synthesized. As all linkers were functionalized with a carboxylic acid moiety, incorporation into SPPS was possible without any additional changes. Small molecule moiety **16** was selected as the initial scaffold for the NEC molecules. In the initial analysis, it

was shown that the functionalization of the aniline moiety in **16** through an amide bond (**40**) has the potential to recover the compound's inhibitory activity.

To obtain the two necessary small molecules, **16** was introduced to the two linkers, **59** and **70**, via the aniline position using thionyl chloride. The resulting probes generated good yields **71** (75%) and **72** (64%) (Scheme 12).

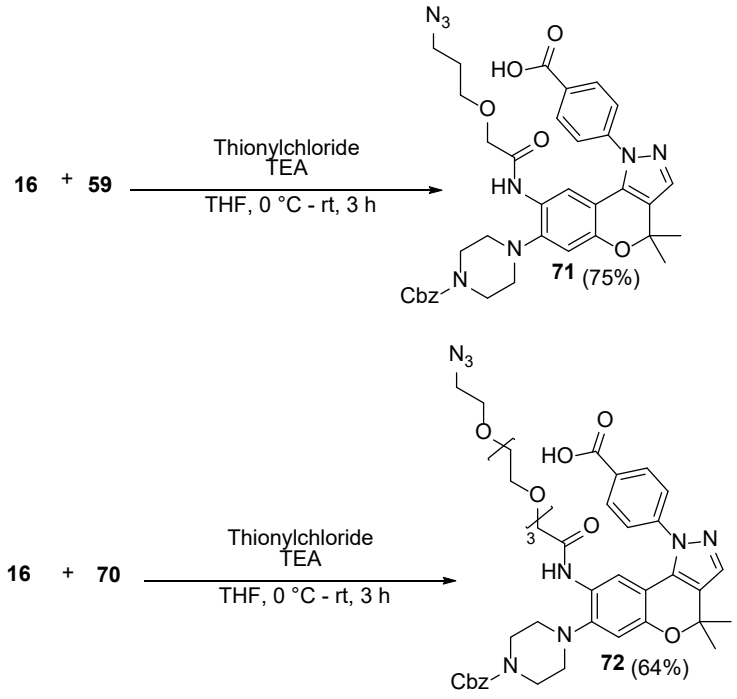

Scheme 12: Introduction of respective azide functionalized linker to generate the final small molecule probes for the NEC strategy.

To generate the library of NEC molecules, copper-catalyzed azide-alkyne cycloaddition chemistry (CuAAC) was employed. Peptides and small molecules were conjugated by CuAAC and the assistance of the ligand Tris[(1-benzyl-1H-1,2,3-triazol-4-yl)methyl]amin) (TBTA) to yield the desired compounds (Scheme 13).

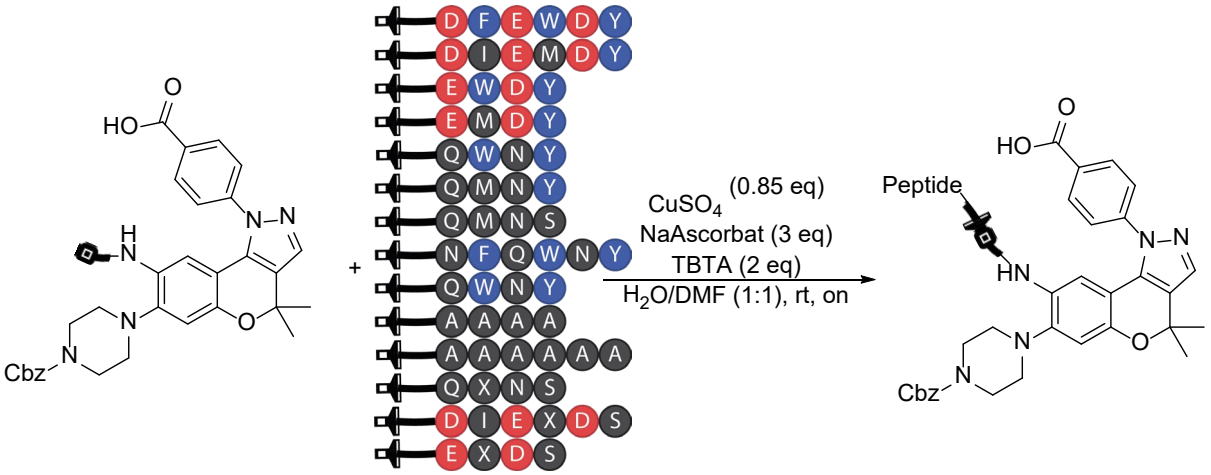

Scheme 13: General reaction for the conjugation of the four generations of NEC molecules. The buckle lock indicates either long or short azide linker, the buckle link indicates the short or long alkyne linker. The connected link and lock symbolizes the obtained triazole moiety after performing CuAAC. Red indicates a negatively charged side chain. Blue represents amino acids containing aromatic side chains, and black color contains neither aromatic side chains nor negative charges.

To evaluate the effect of different linker lengths, all combinations with the above-mentioned linkers were produced. First-generation NEC probes employed both short alkyne and azide linkers on the small molecule and peptide, respectively. Whereas second-generation NECs were synthesized as the direct opposite as both azide and alkyne were the longer PEG version. The third generation was conjugated as a combination of a long azide and short alkyne linker and the final generation was the opposite with a short azide but long alkyne linker. The purpose was to potentially induce different orientations for the formed triazole moiety by introducing different degrees of freedom on the two connection positions (Table 8). After the initial evaluation of the acetylated peptides and the first generation of NEC probes, the following generations of NEC molecules were designed in smaller sets as initial results suggested this to be more meaningful. Therefore, the bifunctional probes were reduced from 14 to 9 conjugates per set.

Table 8: Overview of all synthesized NEC moieties. The single letter code X represents the amino acid norleucine as no predefined single letter code is commonly agreed upon.

NEC Generation	Compound	Small Molecule	Peptide	Peptide sequence	Peptide Linker
1	**73**	**71**	**43**	DFEWDY	**61**
1	**74**	**71**	**44**	DIEMDY	**61**
1	**75**	**71**	**45**	EWDY	**61**
1	**76**	**71**	**46**	EMDY	**61**
1	**77**	**71**	**47**	QWNY	**61**
1	**78**	**71**	**48**	QMNY	**61**
1	**79**	**71**	**49**	QMNS	**61**
1	**80**	**71**	**50**	NFQWNY	**61**
1	**81**	**71**	**51**	QWNY	**61**
1	**82**	**71**	**52**	AAAA	**61**
1	**83**	**71**	**54**	QXNS	**61**
1	**84**	**71**	**55**	DIEXDS	**61**
1	**85**	**71**	**56**	EXDS	**61**
2	**86**	**72**	**43**	DFEWDY	**66**
2	**87**	**72**	**44**	DIEMDY	**66**
2	**88**	**72**	**45**	EWDY	**66**
2	**89**	**72**	**46**	EMDY	**66**
2	**90**	**72**	**47**	QWNY	**66**
2	**91**	**72**	**48**	QMNY	**66**
2	**92**	**72**	**49**	QMNS	**66**
2	**93**	**72**	**50**	NFQWNY	**66**
2	**94**	**72**	**56**	EXDS	**66**
3	**95**	**72**	**43**	DFEWDY	**61**
3	**96**	**72**	**44**	DIEMDY	**61**
3	**97**	**72**	**45**	EWDY	**61**
3	**98**	**72**	**46**	EMDY	**61**
3	**99**	**72**	**47**	QWNY	**61**
3	**100**	**72**	**48**	QMNY	**61**
3	**101**	**72**	**49**	QMNS	**61**
3	**102**	**72**	**50**	NFQWNY	**61**
3	**103**	**72**	**56**	EXDS	**61**
4	**104**	**71**	**43**	DFEWDY	**66**
4	**105**	**71**	**44**	DIEMDY	**66**
4	**106**	**71**	**45**	EWDY	**66**
4	**107**	**71**	**46**	EMDY	**66**
4	**108**	**71**	**47**	QWNY	**66**
4	**109**	**71**	**48**	QMNY	**66**
4	**110**	**71**	**49**	QMNS	**66**
4	**111**	**71**	**50**	NFQWNY	**66**
4	**112**	**71**	**56**	EXDS	**66**

3.2.3 Biological Evaluation of NEC Probes in Single-Dose EMSA

Biological evaluation of the bifunctional probes was first performed through single-dose EMSA. The aim of this library was to investigate the NECs ability to perturb the LIN28–*let-7* interaction and identify potential linker length and peptide sequence which improve the affinity compared with the original molecule SB1301 (**7**). This is the first step toward establishing a generally applicable concept to apply the NEC strategy in the field of RBP inhibition. To obtain a general overview of the synthesized compounds, a single dose EMSA was performed at 75 µM compound concentration. LIN28 protein and preE-*let-7-1f*-Cy3 were selected to give a fluorescent readout. For positive controls, an excess of unlabeled preE-*let-7f* and an already published inhibitor PH-31 were used as well.[68] If a compound is potent enough to disrupt the LIN28–let-7 interaction, a band in the lower part of the gel will appear, indicating free preE-*let-7-1f*-Cy3. If the compound does not possess an inhibitory character, only a band in the upper part of the gel will be visible, indicating the intact LIN28–*let-7* complex.

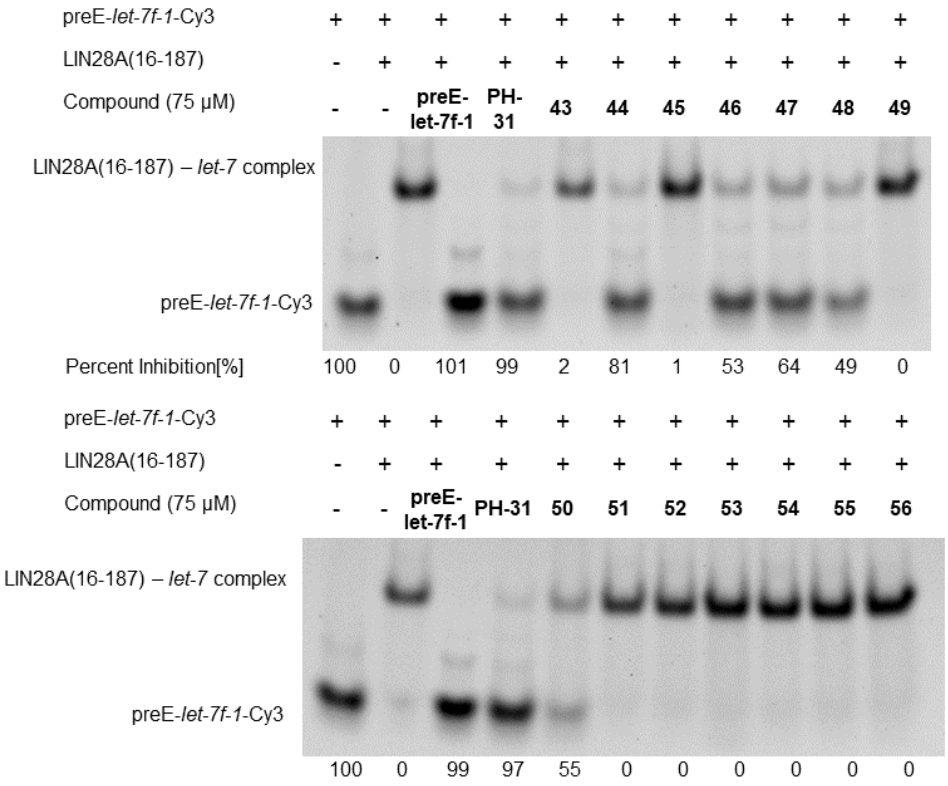

Figure 14: Single Dose Screen of the acetylated peptides. LIN28 was incubated with 75 µM peptide. preE-*let-7f-1*-Cy3 was added to generate a fluorescent readout. RNP can be observed in the upper part of the gel. If the compound can perturb the complex, inhibition can be observed through an electrophoretic mobility shift indicated by a shift of the fluorescent signal to the lower part of the gel. preE-*let-7f-1* and PH-31 are used as positive controls.

The first set of compounds to be evaluated were the acetylated peptides. The most active peptides among the initial batch were **44**, **47,** and **50** with a mean percent inhibition of 75%, 61%, and 63%, respectively. Additionally, both **46** and **48** showed an average percent inhibition of 56%**.** All other acetylated peptides were inactive (Figure 14 and Figure 32). For the initial design, this was already the first hint that the correct criteria were being met. The individual small molecules functionalized with the linker and still containing the azide moiety, **71** and **72**, both showed an average percent inhibition of 99%. This confirmed that the aniline moiety was a good linker attachment point through amide coupling (Figure 17 and Figure 34).

The most active conjugate from the first generation of NEC molecules was **80** with 98% inhibition. The remaining conjugates all displayed less activity in their conjugated form than they showed in their acetylated peptide form. This indicated that two short linkers could have led to increased rigidity of the molecule preventing proper binding to the LIN28 surface (Figure 15 and Figure 32).

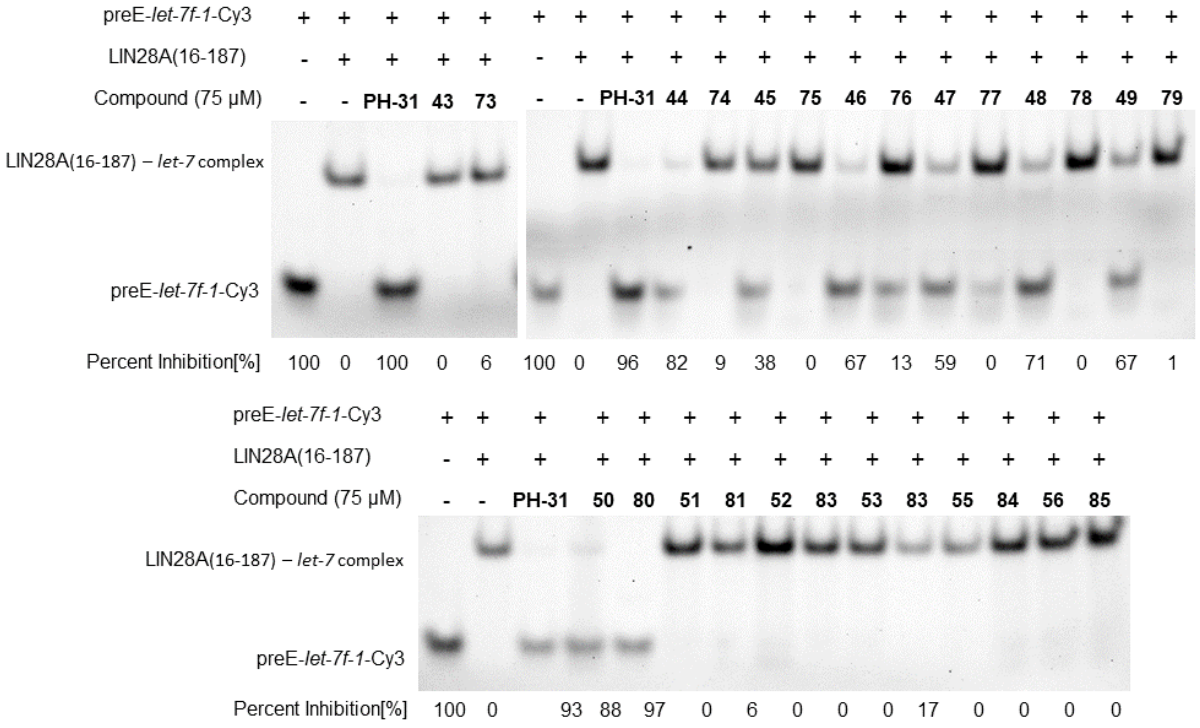

Figure 15: Single Dose Screen of the first-generation NEC peptides. LIN28 was incubated with 75 µM peptide. preE-*let-7f-1*-Cy3 was added to generate a fluorescent readout. RNP can be observed in the upper part of the gel. If the compound can perturb the complex, inhibition can be observed through an electrophoretic mobility shift indicated by a shift of the fluorescent signal to the lower part of the gel. preE-*let-*7f-1 and PH-31 are used as positive controls.

In contrast to the first-generation NECs, peptides from the second generation were synthesized exclusively with the longer linkers. The counterpart to peptide **50** was still active with an average percent inhibition of 100%. Contrary to previous observations, now the corresponding probe to the peptide sequence of **45** was active. During the purification, two fractions were isolated that corresponded to the desired mass of **88**. Both isolated products from the reaction showed activity, **88-F21** displayed an average percent inhibition of 29% whereas **88-F23** showed an average percent inhibition of 63% (Figure 16 and Figure 33). The change in linker length clearly showed a change in LIN28 affinity of the respective peptides but the purely aromatic peptide sequence originally synthesized as **50** seems to be not as influenced by the potential increase in entropic penalty.

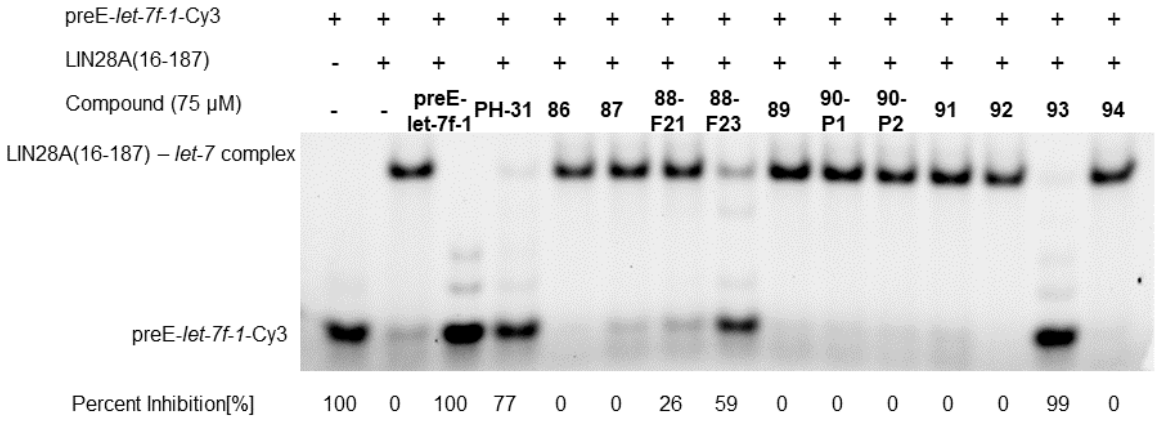

Figure 16: Single Dose Screen of the second-generation NECs. LIN28 was incubated with 75 µM peptide. preE-*let-7f-1*-Cy3 was added to generate a fluorescent readout. RNP can be observed in the upper part of the gel. If the compound can perturb the complex, inhibition can be observed through an electrophoretic mobility shift indicated by a shift of the fluorescent signal to the lower part of the gel. preE-*let-7f-1* and PH-31 are used as positive controls.

The third-generation of NEC compounds was synthesized with a more flexible long linker attached to the small molecule but a more rigid short linker attached to the peptide. Unlike the previous generation, the introduction of a more rigid linker on the peptide component completely removed the inhibitory character form the NEC based on peptide **45**. Nevertheless, **102**, which is again based on the peptide sequence form **50**, still showed an average percent inhibition of 100%. Yet, for the first time, the NEC moiety containing the peptide sequence based on **43** showed slight activity towards LIN28 inhibition with an average percent inhibition of 33%. All other molecules from the third generation of NEC compounds were considered inactive (Figure 17 and Figure 34).

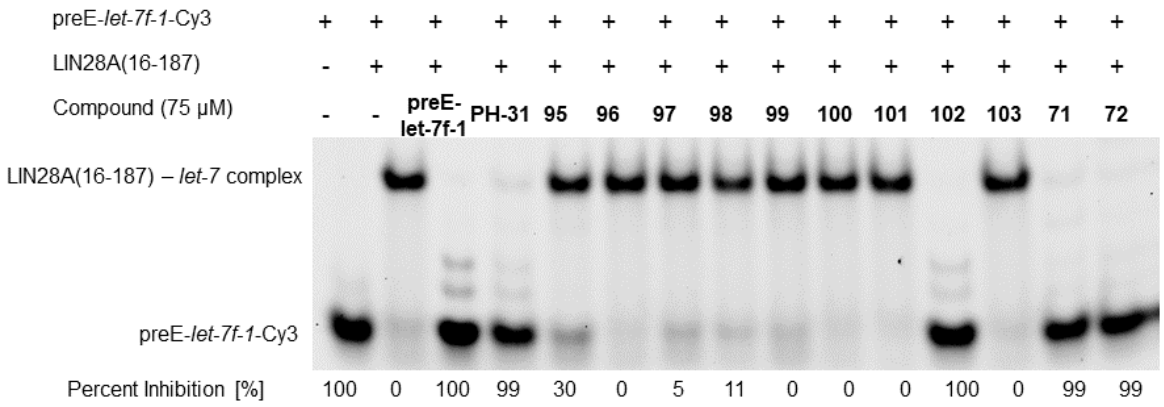

Figure 17: Single Dose Screen of third-generation NECs. LIN28 was incubated with 75 µM peptide. preE-*let-7f-1*-Cy3 was added to generate a fluorescent readout. RNP can be observed in the upper part of the gel. If the compound can perturb the complex, inhibition can be observed through an electrophoretic mobility shift indicated by a shift of the fluorescent signal to the lower part of the gel. preE-*let-7f-1* and PH-31 are used as positive controls.

The fourth-generation of NECs were synthesized with a short linker attached to the small molecule and a long linker fragment attached to the peptide. This linker variation was also unfavorable as all activity on the NEC based on peptide **43** was lost. The only NEC still active was again the peptide based on **50** with an average percent inhibition of 87% (Figure 18 and Figure 35).

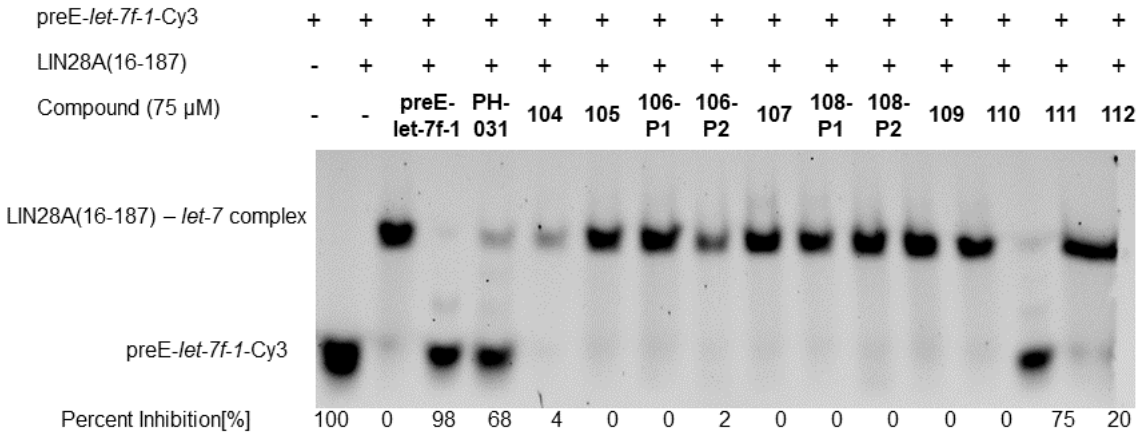

Figure 18: Single Dose Screen of the NEC generation four. LIN28 was incubated with 75 µM peptide. preE-*let-7f-1*-Cy3 was added to generate a fluorescent readout. RNP can be observed in the upper part of the gel. If the compound can perturb the complex, inhibition can be observed through an electrophoretic mobility shift indicated by a shift of the fluorescent signal to the lower part of the gel. preE-*let-7f-1* and PH-31 are used as positive controls.

With these results, the positive hits needed to be further investigated. Several tested NEC probes suggest a comparable inhibitory character in comparison with the positive controls. To get a better impression of the actual affinity of the compounds, dose-response EMSA for selected

NEC probes were performed to uncover a closer estimate of the NECs actual potency to perturb the LIN28–*let-7* interaction.

3.2.4 Biological Evaluation of NEC Probes Dose Response EMSA

EMSA evaluation was assisted by L. Borgelt.

The dose-response evaluation was performed on all compounds resulting in an average percent inhibition above 50% to gain a better understanding of the SAR around the NEC design. Beginning with **80** and **88**. IC_{50} values generated here are to be interpreted as approximations to make the individual compounds numerically comparable. As previously discussed, the assay readout and experimental design of EMSA prevent accurate determination of IC_{50} values if compared with other methods like competitive FP or ITC measurements.

Compound **80** showed very potent inhibition comparable with SB1301 (**7**) and PH-31. The IC_{50} was predicted to be 4.8 µM. The actual IC_{50} value is most certainly lower than this value as the plotted curve does not show the top plateau for both duplicates. Compound **88** showed only moderate inhibition and was determined to have an IC_{50} value of 36.5 µM. Due to the decrease in IC_{50} in comparison with other synthesized molecules, these probes' two fractions were not further investigated. (Figure 19 and Figure 36).

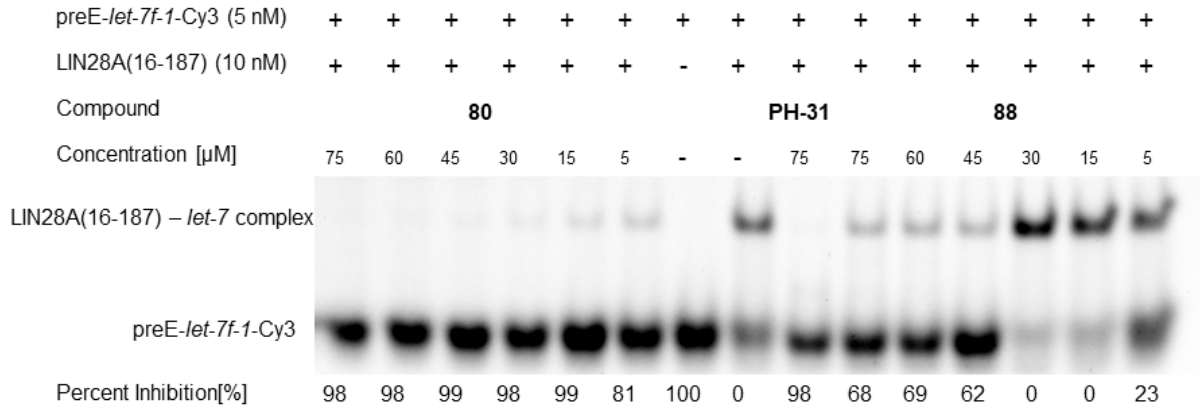

Figure 19: Dose-response EMSA of compounds **80** and **88**. Compound concentrations of 75, 60, 45, 30, 15, and 5 µM were incubated with LIN28. For readout preE-*let-7f-1*-Cy3 was used to generate a fluorescent readout. RNP can be observed in the upper part of the gel. If the compound can perturb the complex, inhibition can be observed through an electrophoretic mobility shift indicated by a shift of the fluorescent signal to the lower part of the gel. PH-31 was used as a positive control.

Analysis of probe **93** provided an IC_{50} of 19.5 µM. In comparison with the probe consisting of two short linkers (**80**), a decrease in affinity was observed. Despite the determination of the IC_{50} being an approximation, the comparison of individual bands showed that **80** seems to contain

the better linker orientation. Compound **102** showed an IC_{50} of 14.9 µM (Figure 20 and Figure 37).

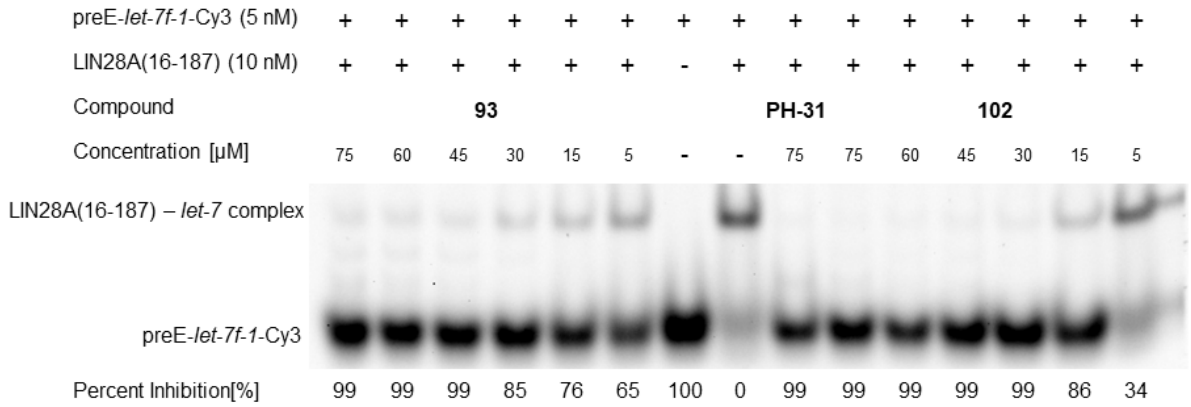

Figure 20: Dose-response EMSA of compounds **93** and **102**. Compound concentrations of 75, 60, 45, 30, 15, and 5 µM were incubated with LIN28. For readout preE-*let-7f-1*-Cy3 was used to generate a fluorescent readout. RNP can be observed in the upper part of the gel. If the compound can perturb the complex, inhibition can be observed through an electrophoretic mobility shift indicated by a shift of the fluorescent signal to the lower part of the gel. PH-31 was used as a positive control.

Dose-response investigation of **106** and **111** was not possible. For the chosen intervals, both bifunctional molecules did not give a suitable band pattern. For the case of **106,** this was due to the probe lacking activity. For **111,** the opposite was the case and lower concentration intervals need to be selected (Figure 21 and Figure 38).

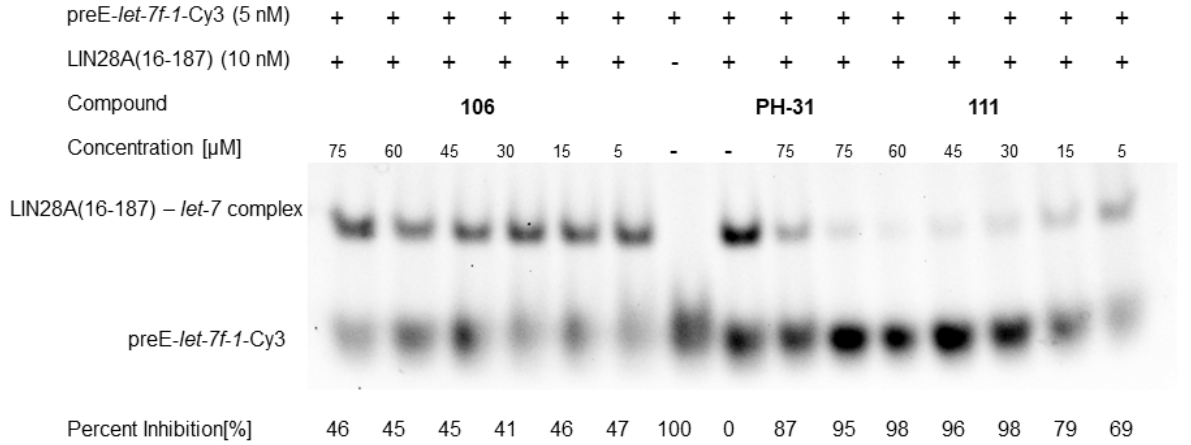

Figure 21: Dose-response EMSA of compounds **106** and **111**. Compound concentrations of 75, 60, 45, 30, 15, and 5 µM were incubated with LIN28. For readout preE-*let-7f-1*-Cy3 was used to generate a fluorescent readout. RNP can be observed in the upper part of the gel. If the compound can perturb the complex, inhibition can be observed through an electrophoretic mobility shift indicated by a shift of the fluorescent signal to the lower part of the gel. PH-31 was used as a positive control.

For **80**, an IC_{50} of 4.9 µM was determined and **111** resulted in an IC_{50} of 4.0 µM. This makes **111** the most potent bifunctional probe out of five generations of NEC probes (Figure 22). To validate these effects, an additional investigation was performed.

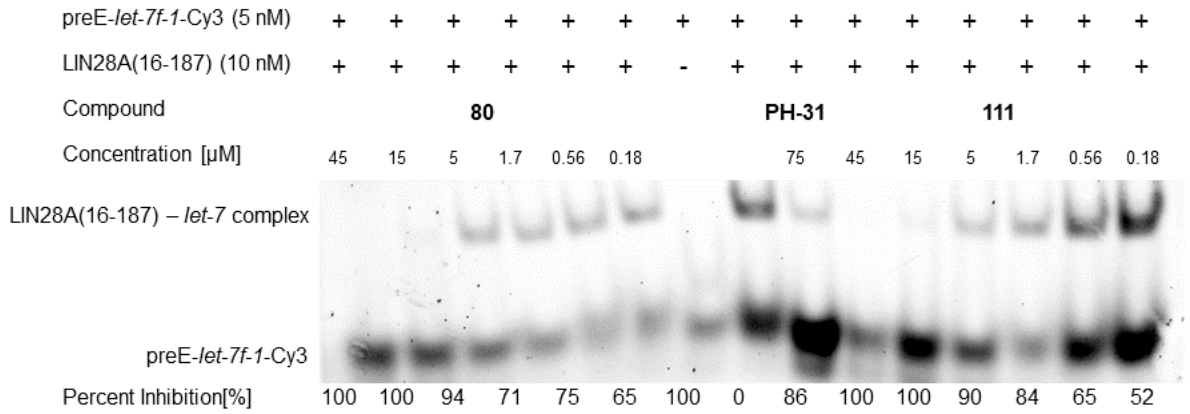

Figure 22: Dose-response EMSA of compounds **80** and **111**. Compound concentrations of 45, 15, 5, 1.7, 0.56, and 0.18 µM were incubated with LIN28. For readout preE-*let-7f-1*-Cy3 was used to generate a fluorescent readout. RNP can be observed in the upper part of the gel. If the compound can perturb the complex, inhibition can be observed through an electrophoretic mobility shift indicated by a shift of the fluorescent signal to the lower part of the gel. preE-*let-7*f-1was used as a positive control.

3.2.5 NanoDSF to Confirm NEC Molecules as LIN28 binders

Another way to prove a ligand-protein binding interaction is by performing a thermal stabilization assay. Once a molecule binds to a protein, a conformational change in the protein usually occurs. This conformational change can have a stabilizing or destabilizing effect on the protein secondary protein structure. This can be monitored in a nanoDSF measurement where the unfolding of a protein can be monitored through the change in intrinsic fluorescence. To prove that the NEC molecules bind LIN28, all dose-response EMSA molecules were investigated in nanoDSF.

The nanoDSF results confirmed what had been observed in the dose-response EMSA. While DMSO has only a minimal effect on protein stability, the control small molecule PH-31 caused T_m to increase by 1.5 °C. With this reference established, it can be seen that only the probes based on peptide **50** had a comparable effect on protein stability. The remaining probes confirmed the results observed previously, that they did not comparably bind to LIN28. Compound **80** caused the T_m to increase by 1.2 °C. In addition, **93** and **102** increased the T_m further by 1.3 and 1.4 °C respectively. All three probes had a less stabilizing effect on LIN28

than the original small molecule probe PH-31. However, the most potent bifunctional NEC molecule, **111**, stabilized the protein with a positive thermal shift of 1.9 °C. This stabilization surpassed even the control molecule and thereby confirmed **111** as the most active bifunctional moiety (Table 9 and Figure 23).

Table 9: Numerical results of the nanoDSF measurement to investigate the stability of LIN28 protein with the respective small molecule or bifunctional moiety. Measurements were performed in triplicate.

Sample	Average T_m[°C]	Δ T_m [°C]
LIN28	38.63±0.13	0
LIN28+DMSO	38.86±0.24	0.227
PH-31	40.14±0.14	1.502
80	39.85±0.74	1.215
88	39.04±0.02	0.405
93	39.95±0.12	1.314
102	40.02±0.25	1.385
106	39.22±0.11	0.584
111	40.51±0.28	1.875

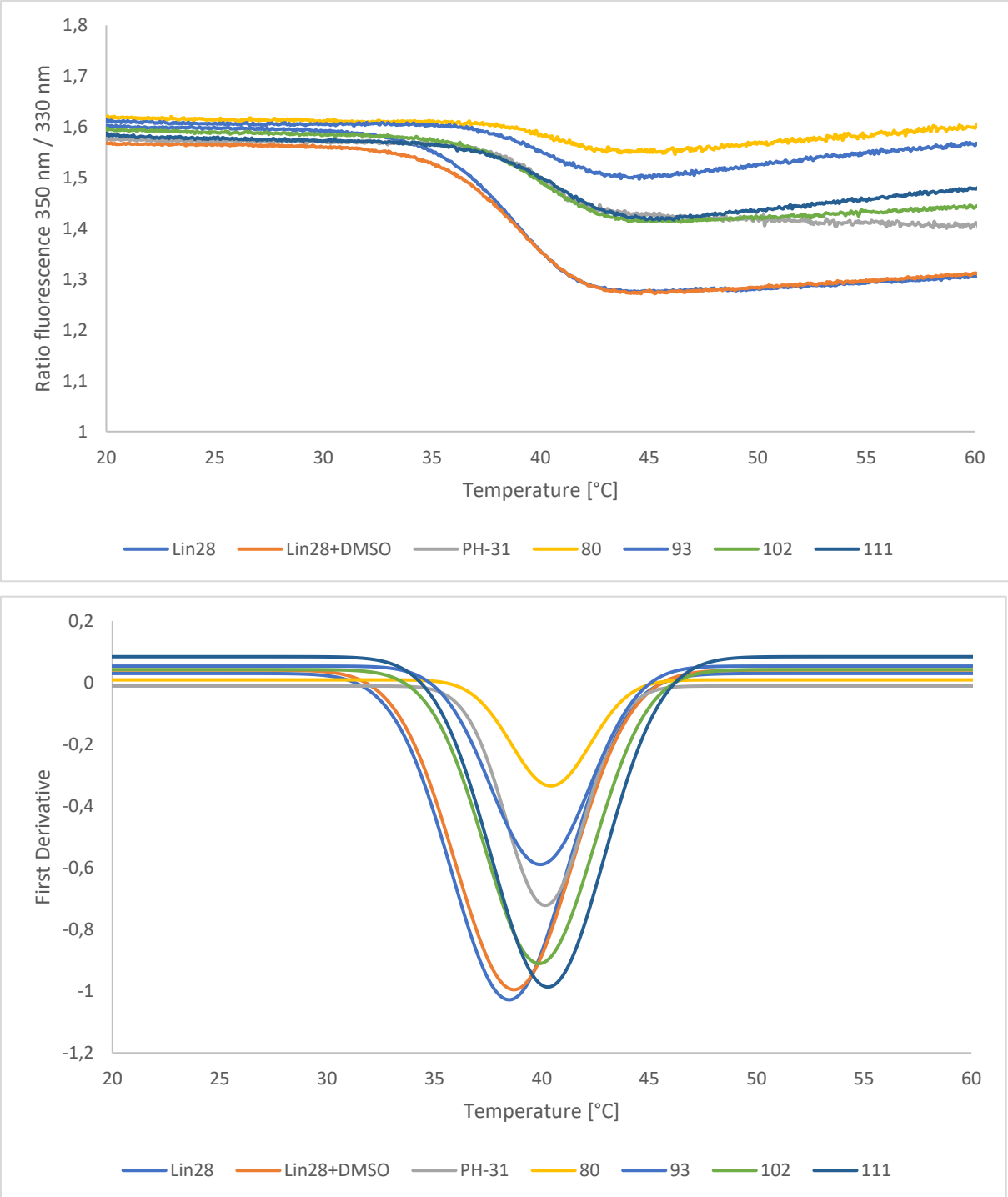

Figure 23: NanoDSF plots. Observed melting temperature T_m difference for LIN28 (blue), LIN28 treated with 5% (v/v) DMSO (orange), PH-31 (grey), **80** (yellow), **93** (green), **102** (dark blue) and **111** (light blue). The average ratio of fluorescence at 350 nm to 330 nm for the respective samples and fit of the average first derivative of the ratio of fluorescence at 350 nm to 330 nm.

3.2.6 NEC Lysate Stability Measurement

One of the main problems of employing small molecule peptide hybrids is the risk of cellular instability due to the peptide segment being degraded. As small molecule peptide conjugates are known to sometimes be resistant to this degradation, a lysate stability assay was performed. The third generation of NEC molecules was employed as a reference for all NEC probes. As only the peptide moiety is most likely to be affected by protease degradation, the generation with the highest flexibility on the peptide side of the molecule should accurately represent all bifunctional moieties.

To investigate the stability of the peptides, cell lysate was prepared from HeLa cells. Samples were incubated for 24 h at 37 °C and analyzed by HPLC to judge the molecular stability. Seven out of the nine samples showed surprising stability. Normally, linear peptides are considered to have a relatively short half-life of several minutes up to one or two hours.[97] Contrary to these expectations, the majority of all nine samples were fully intact after 24 h of lysate exposure. While the most potent peptide from the third generation, **102**, showed the most significant degradation with a 21.8% decrease in area under the curve. This number still indicates that conjugation to the small molecule moiety significantly improves the peptide's stability and hints that after little or no further optimization sufficient stability can be generated to employ these probes in cell-based experiments (Table 10 and Figure 134 to Figure 151).

Table 10: Values for lysate stability assay at 0 and 24 h of incubation at 37 °C in freshly prepared cell lysate. Values are absolute areas integrated from HPLC-MS software determined from the 254nm channel.

	0 h		24 h			
	Control	Molecule	Control	Molecule	Δ Control	Δ Molecule
95	705.7	518.8	793.0	440.4	12.4	-15.1
96	718.7	544.1	751.2	498.1	4.5	-8.5
97	758.7	360.2	767.4	348.3	1.1	-3.3
98	753.6	507.8	768.7	470.2	2.0	-7.4
99	744.4	626.0	749.1	624.7	0.6	-0.2
100	756.2	658.0	705.1	704.4	-6.8	7.1
101	756.7	556.1	736.1	538.8	-2.7	-3.1
102	778.3	127.4	762.6	99.6	-2.0	-21.8
103	776.3	492.1	759.3	520.9	-2.2	5.9

3.2.7 NEC IAM Permeability Measurement

After successful observation that peptide instability is not a major problem for the peptide-small molecule bifunctional moieties, the next known problem with peptides is membrane

permeability. To evaluate the potential of these molecules to interact with the cell membrane, an immobilized artificial membrane (IAM) column was employed. To compare different molecules passing through such a column, a numerical value is determined. The chromatographic hydrophobicity index (CHI) value approximates an acetonitrile concentration that causes the equal distribution of the analyte between the stationary and mobile phases. From the literature, it is known that the most optimal range for CHI values is between 35 and 50. Compounds lower than 35 have too little interaction with the phospholipid to have a chance to pass the membrane. For compounds above the value of 50, they have been found that these can be candidates that induce phospholipidosis, especially if positive charges are present in the molecule.[98]

To begin the analysis, a baseline needed to be established. To have a comparison for the investigation of the bifunctional moieties, all acetylated peptides were screened. Except for **43**, all peptides have CHI values too low to interact with lipids. The first generation of NEC compounds was screened for their potential to interact with the phospholipid bilayer. Contrary to the peptide screen, all probes except **73** were within the optimal interval for CHI values. The second generation, consisting of all the long linker fragments also had only one negative sample. Compound **94** was far outside the optimal interval but all other bifunctional molecules from the second generation of NEC molecules were in the optimal interval. The third and fourth generations did not contain any outliers and all bifunctional molecules were within the optimal interval (Figure 24). Overall, the results of the IAM analysis suggest that through the approach of biofunctionalization the potential to interact with phospholipids has been significantly improved in comparison to the peptide probes.

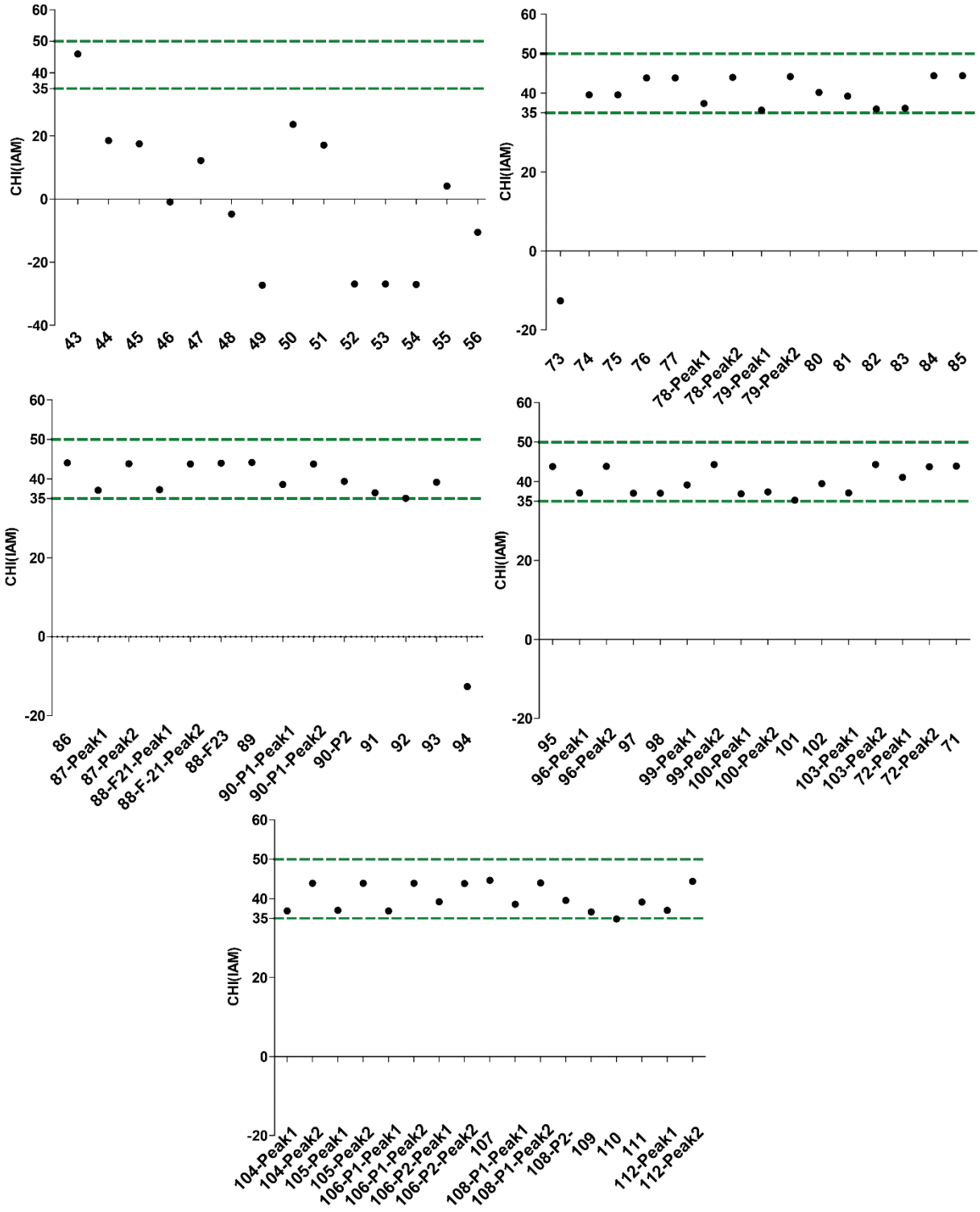

Figure 24: IAM (CHI) values for bifunctional molecules of the acetylated peptides. Green lines indicate the optimal interval of values for interaction with phospholipids.

3.2.8 Final Assessment of NEC Probes

Overall, the NEC strategy was an initial success. Starting from the selection of the small molecule fragment, a LIN28 binder was selected and optimized for moiety attachment.

Furthermore, rationally designed peptides based on a virtual alanine scan and crystal structure data could successfully perturb the interaction. After combining peptidic and small molecule fragments through CuAAC an improved affinity for LIN28 was found. Dose-response EMSA showed a clear improvement in the affinity for the POI giving an IC_{50} value of 4.0 µM for the most potent conjugate **111**. Conjugate **111** contained a short linker on the small molecule and a long linker on the peptide fragment. Furthermore, the affinity-enhancing moiety contained the peptide sequence NFQWNY. This affinity was confirmed by nanoDSF measurements, where the same conjugate showed a T_m increase of 1.9 °C outperforming the reported small molecule inhibitor PH-31. After reconfirming the binding to LIN28, an improvement in pharmacokinetic and pharmacodynamic properties could be shown by IAM and lysate stability assay. A significant improvement in comparison to the pure peptide probes could be shown. All these criteria already show the beneficial effect the NEC moiety exerts on the LIN28 inhibitor.

3.3 Tetrahydroquinolines as Potential NEC Component

Tetrahydroquinoline synthesis was performed by G. L. Goebel. EMSA evaluation was performed by L. Borgelt, L. Hohnen, and G. L. Goebel.

3.3.1 Synthesis of Tetrahydroquinolines

One of the core scaffolds from the literature reported as a LIN28 inhibitor consists of the tricyclic tetrahydroquinoline (THQ) core scaffold.[70] The THQ scaffold is accessible through the Povarov reaction.[99] This multi-component reaction (MCR) enables the synthesis of the product in a single step. While the reaction is classified as an inverse electron-demand aza-Diels-Alder reaction, the exact pathway has not yet been clarified.[100] The first possible pathway is through a concerted [4+2] cycloaddition process.[101] The second theorized pathway follows a sequential Mannich–Pictet Spengler transformation involving the electrophilic attack of the olefin to the activated iminium ion to yield an intermediate that is subsequently trapped by the aryl group to yield the final THQ adduct (Figure 25).[102]

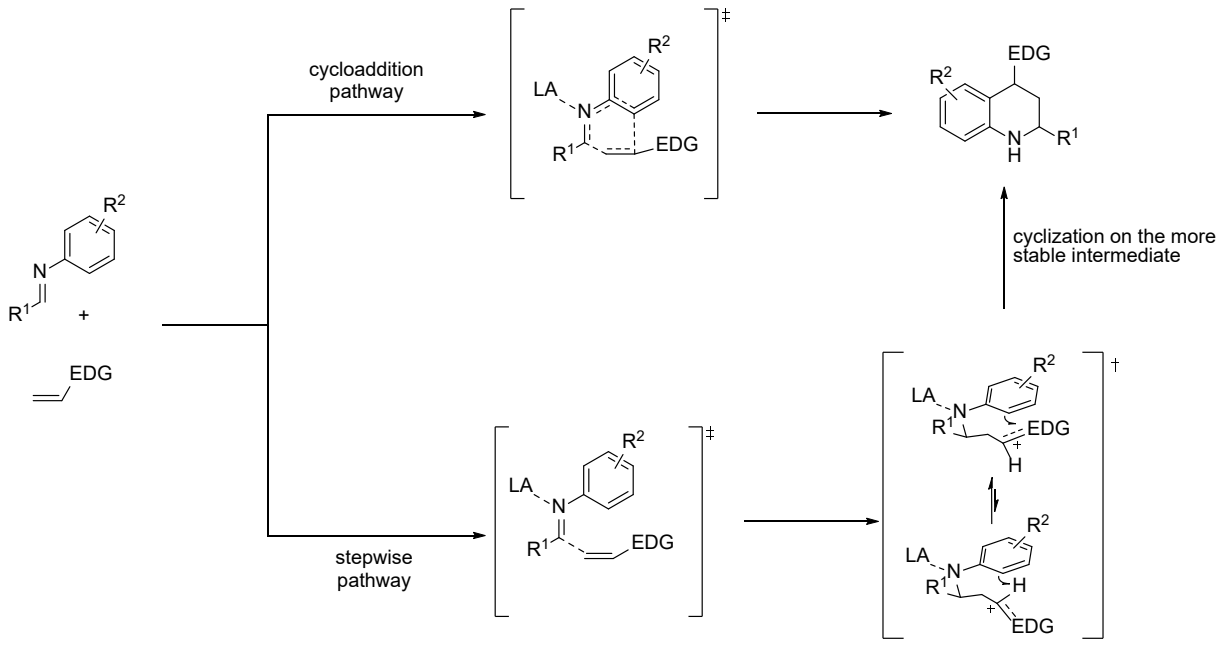

Figure 25: Comparison of the concerted cycloaddition and stepwise Mannich-Pictet Spengler pathway for the Povarov reaction mechanism. LA =Lewis Acid, EDG = Electron Donating Group.[100]

The wide substrate scope and mild reaction conditions make this reaction most suitable for a SAR exploration.[103] The selection of a proton source to lower the activation energy sufficiently to instigate the reaction has a considerable influence on the products formed. It was found that complexing the respective Brønsted or Lewis acid with certain conjugate bases can selectively produce the desired diastereomer in good yields. Examples here are BF_3• Et_2O as employed in

the original work[104] as well as lanthanide triflates, which were discovered to be successful in more recent reports.[105] The enantioselectivity has remained a problem but has been attempted to be solved by employing chiral conjugated bases that coordinate to the respective Brønsted or Lewis acid. One example was prepared from ytterbium triflate ($Yb(OTf)_3$, (R)-(+)-1-1'-bi-2-naphthol (BINOL) and 2,6-di-*t*-butylpyridine (DTBP) was used.[106] A different approach was taken by employing chiral sulfinamidourea.[107]

Initial advances around the SAR of the published inhibitor LI71 were to first confirm its activity using the in-house assay system. Therefore, LI71 was resynthesized as **113**. The original publication also claimed that the carboxylic acid moiety was essential for the interaction, while the ethoxy group on the aromatic ring system was not particularly accessible for modification. In an initial attempt to confirm the carboxylic acid hypothesis, **114** was also synthesized to check if shifting the carboxylic acid around the aromatic ring system already had any effect on the inhibitory activity. As the remaining positions on the THQ scaffold have not been explored yet, a rationally designed approach to substitute each synthetic handle was chosen to explore the potential of this compound class. During the synthesis of **114** and **113**, it was found that only one of the two expected diastereomers could be obtained in major excess. The separation of these was possible through flash column chromatography. This left only the question of enantiomeric purity. Initial NOE experiments suggested that the reaction was following an enantiopure pathway but further investigations through crystallographic analysis needed to be performed to confirm this initial result.

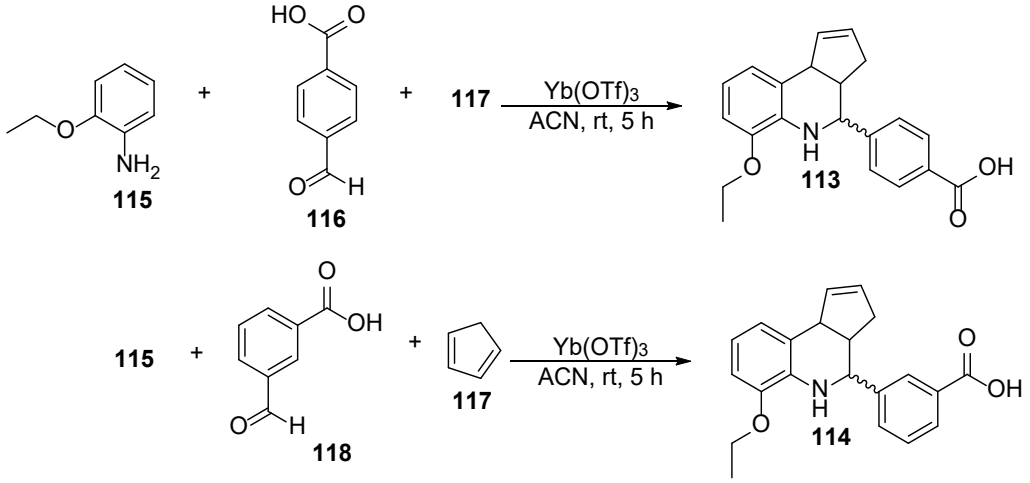

Scheme 14: Tetrahydroquinoline derivates that have been synthesized employing the Povarov MCR.

With the initial synthetic parameters established, the derivatization of the THQ scaffold commenced. After the initial two compounds, three points of modification were chosen: i) the

carboxylic acid, ii) the ethoxy moiety, and iii) the heterocyclic character originating from the diene.

The SAR around the R^1 position on the THQ scaffold was approached with the importance of the carboxylic acid claimed by literature in mind[70]. Hence, the carboxylic acid at the R^1 handle was mainly kept in para positions. It was attempted to substitute the acid by common carboxylic acid substitutes with $-NO_2$ (**121**), $-CF_3$ (**122**), -CN (**119**), and a shift to the meta position on the aromatic moiety (**114**). Additionally, a negative control without the carboxylic acid (**125**) and an -OH substitute in the meta position was also synthesized (**123**) to investigate if a single hydrogen bond acceptor would also be sufficient for the molecular interaction.

Table 11: Derivates of the initial THQ scaffold.

Compound ID	R^1	R^2	X	Yield [%]
113	4-COOH	2-OEt	CH	68
114	3-COOH	2-OEt	CH	59
119	4-CN	2-OEt	CH	76
120	4-COOMe	2-OEt	CH	94
121	4-NO_2	2-OEt	CH	77
122	4-CF_3	2-OEt	CH	76
123	3-OH	2-OEt	CH	62
124	3-COOH	2-OMe	CH	96
125	H	2-OEt	N	43
126	4-COOH	4-CN	CH	21
127	4-COOH	3,4,5-OMe	CH	62
128	4-COOH	4-COMe	CH	23
129	4-COOH	3-COMe	CH	50
130	4-COOH	2,4-Cl	CH	47
131	4-COOH	2-OMe	CH	40
132	4-COOH	2-O-*i*Pr	CH	70

Exploration of R^2 substituents were chosen similarly. The original -OEt residue was exchanged for -OMe (**124**), -O-*i*Pr (**132**), or 3,4,5-OMe (**127**) to grasp if other aliphatic ether moieties enhance the interaction with the target protein. Furthermore, it was also investigated if halogen bond interaction through 2,4,-Cl (**130**) would be possible. Lastly, compounds with more electron-withdrawing characteristics were also included. For this purpose, 4-CN (**126**) and both 4-COMe (**128**) and 3-COMe (**129**) were chosen.

All compounds were obtained in moderate to good yield and from UHPLC chromatograms it was concluded that only one of the two diastereomers were formed in major excess. Since we checked to see if the carboxylic acid on the R^1 handle we next wanted to evaluate the contribution of the aromatic moiety on the interaction with LIN28. To include non-aromatic aldehydes into the THQ synthesis the route was redesigned to introduce the protected ester under more acidic conditions by substituting the previous Lewis acid for trifluoro acetic acid

(TFA). After selective deprotection of the carboxylic acid moiety, **135** was successfully obtained in moderate yield (Scheme 15).

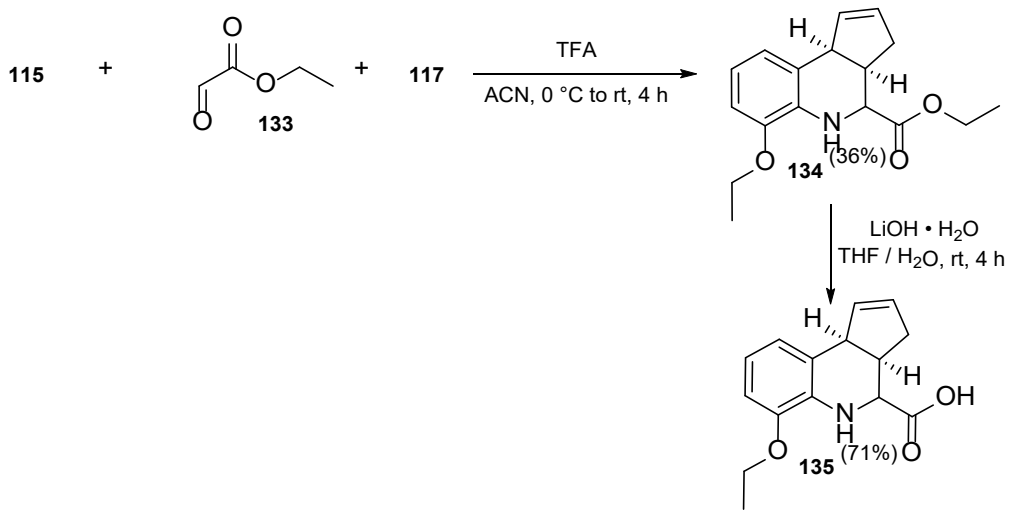

Scheme 15: Altered THQ conditions to include non-aromatic aldehyde component.

The last point of optimization was the electron donor. In the initial approach, a cyclopentadiene moiety was chosen. We hypothesized that potential hydrogen bond acceptors could have a beneficial effect on the affinity. To achieve this, we began by forming the enol selectively before combining it with the respective enol ether. Exchanging the $Yb(OTf)_3$ catalyst to a $Sc(OTf)_3$ was more favorable. Both the furanyl- (**136**) and pyranylvariant (**137**) were obtained after a two-step synthetic route including deprotection to give the carboxylic acid after product formation (Scheme 16).

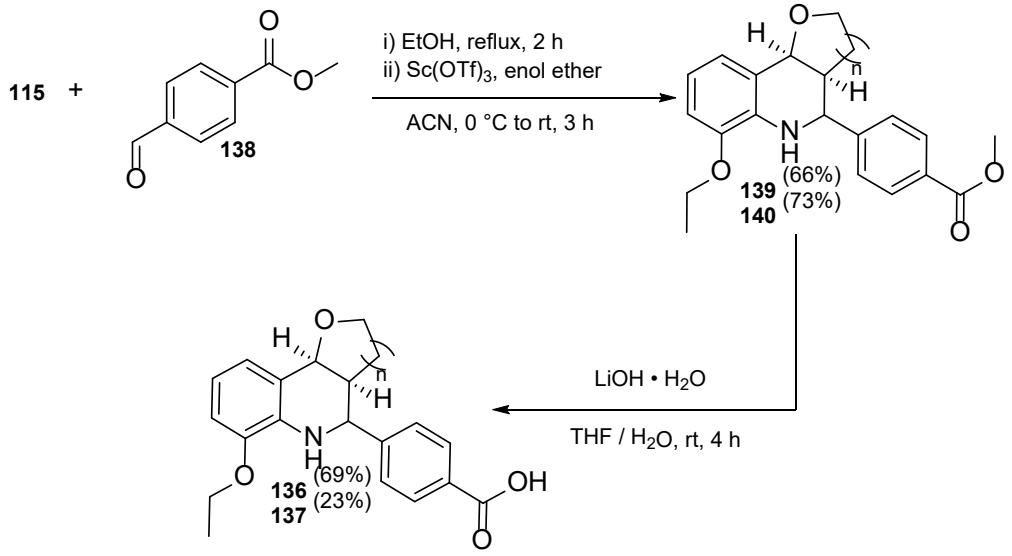

Scheme 16: Synthetic route to obtain the THQ derivatives with hydrogen bond acceptors in the electron-donating starting material.

3.3.2 Biological Evaluation of Tetrahydroquinolines

Evaluation of the synthesized library was performed through an EMSA. The library aimed to enhance the ability of the initial hit compound to restore *let-7* levels in a cellular context by selectively binding to LIN28. The first step to achieve this was to prove this ability *in vitro*. In our assay setup, the compounds were tested as a single dose at 75 µM. preE-*let-7-1f* was used in combination with LIN28 protein. For the readout preE-*let-7-1f*-Cy3 was used. As a positive control, the reported LIN28 inhibitor PH-31 was employed. In the case of a complex perturbation, the band should show a lower band for the released free preE-*let-7-1f*, while a negative result should show the labeled *let-7* in complex with LIN28 located in the upper part of the gel.

Evaluation of our first set of THQ compounds was done in a single-dose screening approach. At a concentration of 75 µM, compounds were checked for their single-dose inhibitory character through EMSA. With this information, we can then follow up on a dose dependent EMSA to get an estimation for the potential IC_{50} for the respective compound. Compound **113** showed inhibition of 40% in comparison to the positive control. Derivative **114**, with the carboxylic acid in the 3-position shows a clear increase in affinity for LIN28. A 65% inhibition was determined in comparison with the positive control. Unfortunately, exchanging the carboxylic acid for a nitrile residue resulted in a complete loss of the scaffold's inhibitory character (**119**). Modifications on the ethoxy residue also resulted in a complete loss of affinity. The exchange to an electron-withdrawing nitrile residue (**126**) was not tolerated and the

exchange from a single 2-OEt residue to 2,3,4-OMe (**127**) did not yield the desired improvement in affinity towards the target protein. The transformation from a 2-OEt group towards the introduction of a carbonyl moiety was also not tolerated by the interaction. Furthermore, 4-COMe (**128**) and 3-COMe (**129**) showed no inhibitory effect on the interaction (Figure 26).

Exchange of the essential 4-COOH on the R^1 handle into a 4-OH (**123**) significantly reduced the affinity to LIN28 in comparison with the currently best inhibitor compound (**114**). The protected 4-COOH derivative without the aromatic moiety in place (**134**) confirmed the importance of the carboxylic acid, as it shows little activity. Even though **134** shows minimal activity, the compound remains weakly active, indicating the aromatic moiety is removable from the molecule. This hypothesis was further confirmed after testing the derivative with the free carboxylic acid (**135**). In our initial single-dose screen, we found **135** to be the most potent inhibitor at a concentration of 75 µM. Hinting that the removal of the aromatic moiety could be a new handle to further improve the affinity of the THQ compound series. The exchange of the cyclopentadiene into a furan-derivative (**136**) did not result in any improved affinity towards LIN28 (Figure 26).

To further confirm the hypothesis from the literature that the 4-COOH moiety on R^1 is essential for the compound's activity, an ester variant with a 4-COOMe (**120**) at R^1 was synthesized. This modification negated any activity towards the target protein. To further validate if any room for modification was available, the introduction of a 4-NO_2 (**120**) and a 4-CF_3 (**122**) group was introduced and tested. Both derivatives showed reduced affinity in perturbing the RNP complex. Since **114** was successful in complex perturbation and **123** still retained some inhibitory character, the conclusion was to test the 3-OH residue on R^1. To further explore the room around the 2-OEt residue at R^2 an -OMe was introduced to see if the removal of a CH_2 group had a significant impact on the inhibitory character. For the 2-OMe derivative with a 4-COOH residue on R^1 (**131**) and the 2-OMe derivative with a 3-COOH residue at R^1, (**124**) a significant decrease in affinity was observed (Figure 26).

The exchange of the R^1 handle from an aromatic carboxylic acid moiety to a pyridine residue (**125**) resulted in a loss in affinity. Similarly, the expansion of the furanyl into a pyranyl ring (**137**) did not yield the desired improvement. Lastly, the exchange of R^2 into a 2-*i*Pr residue also decreased the respective activity (Figure 26).

In conclusion, the preliminary library around the literature hit LI71 showed promising results. While the R^2 handle seems to be very limited about the introduction of other residues, apart from the 2-OEt residue we could see that the carboxylic acid on the R^1 was more suited to introduce change. A shift of the carboxylic acid from the 4- to the 3-position showed significant improvement in the compound's affinity. Similarly, the removal of the entire aromatic moiety yielded the most active compound during this initial screen. Expanding the ring or introducing heteroatoms to the initial cyclopentadiene moiety did not improve the affinity. With these preliminary results, orthogonal validation and determination of the IC_{50} values of the compounds through a dose-dependent EMSA was performed (Figure 26).

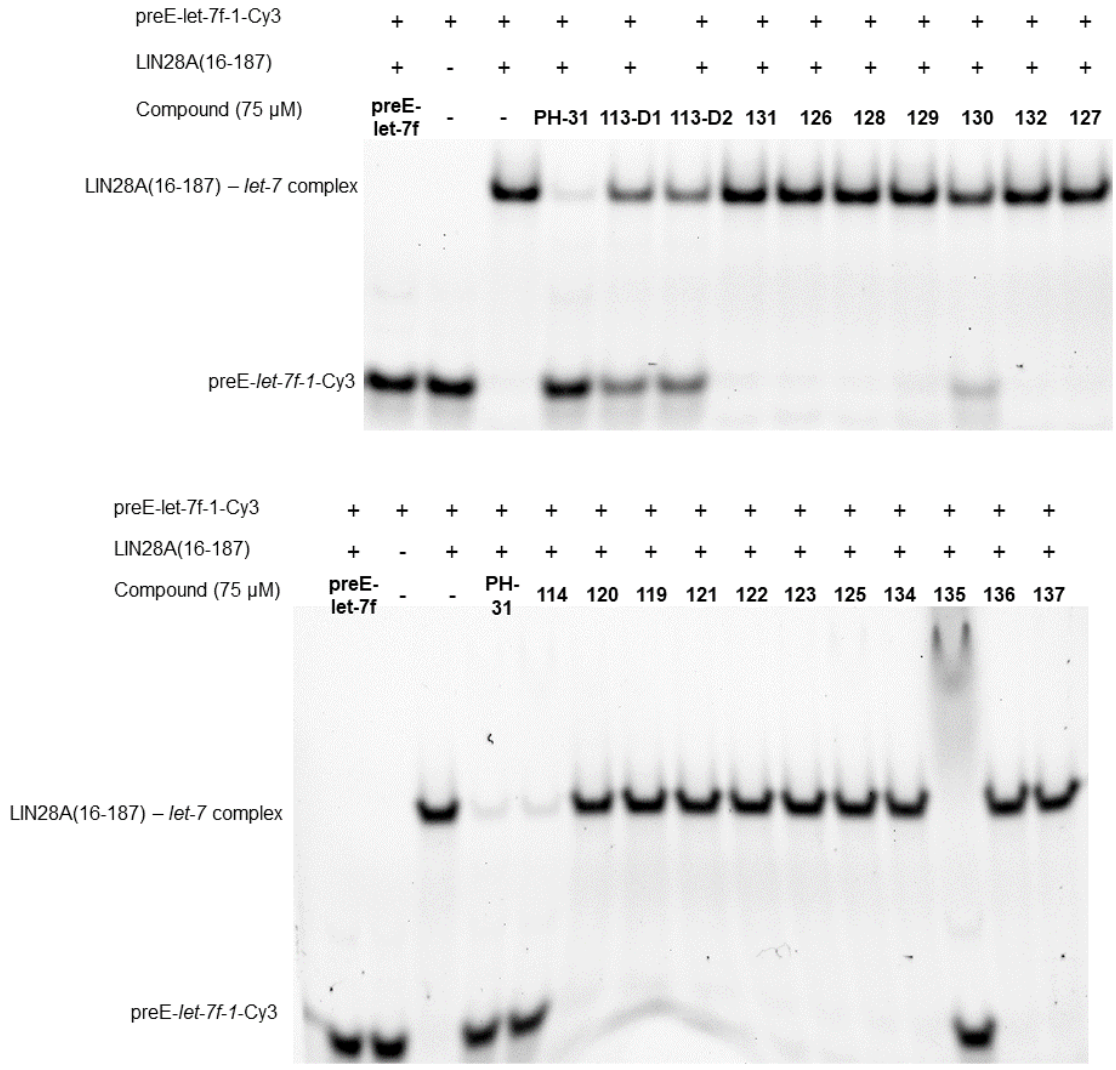

Figure 26: EMSA of LI71 analogs in single dose measurements. Lin28 was treated with 75 µM of the respective compound. After electrophoresis preE-*let-7-1f*-Cy3 allowed for visualization if the RNP Complex was perturbed.

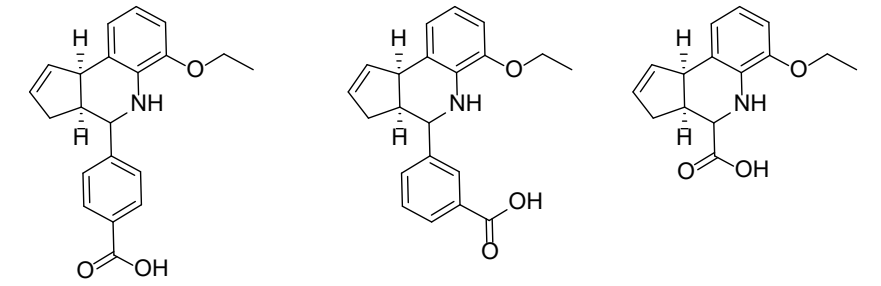

113
Inhibition = 40% (75 µM)

114
Inhibition = 65% (75 µM)

135
Inhibition = 99% (75 µM)

Figure 27: LI71 (**113**) and two analogs from the initial library with enhanced inhibitory activity at the single dose concentration of 75 µM.

3.3.3 Validation and Determination of IC_{50} Values

To confirm our results from the initial single-dose EMSA the most active THQ derivatives were investigated in an orthogonal assay. For this purpose, we chose the Fluorescence Polarization Assay. After establishing the assay three probes were tested. The two most active compounds from the single-dose EMSA were **114** and **135**. Additionally, a competition experiment with unlabeled preE-*let-7-1f* was performed as a positive control. Titration of the unlabeled preE-*let-7-1f* resulted in an IC_{50} value of 55 nM (Figure 28 A). This value corresponds with the reported affinity in the literature.[27] Compound **114** showed inhibition of the interaction in FP-assay as well. An IC_{50} of 4 µM was found. Whereas **135** was not able to be evaluated in the FP-assay. This is most likely due to the autofluorescence of the molecule interfering with the assay readout (Figure 28).

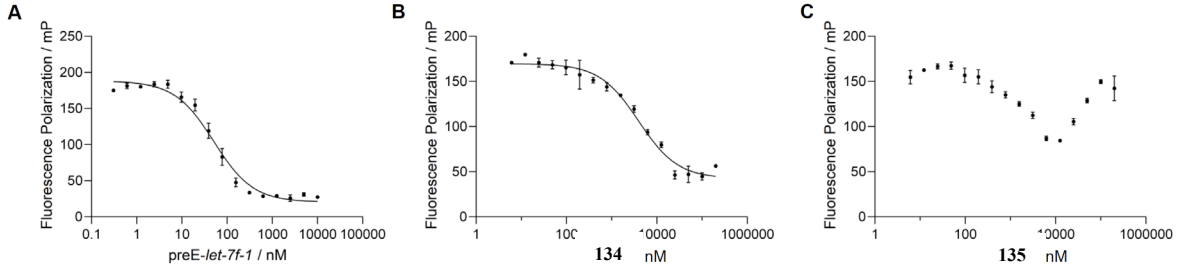

Figure 28: Confirming EMSA-activity of compounds **114** and **135** in the FP using human LIN28A (residues 16-187) and a FAM-labeled preE-*let-7f-1*. (A) Unlabeled preE-*let-7f-1*, which was used as a control, showed IC_{50} of 55 nM. (B) The most active compound **114** showed IC_{50} of 4 µM. (C) The IC_{50} of compound **135** could not be accurately measured in FP due to the shape of the obtained curve.

To determine the IC_{50} values via EMSA the compounds were titrated in different concentrations on the EMSA gel and after electrophoresis, the bands were again analyzed for percent inhibition. The initial hit from the literature was resynthesized in-house and separated into

racemic mixtures of the respective diastereomers. Both diastereomers confirmed the activity already observed in FP, thereby validating **114** as a potent LIN28 inhibitor. EMSA resulted in an IC_{50} value of 21.9 µM. Compound **135**, contrary to the FP assay showed a clear dose dependency in the second round of EMSA evaluation. An IC_{50} of 21.5 µM was observed. Due to the discrepancy with the initial FP validation, **135** can only be classified as a potential LIN28 inhibitor, as this dose-dependent inhibition needs to be validated through other means. To circumvent potential interference with the readout of the assay isothermal titration calorimetry could be a potential option to further investigate this compound (Figure 29).

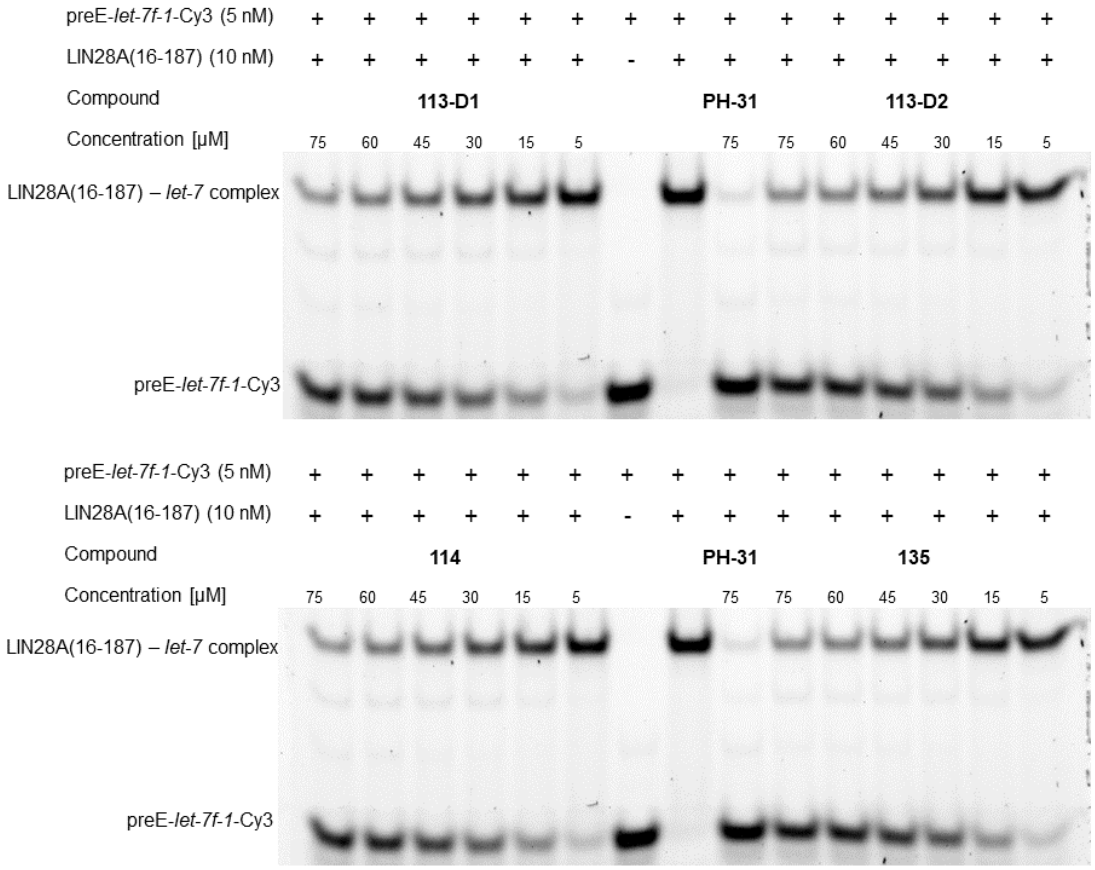

Figure 29: Dose-dependent inhibition of selected Povarov products in EMSA. Compound **113-D1** the racemic mixture of LI71 and LI71 enantiomer showed IC_{50} of 57.6 µM. Compound **113-D2**, the racemic mixture of the LI71 diastereomer, showed IC_{50} of 41.6 µM. (C) Compound **114**, the 2-(3-carboxyphenyl)tetrahydroquinoline analog, showed an IC_{50} of 21.9 µM. (D) Compound **135**, the 2-carboxy-tetrahydroquinoline analog, showed an IC_{50} of 21.5 µM.

3.3.4 Evaluation of THQ Scaffold for the NEC Strategy

The most important criterium for a small molecule probe to be selected for the bifunctional functionalization through the NEC strategy is a linker attachment point. Although the THQ scaffold is a selective potent LIN28 inhibitor, the SAR around this scaffold revealed an

improved LIN28 inhibitor with a 4 μM IC_{50} in FP and 21.9 μM in EMSA [108]. Although this is an improved inhibitor, the limited chemical space tolerated by this interaction does not qualify for a linker attachment point. Therefore, the THQ does not fit the criteria for the NEC strategy.

3.4 Pyrrolinones as Potential NEC Component

FP-assay was performed by L. Borgelt and Dr. P. Lampe. EMSA measurements were performed by L. Borgelt.

3.4.1 Discovery of Pyrrolinones as Novel LIN28–*let-7* Inhibitors

A novel scaffold to target the LIN28–*let-7* interaction was identified through a pilot screen of a high-throughput library performed with ~1400 compounds. The library consisted mainly of natural product-like molecules. FP-assay screening suggested C902 as a potent low micro molar inhibitor. In-house resynthesis and validation through EMSA showed a dose-dependent inhibition of the target protein through C902/PH-31. This confirmed the compound as a potent inhibitor and thereby established the pyrrolinone scaffold as a novel class of LIN28–*let-7* inhibitors (Figure 30).

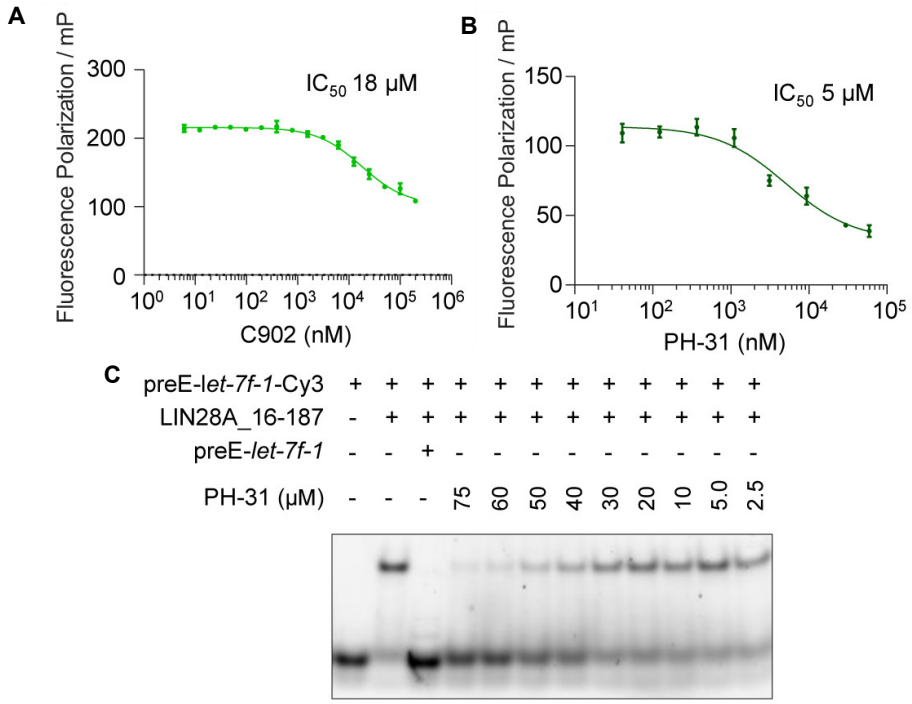

Figure 30: Testing and confirmation of trisubstituted pyrrolinone hit from screening campaign. A: FP-assay of library hit C902. B: FP-assay of in-house resynthesized trisubstituted pyrrolinone hit PH-31. C: Confirmation of FP-assay activity through dose-response EMSA.[68]

3.4.2 Pyrrolinone Library Analysis

With the initial hit PH-31 in hand, a proven dose-dependency, and an established synthetic route to obtain this scaffold, the optimization process could be started. The pyrrolinone core scaffold bears three positions for modifications. From the testing of the initial 23 hits provided by the COMAS library, we could already deduce important features to approach the design of analogs.

The most impactful change to the affinity of the pyrrolinones resulted from the salicylic acid moiety on the aniline component. The carboxylic acid in the 3-position accompanied by a hydroxy group in the 4-position yielded the best IC_{50} values for this compound set. Making C879, C880, C885, C893, C897, and C902 the most promising structures from this initial set. Notably, removing the hydroxy group and changing the position of the carboxylic acid on the aniline moiety negated any affinity for the target protein with compounds C881 and C882. Any improvement of these IC_{50} values can also not be compensated by the introduction of methoxy- or bromide residues on the butanoate moiety. Minimal changes can be introduced by transforming the carboxylic acid from the aldehyde component into one of its bioisosteres. As both nitro and thiazol-2-yl groups are known to function as such.[109] A conclusion about the most optimal aldehyde residue was drawn from internal discussion (data not shown) to favor the thiazol-2-yl residue for this compound class (Table 12).

Table 12: Trisubstituted pyrrolinone derivatives provided from the COMAS facility.

Compound	R^1	R^2	R^3	IC_{50} (µM)[a,b]
C879	H	(thiazol-2-yl)	3-COOH and 4-OH	~20
C880	H	COOH	3-COOH and 4-OH	10-20
C881	H	COOH	3-COOH	> 100[c]
C882	H	COOH	4-COOH	Inactive
C883	OMe	NO_2	3-COOH	Inactive
C884	OMe	NO_2	4-COOH	Inactive
C885	OMe	COOH	3-COOH	20-30
C886	OMe	COOH	3-COOH	> 100[c]
C887	OMe	COOH	4-COOH	> 100[c]
C888	OMe	COOH	3-(1*H*-tetrazol-5-yl)	> 100[c]
C891	OMe	NO_2	3-COOH	> 100[c]
C892	Br	NO_2	3-(1*H*-tetrazol-5-yl)	Inactive
C893	Br	COOH	3-COOH and 4-OH	20-30
C894	Br	COOH	3-COOH	Inactive
C895	Br	COOH	4-COOH	Inactive
C896	Br	(thiazol-2-yl)	3-(1*H*-tetrazol-5-yl)	Inactive
C897	H	(thiazol-2-yl)	3-COOH	20-30
C898	H	(thiazol-2-yl)	3-(1*H*-tetrazol-5-yl)	Inactive
C899	Br	(thiazol-2-yl)	4-COOH	Inactive
C900	OMe	(thiazol-2-yl)	3-COOH	Inactive
C901	OMe	(thiazol-2-yl)	3-(1*H*-tetrazol-5-yl)	Inactive
C902	Br	(thiazol-2-yl)	3-COOH and 4-OH	10-20
C903	Br	(thiazol-2-yl)	3-COOH	Inactive

[a]Each sample was tested in quadruplicate. [b]Compound starting from a concentration of 30 µM with the following 1/3 dilutions (8 concentrations in total). [c]Extrapolated based on the observed IC_{50} curves.[68]

The pyrrolinone scaffold was originally added to the compound library from the works of Prof. Ottmann *et al.*. They employed the scaffold as a precursor to synthesize a set of pyrazoles that would enable them to stabilize *14-3-3* protein-protein interactions.[110] To explore potential off-target effects, a set of five pyrazoles were also evaluated in the initial investigation. Even though the salicylic acid moiety was present in the scaffold, all pyrazole derivatives (C904–908) showed no inhibitory character in the assay (Table 13). With this preliminary result, it was reasonable to progress the pyrrolinone core scaffold as a novel LIN28–*let-7* inhibitor and try to optimize the IC_{50}.

Table 13: Trisubstituted pyrazole derivatives provided by COMAS facility.

ID	R^1	R^2	R^3	IC_{50} (µM) [a-c]
C904	H	NO_2	3-COOH and 4-OH	>100
C905	H	NO_2	4-COOH	>100
C906	H	NO_2	4-methoxyphenylcarbamoyl	>100
C907	H	Br	3-COOH and 4-OH	>100
C908	H	NO_2	4-benzylcarbamoyl	>100

[a]Each sample was tested in quadruplicate. [b]Compound starting from a concentration of 30 µM with the following 1/3 dilutions (8 concentrations in total). [c]Extrapolated based on the observed IC_{50} curves.[68]

3.4.3 Synthesis of Pyrrolinones

The pyrrolinone scaffold is accessible through an MCR mechanistically related to the Doebner reaction.[110] In the traditional Doebner reaction, an aniline, an aldehyde, and a pyruvic acid component form the cinchonic acid scaffold (Scheme 17).

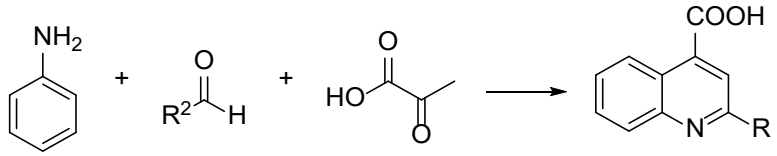

Scheme 17: General reaction scheme for the Doebner condensation between an aniline, an aldehyde, and pyruvic acid to obtain the cinchonic acid.

The exact mechanism for the Doebner Reaction has not yet been elucidated. There are two proposed pathways for the reaction to occur. The first pathway starts with an aldol condensation between the aldehyde and pyruvic acid. The β,γ-unsaturated α-keto-carboxylic acid then reacts with the aniline component through an addition to the unsaturated γ-position. Temperature-induced electron rearrangement in the diketomoiety causes the interruption of the aromatic residue of the amino component. To recover the aromaticity a deprotonation takes place to yield the carboxylic acid. To generate aromaticity in the second ring system a combined release of H_2O and H_2 is proposed by the literature (Scheme 18).[111] The second pathway starts with the formation of a Schiff base. This intermediate then reacts with the pyruvic acid to again form the diketointermediate. The reaction then follows the same pathway of electron rearrangement and condensation to yield the final product (Scheme 18).[112][113]

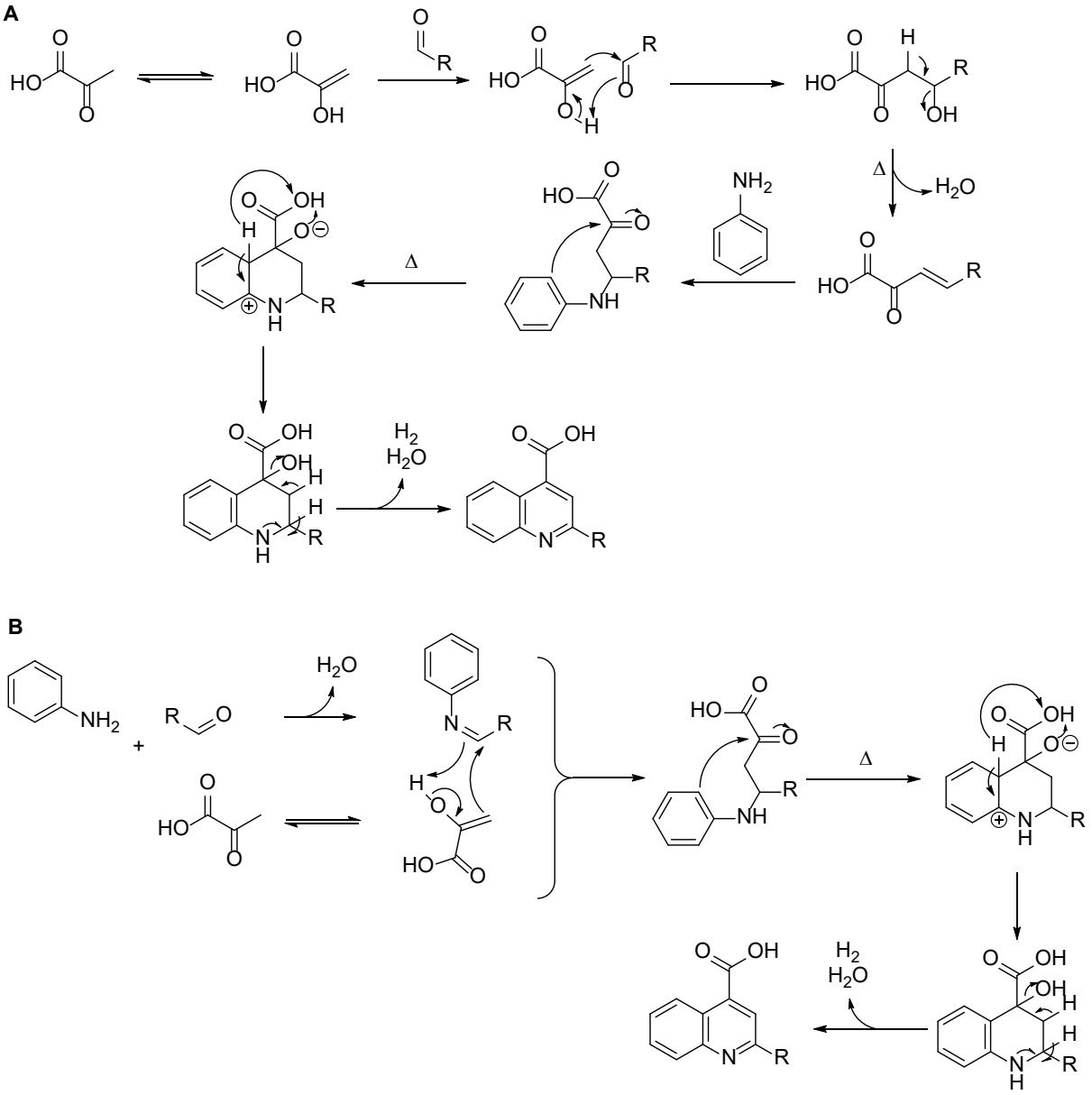

Scheme 18: Two proposed mechanistic pathways for the Doebner Reaction. A: Pathway through aldol condensation, followed by addition of the aniline and recovery of aromaticity. B: Pathway through the formation of a Schiff base, followed by reaction with the pyruvic acid moiety.[113]

In contrast to the general reaction mechanism of the Doebner Reaction, the pyrrolinones were synthesized with a dioxobutanoate component (Scheme 19) instead of the pyruvic acid. Obtaining pyrrolinones through the Doebner Reaction was initially reported as not possible. As side products, they were not the desired cinchonic acid products. It was observed that mainly aromatic amines with deactivated α and γ formed pyrrolinones instead.[114]

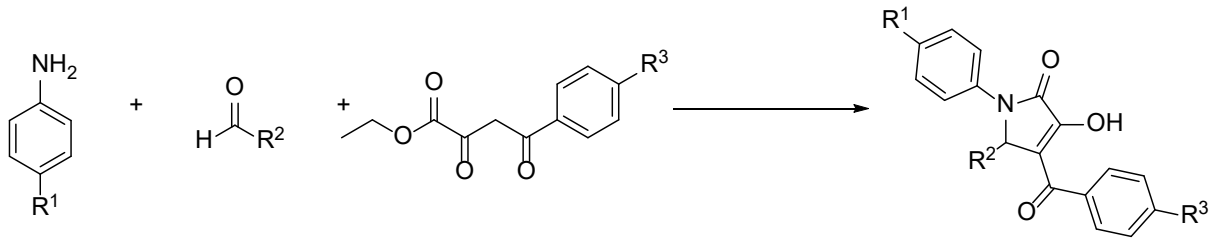

Scheme 19: General reaction scheme for the reaction between an aniline, an aldehyde, and dioxobutanoate to obtain the pyrrolinone scaffold.

Initial hits from the provided library were resynthesized in-house to obtain samples of higher purity and revalidated in the respective assay system. We could reproduce all IC_{50} values with a slight improvement. This improvement was most likely due to the higher grade of purity. Compound **141**/C893, on the other hand, showed complete inactivity after resynthesis in-house (Table 14).

Table 14: Pyrrolinone analogs designed and synthesized based on the initial COMAS library

Compound	R^1	R^2	R^3	IC_{50} (μM)[a,b]
142	4-bromophenyl	thiazol-2-yl	3-OH and 4-COOH	> 100[c]
C902/PH-31	4-bromophenyl	thiazol-2-yl	3-COOH and 4-OH	5
C879/143	phenyl	thiazol-2-yl	3-COOH and 4-OH	12
144	4-bromophenyl	thiazol-2-yl	4-OH	> 100
145	phenyl	COOH	4-OH	>100
146	phenyl	thiazol-2-yl	3-NO_2 and 4-OH	41
147	phenyl	COOH	3-OH and 4-COOH	16
C880/148	phenyl	COOH	3-COOH and 4-OH	6
149	furan-2-yl	thiazol-2-yl	3-COOH and 4-OH	5
150	3,4-dimethoxyphenyl	thiazol-2yl	3-COOH and 4-OH	12
C893/141	4-bromophenyl	COOH	3-COOH and 4-OH	Inactive

[a]Tested in quadruplicate. [b]Starting from a maximum concentration of 60 μM, eight concentrations in total. [c]Starting from 30 μM, eight concentrations in total. [d]Data of the in-house synthesized compound, PH-series. [e]Extrapolated based on the observed IC_{50} curves.

To finalize the decision on the substitution pattern of the aniline moiety, the carboxylic acid and hydroxy group positions were exchanged. Compound **142** showed a complete loss of affinity. Attempts to explore if only the 4-hydroxy group could create the necessary target interaction to retain activity were also undertaken with compounds **144** and **145**. In a final attempt to explore this moiety, the carboxylic acid was exchanged for a nitro group to test for similar interactions, but the loss of acidity would affect the affinity. Compound **146** could retain affinity to a certain extent but confirmed that the salicylic acid moiety with 3-COOH and 4-OH seemed to be the optimal orientation. For R^2, it seems that both thiazol-2-yl, as well as the

carboxylic acid, were well tolerated. To avoid polarity and cell permeability issues at a later stage, alongside the slightly better IC_{50}, we decided to prioritize thiazol-2-yl. Fortunately, it seems that the R^1 residue was more tolerable for modification. (Bromo-)phenyl, 3,4-dimethoxyphenyl as well as the five-membered furan-2-yl seem to influence any affinity only minimally. This suggests that the butanoate moiety is suited for further modification and potentially harbors an attachment point to use to introduce the peptide moiety to transform the pyrrolinones into probes used for the NEC strategy.

3.4.4 Evaluation of Pyrrolinones for NEC Strategy

Overall, more work is necessary to decide if the pyrrolinone can also be employed in the NEC strategy. Currently, there is still a limited structure investigation, and as such does not lead to a decisive conclusion. Nevertheless, the pyrrolinone scaffold has been added to the repertoire of LIN28 inhibitors.

4. Conclusion and Perspective

RBPs are emerging as targets of high biological and pharmacological relevance, and small molecules that bind and modulate RBPs are in high demand. The LIN28–*let-7* interaction is a well-characterized but not yet fully understood interaction, which is essential to many cellular regulatory processes. In this study, we investigated small molecule LIN28 inhibitors of three different core scaffolds to enable the establishment of a general strategy to target the RBP LIN28. The novel NEC approach was based on rationally designed affinity-enhancing moieties to perturb the LIN28–*let-7* PRI through the bifunctionalization of the selected core scaffold.

Compounds with the tetrahydroquinoline core scaffold were previously reported as LIN28 inhibitors. The synthesized tetrahydroquinoline derivatives in this study showed improved LIN28-binding affinity. Compound **114** showed a minor improvement of 21.9 µM in a dose-response EMSA, compared to 41.6 µM of LI-71, the original literature compound. Unfortunately, it also became clear that the tetrahydroquinoline scaffold did not tolerate any linker attachment and was therefore not pursued in bifunctional design.

In a parallel screening-based approach, trisubstituted pyrrolinones were identified as a novel LIN28-inhibiting scaffold. Since substituted pyrrolinones possess polypharmacological character, a rationally designed structural investigation into respective substituents was conducted to elucidate the necessary moieties to bind LIN28 selectively. As a result, PH-31, with an IC_{50} of 18.9 µM in dose-response EMSA, was discovered. After performing an initial structural investigation into the trisubstituted pyrrolinone scaffold, it became obvious that the original butanoate moiety is tolerant towards aromatic substituted residues. Further investigation is needed to determine if this position is also suitable for linker attachment to enable this scaffold for the NEC strategy.

The chromeno[4,3-*c*]pyrazole scaffold was the third scaffold investigated in this work. A library of molecules was synthesized based on modifications that focused on substituent handles on the core scaffold. Both **42** (substituted piperazine) and **40** (substituted aniline) retained sufficient activity to select them for the NEC strategy. Additionally, building block 2-chloroacetic acid emphasized the importance of the carbonyl oxygen in both linker attachment positions. Therefore, **16** was used as the small molecule building blocks for the assembly of the NEC molecules due to its better performance in the EMSA.

A central goal of the study was to develop a novel concept to enhance small molecule affinity towards RBPs, on the example of LIN28–*let-7*. A virtual alanine scan highlighted the involved hotspot amino acids on the *let-7* interacting surface of the LIN28 protein. Based on the characteristic of these amino acid hotspots, two criteria were determined to design an affinity-enhancing moiety: aromaticity and electrostatic interactions. Based on these two criteria, we utilized a design approach based on mimicking the molecular volume of the interacting *let-7* RNA with peptides. With an initial set of 14 peptides, the first generation of NEC bifunctional molecules was obtained via conjugation between chromenopyrazole and peptides through CuAAC. After the initial evaluation, a linker optimization approach was taken to screen for the optimal linker length. Analysis of these synthesized sets of different NECs resulted in the most potent probes **80** with an IC_{50} of 4.9 µM and **111** resulted in an IC_{50} of 4.0 µM. Both probes contained the peptide sequence NFQWNY, underlining the previous observation, that stacking interactions have a more significant impact on PRIs than electrostatic interactions. Furthermore, the binding of NEC molecules with LIN28 was confirmed by nanoDSF. In comparison to the published inhibitor PH-31, **111** has a higher stabilizing effect upon binding to LIN28.

After confirmation that NEC molecules perturbed the LIN28–*let-7* interaction, we evaluated the lysate stability, which showed that the chromeno[4,3-*c*]pyrazole-peptide conjugates showed improved stability in comparison with other reported linear peptides. Furthermore, the potential to interact with phospholipids was drastically increased after forming the conjugates with chromenopyrazole proven by the improved CHI values from the IAM measurements.

With these results, the NEC concept was clearly demonstrated in this study, although the results showed, that a molecular enlargement through aromatic amino acids is much more beneficial in comparison with the incorporation of negatively charged amino acids. Nevertheless, the ability to repel RNA through electrostatic repulsion still needs to be further investigated. The influence of the proposed aromatic amino acids in the affinity-enhancing moiety increased the potency of the compound, even though the peptide was unmodified and linear. Additionally, conjugation to the small molecule reduced the most commonly associated flaws of peptides significantly. To further enhance the compound's target affinity, a reduction in the entropic penalty via macrocyclization should be explored. Potential cyclization positions were already identified during the structural investigations performed in this thesis. For example, a small macrocycle could be generated by connecting the 8-position currently used for peptide attachment with the deprotected piperazine. Alternatively, a larger macrocycle that will be able to cover more hotspot residues can be obtained by connecting the 8-position and the secondary

amine of the quinolino[4,3-*c*]pyrazoles. Overall, this study provides a new approach to target RBPs using small molecule and peptide conjugates, which has the potential to be further developed into a platform strategy to achieve rationally designed RBP inhibitors and PRI disruptors.

5. Appendix

5.1 Chemistry

All commercially available reagents and solvents were used without further purification unless noted otherwise. Dry solvents were purchased from Fischer Scientific and/or Acros and used without further treatment. Oxygen and/or moisture-sensitive solutions were transferred using syringes under inert atmosphere.

Thin layer chromatography (TLC) was run on silica-coated aluminum plates (Merck 60 F254) and visualization happened through UV irradiation (254 nm) or potassium permanganate stain (1.5 g $KMnO_4$, 10 g K_2CO_3, 1.25 mL of 10% aqueous NaOH solution and 200 mL of water).

Analytical UHPLC-MS and LC-MS was run and evaluated on an Agilent 1290 Infinity system equipped with a mass detector (column: Zorbax Eclipse C18 Rapid Resolution 2.1x50 mm 1.8µm). Appropriate gradient systems were generated by mixing Water (+ 0.1% TFA) and Acetonitrile (+ 0.1%).

Purification of crude products was achieved via flash column chromatography (FC, silica gel 60, 0.035–0.070 mm) or automated medium-pressure liquid chromatography (MPLC, Buchi) using suitable solvent mixtures. More challenging separations were additionally performed on the Agilent 1100 preparative HPLC system equipped with a mass detector (columns: Nuleodur C18 gravity VP 125/10 5 µm, Nucleodur C18 gravity VP 125/21 5 µm, Nucleodur C4 gravity VP 125/10 5 µm). Appropriate gradient systems were applied by mixing Water (+ 0.1% TFA) and Acetonitrile (+ 0.1%).

NMR spectra were recorded on Bruker AV 400 Avance III HD (NanoBay), Agilent Technologies DD2, Bruker AV 500 Avance III HD (Prodigy), Bruker AV 600 Avance III HD (CryoProbe) or Bruker AV 700 Avance III HD (CryoProbe) spectrometers. Data is depicted in ppm with reference to the respective deuterated solvent (Chloroform-*d*: 7.26 ppm, 77.16 ppm; DMSO-d_6: 2.50 ppm, 39.52 ppm; CD_2Cl_2: 5.32 ppm, 53.84 ppm; Methanol-d_4: 3.31 ppm, 49.00 ppm; Acetone-d_6: 2.05 ppm, 29.84 ppm, 206.26 ppm).[115]Signals were assigned to the correlating Hydrogens or Carbons based on 2D NMR correlations ($^1H/^1H$ COSY, $^1H/^1H$ NOESY, $^1H/^{13}C$ HSQC, $^1H/^{13}C$ HMBC).

High-resolution mass spectrometry (HRMS) was measured in an LTQ Orbitrap mass spectrometer coupled to an Accela HPLC-System (HPLC column: Hypersyl GOLD, 50 mm x 1 mm, particle size 1.9 µm, ionization method: electron spray ionization (ESI)).

5.2 Synthetic Procedures and Compound Characterization

5.2.1 Chromenopyrazoles

7-Fluoro-2,2-dimethylchoman-4-one (2): To a solution of hydroxy acetophenone (5.00 g, 32.4 mmol, 1.0 equiv.) in EtOH, pyrrolidine (5.3 mL, 64.9 mmol, 2.0 equiv.) and acetone (24.0 mL, 0.3 mol, 10.0 equiv.) were added sequentially and the reaction mixture was stirred at room temperature overnight. After the completion of the reaction monitored by TLC, the reaction mixture was concentrated *in vacuo.* The crude residue was dissolved in dichloromethane and washed several times with 1 N HCl solution. After washing with brine, the combined organic layer was dried over anhydrous $MgSO_4$, filtered, and concentrated under reduced pressure. The resulting mixture was purified by silica gel flash column chromatography to provide a desired product **2** (4.51 g, 72%): **^{1}H NMR** (400 MHz, Chloroform-*d*) δ 7.90–7.85 (m, 1H), 6.68 (ddd, *J* = 8.8, 8.2, 2.4 Hz, 1H), 6.63–6.59 (m, 1H), 2.70 (s, 2H), 1.46 (s, 6H). **R_f**: 0.26 (7% EA in CyHex). The characterization data is consistent with the reported data.[69]

7-Fluoro-2,2-dimethyl-6-nitrochroman-4-one (3): At -5 °C a mixture of conc. HNO_3 (70%, 1.5 ml, 25.5 mmol, 1.1 equiv.) and conc. H_2SO_4 (9.0 mL) is added dropwise into a mixture of **2** (4.50 g, 23.2 mmol, 1 equiv.) in 48 mL conc. H_2SO_4. After addition, the mixture is stirred for 1.5 h at 0 °C. Product formation was monitored via TLC. After completion of the reaction, the mixture is poured into ice water and the residue is filtered and washed. The washed crude mixture was further purified through silica column chromatography to obtain the desired product (5.01 g, 84%): **^{1}H NMR** (700 MHz, Chloroform-*d*) δ 8.68 (t, *J* = 6.7 Hz, 1H), 6.80–6.73 (m, 1H), 2.79 (s, 2H), 1.66 (s, 1H), 1.51 (s, 6H). **^{13}C NMR** (101 MHz, Chloroform-*d*) δ 190.2, 164.8, 164.7, 161.7, 159.0, 126.7, 116.6, 108.0, 107.7, 82.4, 77.5, 77.2, 76.8, 48.4, 26.8. **R_f**: 0.4 (30% EA in PE).

Benzyl 4-(2,2-dimethyl-6-nitro-4-oxochroman-7-yl) piperazine-1-carboxylate (4): 3 (1.62g, 6.8 mmol, 1 equiv.) were dissolved in acetonitrile (34 mL, 0.2 M). Cbz-Piperazine (1.8 mL, 9.5 mmol, 1.4 equiv.) was added in one portion. The mixture was stirred overnight at 40 °C. After the completion of the reaction, as monitored by TLC, the solvent was removed under reduced pressure, and the crude was dissolved in DCM. The organic layer was washed with 1 N HCl (aq) and brine and dried over anhydrous $MgSO_4$. The filtrate was dried under reduced

pressure to yield the desired product without further purification (2.95 g, 99%): **^{1}H NMR** (400 MHz, Chloroform-*d*) δ 8.47 (s, 1H), 7.38–7.31 (m, 5H), 6.43 (s, 1H), 5.17–5.15 (m, 2H), 3.71–3.66 (m, 4H), 3.17–3.07 (m, 4H), 2.71 (s, 2H), 1.49–1.46 (m, 6H). **R_f**: 0.5 (50% EA in PE). The characterization data is consistent with the reported data.[69]

Benzyl 4-(3-(diethoxymethyl)-2,2-dimethyl-6-nitro-4-oxochroman-7-yl) piperazine-1-carboxylate (5): To a solution of triethyl orthoformate (3.4 mL, 20.1 mmol, 3 equiv.) in DCM (22.5 mL), $BF_3{\cdot}OEt_2$ (2.5 mL, 20.1mmol, 3 equiv.) was slowly added over a period of 10 min at -10 °C under an argon atmosphere. The reaction mixture was then gradually warmed up to 0 °C. After 15 min of stirring at 0 °C, the reaction mixture was cooled back to -78 °C. To this reaction mixture, **4** (2.95 g, 6.7 mmol, 1 equiv.) in 12.5 mL of DCM was added, and DIPEA (4.1 mL, 23.5 mmol, 3.5 equiv.) was then added slowly over 30 min. The resulting mixture was stirred at -78 °C for 10 min, and then warmed up to room temperature for an additional 2 h of stirring. The resultant mixture was diluted with DCM and washed with sat. $NaHCO_3$(aq) solution. The combined organic layer was dried over anhydrous $MgSO_4$ and condensed under reduced pressure. The resulting mixture was purified by silica gel flash column chromatography to provide the desired product as a yellow solid (3.42 g, 94%): **^{1}H NMR** (400 MHz, Chloroform-*d*) δ 8.44 (s, 1H), 7.40–7.30 (m, 5H), 6.41 (s, 1H), 5.16 (s, 2H), 4.89 (d, J = 5.4 Hz, 1H), 3.72–3.62 (m, 6H), 3.46 (ddq, J = 36.4, 9.3, 7.0 Hz, 2H), 3.10 (s, 4H), 2.81 (d, J = 5.4 Hz, 1H), 1.56 (s, 3H), 1.43 (s, 3H), 1.18 (t, J = 7.0 Hz, 3H), 1.06 (t, J = 7.0 Hz, 3H). **R_f**: 0.33 (30% EA in CyHex). The characterization data is consistent with the reported data.[69]

Benzyl (*Z*)-4-(3-(hydroxymethylene)-2,2-dimethyl-6-nitro-4-oxochroman-7-yl)piperazine-1-carboxylate (6): To a solution of **5** (6.06 g, 11.2 mmol, 1 equiv.) in acetone (185.0 mL, 0.1 M), iodine (85 mg, 0.3 mmol, 0.03 equiv.) was added in one portion and the reaction mixture was stirred at 35 °C for 14 h. After reaction completion, as monitored by TLC, the solvent was removed under reduced pressure. The resultant crude was dissolved in DCM and washed sequentially with 5% aqueous $Na_2S_2O_3$, ddH_2O, and brine. The organic layer was dried over anhydrous $MgSO_4$ and filtered. Then, the filtrate was condensed under reduced pressure, and the resulting mixture was purified by silica gel flash column chromatography to provide the desired product as a yellow solid (5.32 g, 86%): **^{1}H NMR** (700 MHz, Chloroform-*d*) δ 14.75 (d, J = 8.6 Hz, 1H), 8.48 (s, 1H), 7.89 (d, J = 8.3 Hz, 1H), 7.38–7.35 (m, 4H), 7.33 (ddd, J = 8.5, 5.4, 2.3 Hz, 1H), 6.40 (s, 1H), 5.16 (s, 2H), 3.69 (t, J = 5.4 Hz, 4H), 3.13 (d, J = 30.4 Hz, 4H), 1.62 (s, 6H). **R_f**: 0.3 (30% EA in PE). The characterization data is consistent with the reported data.[69]

General Method 1:

To a solution of arylhydrazine (1.2 equiv.) in AcOH (0.1 M), corresponding enol (1 equiv.) was added carefully and stirred for 2 h at 50 °C. The reaction mixture was diluted with DCM, followed by an aqueous workup with sat. Na_2CO_3 (aq) and brine. The aqueous layer was extracted with DCM three times. The combined organic layer was dried over anhydrous $MgSO_4$ and condensed under reduced pressure. The resulting mixture was purified by silica gel flash column chromatography and reverse phase flash column chromatography.

4-(7-(4-((benzyloxy)carbonyl)piperazin-1-yl)-4,4-dimethyl-8-nitrochromeno[4,3-*c*]pyrazol-1(4H)-yl)benzoic acid (7): Compound was obtained through general method 1. 554 mg, 89%: **^{1}H NMR** (600 MHz, DMSO-d_6) δ 13.30 (s, 1H), 8.15–8.10 (m, 2H), 7.82 (s, 1H), 7.72–7.67 (m, 2H), 7.51 (s, 1H), 7.37 (d, J = 4.5 Hz, 4H), 7.32 (ddd, J = 8.8, 5.2, 3.7 Hz, 1H), 6.80 (s, 1H), 5.10 (s, 2H), 3.52 (s, 4H), 3.05 (t, J = 5.1 Hz, 4H), 1.66 (s, 6H). **^{13}C NMR** (151 MHz, DMSO-d_6) δ 166.5, 157.3, 154.4, 148.1, 142.8, 136.8, 135.6, 133.6, 131.0, 130.7, 129.8, 128.4, 127.9, 127.6, 125.8, 122.8, 121.1, 108.7, 107.3, 79.4, 66.4, 50.5, 43.2, 28.8. **R_f**: 0.5 in 10% MeOH in DCM. **HRMS-ESI** (m/z): $[M+H]^+$ calculated for $C_{31}H_{29}N_5O_7$ = 584.2140; $[M+H]^+$ found, 584.2138.

4-(7-(4-((Benzyloxy)carbonyl)piperazin-1-yl)-4,4-dimethyl-8-nitrochromeno[4,3-c]pyrazol-1(4H)-yl)benzenesulfonic acid (**8**): Compound was obtained through general method 1. 66 mg, 25%: **^{1}H NMR** (600 MHz, DMSO-d_6) δ 8.62 (0.25H), 8.32 (0.25H), 7.83 (d, J = 8.6 Hz, 0.5H), 7.77 (d, J = 8.5 Hz, 2.25H), 7.71 (d, J = 8.6 Hz, 0.5H), 7.56 (s, 0.75H), 7.50 (d, J = 8.4 Hz, 1.5H), 7.41–7.28 (m, 5.5H), 6.79 (s, 0.65H), 6.78 (s, 0.33H), 5.12 (s, 0.66H), 5.10 (s, 1.37H), 3.52 (s, 4H), 3.08 (d, J = 4.8 Hz, 1.33H), 3.05 (s, 2.67H), 1.67 (s, 2H), 1.65 (s, 4H). **^{13}C NMR** (151 MHz, DMSO-d_6) δ 157.7, 157.2, 154.5, 154.4, 148.9, 148.2, 147.9, 146.4, 141.1, 139.3, 139.1, 136.8, 135.2, 135.0, 133.8, 129.5, 128.4, 127.9, 127.6, 127.6, 126.9, 126.8, 125.1, 123.8, 122.6, 122.4, 120.8, 120.7, 117.3, 109.9, 108.8, 108.7, 107.6, 79.3, 66.3, 50.8, 50.5, 43.3, 39.9, 29.6, 28.9. **HRMS-ESI** (m/z): [M+H]+ calculated for $C_{30}H_{30}O_8N_5S$ = 620.1810; found, 620.1808.

6-(7-(4-((Benzyloxy)carbonyl)piperazin-1-yl)-4,4-dimethyl-8-nitrochromeno[4,3-*c*]pyrazol-1(4H)-yl)nicotinic acid (9): Compound was obtained through general method 1. 66 mg, 25%: **^{1}H NMR** (600 MHz, DMSO-d_6) δ 9.27–9.21 (m, 1H), 9.06 (s, 1H), 8.55 (dd, J = 8.5, 2.2 Hz, 1H), 8.04 (d, J = 9.0 Hz, 1H), 7.61 (s, 1H), 7.38 (d, J = 4.4 Hz, 4H), 7.36–7.31 (m, 1H), 6.63 (s, 1H), 5.18 (s, 2H), 3.78–3.66 (m, 4H), 3.10 (d, J = 18.6 Hz, 4H), 1.68 (s, 6H). **^{13}C NMR**

(151 MHz, DMSO-*d*$_6$) δ 168.6, 158.3, 155.9, 155.5, 150.3, 148.8, 140.8, 136.7, 136.6, 135.2, 132.6, 128.7, 128.3, 128.1, 126.6, 125.2, 124.4, 117.3, 109.3, 108.8, 78.4, 67.6, 51.5, 43.9, 28.7. **HRMS-ESI** (m/z): $[M+H]^+$ calculated for $C_{30}H_{29}O_7N_6$ = 585.2092; found, 585.2087.

Benzyl 4-(4,4-dimethyl-8-nitro-1,4-dihydrochromeno[4,3-*c*]pyrazol-7-yl)piperazine-1-carboxylate (10): Compound was obtained through general method 1. 41 mg, 23%: **^{1}H NMR** (600 MHz, Chloroform-*d*) δ 8.45 (s, 1H), 7.75 (s, 1H), 7.59 (s, 1H), 7.37 (d, *J* = 4.4 Hz, 4H), 7.33 (ddq, *J* = 8.6, 5.9, 3.9, 2.7 Hz, 1H), 6.61 (s, 1H), 5.17 (s, 2H), 3.73 – 3.67 (m, 4H), 3.17–3.00 (m, 4H), 1.68 (s, 6H). **^{13}C NMR** (151 MHz, Chloroform-*d*) δ 158.3, 155.4, 149.4, 138.5, 136.7, 136.0, 128.7, 128.3, 128.1, 125.6, 122.5, 120.6, 109.0, 108.9, 79.1, 67.5, 51.6, 43.8, 29.8. **HRMS-ESI** (m/z): $[M+H]^+$ calculated for $C_{24}H_{26}O_5N_5$ = 464.1929; found, 464.1922.

3-(7-(4-((Benzyloxy)carbonyl)piperazin-1-yl)-4,4-dimethyl-8-nitrochromeno[4,3-*c*]pyrazol-1(4H)-yl)benzoic acid (11): Compound was obtained through general method 1. 62 mg, 25%: **^{1}H NMR** (500 MHz, DMSO-*d*$_6$) δ 13.33 (s, 1H), 8.13 (dt, *J* = 7.8, 1.4 Hz, 1H), 8.01 (t, *J* = 1.9 Hz, 1H), 7.84 (ddd, *J* = 7.9, 2.3, 1.2 Hz, 1H), 7.80 (s, 1H), 7.74 (t, *J* = 7.8 Hz, 1H), 7.44 (s, 1H), 7.39–7.28 (m, 5H), 6.79 (s, 1H), 5.10 (s, 2H), 3.34 (s, 4H), 3.08–2.97 (m, 4H), 1.67 (s, 6H). **^{13}C NMR** (126 MHz, DMSO-*d*$_6$) δ 166.2, 157.3, 154.5, 148.1, 139.6, 136.8, 135.4, 133.6, 132.3, 130.2, 130.2, 129.8, 129.8, 128.5, 127.9, 127.6, 126.4, 122.4, 120.9, 108.6, 107.3, 79.5, 66.4, 55.0, 50.5, 43.3, 40.0, 39.9, 39.7, 39.5, 39.4, 39.2, 39.0, 29.0. **HRMS-ESI** (m/z): $[M+Na]^+$ calculated for $C_{31}H_{29}O_7N_5Na$ = 606.1959 $[M+Na]^+$; found 606.1962.

2-(7-(4-((Benzyloxy)carbonyl)piperazin-1-yl)-4,4-dimethyl-8-nitrochromeno[4,3-c]pyrazol-1(4H)-yl)benzoic acid (12): Compound was obtained through general method 1. 79 mg, 32%: **^{1}H NMR** (600 MHz, Chloroform-*d*) δ 8.18 (dd, *J* = 7.8, 1.5 Hz, 1H), 7.75 (td, *J* = 7.6, 1.6 Hz, 1H), 7.70 (td, *J* = 7.7, 1.1 Hz, 1H), 7.54 (s, 1H), 7.48 (d, *J* = 7.1 Hz, 1H), 7.37–7.34 (m, 4H), 7.32 (ddd, *J* = 8.5, 5.4, 2.2 Hz, 1H), 7.17 (s, 1H), 6.57 (s, 1H), 5.15 (s, 2H), 3.67–3.62 (m, 4H), 3.00 (s, 4H), 1.73 (s, 3H), 1.65 (s, 3H). **^{13}C NMR** (151 MHz, Chloroform-*d*) δ 167.1, 158.0, 155.4, 148.9, 138.4, 136.6, 135.1, 134.1, 134.0, 132.9, 132.6, 130.9, 129.2, 128.7, 128.5, 128.3, 128.1, 121.5, 121.4, 108.9, 108.1, 79.7, 67.6, 51.5, 43.8, 27.1. **HRMS-ESI** (m/z): $[M+Na]^+$ calculated for $C_{31}H_{29}O_7N_5Na$ = 606.1959 $[M+Na]^+$; found 606.1959.

Benzyl 4-(4,4-dimethyl-8-nitro-1-phenyl-1,4-dihydrochromeno[4,3-*c*]pyrazol-7-yl)piperazine-1-carboxylate (13): Compound was obtained through general method 1. 39.8 mg, 57%: ^{1}H NMR (600 MHz, Chloroform-*d*) δ 7.58–7.54 (m, 3H), 7.51 (d, *J* = 2.4 Hz, 2H), 7.50–7.47 (m, 2H), 7.36 (d, *J* = 3.2 Hz, 4H), 7.32 (ddt, *J* = 6.9, 3.6, 2.0 Hz, 1H), 6.61 (s, 1H),

5.16 (s, 2H), 3.71–3.63 (m, 4H), 3.03 (s, 4H), 1.70 (s, 6H). **^{13}C NMR** (151 MHz, Chloroform-*d*) δ 157.9, 155.4, 148.5, 139.5, 136.6, 135.4, 134.2, 130.6, 129.9, 129.8, 128.7, 128.3, 128.1, 126.2, 122.3, 121.2, 109.1, 108.8, 79.7, 67.5, 51.5, 43.8, 29.4. **HRMS-ESI** (m/z): $[M+H]^+$ calculated for $C_{30}H_{30}O_5N_5$ = 540.2242 $[M+H]^+$; found 540.2243.

Benzyl 4-(1-benzyl-4,4-dimethyl-8-nitro-1,4-dihydrochromeno[4,3-*c*]pyrazol-7-yl)piperazine-1-carboxylate (14): Compound was obtained through general method 1. 20.3 mg, 34%: **^{1}H NMR** (600 MHz, Chloroform-*d*) δ 8.11 (s, 1H), 7.43 (s, 1H), 7.37 (d, *J* = 1.8 Hz, 2H), 7.36–7.32 (m, 5H), 7.29 (d, *J* = 7.4 Hz, 1H), 7.23 (d, *J* = 7.5 Hz, 2H), 6.58 (s, 1H), 5.65 (s, 2H), 5.16 (s, 2H), 3.71–3.65 (m, 4H), 3.13–2.96 (m, 4H), 1.65 (s, 6H). **^{13}C NMR** (151 MHz, Chloroform-*d*) δ 158.1, 155.4, 148.9, 136.7, 135.8, 135.0, 132.4, 130.5, 129.3, 128.7, 128.3, 128.3, 128.1, 126.8, 122.2, 122.2, 109.1, 108.5, 79.6, 67.5, 60.5, 55.4, 51.6, 43.8, 29.4. **HRMS-ESI** (m/z): $[M+Na]^+$ calculated for $C_{31}H_{31}O_5N_5Na$ = 576.2217$[M+Na]^+$; found 576.2216.

4-(7-(4-((Benzyloxy)carbonyl)piperazin-1-yl)-4,4-dimethylchromeno[4,3-c]pyrazol-1(4H)-yl)benzoic acid (15): Compound was obtained through general method 1. (97 mg, 33%): **^{1}H NMR** (600 MHz, DMSO-d_6) δ 8.25–8.21 (m, 2H), 7.67–7.63 (m, 2H), 7.54 (s, 1H), 7.37 (d, *J* = 4.4 Hz, 4H), 7.33 (dd, *J* = 9.4, 4.1 Hz, 1H), 6.84 (d, *J* = 8.7 Hz, 1H), 6.67 (s, 1H), 6.46 (s, 1H), 5.17 (s, 2H), 3.77–3.65 (m, 4H), 3.23 (s, 4H), 1.64 (s, 6H). **^{13}C NMR** (151 MHz, DMSO-d_6) δ 169.8, 155.1, 154.1, 151.9, 144.5, 140.5, 136.4, 135.0, 132.9, 131.2, 128.9, 128.4, 128.0, 127.8, 125.3, 123.2, 122.7, 108.4, 105.2, 93.9, 67.2, 48.1, 43.3, 28.2. **HRMS-ESI** (m/z): $[M+H]^+$ calculated for $C_{31}H_{31}O_5N_4$ 539.2289; found, 539.2282.

4-(8-Amino-7-(4-((benzyloxy)carbonyl)piperazin-1-yl)-4,4-dimethylchromeno[4,3-*c*]pyrazol-1(4H)-yl)benzoic acid (16): 7 (50.0 mg, 0.1 mmol, 1 equiv.) and $SnCl_2$ (81.2 mg, 0.4 mmol, 4.8 equiv.) were dissolved in absolute ethanol (5.00 mL) and heated to 70 °C under argon atmosphere. After full conversion confirmed by LC-MS, treated with saturated sodium bicarbonate solution, filtered, and extracted with ethyl acetate. The combined organic phase was dried over $MgSO_4$ and the solvent was removed under reduced pressure to yield the final product. (27.0 mg, 57%) **^{1}H NMR** (700 MHz, DMSO-d_6) δ 8.10–8.07 (m, 2H), 7.66 (s, 1H), 7.61–7.58 (m, 2H), 7.38 (d, *J* = 5.4 Hz, 4H), 7.35–7.30 (m, 1H), 6.55 (s, 1H), 6.28 (s, 1H), 5.75 (s, 0H), 5.10 (s, 2H), 3.52 (d, *J* = 21.9 Hz, 5H), 2.77 (t, *J* = 4.9 Hz, 4H), 1.52 (s, 6H). **^{13}C NMR** (176 MHz, DMSO-d_6) δ 154.5, 143.8, 139.4, 136.9, 136.2, 135.2, 132.5, 130.5, 128.4, 127.9, 127.6, 125.0, 123.8, 110.3, 109.3, 107.7, 75.7, 66.3, 49.8, 27.7. **HRMS-ESI** (m/z): $[M+H]^+$ calculated for $C_{31}H_{32}N_5O_5$ $[M+H]^+$ 554.2391; found, 554.2398.

4-(7-(4-((benzyloxy)carbonyl)piperazin-1-yl)-4,4-dimethyl-6-nitrochromeno[4,3-c]pyrazol-1(4H)-yl)benzoic acid (17): Compound was obtained through general method 1. (17.5 mg, 20%). **^{1}H NMR** (600 MHz, Chloroform-*d*) δ 8.30–8.25 (m, 2H), 7.67–7.62 (m, 2H), 7.57 (s, 1H), 7.40 – 7.30 (m, 5H), 6.91 (d, *J* = 8.6 Hz, 1H), 6.55 (d, *J* = 8.7 Hz, 1H), 5.15 (s, 2H), 3.65–3.57 (m, 4H), 2.97 (s, 4H), 1.67 (s, 6H). **^{13}C NMR** (151 MHz, Chloroform-*d*) δ 170.0, 155.4, 145.5, 145.0, 144.1, 139.2, 136.6, 135.4, 131.7, 131.2, 129.7, 128.7, 128.3, 128.1, 125.7, 124.4, 123.8, 113.6, 112.6, 80.1, 67.5, 52.2, 44.3, 28.3. **HRMS-ESI** (m/z): $[M+H]^+$ calculated for $C_{31}H_{30}O_7N_5$ = 584.2140 $[M+H]^+$; found, 584.2142.

4-(4,4-Dimethyl-8-nitro-7-(piperazin-1-yl)chromeno[4,3-*c*]pyrazol-1(4H)-yl)benzoic acid hydrochloride (18): Dissolved **7** (50.0 mg, 0.1 mmol) in the 4 M HCl solution and stirred the mixture at room temperature for 1 h. Dried the solvent and the residue was purified by reverse column chromatography. (23.0 mg, 56%): **^{1}H NMR** (600 MHz, DMSO-d_6) δ 13.34 (s, 1H), 8.80 (s, 2H), 8.13 (d, *J* = 8.6 Hz, 2H), 7.84 (s, 1H), 7.69 (d, *J* = 8.6 Hz, 2H), 7.55 (s, 1H), 6.90 (s, 1H), 3.24 (d, *J* = 5.8 Hz, 4H), 3.21 (d, *J* = 5.1 Hz, 4H), 1.68 (s, 6H). **^{13}C NMR** (151 MHz, DMSO-*d6*) δ 166.5, 157.5, 147.4, 142.8, 135.7, 133.8, 131.1, 130.7, 129.6, 125.9, 122.9, 121.1, 109.3, 108.1, 79.6, 47.9, 42.9, 28.9. **HRMS-ESI** (m/z): $[M+H]^+$ calculated for $C_{23}H_{24}N_5O_5$ $[M+H]^+$ 450.1772; found, 450.1768.

4-(7-(4-(benzylcarbamoyl)piperazin-1-yl)-4,4-dimethyl-8-nitrochromeno[4,3-*c*]pyrazol-1(4H)-yl)benzoic acid (19): Compound was obtained through general method 1 (18.7 mg, 15%). **^{1}H NMR** (600 MHz, DMSO-d_6) δ 8.13 (d, *J* = 8.5 Hz, 2H), 7.82 (s, 1H), 7.69 (d, *J* = 8.3 Hz, 2H), 7.50 (s, 1H), 7.30 (t, *J* = 7.5 Hz, 2H), 7.25 (d, *J* = 7.0 Hz, 2H), 7.20 (t, *J* = 7.2 Hz, 1H), 7.16 (t, *J* = 5.9 Hz, 1H), 6.81 (s, 1H), 4.25 (d, *J* = 5.7 Hz, 2H), 3.48–3.42 (m, 4H), 3.05–3.02 (m, 4H), 1.66 (s, 6H). **^{13}C NMR** (151 MHz, DMSO-d_6) δ 166.5, 157.4, 157.3, 148.2, 140.9, 135.6, 133.5, 130.7, 129.9, 128.1, 127.1, 126.5, 125.8, 122.8, 121.1, 108.4, 107.0, 79.4, 50.6, 43.5, 43.2, 28.9. **LCMS-ESI** (m/z): 583.2 $[M+H]^+$.

4-(7-(4-(benzyl(methyl)carbamoyl)piperazin-1-yl)-4,4-dimethyl-8-nitrochromeno[4,3-*c*]pyrazol-1(4H)-yl)benzoic acid (20): Compound was obtained through general method 1 (16.2 mg, 13%). **^{1}H NMR** (600 MHz, DMSO-d_6) δ 13.26 (s, 1H), 8.13 (d, *J* = 8.5 Hz, 2H), 7.82 (s, 1H), 7.69 (d, *J* = 8.5 Hz, 2H), 7.50 (s, 1H), 7.34 (t, *J* = 7.6 Hz, 2H), 7.26 (t, *J* = 6.7 Hz, 3H), 6.80 (s, 1H), 4.35 (s, 2H), 3.30–3.25 (m, 4H), 3.11–3.06 (m, 4H), 2.70 (s, 3H), 1.65 (s, 6H). **^{13}C NMR** (151 MHz, DMSO-d_6) δ 166.5, 163.5, 157.3, 148.1, 142.9, 138.0, 135.6, 133.5, 131.0, 130.7, 129.9, 128.5, 127.5, 127.0, 125.8, 122.8, 121.1, 108.5, 107.0, 79.4, 52.9, 50.4, 46.2, 36.0,

28.8. **HRMS-ESI** (m/z): $[M+H]^+$ calculated for $C_{32}H_{33}O_6N_6$ = 597.2456 $[M+H]^+$; found, 597.2463.

4-(7-(4-(*tert*-Butoxycarbonyl)piperazin-1-yl)-4,4-dimethyl-8-nitrochromeno[4,3-*c*]pyrazol-1(4H)-yl)benzoic acid (21): Compound was obtained through general method 1. 51 mg, 17%: **^{1}H NMR** (600 MHz, DMSO-d_6) δ 8.13 (d, J = 8.5 Hz, 2H), 7.82 (s, 1H), 7.69 (d, J = 8.5 Hz, 2H), 7.50 (s, 1H), 6.79 (s, 1H), 3.42 (s, 4H), 3.05 – 2.97 (m, 4H), 1.66 (s, 6H), 1.41 (s, 9H). **^{13}C NMR** (151 MHz, DMSO-d_6) δ 166.5, 157.3, 153.9, 148.1, 142.8, 135.6, 133.6, 130.9, 130.7, 129.8, 125.8, 122.8, 121.1, 108.6, 107.2, 79.4, 79.1, 50.6, 42.9, 28.8, 28.0. **HRMS-ESI** (m/z): $[M+H]^+$ calculated for $C_{28}H_{32}N_5O_7$ $[M+H]^+$ 550.2296; found, 550.2299.

4-(7-fluoro-4,4-dimethyl-8-nitrochromeno[4,3-*c*]pyrazol-1(4H)-yl)benzoic acid (22): Compound was obtained through general method 1. (60 mg, 67%): **^{1}H NMR** (500 MHz, DMSO-d_6) δ 11.73 (s, 0H), 8.16–8.13 (m, 2H), 7.90 (s, 1H), 7.74–7.71 (m, 2H), 7.60 (d, J = 8.4 Hz, 1H), 7.29 (d, J = 12.6 Hz, 1H), 1.70 (s, 6H). **^{13}C NMR** (126 MHz, DMSO-d_6) δ 166.5, 142.6, 135.8, 131.2, 130.8, 128.9, 128.6, 125.9, 123.5, 119.9, 80.8, 28.8. **R_f**: 0.3 in 7% MeOH in DCM. **HRMS-ESI** (m/z): $[M+H]^+$ calculated for $C_{19}H_{15}O_5N_3F$ $[M+H]^+$ 384.0990; found, 384.0990.

4-(4,4-Dimethyl-7-morpholino-8-nitrochromeno[4,3-*c*]pyrazol-1(4H)-yl)benzoic acid (23): Compound was obtained through general method 1. 57 mg, 23%: **^{1}H NMR** (600 MHz, DMSO-d_6) δ 8.13 (d, J = 8.5 Hz, 2H), 7.81 (s, 1H), 7.69 (d, J = 8.5 Hz, 2H), 7.49 (s, 1H), 6.79 (s, 1H), 3.72–3.65 (m, 4H), 3.05–2.99 (m, 4H), 1.66 (s, 6H). **^{13}C NMR** (151 MHz, DMSO-d_6) δ 166.5, 157.3, 148.1, 142.8, 135.6, 133.6, 131.0, 130.7, 129.8, 125.8, 122.7, 121.1, 108.3, 107.1, 79.4, 65.9, 51.1, 28.8. **HRMS-ESI** (m/z): $[M+H]^+$ calculated for $C_{23}H_{22}N_4O_6$ $[M+H]^+$ 451.1612; found 451.1613.

4-(4,4-Dimethyl-8-nitro-7-(piperidin-1-yl)chromeno[4,3-*c*]pyrazol-1(4H)-yl)benzoic acid (24): Compound was obtained through general method 1. 74 mg, 30%: **^{1}H NMR** (600 MHz, DMSO-d_6) δ 8.12 (d, J = 8.5 Hz, 2H), 7.80 (s, 1H), 7.69 (d, J = 8.5 Hz, 2H), 7.46 (s, 1H), 6.74 (s, 1H), 3.01–2.96 (m, 4H), 1.65 (s, 6H), 1.61–1.58 (m, 4H), 1.56–1.52 (m, 2H). **^{13}C NMR** (151 MHz, DMSO-d_6) δ 166.5, 157.2, 148.8, 142.9, 135.6, 133.3, 130.9, 130.7, 130.0, 125.8, 122.7, 121.1, 108.1, 106.3, 79.2, 51.9, 28.8, 25.3, 23.4. **HRMS-ESI** (m/z): $[M+H]^+$ calculated for $C_{24}H_{25}N_4O_5$ $[M+H]^+$ 449.1820; found, 449.1818.

(R)-4-(7-((1-(tert-butoxycarbonyl)piperidin-3-yl)amino)-4,4-dimethyl-8-nitrochromeno[4,3-*c*]pyrazol-1(4H)-yl)benzoic acid (25) :

Compound **22** (30.0 mg, 0.1 mmol, 1 equiv.) was dissolved in 2.00 mL acetonitrile. (R)-1-Boc-3-aminopiperidine (21.9 mg, 0.1 mmol, 1.4 equiv.) was added. The mixture was stirred overnight at 40 °C. After the completion of the reaction, as monitored by TLC, the reaction mixture was condensed under reduced pressure, and the condensed reaction mixture was dissolved in DCM. The organic layer was washed with 1 N HCl (aq) and brine dried over anhydrous $MgSO_4$ and condensed under reduced pressure. The crude was purified by silica gel flash column chromatography to provide the desired product as a yellow solid (11.6 mg, 26%): **^{1}H NMR** (500 MHz, Chloroform-*d*) δ 8.31–8.27 (m, 2H), 7.91 (s, 1H), 7.68–7.63 (m, 2H), 7.55 (s, 1H), 6.50 (s, 1H), 4.02 (s, 1H), 3.91–3.43 (m, 2H), 3.07 (d, *J* = 55.9 Hz, 2H), 2.08 (s, 1H), 1.80 (d, *J* = 13.7 Hz, 1H), 1.68 (d, *J* = 10.8 Hz, 6H), 1.49 (s, 9H), 1.25 (s, 2H). **^{13}C NMR** (126 MHz, Chloroform-*d*) δ 169.4, 160.0, 146.2, 143.9, 135.2, 131.7, 130.9, 129.5, 126.5, 125.4, 122.9, 121.7, 104.7, 100.6, 80.2, 79.4, 29.2, 28.4. **R**f: 0.3 in 10% MeOH in DCM. **HRMS-ESI** (m/z): $[M+H]^+$ calculated for $C_{29}H_{34}N_5O_7$ $[M+H]^+$ 564.2453; found, 564.2450.

Benzyl 4-(2,2-dimethyl-4-oxochroman-7-yl)piperazine-1-carboxylate (26): To a solution of **2** (500.0 mg, 2.6 mmol, 1 equiv.) in DMSO, 1-Cbz piperazine (793.0 mg, 3.6 mmol, 1.4 equiv.) and K_2CO_3 (1.08 g, 7.8 mmol, 3 equiv.) were added and stirred at 100 °C for overnight. After the completion of the reaction, as monitored by TLC, the reaction mixture was diluted with EtOAc. The organic layer was washed with water and brine and dried over anhydrous $MgSO_4$. The organic layer was filtered and condensed under reduced pressure, and the resulting mixture was purified by silica gel flash column chromatography to provide 34. (851.0 mg, 83%): **^{1}H NMR** (500 MHz, DMSO-d_6): δ 7.55 (d, *J* = 8.95 Hz, 1H), 7.38–7.30 (m, 5H), 6.61 (dd, *J* = 8.95 Hz, 2.35 Hz, 1H), 6.31 (d, *J* = 2.3 Hz, 1H), 5.09 (s, 2H), 3.49 (s, 4H), 3.37–3.36 (m, 4H), 2.61 (s, 2H), 1.35 (s, 6H). **^{13}C NMR** (126 MHz, DMSO-d_6): δ 189.4, 161.0, 155.8, 154.3, 136.7, l28.3, 127.8, 127.5, 127.2, 110.7, 107.6, 100.0, 78.9, 66.2, 47.7, 45.9, 42.7, 26.2. **LCMS-ESI** (m/z): 395.2 $[M+H]^+$.

Benzyl 4-(3-(diethoxymethyl)-2,2-dimethyl-4-oxochroman-7-yl)piperazine-1-carboxylate (27): Using **26** (500.0 mg, 1.3 mmol, 1 equiv.) as the starting material, intermediate **27** was obtained by the method for preparing **5**. (491 mg, 78%): **^{1}H NMR** (500 MHz, Chloroform-*d*): δ 7.72 (d, *J* = 8.85 Hz, 1H), 7.38–7.31 (m, 5H), 6.50 (dd, *J* = 8.9 Hz, 2.4 Hz, 1H), 6.22 (d, *J* = 2.35 Hz, 1H), 5.16 (s, 2H), 4.91 (d, *J* = 5.9 Hz, 1H), 3.74–3.37 (m, 8H), 3.33 (s, 4H), 2.73 (d, *J*

= 5.9 Hz, 1H), 1.52 (s, 3H), 1.40 (s, 3H), 1.19 (t, *J* = 7.05 Hz, 3H), 1.05 (t, *J* = 7.0 Hz, 3H). **^{13}C NMR** (126 MHz, Chloroform-*d*): δ 190.1, 160.6, 156.0, 155.1, 136.3, 128.5, 128.1, 128.1, 127.9, 112.5, 108.2, 100.9, 99.7, 80.8, 67.3, 62.5, 61.8, 58.3, 47.0, 26.2, 25.7, 15.1, 14.9. **LCMS-ESI** (m/z): 497.2 $[M+H]^+$.

Benzyl (Z)-4-(3-(hydroxymethylene)-2,2-dimethyl-4-oxochroman-7-yl)piperazine-1-carboxylate (28): Using **27** (300.0 mg, 0.6 mmol, 1.0 equiv.) as the starting material, intermediate **28** was obtained by the method for preparing **6**. (202.0 mg, 79%): **^{1}H NMR** (400 MHz, Chloroform-*d*): δ 15.08 (d, *J* = 7.08 Hz, 1H), 7.76 (d, *J* = 8.88 Hz, 1H), 7.72 (d, *J* = 4.88 Hz, 1H), 7.38–7.32 (m, 5H), 6.54 (dd, *J* = 8.92 Hz, 2.32 Hz, 1H), 6.23 (d, *J* = 2.28 Hz, 1H), 5.17 (s, 2H), 3.66 (t, *J* = 5.0 Hz, 4H), 3.38 (t, *J* = 5.6 Hz, 4H), 1.57 (s, 6H). **^{13}C NMR** (101 MHz, Chloroform-*d*): δ 181.9, 166.4, 160.5, 156.0, 155.0, 136.3, 128.4, 128.0, 127.9, 127.9, 113.6, 110.9, 108.4, 101.0, 78.4, 67.3, 46.7, 43.1, 28.2. **LCMS-ESI** (m/z): 423.2 $[M+H]^+$.

4-(2-Amino-4-fluoro-phenyl)-2-methyl-but-3-yn-2-ol (29): $Pd(PPh_3)_2Cl_2$ (118.8 mg, 0.2 mmol), CuI (72.3 mg, 0.4 mmol) and Et_3N (12.7 ml, 90.8 mmol) were added to a stirred solution of 5-Fluoro-2-iodoaniline (1.000 g, 4.2 mmol) and 2-methylbut-3-yn-2-ol (0.83 ml, 8.4 mmol) in dry MeCN (40.0 mL) at room temperature under an argon atmosphere. The mixture was heated at 50 ˚C for 1.5 h with stirring. The reaction mixture was allowed to cool down to room temperature, and DCM (2.0 mL) was added. The mixture was poured into H_2O and extracted with DCM. The combined organic layers were washed with H_2O and dried with anhydrous $MgSO_4$. After the evaporation of the solvent under reduced pressure, the crude product was purified by flash chromatography to afford the title compound as an oil (709.3 mg, 87 %).[116] **^{1}H NMR** (400 MHz, Chloroform-*d*): δ 7.22–7.18 (m, 1H), 6.40–6.35 (m, 2H), 4.28 (s, 2H), 2.08 (s, 1H), 1.64 (s, 6H). **LCMS-ESI** (m/z): 176.1 $[M+H-H_2O]^+$

7-Fluoro-2,2-dimethyl-2,3-dihydro-1*H*-quinolin-4-one (30): PTSA (359.0 mg, 1.9 mmol) was added to the solution of **29** (202.6 mg, 1.1 mmol) in 28.0 mL of EtOH. The mixture was heated under reflux with stirring overnight, cooled to room temperature, diluted with DCM, poured into H_2O, and extracted with DCM. The combined organic layers were washed with H_2O and dried with anhydrous $MgSO_4$. The solvent was evaporated in vacuo to give the crude product, which was purified by flash chromatography to afford the title compound as a light brown solid (545.8 mg, 77 %). **^{1}H NMR** (400 MHz, Chloroform-*d*): δ 7.84 (dd, *J* = 8.8 Hz, 6.64 Hz, 1H), 6.43 (td, *J* = 8.76 Hz, 2.32 Hz, 1H), 6.28 (dd, *J* = 10.44 Hz, 2.32 Hz, 1H), 4.34 (s, 1H), 2.57 (s, 2H), 1.33 (s, 6H).

7-Fluoro-2,2-dimethyl-6-nitro-2,3-dihydroquinolin-4(1*H*)-one (32): To the solution of **30** (1.81 g, 9.4 mmol) in sulfuric acid (17.0 ml), 70% nitric acid (0.7 ml, 10.3 mmol) in sulfuric acid (6.0 ml) was added dropwise at -10 °C, and the resultant was stirred for 1 h. Water was added dropwise to the reaction mixture, followed by the addition of ethyl acetate. The organic layer was separated, sequentially washed with a saturated aqueous sodium bicarbonate solution and a saturated aqueous sodium chloride solution, and dried over anhydrous sodium sulfate, and the solvent was distilled off under reduced pressure. The obtained residue was purified by silica gel column chromatography (PE: EtOAc) to give the final compound (572.7 mg, 26%).**^{1}H NMR** (700 MHz, Chloroform-*d*) δ 8.61 (d, *J* = 8.5 Hz, 1H), 6.31 (d, *J* = 12.3 Hz, 1H), 4.87 (s, 1H), 2.58 (s, 2H), 1.32 (s, 6H).

Benzyl 4-(2,2-dimethyl-6-nitro-4-oxo-1,2,3,4-tetrahydroquinolin-7-yl)piperazine-1-carboxylate (33): 32 (572.7 mg, 2.4 mmol) in 12.0 mL of acetonitrile, 1-Cbz-protected piperazine (0.6 ml, 2.9 mmol) was added and stirred at 40 °C overnight. After the completion of the reaction, as monitored by TLC, the reaction mixture was condensed under reduced pressure, and the condensed reaction mixture was redissolved in DCM. The organic layer was washed with 1 N HCl (aq.) and brine and dried over anhydrous MgSO4. The filtrate was condensed under reduced pressure, and the resulting mixture was purified by silica gel flash column chromatography to provide the desired product as a yellow solid (495.1 mg, 47%). **^{1}H NMR** (400 MHz, Chloroform-*d*) δ 8.49 (s, 1H), 7.33–7.24 (m, 5H), 5.93 (s, 1H), 5.09 (s, 2H), 4.65 (s, 1H), 3.72–3.48 (m, 4H), 2.97 (s, 4H), 2.52 (s, 2H), 1.28 (s, 6H).

Benzyl 4-(3-(diethoxymethyl)-2,2-dimethyl-6-nitro-4-oxo-1,2,3,4-tetrahydroquinolin-7-yl)piperazine-1-carboxylate (34): To a solution of triethyl orthoformate (0.5 ml, 3.1 mmol) in DCM (1.5 mL), $BF_3 \cdot OEt_2$ (0.4 ml, 3.1 mmol) in DCM (0.5 mL) was slowly added over a period of 10 min at -10 °C under an argon atmosphere. The reaction mixture was then gradually warmed up to 0 °C. After 15 min of stirring at 0 °C, the reaction mixture was cooled back to -78 °C. To this reaction mixture, **33** (450. 0 mg, 1.0 mmol) in 1 mL of DCM was added, and DIPEA (0.5 ml, 2.7 mmol) in 1.0 mL of DCM was then added slowly over 30 min. The resulting mixture was stirred at -78 °C for 10 min, and then warmed up to room temperature for an additional 2 h of stirring. The resultant mixture was diluted with DCM and washed with sat. $NaHCO_3$(aq) solution. The combined organic layer was dried over anhydrous $MgSO_4$ and condensed under reduced pressure. The resulting mixture was purified by silica gel flash column chromatography to provide the desired product as a yellow oil (554.8 mg, 100%). **^{1}H NMR** (700 MHz, Chloroform-*d*) δ 8.45 (s, 1H), 7.35–7.24 (m, 5H), 5.93 (s, 1H), 5.09 (s, 2H),

4.77 (d, *J* = 6.3 Hz, 1H), 4.64 (s, 1H), 3.67–3.60 (m, 4H), 3.58–3.51 (m, 4H), 3.04–2.90 (m, 4H), 2.61 (dd, *J* = 6.3, 1.4 Hz, 1H), 1.35 (s, 3H), 1.22 (s, 3H), 1.11 (t, *J* = 7.1 Hz, 3H), 0.96 (t, *J* = 7.0 Hz, 3H).

Benzyl (Z)-4-(3-(hydroxymethylene)-2,2-dimethyl-6-nitro-4-oxo-1,2,3,4-tetrahydroquinolin-7-yl)piperazine-1-carboxylate (35): To a solution of **34** (555.0 mg, 1.1 mmol) in acetone (17.0 ml), iodine (80.2 mg, 0.4 mmol) was added in one portion and the reaction mixture was stirred at 35 °C overnight. After reaction completion, as monitored by TLC, the solvent was removed under reduced pressure. The resultant was diluted with DCM and washed sequentially with 5% aqueous $Na_2S_2O_3$, H_2O, and brine. The organic layer was dried over anhydrous $MgSO_4$ and filtered. Then, the filtrate was condensed under reduced pressure, and the resulting mixture was purified by silica gel flash column chromatography to provide the desired product as an orange solid (351.8 mg, 72%). **^{1}H NMR** (400 MHz, Chloroform-*d*) δ 8.55 (s, 1H), 8.22 (s, 1H), 7.47–7.28 (m, 5H), 5.92 (s, 1H), 5.16 (s, 2H), 3.78–3.62 (m, 4H), 3.17–2.94 (m, 4H), 1.52 (s, 6H).

4-(7-(4-((Benzyloxy)carbonyl)piperazin-1-yl)-4,4-dimethyl-8-nitro-4,5-dihydro-1*H*-pyrazolo[4,3-*c*]quinolin-1-yl)benzoic acid (36): Compound was obtained through general method 1. (28.2 mg, 45%). ^{1}H NMR (700 MHz, DMSO-d_6) δ 13.26 (s, 1H), 8.12 (d, *J* = 8.5 Hz, 2H), 7.77 (s, 1H), 7.67 (s, 1H), 7.64 (d, *J* = 8.5 Hz, 2H), 7.51 (s, 1H), 7.40–7.30 (m, 5H), 6.28 (s, 1H), 5.10 (s, 2H), 3.53 (s, 4H), 2.98–2.91 (m, 4H), 1.35 (s, 6H). ^{13}C NMR (176 MHz, DMSO-d_6) δ 166.1, 154.1, 151.1, 149.6, 149.1, 143.2, 138.8, 136.5, 135.8, 130.7, 130.3, 128.4, 128.1, 127.5, 127.2, 126.0, 121.8, 103.4, 101.7, 65.9, 50.6, 43.0, 34.0, 30.0. HRMS-ESI (m/z): $[M+H]^+$ calculated for $C_{31}H_{31}N_6O_6$ $[M+H]^+$ 583.2300; found, 583.2309.

6-(7-(4-((Benzyloxy)carbonyl)piperazin-1-yl)-4,4-dimethyl-8-nitro-4,5-dihydro-1*H*-pyrazolo[4,3-*c*]quinolin-1-yl)nicotinic acid (37): Compound was obtained through general method 1. (62.0 mg, 38%). ^{1}H NMR (400 MHz, Chloroform-*d*) δ 9.22 (s, 1H), 8.76 (s, 1H), 8.55 (d, *J* = 8.2 Hz, 1H), 7.96 (d, *J* = 8.4 Hz, 1H), 7.62 (s, 1H), 7.39–7.30 (m, 5H), 7.26 (s, 1H), 6.10 (s, 1H), 5.17 (s, 2H), 3.71 (t, *J* = 4.9 Hz, 4H), 3.03 (s, 4H), 1.61 (s, 6H). ^{13}C NMR (151 MHz, Chloroform-*d*) δ 167.5, 156.0, 155.3, 150.2, 149.4, 149.1, 140.6, 137.1, 136.5, 133.4, 131.7, 128.5, 128.1, 127.9, 126.9, 125.2, 124.4, 118.0, 105.7, 103.1, 67.3, 52.8, 51.9, 43.9, 32.0. HRMS-ESI (m/z): $[M+H]^+$ calculated for $C_{30}H_{30}N_7O_6$ $[M+H]^+$ 584.2252; found, 584.2266.

Benzyl 4-(4,4-dimethyl-8-nitro-4,5-dihydro-1*H*-pyrazolo[4,3-*c*]quinolin-7-yl)piperazine-1-carboxylate (38): Compound was obtained through general method 1. (72 mg, 56%). **^{1}H**

NMR (400 MHz, DMSO-d_6) δ 12.82 (s, 1H), 8.28 (s, 1H), 7.41 (s, 1H), 7.39–7.28 (m, 5H), 6.25 (s, 1H), 5.11 (s, 2H), 3.63–3.44 (m, 4H), 2.99–2.85 (m, 4H), 1.46 (s, 6H). **HRMS-ESI** (m/z): $[M+H]^+$ calculated for $C_{24}H_{27}N_6O_4$ $[M+H]^+$ 463.2088; found, 463.2095.

4-(7-(4-((benzyloxy)carbonyl)piperazin-1-yl)-8-((2-chloroethyl)amino)-4,4-dimethylchromeno[4,3-*c*]pyrazol-1(4H)-yl)benzoic acid (39): The 1-bromo-2-chloro-ethane (5.4 µL, 0.1 mmol, 1.4 equiv.), **16** (30.0 mg, 0.1 mmol) and potassium carbonate (15.0 mg, 0.1 mmol, 2 equiv.) were assembled in acetonitrile and the reaction mixture was stirred overnight at reflux. The solvent was removed under reduced pressure and water was added, the aqueous phase was extracted with EtOAc, then the organic layer was washed with brine and dried over $MgSO_4$. The solvent was removed under reduced pressure. The crude was purified by flash column chromatography (10.8 mg, 32%): **^{1}H NMR** (500 MHz, Chloroform-*d*) δ 8.21–8.15 (m, 2H), 7.66–7.61 (m, 2H), 7.49 (s, 1H), 7.39–7.31 (m, 6H), 7.26 (s, 1H), 6.66 (s, 1H), 6.31 (s, 1H), 5.16 (s, 2H), 4.61 (t, *J* = 5.6 Hz, 2H), 3.85 (dd, *J* = 6.3, 5.0 Hz, 2H), 3.64 (s, 4H), 2.88 (s, 4H), 1.61 (s, 6H). **^{13}C NMR** (126 MHz, Chloroform-*d*) δ 165.6, 155.4, 144.4, 136.7, 135.4, 131.0, 129.3, 128.7, 128.3, 128.1, 125.5, 124.6, 110.4, 67.4, 64.9, 50.8, 44.4, 41.8, 28.1. **R_f**: 0.3 in 3% MeOH in DCM. **HRMS-ESI** (m/z): $[M+H]^+$ calculated for $C_{33}H_{35}N_5O_5Cl$ $[M+H]^+$ 616.321; found, 616.2320.

4-(7-(4-((benzyloxy)carbonyl)piperazin-1-yl)-8-(2-chloroacetamido)-4,4-dimethylchromeno[4,3-*c*]pyrazol-1(4H)-yl)benzoic acid (40): 16 (40.0 mg, 0.1 mmol, 1 equiv.) was dissolved in anhydrous tetrahydrofuran (2.00 mL), and triethylamine (50.4 µL, 0.4 mmol, 5 equiv.) was added, followed by slow addition of a solution of chloroacetyl chloride (11.5 µL, 0.1 mmol, 2 equiv.) in tetrahydrofuran (1.00 mL) at room temperature. The mixture was then stirred for about 1 hour at room temperature. Upon the completion of the reaction, the solvent was removed on rotavap and the residue was taken up in dichloromethane and washed with brine and water. The organic layer was separated, concentrated down, and dried on the pump. The crude residue was then taken up in dichloromethane and purified by column chromatography to give the desired product (6.8 mg, 15%): **^{1}H NMR** (400 MHz, Chloroform-*d*) δ 9.53 (s, 1H), 8.31–8.21 (m, 2H), 8.08 (s, 1H), 7.67–7.62 (m, 2H), 7.53 (d, *J* = 0.3 Hz, 1H), 7.41–7.31 (m, 5H), 6.82 (s, 1H), 5.17 (s, 2H), 4.30 (s, 2H), 3.70 (s, 4H), 2.86 (s, 4H), 1.67 (s, 6H). **^{13}C NMR** (151 MHz, Chloroform-*d*) δ 168.1, 164.6, 155.3, 150.2, 143.7, 143.2, 136.4, 134.9, 132.2, 131.5, 130.2, 128.6, 128.2, 128.1, 125.7, 125.4, 123.7, 114.0, 112.0, 111.0, 77.6, 67.5, 43.1, 40.7, 28.5.**R_f**: 0.2 in 10% MeOH in DCM. **HRMS-ESI** (m/z): $[M+H]^+$ calculated for $C_{33}H_{35}N_5O_6Cl$ $[M+H]^+$ 630.2114; found, 630.2113.

4-(7-(4-(2-chloroacetyl)piperazin-1-yl)-4,4-dimethyl-8-nitrochromeno[4,3-*c*]pyrazol-1(4H)-yl)benzoic acid (**42**): **18** (25.0 mg, 0.1 mmol, 1 equiv.) was dissolved in anhydrous tetrahydrofuran (2.00 mL), and triethylamine (38.8 µL, 0.3 mmol, 5 equiv.) was added, followed by slow addition of a solution of chloroacetyl chloride (11.1 µL, 0.1 mmol, 2 equiv.) in tetrahydrofuran (1.00 mL) at room temperature. The mixture was then stirred for 1 h at room temperature. Upon the completion of the reaction, the solvent was removed under reduced pressure and the residue was taken up in DCM and washed with brine in a separatory funnel. The organic layer was separated, concentrated, and dried on the pump. The crude residue was then taken up in dichloromethane and purified by flash column chromatography (16.9 mg, 58%): **^{1}H NMR** (600 MHz, Chloroform-*d*) δ 8.23 (d, *J* = 8.5 Hz, 1H), 7.62 (s, 1H), 7.60–7.55 (m, 2H), 4.08 (s, 1H), 7.51 (s, 1H), 6.60 (s, 1H), 4.05 (s, 2H), 3.70 (dt, *J* = 63.7, 5.0 Hz, 4H), 3.06 (dt, *J* = 15.2, 5.1 Hz, 4H), 1.63 (s, 6H). **^{13}C NMR** (151 MHz, Chloroform-*d*) δ 169.6, 165.5, 157.9, 148.2, 143.8, 135.3, 131.8, 129.8, 125.5, 123.6, 121.7, 109.5, 108.9, 79.6, 52.0, 46.3, 40.6, 29.2. **R_f**: 0.8 in 10% MeOH in DCM. **HRMS-ESI** (m/z): $[M+H]^+$ calculated for $C_{25}H_{25}N_5O_6Cl$ $[M+H]^+$ 526.1488; found, 526.1484.

5.2.2 NEC Molecule Building Blocks

3-azidopropan-1-ol (58): 3-Bromopropan-1-ol (1.0 ml, 11.1 mmol, 1 equiv.) was dissolved in water (H_2O, 11.0 mL) at a concentration of 1M. Sodium azide (1.44 g, 22.1 mmol, 2 equiv.) was added, and the mixture was stirred in an oil bath at 60 °C for 1-3 days. The mixture was extracted with Et2O, the combined organic layers were dried over sodium sulfate (Na_2SO_4), and the solvent was removed under reduced pressure. The product was purified by column filtration pentane/Et2O 1:1 (1.00 g, 91%). **^{1}H NMR** (400 MHz, Chloroform-*d*) δ 3.76 (t, *J* = 6.0 Hz, 2H), 3.46 (t, *J* = 6.6 Hz, 2H), 1.93 – 1.77 (m, 2H). Data in accordance with the literature.[117]

2-(3-azidopropoxy)acetic acid (59): A solution of **58** (1.00 g, 9.9 mmol, 1 equiv.) in 10.0 mL (1 M) of THF was added dropwise, in 1.5 hours, to a mechanically stirred suspension of NaH (60% in mineral oil, 1.19 g, 29.7 mmol, 3 equiv.) in 30.0 mL (1 M) of THF. During the addition of **58**, a gentle reflux was maintained. This was followed by the addition of Nal (148.3 mg, 989.1 mmol, 0.1 equiv.) and sodium bromoacetate (1.65 g, 11.9 mmol, 1.2 equiv.) also in 5.0 mL THF. The reaction mixture was heated at reflux temperature for 19 hours, cooled, quenched initially with 20.0 mL of water (added dropwise) and then with 300.0 mL of water, washed with EtOAc (3*200 mL), acidified with concentrated HCl to pH=2, and

extracted with dichloromethane (6*100 mL). The combined dichloromethane extracts were dried ($MgSO_4$), purified by flash column chromatography, and the excess solvent was removed in vacuo to give **59** of the title compound as a yellow viscous oil (920.6 mg, 58%).**^{1}H NMR** (600 MHz, DMSO-d_6) δ 12.48 (s, 1H), 3.99 (s, 2H), 3.51 (t, J = 6.2 Hz, 2H), 3.40 (t, J = 6.8 Hz, 2H), 1.76 (p, J = 6.5 Hz, 2H).**^{13}C NMR** (151 MHz, DMSO-d_6) δ 171.7, 67.5, 67.4, 47.8, 28.6.

2-(prop-2-yn-1-yloxy)acetic acid (61): A round bottom flask was equipped with a magnetic stirrer, flushed with N_2 (gas), and 30 mL of dry THF was added, followed by sodium hydride (60% dispersion in mineral oil, 1.65 g, 41.2 mmol, 2.4 equiv.). Then, propargyl alcohol (1.0 ml, 17.2 mmol, 1 equiv.) was added dropwise and, when the mixture attained room temperature, chloroacetic acid (1,79 g, 18.9 mmol, 1.1 equiv.) was slowly added (over a 2 h period). The reaction mixture was left to stir overnight. The next day, 50 mL of water was added, and the solution was acidified to pH 2 with sulfuric acid. After evaporation, the crude product was dissolved in water and extracted with diethyl ether three times. The organic layers were collected, dried over MgSO4, concentrated, and purified by column chromatography (a linear gradient of MeOH in DCM from 0% to 2% with 1% acetic acid). Fractions containing product were pooled and concentrated giving **61** (1.59 g, 81%). **^{1}H NMR** (600 MHz, Chloroform-*d*) δ 4.33 (d, J = 2.4 Hz, 2H), 4.27 (s, 2H), 2.51 (t, J = 2.4 Hz, 1H). **^{13}C NMR** (151 MHz, Chloroform-*d*) δ 174.9, 78.1, 76.2, 65.8, 58.6.

3,6,9,12-tetraoxapentadec-14-yn-1-ol (64): To a solution of tetra ethylene glycol (2.7 ml, 15.5 mmol, 1 equiv.) in THF (12 mL) at 0 °C, NaH (60% dispersion in mineral oil, 741.3 mg, 18.5 mmol, 1.2 equiv.) was added portion wise. The mixture was stirred for 20 min at room temperature. Propargyl bromide (80% wt. % in toluene, 1.5 ml, 13.9 mmol, 0.9 equiv.) was added dropwise to the mixture. The reaction was quenched with ice-cold water (50 mL) and the pH was adjusted to pH 2 with 1N HCl solution. Extract the mixture with DCM (3 × 25 mL), wash the organic phase with brine (50 mL), and dry it with MgSO4. The solvent was removed in vacuo and the crude product was purified by flash chromatography (0-2% MeOH in DCM) to give the product as a yellow liquid (88.3 mg, 23%). **^{1}H NMR** (400 MHz, Chloroform-*d*) δ 4.20 (d, J = 2.4 Hz, 2H), 3.75–3.64 (m, 14H), 3.63–3.59 (m, 2H), 2.42 (t, J = 2.4 Hz, 1H), 2.33 (s, 1H). Data in accordance with the literature.[118]

3,6,9,12,15-pentaoxaoctadec-17-ynoic acid (66): To a suspension of NaH (60% dispersion in mineral oil, 413.3 mg, 10.3 mmol, 2.4 equiv.) in THF (40 mL), **64** (1.00 g, 4.3 mmol, 1 equiv.) was added dropwise over 10 min to the mixture at room temperature and under Argon.

bromoacetic acid (676.0 mg, 4.9 mmol, 1.13 equiv.) was dissolved in THF (10 mL) and added dropwise over 10 min. The reaction was stirred overnight and monitored by TLC. Water (25 mL) was added, and the solution was acidified with sulfuric acid to pH = 2. The THF was removed *in vacuo*. The Product was extracted using DCM (3 × 20 mL). The organic layer was dried using MgSO4. The solvent was removed *in vacuo* to give the product as a yellow liquid (1.2 g, 93%). **^{1}H NMR** (400 MHz, Chloroform-*d*) δ 4.20 (d, *J* = 2.4 Hz, 2H), 4.16 (s, 2H), 3.76 (d, *J* = 8.1 Hz, 2H), 3.71–3.64 (m, 14H), 2.42 (t, *J* = 2.8 Hz, 1H). Data in accordance with the literature.[119]

2-(2-(2-(2-hydroxyethoxy)ethoxy)ethoxy)ethyl 4-methylbenzenesulfonate (68): The commercially available tetra ethylene glycol (4.58 g, 23.6 mmol, 3 equiv.) was dissolved in dry CH_2Cl_2 (80 mL) under inert atmosphere; then DMAP (192.2 mg, 1.6 mmol, 0.2 equiv.) and Et_3N (3.3 mL, 23.6 mmol, 3 equiv.) were added. The mixture was cooled at 0 °C and a solution of TsCl (1.50 g, 7.9 mmol, 1 equiv.) in dry CH_2Cl_2 (40 mL) was added dropwise. The reaction was stirred at room temperature for 2 h. Then, 100 mL of CH_2Cl_2 was added and the mixture was washed with a solution of HCl 1 M (2 × 40 mL) and brine (1 × 50 mL). The organic phase was dried over Na_2SO_4 and concentrated. The obtained crude was purified by flash column chromatography to yield the pure product (2.48 g, 90%). **^{1}H NMR** (700 MHz, Chloroform-*d*) δ 7.81–7.78 (m, 2H), 7.34 (d, *J* = 8.5 Hz, 2H), 4.16 (s, 2H), 3.72–3.54 (m, 14H), 2.45 (s, 3H), 1.96 (s, 1H). **^{13}C NMR** (176 MHz, Chloroform-*d*) δ 144.9, 133.2, 130.0, 128.1, 72.6, 70.9, 70.8, 70.7, 70.6, 70.5, 69.4, 68.9, 61.9, 21.8.

2-(2-(2-(2-azidoethoxy)ethoxy)ethoxy)ethan-1-ol (69): Dissolve **68** (800.0 mg, 2.3 mmol, 1 equiv.) and NaN_3 (298.5 mg, 4.6 mmol, 2 equiv.) in DMF (2 mL). Allow the reaction to proceed for 2 h at 65°C under Argon atmosphere. Cool the mixture to room temperature and add water (100 mL). Extract the solution with Et_2O (100 mL × 2) and DCM (100 mL × 2). Dry the organic solvent over $MgSO_4$, filter, and evaporate under a vacuum (377.4 mg, 75%). **^{1}H NMR** (700 MHz, Chloroform-*d*) δ 3.73 – 3.60 (m, 14H), 3.39 (q, *J* = 5.2 Hz, 2H), 2.42 (s, 1H). Data in accordance with the literature.[119]

14-azido-3,6,9,12-tetraoxatetradecanoic acid (70): To a suspension of NaH (60% dispersion in mineral oil, 218.9 mg, 5.5 mmol, 2.4 equiv.) in THF (20 mL), **69** (500.0 mg, 2.3 mmol, 1 equiv.) was added dropwise over 10 min to the mixture at room temperature and under Argon. Bromoacetic acid (380.3 mg, 2.7 mmol, 1.2 equiv.) was dissolved in THF (10 mL) and added dropwise over 20 min. The reaction was stirred overnight and monitored by TLC. Water (25 mL) was added, and the solution was acidified with sulfuric acid to pH = 2. The THF was

removed *in vacuo*. The product was extracted using DCM (3 × 20 mL). The organic layer was dried using $MgSO_4$. The solvent was removed *in vacuo* to give the product as a yellow liquid (241.9 mg, 38%). **^{1}H NMR** (400 MHz, Chloroform-*d*) δ 4.16 (s, 2H), 3.80–3.74 (m, 2H), 3.67 (s, 12H), 3.40 (s, 2H). Data in accordance with the literature.[119]

4-(8-(2-(3-azidopropoxy)acetamido)-7-(4-((benzyloxy)carbonyl)piperazin-1-yl)-4,4-dimethylchromeno[4,3-*c*]pyrazol-1(4*H*)-yl)benzoic acid (71): To a room temperature solution of **59** (27.2 mg, 0.2 mmol, 2 equiv.) in dry DCM (2 mL) was added thionyl chloride (18.6 µl, 0.3 mmol, 3 equiv.) followed by 2 drops of DMF. The reaction was brought to reflux and stirred for 1h. After cooling down to room temperature, the reaction mixture was concentrated *in vacuo* to remove excess reagents. The resulting crude yellow oil was dissolved in CH_2Cl_2 (2 mL) and cooled to 0 ºC. To this solution was added **16** (47.3 mg, 0.1 mmol, 1 equiv.) in CH_2Cl_2 (3 mL) followed by DIPEA (72.6 µl, 0.4 mmol, 5 equiv.). Stirring was maintained at this temperature for 0.5 hours. The reaction mixture was concentrated *in vacuo* then taken up into EtOAc and washed with $NaHCO_3$, washed with brine, dried over $MgSO_4$, filtered, and concentrated *in vacuo*. Flash column purification was performed with the crude to give the desired product (44.4 mg, 75%). **^{1}H NMR** (600 MHz, DMSO-d_6) δ 13.10 (s, 1H), 8.96 (s, 1H), 8.07 (d, J = 8.6 Hz, 2H), 7.92 (s, 1H), 7.74 (s, 1H), 7.61 (d, J = 8.5 Hz, 2H), 7.41 – 7.28 (m, 5H), 6.87 (s, 1H), 5.11 (s, 2H), 3.94 (s, 2H), 3.58 – 3.49 (m, 6H), 3.42 (t, J = 6.8 Hz, 2H), 2.80 (t, J = 5.0 Hz, 4H), 1.82 (p, J = 6.5 Hz, 2H), 1.59 (s, 6H). **^{13}C NMR** (151 MHz, DMSO-d_6) δ 167.0, 158.5, 158.3, 154.9, 149.2, 143.7, 137.3, 135.8, 132.1, 131.2, 128.9, 128.4, 128.1, 126.1, 125.8, 124.0, 120.8, 118.8, 116.8, 114.8, 113.9, 111.0, 77.4, 70.3, 68.4, 66.9, 51.5, 48.1, 44.4, 28.9, 28.6. **HRMS-ESI** (m/z): $[M+H]^+$ calculated for $C_{36}H_{39}N_8O_7$ $[M+H]^+$ 695.2936; found, 695.2935.

4-(8-(14-azido-3,6,9,12-tetraoxatetradecanamido)-7-(4-((benzyloxy)carbonyl)piperazin-1-yl)-4,4-dimethylchromeno[4,3-*c*]pyrazol-1(4*H*)-yl)benzoic acid (72): To a room temperature solution of **90** (220.4 mg, 0.8 mmol, 1.1 equiv.) in dry THF (2 mL) was added thionyl chloride (157.2 µl, 2.2 mmol, 3 equiv.) followed by 2 drops of DMF. The reaction was brought to reflux and stirred for 1h. After cooling down to room temperature, the reaction mixture was concentrated in vacuo to remove excess reagents. The resulting crude yellow oil was dissolved in THF (2 mL) and cooled to 0 ºC. To this solution was added **16** (400.0 mg, 0.7 mmol, 1 equiv.) in THF (2 mL) followed by DIPEA (614.4 µl, 3.6 mmol, 5 equiv.). Stirring was maintained at this temperature for 0.5 hours. The reaction mixture was concentrated in vacuo then taken up into DCM and washed with 1 M HCl, washed with brine, dried over

$MgSO_4$, filtered, and concentrated *in vacuo.* Flash column chromatography was performed on the crude to give the desired product (376.8 mg, 64%). **^{1}H NMR** (700 MHz, DMSO-d_6) δ 13.15 (s, 1H), 9.04 (s, 1H), 8.07 (d, J = 8.6 Hz, 2H), 7.95 (s, 1H), 7.74 (s, 1H), 7.61 (d, J = 8.6 Hz, 2H), 7.38 (d, J = 4.8 Hz, 4H), 7.33 (d, J = 14.0 Hz, 1H), 6.86 (s, 1H), 5.11 (s, 2H), 3.96 (s, 2H), 3.64 (d, J = 8.8 Hz, 2H), 3.58 (d, J = 8.9 Hz, 2H), 3.55–3.52 (m, 4H), 3.49–3.41 (m, 9H), 3.34–3.32 (m, 2H), 2.81–2.78 (m, 4H), 1.59 (s, 6H). **^{13}C NMR** (176 MHz, DMSO-d_6) δ 166.7, 166.5, 154.4, 148.6, 143.1, 143.0, 136.8, 135.3, 131.6, 130.7, 128.4, 127.9, 127.6, 125.7, 125.3, 123.5, 113.1, 110.5, 76.9, 70.2, 70.1, 69.8, 69.7, 69.7, 69.7, 69.6, 69.2, 66.4, 55.8, 51.0, 50.0, 49.9, 40.0, 28.1. **HRMS-ESI** (m/z): $[M+H]^+$ calculated for $C_{41}H_{49}N_8O_{10}$ $[M+H]^+$ 813.3566; found, 813.3566.

5.2.3 Tetrahydroquinoline

General Procedure 2 for the Povarov reaction

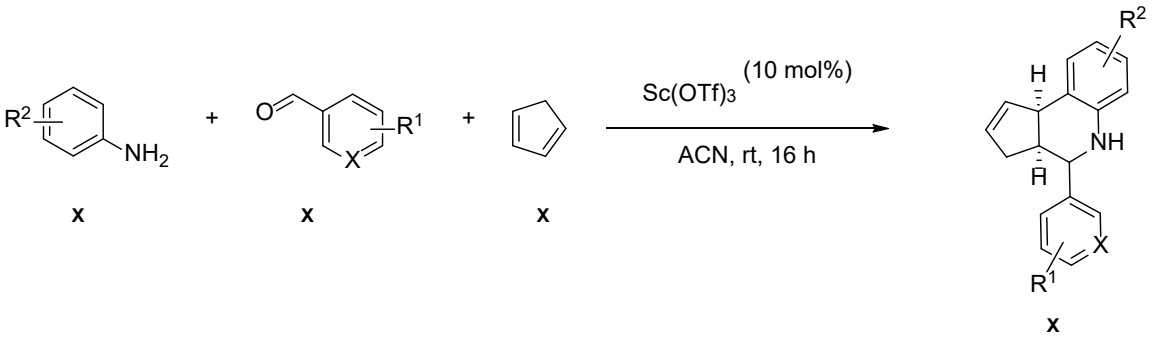

In a two-neck round bottom flask, scandium trifluoromethanesulfonate (0.1 mmol, 0.1 equiv.) in catalytic amounts dissolved in anhydrous acetonitrile (3.0 mL) was added to a mixture of an aldehyde (0.5 mmol, 1 equiv.) and an aniline derivative (0.5 mmol, 1 equiv.) under an inert atmosphere. Then, freshly distilled cyclopentadiene (2.0 mmol, 4 equiv.) was slowly added to the stirring solution. The reaction mixture was stirred at room temperature for another 16 h. Afterward, excess solvent was evaporated and purification of the crude material by flash chromatography on silica gel yielded the corresponding tricyclic tetrahydroquinoline product.[108]

4-(6-ethoxy-3a,4,5,9b-tetrahydro-3*H*-cyclopenta[*c*]quinolin-4-yl)benzoic acid (113): Catalytic amount of ytterbium trifluoromethanesulfonate (40.1 mg, 0.1 mmol, 0.1 equiv.) and activated 3 Å molecular sieves in dry acetonitrile (8.0 mL) were stirred at room temperature. Then a mixture of 4-formylbenzoic acid (100.0 mg, 0.7 mmol, 1.0 equiv.) and 2-ethoxyaniline (86.1 µL, 0.7 mmol, 1 equiv.) in dry acetonitrile (2.0 mL) was added. Freshly distilled

cyclopentadiene (266.9 µL, 3.2 mmol, 5 equiv.) was added to the reaction mixture at 0 °C. The mixture was further stirred at room temperature for 16 h.[108] After evaporating excess solvent under reduced pressure, purification of the crude material by flash chromatography on silica gel yielded the desired product as a brownish solid (150.0 mg, 0.4 mmol, 68% (dr: 2:1)). **R_f:** 0.5 (petroleum ether/EtOAc: 1/1 and 0.1% AcOH) **^{1}H NMR** (700 MHz, DMSO-d_6) δ 12.85 (s, 1H), 7.97 (d, J = 8.3 Hz, 2H), 7.58 (d, J = 8.3 Hz, 2H), 6.72–6.59 (m, 3H), 5.90–5.83 (m, 1H), 5.58 (d, J = 4.3 Hz, 1H), 4.60 (d, J = 3.3 Hz, 1H), 4.53 (d, J = 2.0 Hz, 1H), 4.13–4.02 (m, 2H), 4.01–3.94 (m, 1H), 3.03–2.93 (m, 1H), 2.46–2.39 (m, 1H), 1.62 (dd, J = 16.1, 8.6 Hz, 1H), 1.33 (t, J = 6.9 Hz, 3H). **^{13}C NMR** (176 MHz, DMSO-d_6) δ 167.7, 148.6, 146.5, 135.2, 135.0, 129.9, 127.0, 126.0, 121.0, 118.4, 108.7, 63.9, 57.0, 46.1, 45.4, 31.6, 24.6, 15.2. **HRMS-ESI** *m/z* calculated for $C_{21}H_{21}NO_3$ $[M+H]^+$ 336.1594, found *m/z* 336.1598. [108]

3-(6-ethoxy-3a,4,5,9b-tetrahydro-3*H*-cyclopenta[*c*]quinolin-4-yl)benzoic acid (114): A catalytic amount of ytterbium trifluoromethanesulfonate (40.1 mg, 0.1 mmol, 0.1 equiv.) and activated 3 Å molecular sieves in dry acetonitrile (8.0 mL) were stirred at room temperature. Then a mixture of 3-formylbenzoic acid (100.0 mg, 0.7 mmol, 1 equiv.) and 2-ethoxyaniline (86.1 µL, 0.7 mmol, 1 equiv.) in dry acetonitrile (2.0 mL) was added. Freshly distilled cyclopentadiene (266.9 µL, 3.2 mmol, 5 equiv.) was added to the reaction mixture at 0 °C. The mixture was further stirred at room temperature for an additional 16 h. Afterward, the solvent was evaporated and the crude was purified by flash chromatography on silica gel to afford the desired product as a brown solid (129.4 mg, 0.4 mmol, 59%). **R_f:** 0.45 (petroleum ether/EtOAc: 1/1 and 0.1% AcOH) **^{1}H NMR** (700 MHz, DMSO-d_6) δ 12.97 (s, 1H), 8.05 (s, 1H), 7.88 (d, J = 7.7 Hz, 1H), 7.71 (d, J = 7.8 Hz, 1H), 7.53 (t, J = 7.6 Hz, 1H), 6.72–6.58 (m, 3H), 5.87 (dt, J = 5.9, 2.9 Hz, 1H), 5.58 (d, J = 6.4 Hz, 1H), 4.60 (d, J = 3.4 Hz, 1H), 4.51 (d, J = 2.3 Hz, 1H), 4.11–4.02 (m, 2H), 4.00–3.94 (m, 1H), 2.96 (q, J = 9.0 Hz, 1H), 2.43 (ddd, J = 16.2, 9.5, 2.4 Hz, 1H), 1.63 (dd, J = 16.3, 8.5 Hz, 1H), 1.33 (t, J = 6.9 Hz, 3H). **^{13}C NMR** (176 MHz, DMSO-d_6) δ 167.9, 146.5, 144.1, 135.3, 135.1, 131.5, 131.3, 129.9, 129.1, 128.5, 127.6, 126.0, 121.1, 118.4, 108.7, 63.9, 56.9, 46.1, 45.6, 31.6, 15.2. **HRMS-ESI** *m/z* calculated for $C_{21}H_{22}NO_3$ $[M + H]^+$ 336.1594, found *m/z* 336.1598. [108]

Synthesis of 4-(6-ethoxy-3a,4,5,9b-tetrahydro-3*H*-cyclopenta[*c*]quinolin-4-yl)benzonitrile (119): Following the general procedure 2, the product was obtained as an orange solid using silica gel flash chromatography (135.4 mg, 0.4 mmol, 76%). **R_f:** 0.5 (petroleum ether/EtOAc: 5/1) **^{1}H NMR** (600 MHz, DMSO-d_6) δ 7.86 (d, J = 8.3 Hz, 2H), 7.66 (d, J = 8.3 Hz, 2H), 6.70–6.58 (m, 3H), 5.87 (t, J = 6.4 Hz, 1H), 5.57 (d, J = 7.4 Hz, 1H), 4.61 (s, 2H), 4.11–3.91 (m,

3H), 2.97 (q, *J* = 9.1 Hz, 1H), 2.43–2.31 (m, 1H), 1.65–1.52 (m, 1H), 1.33 (t, *J* = 6.9 Hz, 3H). **^{13}C NMR** (151 MHz, DMSO-d_6) δ 149.4, 146.6, 135.1, 135.0, 132.8, 129.8, 127.9, 125.9, 121.0, 119.4, 118.5, 110.1, 108.7, 63.9, 56.9, 46.0, 45.2, 31.6, 15.2. **HRMS-ESI** *m/z* calculated for $C_{21}H_{21}N_2O$ $[M+H]^+$ 317.1648, found *m/z* 317.1651. [108]

Synthesis of methyl 4-(6-ethoxy-3a,4,5,9b-tetrahydro-3*H*-cyclopenta[*c*]quinolin-4-yl)benzoate (120): Following the general procedure 2, the product was obtained as an orange solid using silica gel flash chromatography (163.8 mg, 0.5 mmol, 94%). **R*f*:** 0.5 (petroleum ether/EtOAc: 6/1) **^{1}H NMR** (600 MHz, DMSO-d_6) δ 7.99 (d, *J* = 8.3 Hz, 2H), 7.61 (d, *J* = 8.3 Hz, 2H), 6.75 – 6.54 (m, 3H), 5.87 (dtd, *J* = 5.8, 2.8, 1.4 Hz, 1H), 5.57 (ddt, *J* = 5.8, 2.9, 1.3 Hz, 1H), 4.61 (d, *J* = 3.4 Hz, 1H), 4.57–4.51 (m, 1H), 4.15–3.88 (m, 4H), 3.33 (s, 2H), 2.97 (qdd, *J* = 9.0, 3.4, 2.0 Hz, 1H), 2.43 (d, *J* = 2.3 Hz, 1H), 2.44–2.38 (m, 1H), 1.60 (dddd, *J* = 16.3, 8.9, 2.7, 1.5 Hz, 1H), 1.33 (t, *J* = 7.0 Hz, 3H). **^{13}C NMR** (151 MHz, DMSO-d_6) δ 166.6, 149.1, 146.5, 135.0, 129.8, 128.8, 127.2, 126.0, 121.0, 118.4, 108.7, 63.9, 57.0, 52.6, 46.1, 45.4, 31.6, 24.6, 17.9, 15.2. **HRMS-ESI** *m/z* calculated for $C_{22}H_{24}NO_3$ $[M + H]^+$ 350.1751, found *m/z* 350.1754. [108]

Synthesis of 6-ethoxy-4-(4-nitrophenyl)-3a,4,5,9b-tetrahydro-3*H*-cyclopenta[*c*]quinoline (121): Following the general procedure 2, the product was obtained as yellow crystals using silica gel flash chromatography (129.2 mg, 0.4 mmol, 77%). **R*f*:** 0.8 (petroleum ether/EtOAc: 4/1) **^{1}H NMR** (700 MHz, Chloroform-*d*) δ 8.26 (d, *J* = 8.7 Hz, 2H), 7.68 (d, *J* = 8.9 Hz, 2H), 6.75–6.71 (m, 2H), 6.63 (dd, *J* = 7.4, 1.8 Hz, 1H), 5.87 (dtd, *J* = 5.8, 2.9, 1.4 Hz, 1H), 5.67–5.61 (m, 1H), 4.70 (d, *J* = 3.4 Hz, 1H), 4.40 (s, 1H), 4.18–4.14 (m, 1H), 4.13–4.07 (m, 1H), 4.03 (dq, *J* = 9.2, 6.9 Hz, 1H), 3.02 (qd, *J* = 8.9, 3.4 Hz, 1H), 2.61 (ddq, *J* = 16.5, 9.5, 2.5 Hz, 1H), 1.74 (dddd, *J* = 16.2, 8.7, 2.7, 1.5 Hz, 1H), 1.42 (t, *J* = 7.0 Hz, 3H). **^{13}C NMR** (176 MHz, Chloroform-*d*) δ 150.8, 147.2, 146.5, 134.4, 133.9, 130.0, 127.4, 126.1, 123.8, 120.7, 118.7, 108.1, 63.8, 57.4, 46.2, 45.7, 31.3, 15.0. **HRMS-ESI** *m/z* calculated for $C_{20}H_{21}N_2O_3$ $[M + H]^+$ 337.1547, found *m/z* 337.1550. [108]

Synthesis of 6-ethoxy-4-(4-(trifluoromethyl)phenyl)-3a,4,5,9b-tetrahydro-3*H*-cyclopenta[*c*]quinoline (122): Following the general procedure 2, the product was obtained as white crystals using a silica gel flash chromatography (135.8 mg, 0.4 mmol, 76%). **R*f*:** 0.8 (petroleum ether/EtOAc: 4/1) **^{1}H NMR** (700 MHz, Chloroform-*d*) δ 7.72–7.62 (m, 4H), 6.74 (d, *J* = 5.5 Hz, 2H), 6.69–6.61 (m, 1H), 5.89 (dtd, *J* = 5.7, 2.9, 1.4 Hz, 1H), 5.67 (dh, *J* = 5.7, 1.3 Hz, 1H), 4.68 (d, *J* = 3.4 Hz, 1H), 4.43 (s, 1H), 4.19–4.15 (m, 1H), 4.12–4.02 (m, 2H), 3.04 (qd, *J* = 9.0, 3.4 Hz, 1H), 2.66 (ddq, *J* = 16.6, 9.5, 2.5 Hz, 1H), 1.80 (dddd, *J* = 16.2, 8.7, 2.7,

1.5 Hz, 1H), 1.43 (t, *J* = 7.0 Hz, 3H). **^{13}C NMR** (176 MHz, Chloroform-*d*) δ 147.3, 146.5, 134.8, 133.9, 130.2, 127.0, 126.2, 125.4, 123.5, 120.7, 118.5, 108.0, 63.8, 57.5, 46.3, 45.8, 31.4, 15.0. **HRMS-ESI** *m/z* calculated for $C_{21}H_{21}NOF$ $[M + H]^+$ 360.1570, found *m/z* 360.1574. [108]

Synthesis of 3-(6-ethoxy-3a,4,5,9b-tetrahydro-3*H*-cyclopenta[*c*]quinolin-4-yl)phenol (123): Following the general procedure 2, the product was obtained as yellow crystals using silica gel flash chromatography (93.9 mg, 0.3 mmol, 62%). **R_f:** 0.4 (petroleum ether/EtOAc: 6/1) **^{1}H NMR** (500 MHz, DMSO-d_6) δ 9.42 (d, *J* = 1.3 Hz, 1H), 7.17 (t, *J* = 7.8 Hz, 1H), 6.91–6.84 (m, 2H), 6.71–6.57 (m, 4H), 5.84 (ddq, *J* = 5.8, 2.9, 1.4 Hz, 1H), 5.63–5.52 (m, 1H), 4.42 (d, *J* = 3.2 Hz, 1H), 4.32 (d, *J* = 1.9 Hz, 1H), 4.08–4.01 (m, 2H), 4.00–3.92 (m, 1H), 2.92 (qdd, *J* = 9.0, 3.3, 1.9 Hz, 1H), 2.44 (ddq, *J* = 16.5, 9.4, 2.5 Hz, 1H), 1.78–1.61 (m, 1H), 1.33 (t, *J* = 6.9 Hz, 3H). **^{13}C NMR** (126 MHz, DMSO-d_6) δ 157.9, 146.4, 144.9, 135.4, 135.0, 130.0, 129.9, 126.1, 121.1, 118.2, 117.4, 114.4, 113.4, 108.5, 63.8, 57.1, 46.2, 45.7, 31.8, 15.2. **HRMS-ESI** *m/z* calculated for $C_{20}H_{22}NO_2$ $[M + H]^+$ 308.1645, found *m/z* 3308.1647. [108]

Synthesis of 3-(6-methoxy-3a,4,5,9b-tetrahydro-3*H*-cyclopenta[*c*]quinolin-4-yl)benzoic acid (124): Following the general procedure 2, the product was obtained as a brownish solid using silica gel flash chromatography (154.1 mg, 0.5 mmol, 96%). **R_f:** 0.4 (petroleum ether/EtOAc: 1/1 and 0.1% AcOH) **^{1}H NMR** (700 MHz, DMSO-d_6) δ 12.94 (s, 1H), 8.05 (t, *J* = 1.8 Hz, 1H), 7.88 (dt, *J* = 7.7, 1.4 Hz, 1H), 7.70 (ddd, *J* = 7.3, 2.0, 1.0 Hz, 1H), 7.51 (t, *J* = 7.7 Hz, 1H), 6.72–6.61 (m, 3H), 5.87 (dtd, *J* = 5.8, 2.8, 1.4 Hz, 1H), 5.57 (dh, *J* = 5.7, 1.3 Hz, 1H), 4.60 (d, *J* = 3.3 Hz, 1H), 4.56–4.52 (m, 1H), 4.11–4.05 (m, 1H), 3.77 (s, 3H), 2.97 (qdd, *J* = 8.9, 3.5, 1.9 Hz, 1H), 2.47–2.34 (m, 1H), 1.62 (dddd, *J* = 16.1, 8.7, 2.7, 1.5 Hz, 1H). **^{13}C NMR** (176 MHz, DMSO-d_6) δ 167.9, 147.4, 144.0, 135.2, 135.1, 131.5, 131.3, 129.9, 129.1, 128.4, 127.5, 125.9, 121.1, 118.3, 107.7, 56.8, 55.8, 46.0, 45.5, 31.6. **HRMS-ESI** *m/z* calculated for $C_{20}H_{20}NO_3$ $[M + H]^+$ 322.1438, found *m/z* 322.1442. [108]

Synthesis of 6-ethoxy-4-(pyridin-3-yl)-3a,4,5,9b-tetrahydro-3*H*-cyclopenta[*c*]quinoline (125): Following the general procedure 2, silica gel flash chromatography afforded a brown oil which then was recrystallized to afford the desired product as brown needles (dr: 83:17) (68.2 mg, 0.2 mmol, 43%). **R_f:** 0.3 (petroleum ether / EtOAc: 5/1) **^{1}H NMR** (500 MHz, Chloroform-*d*) δ 8.77 (q, *J* = 0.9 Hz, 1H), 8.60 (dd, *J* = 4.9, 1.8 Hz, 1H), 7.92–7.86 (m, 1H), 7.37 (ddd, *J* = 7.8, 4.8, 0.9 Hz, 1H), 6.77–6.72 (m, 2H), 6.67–6.62 (m, 1H), 5.89 (dtd, *J* = 5.8, 2.9, 1.5 Hz, 1H), 5.67 (dh, *J* = 5.7, 1.4 Hz, 1H), 4.66 (d, *J* = 3.3 Hz, 1H), 4.38 (s, 1H), 4.23–3.99 (m, 4H), 3.03 (qd, *J* = 8.9, 3.3 Hz, 1H), 2.69 (ddq, *J* = 16.5, 9.5, 2.4 Hz, 1H), 1.85 (dddd,

J = 16.1, 8.6, 2.7, 1.5 Hz, 1H), 1.43 (t, *J* = 6.9 Hz, 3H). **^{13}C NMR** (126 MHz, Chloroform-*d*) δ 148.5, 148.5, 146.5, 138.7, 134.7, 134.5, 134.0, 130.2, 126.2, 123.6, 120.7, 118.6, 108.0, 63.8, 55.7, 46.2, 45.8, 31.4, 15.0. **HRMS-ESI** *m/z* calculated for $C_{19}H_{21}N_2O$ $[M + H]^+$ 293.1648, found *m/z* 293.1653. [108]

Synthesis of 4-(8-cyano-3a,4,5,9b-tetrahydro-3*H*-cyclopenta[*c*]quinolin-4-yl)benzoic acid (126): Following the general procedure 2, the product was obtained as a brownish solid using a silica gel flash chromatography (33.4 mg, 0.1 mmol, 21%). **R_f:** 0.25 (petroleum ether/EtOAc: 1/1 and 0.1% AcOH) **^{1}H NMR** (700 MHz, DMSO-d_6) δ 12.88 (s, 1H), 8.00–7.94 (m, 2H), 7.59–7.55 (m, 2H), 7.46–7.41 (m, 1H), 7.30 (dd, *J* = 8.4, 2.0 Hz, 1H), 6.84 (d, *J* = 8.4 Hz, 1H), 6.74 (d, *J* = 1.8 Hz, 1H), 5.97 (dtd, *J* = 5.9, 2.9, 1.3 Hz, 1H), 5.60 (ddt, *J* = 5.6, 2.8, 1.4 Hz, 1H), 4.76 (d, *J* = 3.6 Hz, 1H), 4.09–4.00 (m, 1H), 3.03–2.90 (m, 1H), 2.33 (ddq, *J* = 16.5, 9.8, 2.3 Hz, 1H), 1.61 (dddd, *J* = 16.2, 8.6, 2.6, 1.4 Hz, 1H). **^{13}C NMR** (176 MHz, DMSO-d_6) δ 167.6, 150.8, 147.4, 134.8, 133.5, 130.6, 130.3, 130.1, 129.8, 127.2, 125.6, 120.8, 116.3, 98.5, 56.0, 45.1, 45.1, 31.7. **HRMS-ESI** *m/z* calculated for $C_{20}H_{17}N_2O_2$ $[M + H]^+$ 317.1285, found *m/z* 317.1288. [108]

Synthesis of 4-(7,8,9-trimethoxy-3a,4,5,9b-tetrahydro-3*H*-cyclopenta[*c*]quinolin-4-yl)benzoic acid (127): Following the general procedure 2, the product was obtained as a white solid using a silica gel flash chromatography (118.3 mg, 0.3 mmol, 62%). **R_f:** 0.3 (petroleum ether/EtOAc: 1/1 and 0.1% AcOH) **^{1}H NMR** (600 MHz, DMSO-d_6) δ 12.85 (s, 1H), 7.95 (d, *J* = 8.4 Hz, 2H), 7.55 (d, *J* = 8.3 Hz, 2H), 6.27 (s, 1H), 5.85 (dtd, *J* = 5.6, 2.7, 1.4 Hz, 1H), 5.62–5.32 (m, 2H), 4.49 (d, *J* = 3.2 Hz, 1H), 4.08–3.99 (m, 1H), 3.83 (s, 3H), 3.68 (s, 3H), 3.64 (s, 3H), 2.97 (qd, *J* = 9.1, 3.2 Hz, 1H), 2.43 (ddt, *J* = 16.3, 9.3, 2.4 Hz, 1H), 1.57 (dd, *J* = 16.2, 8.7 Hz, 1H). **^{13}C NMR** (151 MHz, DMSO-d_6) δ 167.7, 152.0, 151.8, 148.4, 143.2, 134.7, 134.1, 129.8, 129.7, 129.5, 127.1, 111.0, 96.3, 60.8, 60.7, 57.4, 55.9, 45.3, 42.9, 31.7. **HRMS-ESI** *m/z* calculated for $C_{22}H_{24}NO_5$ $[M + H]^+$ 382.1649, found *m/z* 382.1653. [108]

Synthesis of 4-(8-acetyl-3a,4,5,9b-tetrahydro-3*H*-cyclopenta[*c*]quinolin-4-yl)benzoic acid (128): Following the general procedure 2, the product was obtained as a white solid using a silica gel flash chromatography (41.3 mg, 0.1 mmol, 23%). **R_f:** 0.5 (petroleum ether/EtOAc: 1/1 and 0.1% AcOH) **^{1}H NMR** (700 MHz, DMSO-d_6) δ 12.83 (s, 1H), 7.97 (d, *J* = 8.4 Hz, 2H), 7.65–7.62 (m, 1H), 7.58 (d, *J* = 8.3 Hz, 2H), 7.55 (dd, *J* = 8.5, 2.1 Hz, 1H), 6.80 (d, *J* = 8.5 Hz, 1H), 6.62 (d, *J* = 1.8 Hz, 1H), 5.98 (td, *J* = 5.0, 4.4, 2.1 Hz, 1H), 5.61–5.56 (m, 1H), 4.75 (d, *J* = 3.6 Hz, 1H), 4.10 (d, *J* = 8.2 Hz, 1H), 3.02–2.94 (m, 1H), 2.43 (s, 3H), 2.39–2.30 (m, 1H).

^{13}C NMR (176 MHz, DMSO-d_6) δ 196.0, 167.7, 151.3, 147.7, 135.2, 130.3, 130.0, 129.8, 127.6, 127.4, 127.2, 124.2, 115.4, 56.3, 45.4, 45.4, 31.8, 26.5, 21.5. **HRMS-ESI** *m/z* calculated for $C_{21}H_{20}NO_3$ $[M + H]^+$ 334.1438, found *m/z* 334.1441. [108]

Synthesis of 4-(7-acetyl-3a,4,5,9b-tetrahydro-3*H*-cyclopenta[*c*]quinolin-4-yl)benzoic acid (129): Following the general procedure 2, the product was obtained as a white solid using a silica gel flash chromatography (dr: 88:12) (65.6 mg, 0.2 mmol, 50%). **R*f*:** 0.5 (petroleum ether/EtOAc: 1/1 and 0.1% AcOH) **^{1}H NMR** (600 MHz, DMSO-d_6) δ 12.85 (s, 1H), 7.96 (dd, *J* = 8.4, 3.8 Hz, 2H), 7.58 (dd, *J* = 8.3, 6.6 Hz, 2H), 7.40–6.92 (m, 3H), 5.99 (dd, *J* = 52.5, 1.9 Hz, 1H), 5.74 (ddtd, *J* = 169.0, 5.8, 2.9, 1.3 Hz, 1H), 5.56–5.47 (m, 1H), 4.78–4.54 (m, 1H), 4.16–4.06 (m, 1H), 3.11–2.95 (m, 1H), 2.54 (d, *J* = 8.4 Hz, 2H), 2.48 (s, 2H), 1.68–1.49 (m, 1H). **^{13}C NMR** (151 MHz, DMSO-d_6) δ 203.7, 198.1, 167.7, 146.8, 139.0, 135.4, 134.5, 130.9, 130.4, 129.8, 127.2, 126.2, 120.1, 118.3, 115.9, 56.8, 46.2, 45.4, 44.1, 30.5, 27.0. **HRMS-ESI** *m/z* calculated for $C_{21}H_{20}NO_3$ $[M + H]^+$ 334.1438, found *m/z* 334.1441. [108]

Synthesis of 4-(6,8-dichloro-3a,4,5,9b-tetrahydro-3*H*-cyclopenta[*c*]quinolin-4-yl)benzoic acid (130): Following the general procedure 2, the product was obtained as a white solid using a silica gel flash chromatography elution system of 9% EtOAc (+0.1% AcOH) in petroleum ether (84.3 mg, 0.2 mmol, 47%). **R*f*:** 0.3 (petroleum ether/EtOAc: 1/1 and 0.1% AcOH) **^{1}H NMR** (700 MHz, DMSO-d_6) δ 12.89 (s, 1H), 7.97 (d, *J* = 8.3 Hz, 2H), 7.58 (d, *J* = 8.4 Hz, 2H), 7.24 (d, *J* = 2.4 Hz, 1H), 7.17 (d, *J* = 2.4 Hz, 1H), 5.94 (dtd, *J* = 5.8, 2.9, 1.4 Hz, 1H), 5.62 (dh, *J* = 5.6, 1.3 Hz, 1H), 5.11 (s, 1H), 4.71 (d, *J* = 3.5 Hz, 1H), 4.14–4.07 (m, 1H), 3.03–2.93 (m, 1H), 2.33 (ddq, *J* = 16.6, 9.7, 2.4 Hz, 1H), 1.62 (dddd, *J* = 16.4, 8.6, 2.7, 1.5 Hz, 1H). **^{13}C NMR** (176 MHz, DMSO-d_6) δ 167.7, 147.8, 141.2, 134.5, 130.7, 130.0, 129.9, 129.2, 127.9, 127.0, 126.0, 121.7, 120.0, 56.6, 45.9, 44.9, 31.7. **HRMS-ESI** *m/z* calculated for $C_{19}H_{16}NO_2{}^{37}Cl_2$ $[M + H]^+$ 364.0494, found *m/z* 364.0493. [108]

Synthesis of 4-(6-methoxy-3a,4,5,9b-tetrahydro-3*H*-cyclopenta[*c*]quinolin-4-yl)benzoic acid (131): Following the general procedure 2, the product was obtained as a white solid using a silica gel flash chromatography (66.2 mg, 0.2 mmol, 41%). **R*f*:** 0.4 (petroleum ether/EtOAc: 1/1 and 0.1% AcOH) **^{1}H NMR** (700 MHz, DMSO-d_6) δ 7.96 (d, *J* = 8.3 Hz, 2H), 7.58 (d, *J* = 8.3 Hz, 2H), 6.71–6.63 (m, 3H), 5.87 (dtd, *J* = 5.8, 2.9, 1.4 Hz, 1H), 5.57 (dh, *J* = 5.7, 1.3 Hz, 1H), 4.60 (d, *J* = 3.3 Hz, 1H), 4.55 (d, *J* = 2.0 Hz, 1H), 4.09–4.05 (m, 1H), 3.77 (s, 3H), 2.98 (qdd, *J* = 8.9, 3.5, 1.9 Hz, 1H), 2.41 (ddq, *J* = 16.6, 9.5, 2.4 Hz, 1H), 1.62 (dddd, *J* = 16.2, 8.8, 2.7, 1.5 Hz, 1H). **^{13}C NMR** (176 MHz, DMSO-d_6) δ 167.7, 148.6, 147.4, 135.1, 135.0, 129.9

(2C), 127.0, 125.9, 121.1, 118.4, 107.8, 60.2, 56.9, 55.9, 46.0, 45.4, 31.6. **HRMS-ESI** *m/z* calculated for $C_{20}H_{20}NO_3$ $[M + H]^+$ 322.1438, found *m/z* 322.1441. [108]

Synthesis of 4-(6-isopropoxy-3a,4,5,9b-tetrahydro-3*H*-cyclopenta[*c*]quinolin-4-yl)benzoic acid (132): Following the general procedure 2, the product was obtained as a brownish solid using a silica gel flash chromatography (122.7 mg, 0.4 mmol, 70%). **R_f:** 0.4 (petroleum ether/EtOAc: 1/1 and 0.1% AcOH) **^{1}H NMR** (500 MHz, DMSO-d_6) δ 12.91 (s, 1H), 8.04–7.93 (m, 2H), 7.58 (d, *J* = 8.1 Hz, 2H), 6.70–6.65 (m, 2H), 6.65–6.59 (m, 1H), 5.86 (ddt, *J* = 5.7, 2.9, 1.4 Hz, 1H), 5.57 (q, *J* = 2.3 Hz, 1H), 4.59 (d, *J* = 3.3 Hz, 1H), 4.53 (h, *J* = 6.0 Hz, 1H), 4.48 (d, *J* = 1.9 Hz, 1H), 4.10–4.00 (m, 1H), 2.97 (qt, *J* = 9.3, 2.1 Hz, 1H), 2.42 (ddq, *J* = 16.5, 9.3, 2.4 Hz, 1H), 1.61 (ddt, *J* = 16.1, 8.7, 2.1 Hz, 1H), 1.31 (d, *J* = 6.0 Hz, 3H), 1.23 (d, *J* = 6.0 Hz, 3H). **^{13}C NMR** (126 MHz, DMSO-d_6) δ 167.7, 148.6, 145.3, 136.1, 135.0, 130.0, 129.9, 126.9, 126.3, 121.1, 118.4, 110.4, 70.4, 60.2, 57.0, 46.1, 45.4, 31.6, 22.5, 22.3, 21.2, 14.6. **HRMS-ESI** *m/z* calculated for $C_{22}H_{24}NO_3$ $[M + H]^+$ 350.1751, found *m/z* 350.1754. [108]

Synthesis of ethyl 6-ethoxy-3a,4,5,9b-tetrahydro-3*H*-cyclopenta[*c*]quinoline-4-carboxylate (134): Trifluoroacetic acid (115.6 µL, 1.5 mmol, 1 equiv.) was added to a solution of 2-ethoxyaniline (187.4 µL, 1.5 mmol, 1 equiv.) in dry acetonitrile (4.0 mL) at 0 °C. The resulting mixture was then combined with freshly distilled cyclopentadiene (371.8 µL, 4.5 mmol, 3 equiv.), followed by an ethyl glyoxalate solution (50% in toluene, 350.0 µL, 1.8 mmol, 1.2 equiv.). Afterward, the reaction mixture was stirred at room temperature for 1 h until the starting material was used up (controlled by TLC). The solvent was evaporated, and the residue was washed with a saturated $NaHCO_3$ solution until the pH was neutral. The resulting aqueous solution was extracted with EtOAc, and the organic layer was concentrated *in vacuo*. Purification by flash column chromatography afforded the desired ester as a purple oil (170.2 mg, 0.5 mmol, 36%). **Rr:** 0.8 (petroleum ether/EtOAc: 3/1) **^{1}H NMR** (700 MHz, Chloroform-*d*) δ 6.62–6.57 (m, 2H), 6.52 (dd, *J* = 6.8, 2.4 Hz, 1H), 5.68 (dtd, *J* = 5.7, 2.8, 1.7 Hz, 1H), 5.60–5.56 (m, 1H), 4.25 (dq, *J* = 10.8, 7.1 Hz, 1H), 4.17 (dq, *J* = 10.8, 7.1 Hz, 1H), 4.04 – 4.01 (m, 1H), 4.00 (dd, *J* = 3.5, 1.0 Hz, 1H), 3.99–3.92 (m, 2H), 3.27 (qd, *J* = 8.9, 3.5 Hz, 1H), 2.46 (ddq, *J* = 16.1, 8.6, 2.5 Hz, 1H), 2.26 (ddt, *J* = 16.2, 9.0, 2.2 Hz, 1H), 1.36 (t, *J* = 7.0 Hz, 3H), 1.26 (t, *J* = 7.1 Hz, 3H). **^{13}C NMR** (176 MHz, Chloroform-*d*) δ 170.9, 145.4, 133.0, 132.6, 128.9, 125.1, 119.3, 117.3, 107.1, 62.8, 60.1, 55.3, 45.3, 39.8, 31.5, 13.9, 13.3. **HRMS-ESI** *m/z* calculated for $C_{17}H_{22}NO_3$ $[M + H]^+$ 288.1594, found *m/z* 288.1597. [108]

Synthesis of 6-ethoxy-3a,4,5,9b-tetrahydro-3*H*-cyclopenta[*c*]quinoline-4-carboxylic acid (135): To a suspension of ethyl 6-ethoxy-3a,4,5,9b-tetrahydro-3*H*-cyclopenta[*c*]quinoline-4-

carboxylate (170.2 mg, 0.6 mmol, 1 equiv.) in 1.5 mL of THF 0.8 mL of water and lithium hydroxide monohydrate (62.1 mg, 1.5 mmol, 2.5 equiv.) were added. The mixture was then stirred and heated at 50 °C for 3 h. Then the solution was treated with 1 M aqueous HCl solution and extracted with EtOAc (3 x 15.0 mL). The organic layer was washed with 20.0 mL of saturated aqueous NaCl solution, dried over $MgSO_4$, and purified by silica gel flash column chromatography. After evaporation of the solvent *in vacuo*, the desired acid was obtained as a greenish solid (109.6 mg, 0.4 mmol, 71%). **Rf:** 0.1 (EtOAc) **^{1}H NMR** (700 MHz, DMSO-d_6) δ 12.95 (s, 1H), 6.69–6.47 (m, 3H), 5.75 (dtd, J = 5.6, 2.8, 1.6 Hz, 1H), 5.61 (dddd, J = 4.4, 3.5, 2.3, 1.3 Hz, 1H), 4.56 (s, 1H), 4.09–3.90 (m, 4H), 3.19 (qd, J = 9.0, 3.5 Hz, 1H), 2.36–2.20 (m, 2H), 1.35 (t, J = 7.0 Hz, 3H).**^{13}C NMR** (176 MHz, DMSO-d_6) δ 173.5, 146.1, 135.2, 134.1, 129.7, 126.0, 120.9, 118.1, 108.6, 63.8, 55.7, 46.3, 40.6, 32.7, 15.3. **HRMS-ESI** *m/z* calculated for $C_{15}H_{18}NO_3$ $[M + H]^+$ 260.1281, found *m/z* 260.1282. [108]

Synthesis of 4-(6-ethoxy-2,3,3a,4,5,9b-hexahydrofuro[3,2-*c*]quinolin-4-yl)benzoic acid (136): To a suspension of methyl 4-(6-ethoxy-2,3,3a,4,5,9b-hexahydrofuro[3,2-*c*]quinolin-4-yl)benzoate (179.2 mg, 0.5 mmol, 1 equiv.) in 1.5 mL of THF 0.8 mL of water and lithium hydroxide monohydrate (53.2 mg, 1.3 mmol, 2.5 equiv.) was added. The mixture was then stirred and heated at 50 °C for 4 h. Afterward, the solution was treated with 1 M aqueous HCl solution and extracted with EtOAc (3 x 15.0 mL). The organic layer was then washed with 15.0 mL of brine, dried over $MgSO_4$, and concentrated. Purification by flash column chromatography afforded the desired acid as a white solid (118.2 mg, 0.4 mmol, 69%). **Rf:** 0.3 (broad spot on TLC in EtOAc) **^{1}H NMR** (600 MHz, DMSO-d_6) δ 12.93 (s, 1H), 7.97 (dd, J = 8.3, 1.9 Hz, 2H), 7.60 (dd, J = 8.4, 2.1 Hz, 2H), 6.91 – 6.60 (m, 3H), 5.29 – 4.43 (m, 2H), 4.14 – 3.94 (m, 2H), 3.93–3.51 (m, 3H), 2.37 (ddd, J = 10.6, 5.3, 2.7 Hz, 1H), 2.04–1.85 (m, 1H), 1.56 (dddd, J = 12.7, 8.3, 6.0, 2.4 Hz, 1H), 1.32 (dt, J = 29.4, 6.9 Hz, 3H). **^{13}C NMR** (151 MHz, DMSO-d_6) δ 167.6, 147.8, 145.8, 135.6, 129.9, 128.9, 127.1, 123.1, 120.4, 117.1, 110.6, 75.5, 66.1, 63.9, 56.7, 44.9, 43.0, 28.8, 24.8, 15.1. **HRMS-ESI** *m/z* calculated for $C_{20}H_{22}NO_4$ $[M + H]^+$ 340.1543, found *m/z* 340.1546. [108]

Synthesis of 4-(7-ethoxy-3,4,4a,5,6,10b-hexahydro-2H-pyrano[3,2-*c*]quinolin-5-yl)benzoic acid (137): To a suspension of methyl 4-((4a*R*,10b*R*)-7-ethoxy-3,4,4a,5,6,10b-hexahydro-2*H*-pyrano[3,2-*c*]quinolin-5-yl)benzoate (268.7 mg mixture containing 0.4 mmol of desired product, 1.0 equiv.) in 2.0 mL of THF 1 mL of water and lithium hydroxide monohydrate (38.34 mg, 0.9 mmol, 2.5 equiv.) were added. The mixture was stirred and heated at 50 °C for 5 h before treatment with 1 M aqueous HCl solution and extraction with EtOAc (3

x 15.0 mL). After filtration of a white precipitate, the organic layer was washed with 15.0 mL of brine, dried, and concentrated. Purification by flash column chromatography afforded the desired acid as a yellowish solid (30.4 mg, 0.1 mmol, 24%). **Rf:** 0.3 (broad spot on TLC in EtOAc) **^{1}H NMR** (500 MHz, DMSO-d_6) δ 12.91 (s, 1H), 7.95 (d, J = 7.9 Hz, 2H), 7.53 (d, J = 8.0 Hz, 2H), 6.81–6.69 (m, 2H), 6.55 (t, J = 7.8 Hz, 1H), 5.06 (s, 1H), 4.60 (d, J = 9.8 Hz, 1H), 4.32 (d, J = 3.1 Hz, 1H), 4.07–3.92 (m, 3H), 3.89–3.77 (m, 1H), 3.59 (td, J = 10.9, 2.7 Hz, 1H), 2.00 (d, J = 6.8 Hz, 2H), 1.80–1.59 (m, 2H), 1.35–1.15 (m, 7H). **^{13}C NMR** (126 MHz, DMSO-d_6) δ 167.7, 148.7, 145.3, 135.0, 130.4, 129.9, 128.2, 120.5, 116.0, 110.9, 63.9, 60.2, 54.5, 38.5, 24.3, 22.5, 21.2, 15.2, 14.6. **HRMS-ESI** *m/z* calculated for $C_{21}H_{24}NO_4$ $[M + H]^+$ 354.1610, found *m/z* 354.1701. [108]

Synthesis of methyl 4-(6-ethoxy-2,3,3a,4,5,9b-hexahydrofuro[3,2-*c*]quinolin-4-yl)benzoate (139): A mixture of 2-ethoxyaniline (124.9 µL, 1.0 mmol, 1 equiv.) and methyl 4-formylbenzoate (164.2 mg, 1.0 mmol, 1 equiv.) in 3.0 mL of EtOH was heated at reflux for 2 h. Then, the mixture was cooled down and the solvent was evaporated *in vacuo*. After suspending the methyl 4-phenylimino-benzoate-containing mixture in 3.0 mL of anhydrous acetonitrile, it was cooled down to 0 °C before addition of 2,3-dihydrofurane (113.4 µL, 1.5 mmol, 1.5 equiv.) and the catalyst ytterbium triflate (31.0 mg, 5 mol%, 0.1 equiv.). The mixture was stirred at 0 °C for 30 min and was then gradually warmed up to stir for an additional 2 h at room temperature. Then, the solvent was evaporated *in vacuo* and the residue was re-dissolved in EtOAc. The resulting solution was washed with aqueous saturated $NaHCO_3$ solution and brine, then dried and concentrated under *in vacuo*. This mixture was then purified by silica gel chromatography to afford the desired product as a colorless oil (233.1 mg, 0.7 mmol, 66%). **Rf:** 0.4 (petroleum ether/EtOAc: 3/1) **^{1}H NMR** (700 MHz, Chloroform-*d*) δ 8.10 (dq, J = 8.4, 1.9 Hz, 2H), 7.64–7.56 (m, 2H), 7.10–6.99 (m, 1H), 6.82–6.70 (m, 2H), 4.77–4.44 (m, 2H), 4.18–4.01 (m, 3H), 3.96 (d, J = 2.0 Hz, 3H), 3.89–3.67 (m, 2H), 2.87–2.42 (m, 1H), 2.06–1.66 (m, 2H), 1.41 (dt, J = 37.4, 7.0 Hz, 3H). [108]

Synthesis of methyl 4-(7-ethoxy-3,4,4a,5,6,10b-hexahydro-2H-pyrano[3,2-c]quinolin-5-yl)benzoate (140): A mixture of 2-ethoxyaniline (124.9 µL, 1.0 mmol, 1 equiv.) and methyl 4-formylbenzoate (164.2 mg, 1.0 mmol, 1 equiv.) in 3.0 mL of EtOH was heated at reflux for 2 h. Then, the mixture was cooled to rt, and solvent was removed **in vacuo**. After suspending the methy l 4-phenylimino-benzoate-containing mixture in 3.0 mL of ACN it was further cooled to 0 °C before adding 2,3-dihydropyrane (136.1 µL, 1.5 mmol, 1.5 equiv.) and scandium triflate (24.6 mg, 5 mol%, 0.1 equiv.) as a catalyst. The mixture was stirred at 0 °C for 30 min and

gradually warmed up to room temperature for an additional 2 h. After the desired reaction time monitored by TLC, the solvent removed *in vacuo* and the residue was re-dissolved in EtOAc. The resulting solution was washed with aqueous saturated $NaHCO_3$ solution and saturated brine, then dried and concentrated. The resulting mixture was purified by silica gel flash chromatography to afford a mixture containing the desired product as a yellow oil (268.7 mg, 0.7 mmol, 73%). For the following reaction step, the mixture was used without further purification. **Rf:** 0.4 (petroleum ether/EtOAc: 3/1).[108]

5.2.4 Pyrrolinones

General procedure for the Doebner condensation reaction

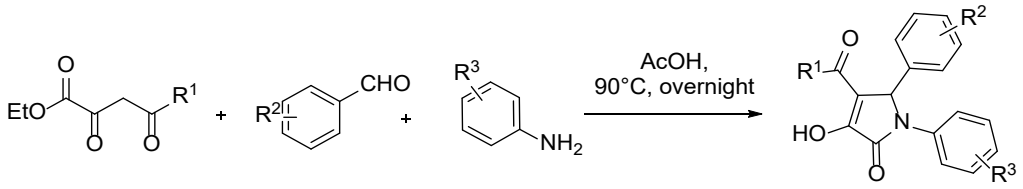

The benzaldehyde derivative (1 equiv.) followed by a selected aniline derivative (1 equiv.) was added to a suspension (0.06 M) of the dioxobutanoate derivative (1 equiv.) in acetic acid stirring at 90 °C.[68,121] The reaction mixture was stirred overnight. Reaction progress was controlled through HPLC. If one of the starting materials was not observable on the LC-MS the reaction was considered to be done. Then the reaction was cooled to room temperature and the mixture was diluted with Et_2O and filtered. The residue was further washed with Et_2O to give the desired pyrrolinone derivative after drying. In the case that the precipitation did not yield a pure product, the precipitate was redissolved in appropriate ACN/H_2O mixtures further purified with an appropriate gradient on a suitable preparative HPLC system.

5-(3-(4-bromobenzoyl)-2-(4-carboxyphenyl)-4-hydroxy-5-oxo-2,5-dihydro-1*H*-pyrrol-1-yl)-2-hydroxybenzoic acid (141): Purified by preparative HPLC, obtained the target compound as a yellow solid (8.2 mg) **^{1}H NMR** (600 MHz, Methanol-d_4) δ 8.01 (d, J = 2.7 Hz, 1H), 7.88 (d, J = 8.4 Hz, 2H), 7.69 (d, J = 8.5 Hz, 2H), 7.63–7.58 (m, 3H), 7.45 (d, J = 8.3 Hz, 2H), 6.88 (d, J = 9.0 Hz, 1H), 6.23 (s, 1H). **^{13}C NMR** (151 MHz, Methanol-d_4) δ 190.2, 172.8, 169.2, 166.3, 161.3, 142.7, 138.4, 132.5, 132.0, 131.8, 131.0, 129.1, 128.9, 128.5, 126.5, 120.7, 118.7, 114.0, 63.8. **HRMS-ESI** (m/z): $[M+H]^+$ calculated for $C_{25}H_{17}NO_8Br$ $[M+H]^+$ 538.0129; found, 538.0129. $[M+H]^+$ calculated for $C_{25}H_{17}NO_8{}^{81}Br$ $[M+H]^+$ 540.0112; found, 540.0108. [68]

4-(3-(4-Bromobenzoyl)-4-hydroxy-5-oxo-2-(4-(thiazol-2-yl)phenyl)-2,5-dihydro-1*H*-pyrrol-1-yl)-2-hydroxybenzoic acid (**142**): Purified by preparative HPLC, obtained the target compound as a brown solid (18.1 mg). **^{1}H NMR** (600 MHz, Methanol-d_4) δ 8.02 (d, J = 2.5 Hz, 1H), 7.80 (dd, J = 9.8, 5.6 Hz, 3H), 7.71 (d, J = 8.0 Hz, 2H), 7.61 (d, J = 7.6 Hz, 3H), 7.55 (d, J = 3.1 Hz, 1H), 7.46 (d, J = 7.9 Hz, 2H), 6.87 (d, J = 8.8 Hz, 1H), 6.21 (s, 1H). **^{13}C NMR** (151 MHz, Methanol-d_4) δ 190.3, 172.9, 169.5, 166.3, 163.1, 161.3, 144.4, 139.8, 138.5, 134.6, 132.5, 132.0, 131.8, 129.8, 128.9, 128.5, 127.9, 126.7, 121.0, 120.7, 118.7, 114.2, 63.8. **R$_f$**: 0.6 in 30% MeOH in DCM. **HRMS-ESI** (m/z): $[M+H]^+$ calculated for $C_{27}H_{18}N_2O_6BrS$ $[M+H]^+$ 577.0064; found, 577.0062. $[M+H]^+$ calculated for $C_{27}H_{18}N_2O_6{}^{81}BrS$ $[M+H]^+$ 579.0043; found, 579.0041. [68]

5-(3-(4-Bromobenzoyl)-4-hydroxy-5-oxo-2-(4-(thiazol-2-yl)phenyl)-2,5-dihydro-1*H*-pyrrol-1-yl)-2-hydroxybenzoic acid (C902/PH-31): Yellow solid (119.6 mg, 31%). **^{1}H NMR** (500 MHz, Acetone-d_6) δ 8.20 (d, J = 2.7 Hz, 1H), 7.87 (d, J = 8.4 Hz, 2H), 7.80 (dt, J = 7.3, 3.3 Hz, 4H), 7.67 (d, J = 8.5 Hz, 2H), 7.60 (d, J = 8.3 Hz, 2H), 7.57 (d, J = 3.2 Hz, 1H), 6.92 (d, J = 9.0 Hz, 1H), 6.37 (s, 1H). **^{1}H NMR** (600 MHz, DMSO-d_6) δ 14.08 (s, 1H), 11.98 (s, 1H), 11.21 (s, 1H), 8.02 (d, J = 2.7 Hz, 1H), 7.86 (d, J = 3.2 Hz, 1H), 7.81–7.76 (m, 2H), 7.73 (d, J = 3.2 Hz, 1H), 7.72–7.63 (m, 5H), 7.52–7.48 (m, 2H), 6.91 (d, J = 8.9 Hz, 1H), 6.31 (s, 1H). **^{13}C NMR** (126 MHz, Acetone-d_6) δ 188.9, 172.0, 167.7, 165.0, 160.6, 151.5, 144.7, 139.2, 138.0, 134.5, 132.3, 131.7, 131.6, 129.6, 129.1, 127.9, 127.3, 125.6, 120.5, 120.4, 118.4, 113.1, 62.8. **R$_f$**: 0.3 in 40% MeOH in DCM. **HRMS-ESI** (m/z): $[M+H]^+$ calculated for $C_{27}H_{18}N_2O_6BrS$ $[M+H]^+$ 577.0064; found, 577.0063. $[M+H]^+$ calculated for $C_{27}H_{18}N_2O_6{}^{81}BrS$ $[M+H]^+$ 579.0043; found, 579.0040. [68]

5-(3-Benzoyl-4-hydroxy-5-oxo-2-(4-(thiazol-2-yl)phenyl)-2,5-dihydro-1*H*-pyrrol-1-yl)-2-hydroxybenzoic acid (143): Purified by preparative HPLC, obtained the target compound as a yellow solid (12.1 mg). **^{1}H NMR** (600 MHz, DMSO-d_6) δ 14.14 (s, 1H), 11.97 (s, 1H), 11.17 (s, 1H), 8.03 (d, J = 2.7 Hz, 1H), 7.85 (d, J = 3.2 Hz, 1H), 7.81–7.76 (m, 2H), 7.75–7.68 (m, 4H), 7.60–7.54 (m, 1H), 7.53–7.42 (m, 4H), 6.91 (d, J = 9.0 Hz, 1H), 6.33 (s, 1H). **^{13}C NMR** (151 MHz, DMSO-d_6) δ 189.2, 171.2, 166.4, 164.5, 158.7, 150.4, 143.8, 138.5, 137.9, 132.7, 130.6, 128.7, 128.7, 128.2, 127.7, 126.3, 124.9, 120.6, 119.6, 117.5, 112.9, 61.3. **R$_f$**: 0.32 in 40% MeOH in DCM + 0.1% AcOH. **HRMS-ESI** (m/z): $[M+H]^+$ calculated for $C_{27}H_{19}N_2O_6S$ $[M+H]^+$ 499.0958; found, 499.0953. [68]

4-(4-Bromobenzoyl)-3-hydroxy-1-(4-hydroxyphenyl)-5-(4-(thiazol-2-yl)phenyl)-1,5-dihydro-2*H*-pyrrol-2-one (144): Grey solid (82.7 mg, 34%). **^{1}H NMR** (500 MHz, DMSO-d_6) δ 12.15 (s, 1H), 9.47 (s, 1H), 7.86 (d, *J* = 3.2 Hz, 1H), 7.77 (d, *J* = 8.3 Hz, 2H), 7.73 (d, *J* = 3.2 Hz, 1H), 7.69–7.62 (m, 4H), 7.47 (d, *J* = 8.3 Hz, 2H), 7.36 (d, *J* = 8.9 Hz, 2H), 6.68 (d, J = 8.9 Hz, 2H), 6.22 (s, 1H). **^{13}C NMR** (176 MHz, DMSO-d_6) δ 208.0, 187.9, 166.4, 164.1, 155.3, 143.7, 138.9, 137.1, 132.5, 131.2, 130.6, 128.6, 127.6, 126.3, 126.1, 124.7, 120.4, 115.2, 61.3. **R_f**: 0.5 in 20% MeOH in DCM + 0.1% AcOH. **HRMS-ESI** (m/z): $[M+H]^+$ calculated for $C_{26}H_{18}N_2O_4BrS$ $[M+H]^+$ 533.0165; found, 533.0163. $[M+H]^+$ calculated for $C_{26}H_{18}N_2O_4{}^{81}BrS$ $[M+H]^+$ 535.0145; found, 535.0141. [68]

4-(3-Benzoyl-4-hydroxy-1-(4-hydroxyphenyl)-5-oxo-2,5-dihydro-1*H*-pyrrol-2-yl)benzoic acid (145): Yellow solid (104.6 mg, 55%). **^{1}H NMR** (600 MHz, DMSO-d_6) δ 12.75 (s, 1H), 11.95 (s, 1H), 9.45 (s, 1H), 7.75 (d, J = 8.1 Hz, 2H), 7.69 (d, J = 7.3 Hz, 2H), 7.55 (t, J = 7.4 Hz, 1H), 7.48 – 7.41 (m, 4H), 7.36 – 7.33 (m, 2H), 6.75 – 6.54 (m, 2H), 6.24 (s, 1H). **^{13}C NMR** (151 MHz, DMSO-d_6) δ 189.0, 166.8, 164.3, 155.3, 138.1, 132.5, 130.3, 129.8, 129.3, 128.7, 128.7, 128.1, 128.0, 127.6, 127.5, 124.7, 115.2, 61.4. **R_f**: 0.5 in 40% MeOH in DCM + 0.1% AcOH. **HRMS-ESI** (m/z): $[M+H]^+$ calculated for $C_{24}H_{18}NO_6$ $[M+H]^+$ 416.1129; found, 416.1127. [68]

4-Benzoyl-3-hydroxy-1-(4-hydroxy-3-nitrophenyl)-5-(4-(thiazol-2-yl)phenyl)-1,5-dihydro-2*H*-pyrrol-2-one (146): Purified by preparative HPLC, obtained the target compound as a yellow solid (2.0 mg). **^{1}H NMR** (500 MHz, DMSO-d_6) δ 12.05 (s, 1H), 11.04 (s, 1H), 8.25 (d, *J* = 2.6 Hz, 1H), 7.86 (d, *J* = 3.2 Hz, 1H), 7.82–7.77 (m, 2H), 7.77–7.70 (m, 4H), 7.60–7.52 (m, 3H), 7.46 (t, *J* = 7.8 Hz, 2H), 7.07 (d, *J* = 9.1 Hz, 1H), 6.39 (s, 1H). **^{13}C NMR** (126 MHz, DMSO-d_6) δ 189.3, 166.4, 164.6, 150.2, 149.6, 143.9, 138.2, 137.8, 136.3, 132.8, 129.7, 129.2, 128.8, 128.8, 128.3, 127.7, 126.3, 120.7, 119.8, 119.3, 119.2, 61.1.**R_f**: 0.28 in 10% MeOH in DCM + 0.1% AcOH. **HRMS-ESI** (m/z): $[M+H]^+$ calculated for $C_{26}H_{18}N_3O_6S$ $[M+H]^+$ 500.0911; found, 500.0906. [68]

4-(3-Benzoyl-2-(4-carboxyphenyl)-4-hydroxy-5-oxo-2,5-dihydro-1*H*-pyrrol-1-yl)-2-hydroxybenzoic acid (147): Purified by preparative HPLC, obtained the target compound as a white powder (3.0 mg). **^{1}H NMR** (500 MHz, DMSO-d_6) δ 13.90 (s, 1H), 12.90 (s, 1H), 12.08 (s, 1H), 11.29 (s, 1H), 7.78 (d, *J* = 8.3 Hz, 2H), 7.69 (d, *J* = 8.6 Hz, 3H), 7.56 (dd, *J* = 7.8, 3.5 Hz, 3H), 7.45 (t, *J* = 7.7 Hz, 2H), 7.32 (d, *J* = 2.1 Hz, 1H), 7.26 (dd, *J* = 8.7, 2.1 Hz, 1H), 6.44 (s, 1H).**^{13}C NMR** (126 MHz, DMSO-d_6) δ 178.7, 171.3, 166.8, 165.2, 161.4, 142.3, 141.4,

137.7, 132.9, 130.8, 130.5, 129.4, 128.8, 128.8, 128.3, 127.9, 120.1, 112.5, 109.6, 109.2, 60.6. **Rf**: 0.17 in 40% MeOH in DCM + 0.1% AcOH. **HRMS-ESI** (m/z): $[M+H]^+$ calculated for $C_{25}H_{18}NO_8$ $[M+H]^+$ 460.1027; found, 460.1025. [68]

5-(3-Benzoyl-2-(4-carboxyphenyl)-4-hydroxy-5-oxo-2,5-dihydro-1*H*-pyrrol-1-yl)-2-hydroxybenzoic acid (C880/148): Purified by preparative HPLC, obtained the target compound as a white powder (3.8 mg). **^{1}H NMR** (500 MHz, Acetone-d_6) δ 8.18 (d, J = 2.7 Hz, 1H), 7.91–7.82 (m, 4H), 7.78 (dd, J = 9.0, 2.8 Hz, 1H), 7.58 (dd, J = 19.9, 7.9 Hz, 3H), 7.46 (t, J = 7.7 Hz, 2H), 6.90 (d, J = 9.0 Hz, 1H), 6.41 (s, 1H). **^{13}C NMR** (126 MHz, Acetone-d_6) δ 190.0, 172.2, 170.8, 167.0, 165.1, 160.6, 142.5, 139.0, 133.6, 131.5, 131.4, 130.6, 129.8, 129.1, 129.0, 125.6, 120.7, 118.4, 113.2, 62.9. **Rf**: 0.38 in 40% MeOH in DCM + 0.1% AcOH. **HRMS-ESI** (m/z): $[M+H]^+$ calculated for $C_{25}H_{18}NO_8$ $[M+H]^+$ 460.1027; found, 460.1024. [68]

5-(3-(Furan-2-carbonyl)-4-hydroxy-5-oxo-2-(4-(thiazol-2-yl)phenyl)-2,5-dihydro-1H-pyrrol-1-yl)-2-hydroxybenzoic acid (149): Purified by preparative HPLC, obtained the target compound as a yellow solid (20.2 mg). **^{1}H NMR** (600 MHz, Acetone-d_6) δ 10.98 (s, 1H), 8.14 (d, J = 2.7 Hz, 1H), 7.90–7.84 (m, 3H), 7.81 (d, J = 3.2 Hz, 1H), 7.77 (dd, J = 9.0, 2.7 Hz, 1H), 7.59–7.53 (m, 4H), 6.92 (d, J = 9.0 Hz, 1H), 6.67 (dd, J = 3.6, 1.7 Hz, 1H), 6.50 (s, 1H). **^{13}C NMR** (151 MHz, Acetone-d_6) δ 175.3, 171.1, 166.8, 163.0, 159.9, 155.7, 151.5, 147.9, 143.8, 138.5, 133.6, 131.5, 128.9, 128.1, 126.4, 125.3, 119.9, 119.6, 118.3, 117.6, 112.6, 112.1, 61.8. **HRMS-ESI** (m/z): $[M+H]^+$ calculated for $C_{25}H_{17}N_2O_7S$ $[M+H]^+$ 489.0751; found, 489.0746. [68]

5-(3-(3,4-Dimethoxybenzoyl)-4-hydroxy-5-oxo-2-(4-(thiazol-2-yl)phenyl)-2,5-dihydro-1*H*-pyrrol-1-yl)-2-hydroxybenzoic acid (150): Purified by preparative HPLC, obtained the target compound as a yellow solid (14.7 mg). **^{1}H NMR** (600 MHz, Acetone-d_6) δ 8.20 (d, J = 2.7 Hz, 1H), 7.86 (d, J = 8.4 Hz, 2H), 7.82 (dd, J = 9.0, 2.8 Hz, 1H), 7.80 (d, J = 3.2 Hz, 1H), 7.62 (dd, J = 8.4, 2.0 Hz, 1H), 7.59–7.54 (m, 3H), 7.44 (d, J = 2.0 Hz, 1H), 7.00 (d, J = 8.5 Hz, 1H), 6.92 (d, J = 9.0 Hz, 1H), 6.39 (s, 1H), 3.87 (s, 3H), 3.84 (s, 3H). **^{13}C NMR** (151 MHz, Acetone-d_6) δ 187.5, 171.1, 166.8, 164.3, 159.5, 153.9, 149.1, 143.8, 138.3, 133.6, 130.8, 130.4, 128.7, 128.5, 126.5, 124.6, 124.3, 120.5, 119.6, 117.5, 112.0, 111.6, 110.5, 62.2, 55.3, 55.2. **HRMS-ESI** (m/z): $[M+H]^+$ calculated for $C_{29}H_{23}N_2O_8S$ $[M+H]^+$ 559.1170; found, 559.1167. [68]

5.2.5 Peptide Synthesis Methods

Synthesis was performed on Chlorotrityl chloride (1.0-1.6 mmol/g) or Rink Amide MBHA resin (0.61 mmol/g) using standard Fmoc chemistry and solid phase peptide synthesis methods.[95] Solvents and reagents were removed by filtration. Manual washing steps were performed with DMF and DCM using 1 mL solvent per 100 mg resin. Coupling efficiency and monitoring were conducted through ESI-MS and/or HPLC analysis.

The resin was swollen in DCM. After washing with DMF the first amino acid in sequence for all peptides was coupled manually corresponding to the respective resin requirements. Double couplings with 4 equiv. Fmoc protected amino acid, 4 equiv. PyBOP and 8 equiv. of DIPEA for 2 h per coupling were performed. Afterward, the resin was washed sequentially with DMF, DCM, and DMF.

After the determination of respective resin loading by Fmoc-monitoring peptide synthesis was continued on Syro II parallel peptide synthesizer. All couplings were performed using 4 equiv. of amino acid, 4 equiv. of PyBOP, and 8 equiv. of DIPEA in DMF at rt for 50 min. All amino acid couplings were performed as double couplings. Equivalents were calculated on the theoretical loading of the resin used. Fmoc protection was removed with 20% piperidine in DMF for 5 min in two sequential cycles. Capping steps were performed through acetylation reaction on resin-bound peptide using Ac_2O (10 equiv.) and DIPEA (12 equiv.) in DMF over 30 min at rt. Respective alkyne linkers were introduced through the same conditions as amino acid couplings on the Syro II synthesizer. Cleavage and full deprotection of the peptide from the resin were achieved through treatment of the dried resin with TFA/H_2O/DODT/TIPS (90:5:2.5:2.5) over 2 h at rt. The cleavage mixture was evaporated, and the crude peptide was precipitation through the addition of cold Et_2O. After addition, centrifugation (10 min, 3.500 rpm at 4 °C) the supernatant was discarded. The pellet was redissolved in Et_2O and centrifuged again two more times. Peptide crude was dissolved in H_2O/ACN (1:1) and lyophilized.

Acetylated peptide crudes were purified after lyophilization using HPLC (ACN+0.1% and H_2O + 0.1% TFA as mobile phase) to afford final products. Crude alkyne-labeled peptides were lyophilized overnight and used in following click chemistry reactions without further purification.

Table 15: HRMS results for purified acetylated peptides. C indicates synthesis on Chlorotrityl resin and R indicates synthesis on Rink amide resin.

Compound	Resin	Calculated m/z $[M+H]^+$	Measured m/z $[M+H]^+$
43	**C**	916.3359	916.3364
44	**C**	827.3128	827.3131
45	**C**	654.2406	654.2404
46	**C**	599.2018	599.2014
47	**C**	652.2726	652.2724
48	**C**	597.2337	597.2335
49	**C**	521.2024	521.2020
50	**R**	912.3999	912.4003
51	**R**	651.2885	651.2883
52	**R**	344.1929	344.1930
53	**R**	486.2671	486.2666
54	**R**	502.2620	502.2615
55	**C**	733.3250	733.3250
56	**C**	505.2140	505.2134

5.2.6 Click chemistry conditions

Azide tagged small molecule (1 equiv.) was added to a reaction vial with alkyne tagged peptide (1 equiv.). Degassed DMF and degassed H_2O 3:1 (0.1 M) were added to the vial, $CuSO_4$ (0.8 equiv.), sodium ascorbate (6 equiv.) and TBTA (2 equiv.) were also added. The reaction vial was closed and put under an argon atmosphere. Reactions were stirred overnight. After confirming full conversion via HPLC the respective reaction mixtures were diluted with ACN/H_2O 1:1 and lyophilized overnight. The dried crude was redissolved in an appropriate mixture of ACN/H_2O and purified using preparative HPLC with ACN + 0.1% TFA and H_2O + 0.1% TFA as mobile phase to afford the final products.

Table 16: HRMS results and yields for all bifunctional molecules.

Compound	Calculated m/z $[M+H]^+$	Measured m/z $[M+H]^+$	Calculated m/z $[M+2H]^{2+}$	Measured m/z $[M+2H]^{2+}$	Yield [mg]	Yield [%]
73	1664.6329	1664.6336	832.8201	832.8206	5.2	22
74	1575.6097	1575.6068	788.3085	788.3075	6.8	30

75	1402.5375	1402.5384	707.7724	701.7725	4.8	24
76	1347.4987	1347.4993	674.2597	674.2532	7.6	39
77	1400.5695	1400.5701	700.7884	700.7887	10.0	50
78	1345.5306	1345.5266	673.2690	673.2672	4.1	21
79	1269.4993	1269.5001	635.2533	635.2534	1.6	9
80			830.8520	830.8520	0.8	2
81	1399.5855	1399.5867	700.2936	700.2964	3.7	18
82	1092.4876	1092.4900	546.7485	546.7482	3.2	20
83	1250.5589	1250.5573	625.7809	625.7831	2.0	11
84	1481.6220	1481.6227	741.3146	741.3147	3.6	17
85	1253.5109	1253.5113	627.2591	627.2591	4.5	25
86	1958.7829	1958.7837	979.8951	979.8972	4.9	29
87	1869.7775	1869.7780	935.3924	935.3936	6.5	40
88	1696.7054	1696.7056	848.8563	848.8571	3.0	21
89	1641.6665	1641.6666	821.3369	821.3376	3.4	24
90	1694.7373	1694.7378	847.8723	847.8731	4.4	30
91	1639.6985	1639.6993	820.3529	820.3537	4.7	33
92	1563.6672	1563.6677	782.3372	782.3379	5.5	41
93			977.9360	977.9366	1.1	7
94	1547.6788	1547.6794	774.3430	774.3437	5.6	42
95	1782.6958	1782.6954	891.8516	891.8524	7.9	36
96	1693.6727	1693.6729	847.3400	847.3408	9.3	45
97	1520.6005	1520.6012	760.8039	760.8043	2.6	14
98	1465.5617	1465.5630	733.2845	733.2848	1.4	8
99	1518.6325	1518.6332	759.8199	759.8203	5.3	28
100	1463.5936	1463.5947	732.3005	732.3010	4.7	26
101	1387.5623	1387.5632	694.2848	694.2849	3.9	23
102	1778.7598	1778.7610	889.8835	889.8844	0.8	4
103	1371.5739	1371.5727	686.2906	686.2907	6.4	38
104	1840.7377	1840.7377	920.8725	920.8735	3.6	19
105	1751.7145	1751.7147	876.3609	876.3614	1.2	7
106	1578.6424	1578.6435	789.8248	789.8252	1.1	7
107	1523.6035	1523.6046	762.3054	762.3058	1.8	12
108	1576.6743	1576.6753	788.8408	788.8413	1.8	11
109	1521.6355	1521.6365	761.3214	761.3218	3.6	23
110	1445.6042	1445.6051	723.3057	723.3060	3.0	21
111			918.9045	918.9048	0.6	3
112	1429.6158	1429.6170	715.3115	715.3117	2.9	20

5.3 Biology and Biophysical Methods

LIN28 expression and purification. Human LIN28A (residues 16-187) was expressed in *Escherichia coli BL21(DE3).* Incubation of the culture at 37 °C until absorbance reached 0.5–

0.7 at 600 nm (OD600). Then IPTG was added to a final concentration of 300 µM. The induction was performed at 18 °C overnight. After centrifugation on the next day, the bacterial pellet was resuspended in lysis buffer (pH 7.5, 50 mM NaH_2PO_4, 300 mM NaCl, 0.1 mM PMSF) and lysed using a Microfluidizer. Afterward, a fresh portion of 0.1 mM PMSF and Triton X-100 (1% final concentration) were added. The lysate was then cleared by ultracentrifugation at 3000 xg and 4 °C for 1 h. Immobilized nickel affinity chromatography (HisTrap, GE Healthcare) in buffer containing 50 mM NaH_2PO_4 (pH 8), 300 mM NaCl and 5 % glycerol was used for the purification of the obtained protein. A maximum concentration of 0.5 M imidazole was used for the gradient elution, the affinity tag was cleaved using His6-TEV-protease, and the protease and unspecific binders were removed through a second nickel affinity chromatography. Upon concentration, LIN28A containing fractions were combined, concentrated and applied to a High Load Superdex 75 pg 16/600 column (GE Healthcare) with gel-filtration buffer (pH 7.5, 30 mM NaH_2PO_4, 50 mM NaCl, 5% glycerol, 2 mM β-ME). The purified protein was concentrated and then stored at -80 °C. [68, 108]

Electrophoretic mobility shift assay (EMSA). Purified LIN28A (residues 16-187) was incubated with individual compounds and 5 U recombinant ribonuclease inhibitor (Takara Bio) in EMSA reaction buffer (50 mM Tris (pH 7.5), 100 mM NaCl, 10 mM β-mercaptoethanol, 50 µM $ZnCl_2$, 2 % DMSO, 0.01 % Tween 20, 12 % glycerol) for 2 hours at room temperature. Subsequently, preE-*let-7f-1-Cy3* (*mus musculus*), purchased from IDT, was added to a final concentration of 5 nM and a reaction volume of 50 µL. The final concentration of LIN28A was 10 nM and compound concentrations rangeing from 0.18 µM to 75 µM were used, depending on the EMSA. The reaction mixtures were incubated for another 15 minutes. Then 10 µL of each reaction was separated in an 8 % polyacrylamide TAE gel at 4 °C and 220 V for 1 h using 0.25x TAE as a running buffer. Cy3 fluorescence was resolved with a ChemiDoc MP (Bio-Rad) and 2 minutes of exposure time. Band intensities were measured with Image Lab (Bio-

Rad). Corresponding IC_{50} values were determined by curve fitting with GraphPad Prism 5. [68, 108]

Thermal shift assay (nanoDSF). Measurements were performed with a NanoTemper Prometheus NT.48 nanoDSF instrument to assess of melting temperatures of CSD–compound complexes. Compounds (75 µM, 5% DMSO) were incubated with the LIN28A_CSD (residues 16-126, 30 µM) for 45 min in nanoDSF buffer (30 mM NaH_2PO_4, pH 8.0, 50 mM NaCl, 1 mM $MgCl_2$). A temperature scan ranging from 20 °C to 90 °C with a slope of 1°C/min with an excitation power of 90 % was performed. The ratio of intrinsic tryptophan and tyrosine fluorescence at 350 nm and 330 nm was measured and the first derivative was determined using GraphPad Prism 5 and OriginPro 2022b.

Peptide Stability Assay Peptide stability was tested in a whole-cell lysate prepared from HeLa cells using the freeze-thaw method. Peptides were dissolved in the lysate (normalized to 5 mg/mL protein using PBS) at 600 µM and incubated at 37 °C while gently stirring. Samples were taken at 0 min and 24 h and mixed in a 1:1 ratio with cold MeOH containing 0.05 mg/mL ethylparaben as an internal standard. Samples were then mixed and incubated for 15 min on ice, centrifuged at 15000 rpm at 4 °C for 10 min and the resulting supernatant was carefully removed and analysed by HPLC.

HPLC-based lipophilicity analysis. Chromatographic Hydrophobicity Index (CHI) values were determined using IAM.PC.DD2 column 4.6 x 100 from Regis Technologies, Inc.. A mobile phase of 50 mM ammonium acetate adjusted to pH 7.4 and acetonitrile was used with a flow rate of 1.5 mL/min. Gradients were run from 0 to 85% acetonitrile in 4.75 min. Then 85% acetonitrile was kept for 0.25 min and then flushed back to 0% acetonitrile in 0.25 min. Re-equilibration of the column with pure aqueous buffer was done for the remaining time of the overall 6 min run. Each run was calibrated with an internal standard to ensure comparability.

The readout was either 210 or 254 nm depending on if peptides or bifunctional molecules were measured. CHI values were derived through a calibration plot to evaluate the molecule's lipophilicity and potential for phospholipidosis.[98]

5.4 PRI Score Data

Table 17: Numerical results from PRI HotScore virtual alanine scan.[91] Results show the interaction score for the crystal structure of LIN28–*let-7* (PDB: 5UDZ). Scores are classified into hotspots with values >2 (red), warmspots with values ≥1 and ≤2 (orange), and irrelevant amino acids with values ≤1 (white).

#Res-ID	AA	Chain	Interaction Score	#Res-ID	AA	Chain	Interaction Score
45	K	A	0,516	**45**	K	B	0,466
46	W	A	1,141	**46**	W	B	1,403
47	F	A	0,475	**47**	F	B	0,392
48	N	A	0,933	**48**	N	B	1,186
49	V	A	-	**49**	V	B	0,027
50	R	A	2,926	**50**	R	B	3,387
51	M	A	1,291	**51**	M	B	0,79
53	F	A	2,231	**53**	F	B	2,498
55	F	A	2,169	**55**	F	B	1,563
71	D	A	-	**71**	D	B	-
73	F	A	2,332	**72**	V	B	0,119
75	H	A	2,02	**73**	F	B	2,125
76	Q	A	0,806	**75**	H	B	1,891
77	S	A	0,287	**76**	Q	B	0,8
78	K	A	0,361	**77**	S	B	0,26
84	F	A	2,507	**78**	K	B	0,387
85	R	A	0,605	**84**	F	B	1,865
86	S	A	0,056	**88**	K	B	0,077
88	K	A	-	**89**	E	B	-
89	E	A	-	**100**	S	B	0,244
100	S	A	0,275	**102**	K	B	1,288
102	K	A	1,27	**104**	L	B	0,356
104	L	A	0,27	**105**	E	B	-
105	E	A	-	**120**	S	B	0,045
120	S	A	0,112	**122**	R	B	1,332
121	E	A	-	**123**	R	B	0,287
122	R	A	1,415	**125**	K	B	0,642
123	R	A	0,068	**137**	D	B	0,428
125	K	A	0,654	**138**	R	B	0,667
137	D	A	0,383	**139**	C	B	0,307
138	R	A	0,601	**140**	Y	B	3,158
139	C	A	0,301	**141**	N	B	0,825

140	Y	A	3,504	**147**	H	B	0,166
141	N	A	0,921	**148**	H	B	1,86
147	H	A	0,088	**150**	K	B	0,333
148	H	A	1,14	**157**	Q	B	-
150	K	A	0,3	**159**	K	B	1,845
157	Q	A	-	**160**	K	B	0,239
159	K	A	1,911	**161**	C	B	0,239
160	K	A	0,286	**162**	H	B	3,462
161	C	A	0,169	**163**	F	B	0,517
162	H	A	3	**169**	H	B	0,104
163	F	A	0,411	**170**	M	B	0,912
169	H	A	0,114	**171**	V	B	0,244
170	M	A	1,063	**177**	K	B	2,057
171	V	A	0,239	**180**	Q	B	0,13
177	K	A	1,92				0,466

5.5 Biophysical Data

5.5.1 EMSA Gels

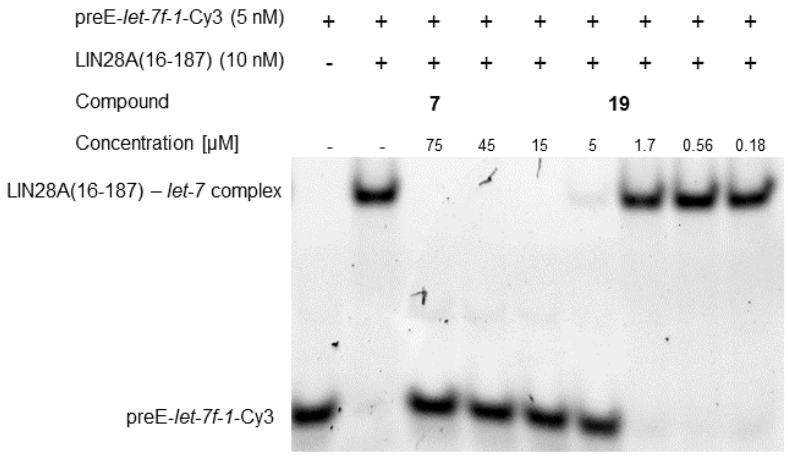

Figure 31: Dose-response EMSA of compound **19**. Compound concentrations of 45, 15, 5, 1.7, 0.56, and 0.18 µM were incubated with LIN28. For readout preE-*let-7*f-1-Cy3 was used to generate a fluorescent readout. RNP can be observed in the upper part of the gel. If the compound can perturb the complex, inhibition can be observed through an electrophoretic mobility shift indicated by a shift of the fluorescent signal to the lower part of the gel. **7** was used as a positive control (representative).

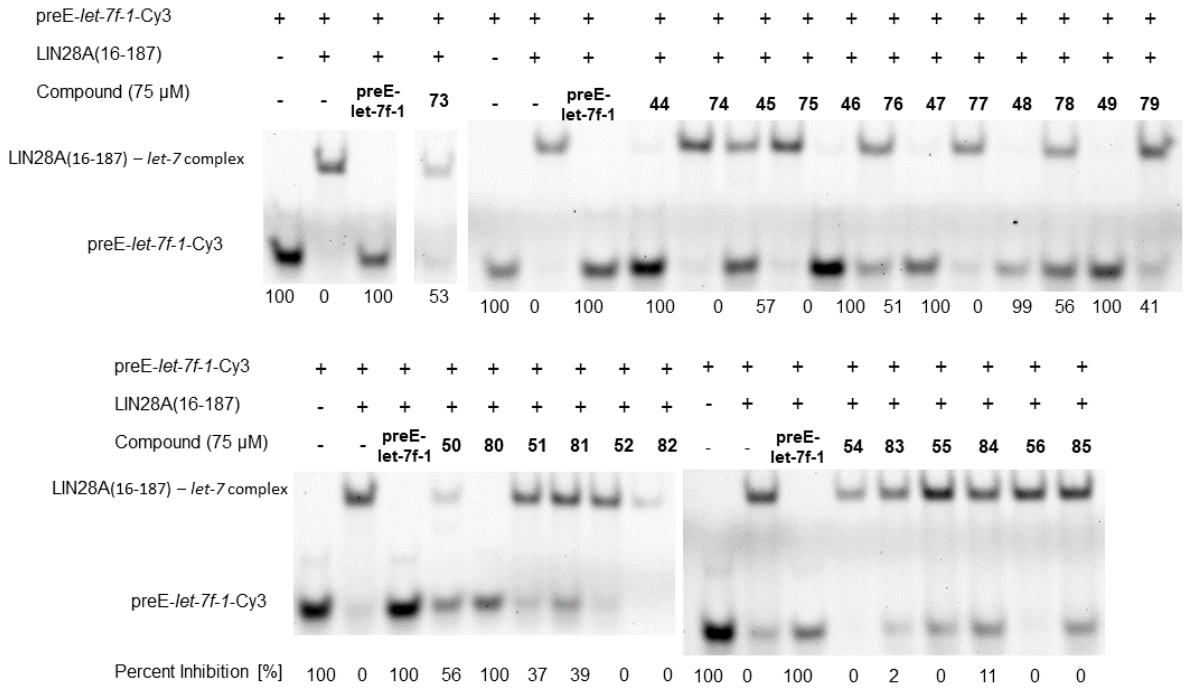

Figure 32: Single Dose Screen of the acetylated peptides and NEC generation 1. LIN28 was incubated with 75 µM peptide. preE-*let-7f-1*-Cy3 was added to generate a fluorescent readout. RNP can be observed in the upper part of the gel. If the compound can perturb the complex, inhibition can be observed through an electrophoretic

mobility shift indicated by a shift of the fluorescent signal to the lower part of the gel. preE-*let-7f-1* and PH-31 are used as positive controls.

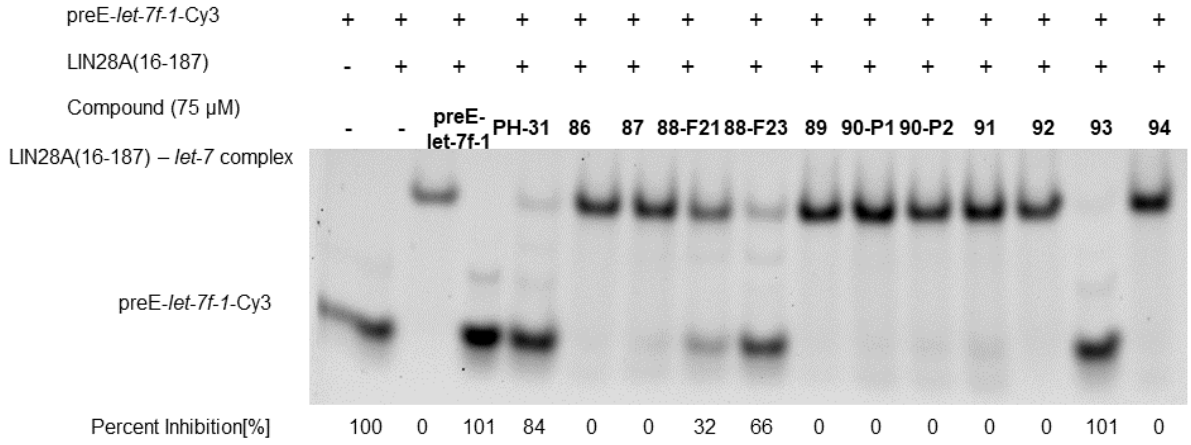

Figure 33: Single Dose Screen of the NEC generation two. LIN28 was incubated with 75 µM peptide. preE-*let-7f-1*-Cy3 was added to generate a fluorescent readout. RNP can be observed in the upper part of the gel. If the compound can perturb the complex, inhibition can be observed through an electrophoretic mobility shift indicated by a shift of the fluorescent signal to the lower part of the gel. preE-*let-7f-1* and PH-31 are used as positive controls.

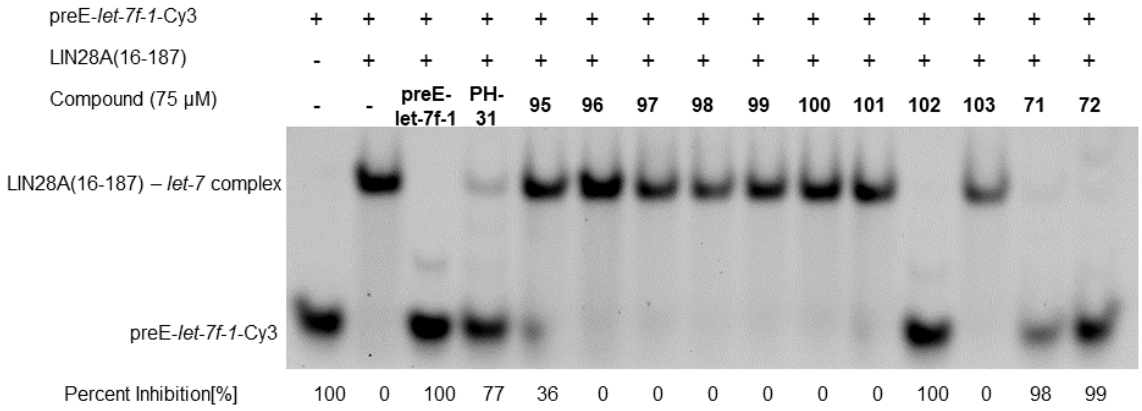

Figure 34: Single Dose Screen of the NEC generation three. LIN28 was incubated with 75 µM peptide. preE-*let-7*f-1-Cy3 was added to generate a fluorescent readout. RNP can be observed in the upper part of the gel. If the compound can perturb the complex, inhibition can be observed through an electrophoretic mobility shift indicated by a shift of the fluorescent signal to the lower part of the gel. preE-*let-7*f-1 and PH-31 are used as positive controls.

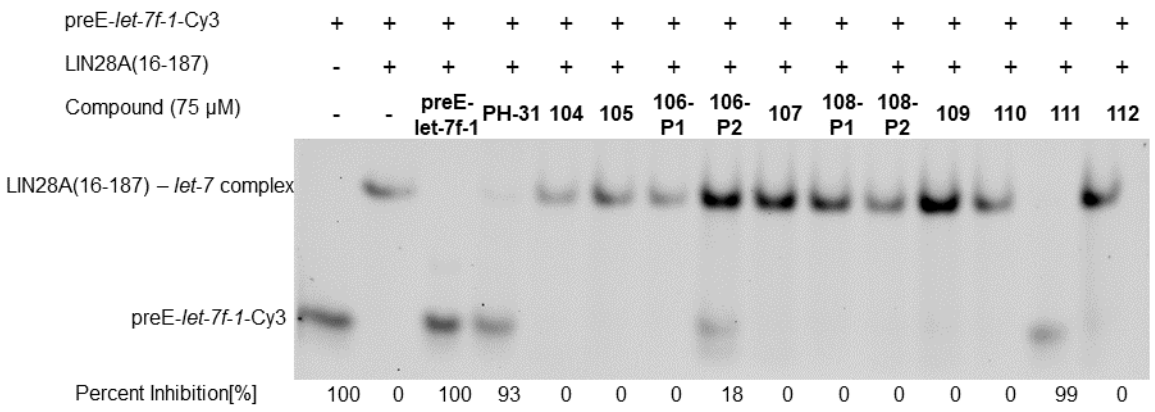

Figure 35: Single Dose Screen of the NEC generation four. LIN28 was incubated with 75 µM peptide. preE-*let-7*f-1-Cy3 was added to generate a fluorescent readout. RNP can be observed in the upper part of the gel. If the compound can perturb the complex, inhibition can be observed through an electrophoretic mobility shift indicated by a shift of the fluorescent signal to the lower part of the gel. preE-*let-7*f-1 and PH-31 are used as positive controls.

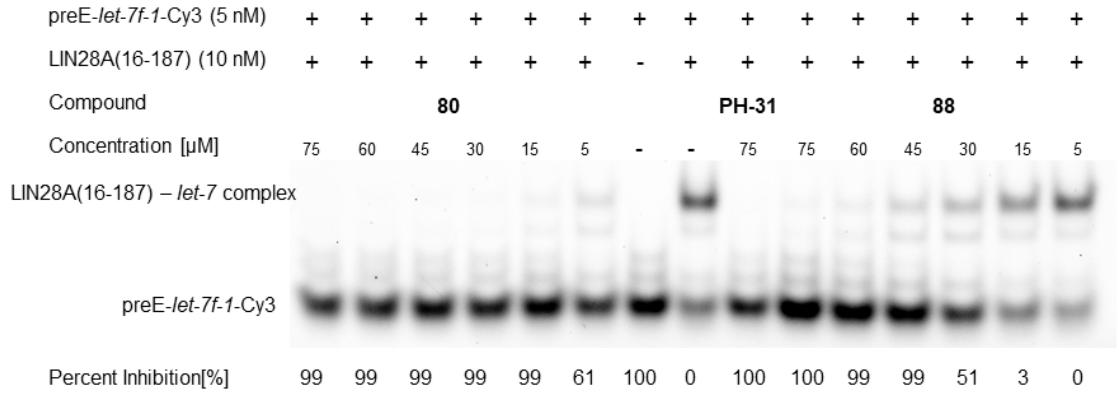

Figure 36: Dose-response EMSA of compounds **80** and **88**. Compound concentrations of 75, 60, 45, 30, 15, and 5 µM were incubated with LIN28. For readout preE-*let-7*f-1-Cy3 was used to generate a fluorescent readout. RNP can be observed in the upper part of the gel. If the compound can perturb the complex, inhibition can be observed through an electrophoretic mobility shift indicated by a shift of the fluorescent signal to the lower part of the gel. PH-31 was used as a positive control.

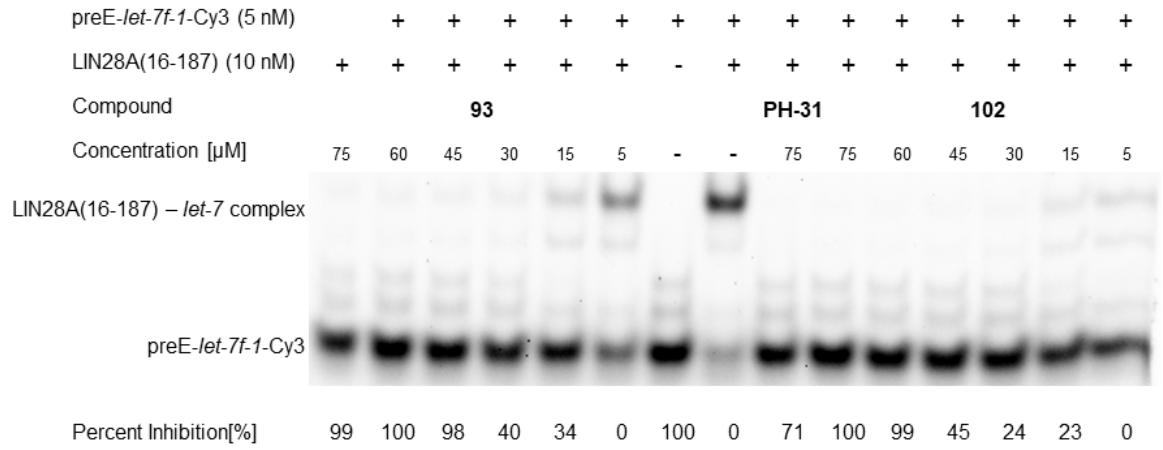

Figure 37: Dose-response EMSA of compounds **93** and **102**. Compound concentrations of 75, 60, 45, 30, 15, and 5 µM were incubated with LIN28. For readout preE-*let-7*f-1-Cy3 was used to generate a fluorescent readout. RNP can be observed in the upper part of the gel. If the compound can perturb the complex, inhibition can be observed through an electrophoretic mobility shift indicated by a shift of the fluorescent signal to the lower part of the gel. PH-31 was used as a positive control.

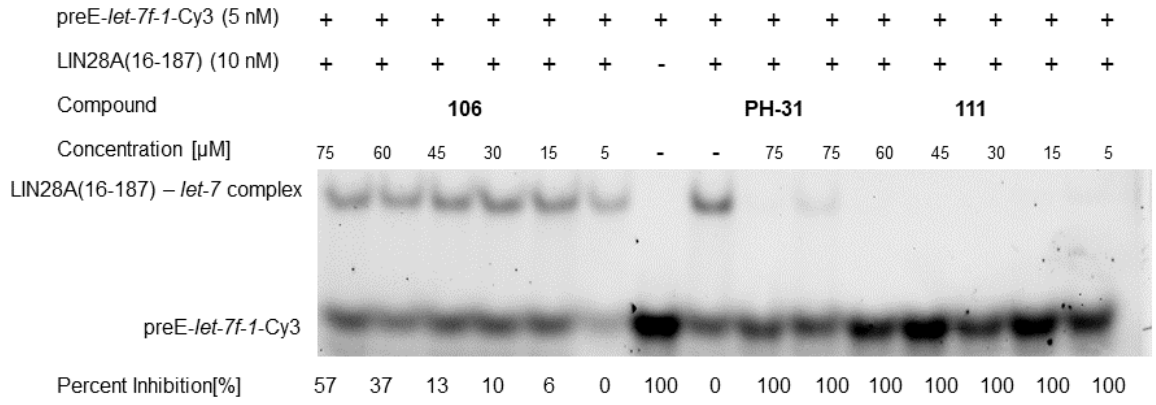

Figure 38: Dose-response EMSA of compounds **106** and **111**. Compound concentrations of 75, 60, 45, 30, 15, and 5 µM were incubated with LIN28. For readout preE-*let-7*f-1-Cy3 was used to generate a fluorescent readout. RNP can be observed in the upper part of the gel. If the compound can perturb the complex, inhibition can be observed through an electrophoretic mobility shift indicated by a shift of the fluorescent signal to the lower part of the gel. PH-31 was used as a positive control.

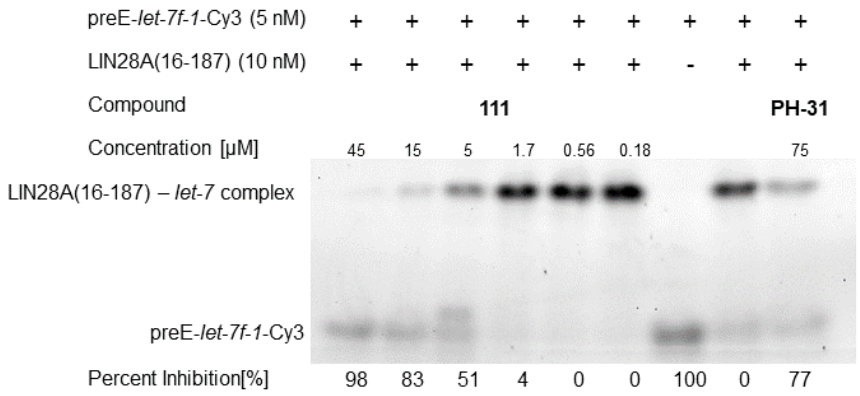

Figure 39: Dose-response EMSA of compound **111**. Compound concentrations of 45, 15, 5, 1.7, 0.56, and 0.18 µM were incubated with LIN28. For readout preE-*let-7*f-1-Cy3 was used to generate a fluorescent readout. RNP can be observed in the upper part of the gel. If the compound can perturb the complex, inhibition can be observed through an electrophoretic mobility shift indicated by a shift of the fluorescent signal to the lower part of the gel. PH-31 was used as a positive control.

5.5.2 HPLC Chromatograms

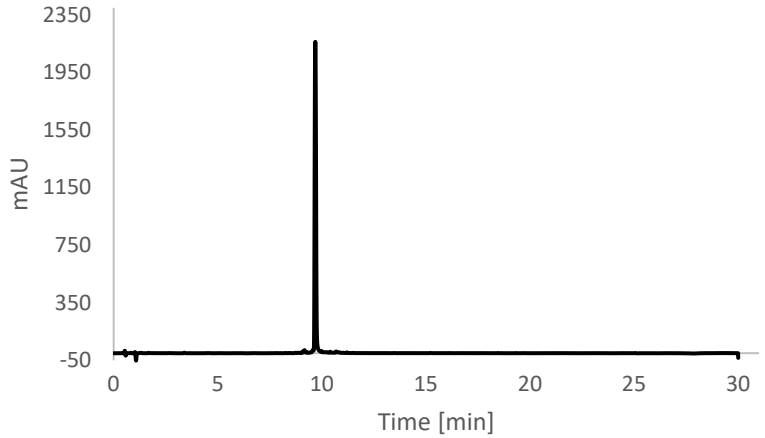

Figure 40: HPLC analysis of peptide **43** at 210 nm.

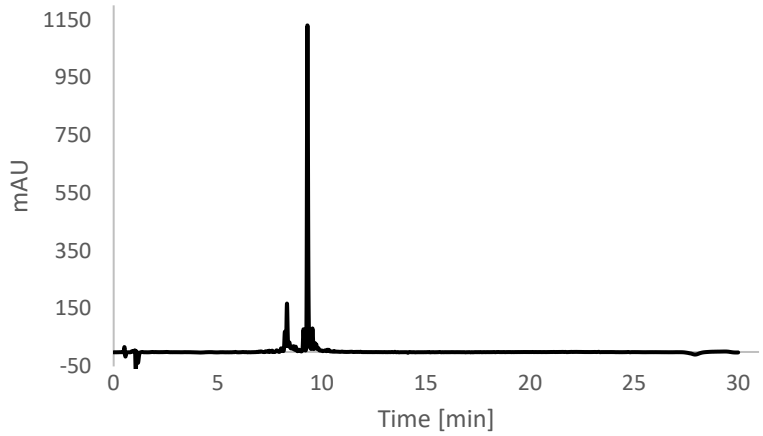

Figure 41: HPLC analysis of peptide **44** at 210 nm.

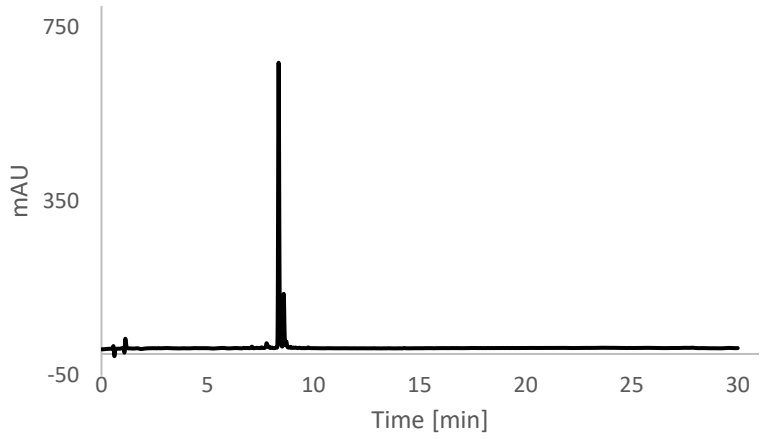

Figure 42: HPLC analysis of peptide **45** at 210 nm.

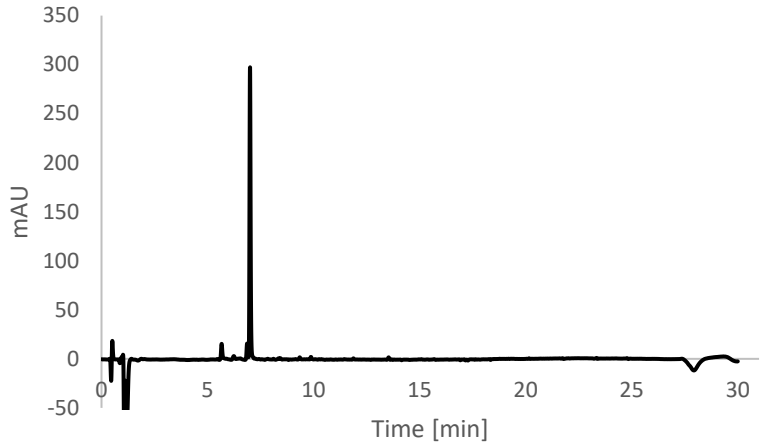

Figure 43: HPLC analysis of peptide **46** at 210 nm.

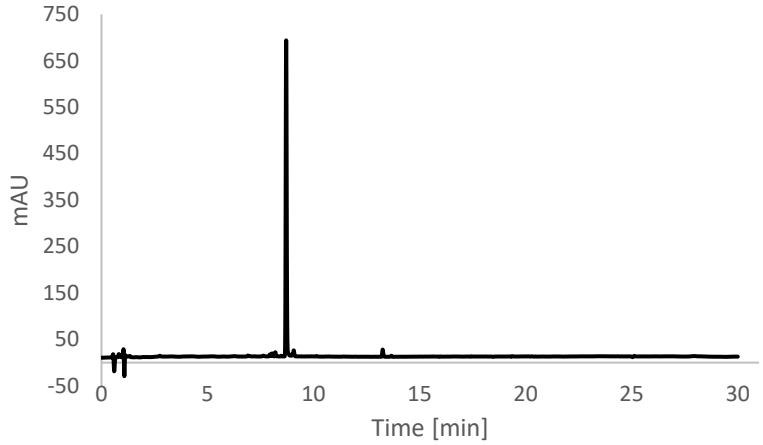

Figure 44: HPLC analysis of peptide **47** at 210 nm.

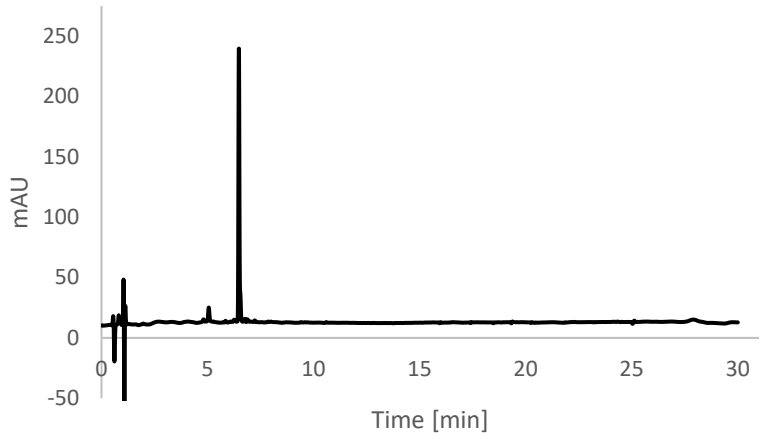

Figure 45: HPLC analysis of peptide **48** at 210 nm.

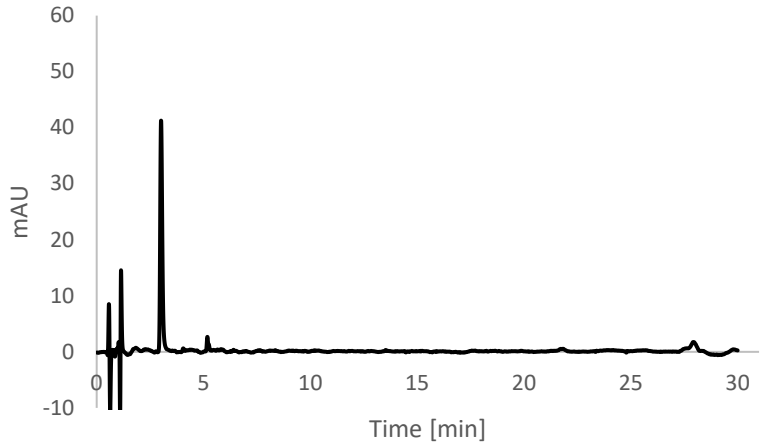

Figure 46: HPLC analysis of peptide **49** at 210 nm.

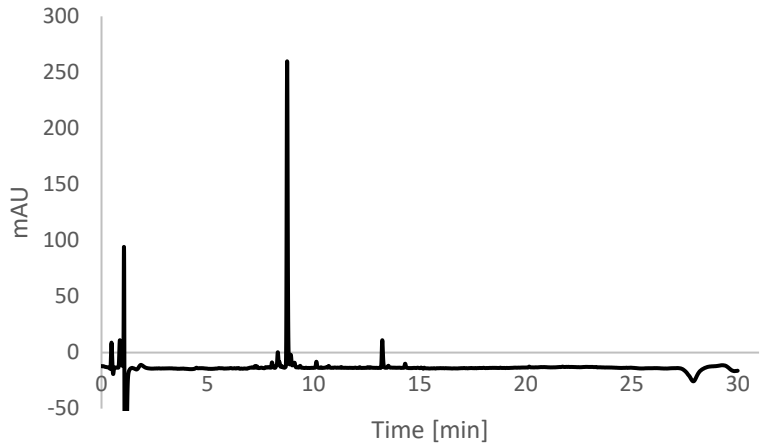

Figure 47: HPLC analysis of peptide **50** at 210 nm.

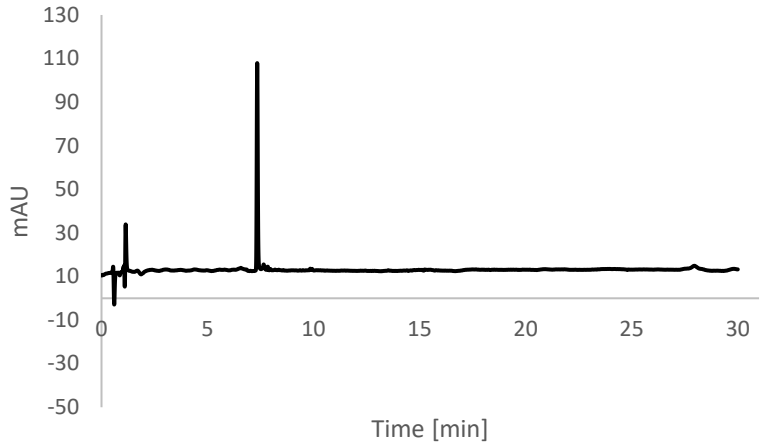

Figure 48: HPLC analysis of peptide **51** at 210 nm.

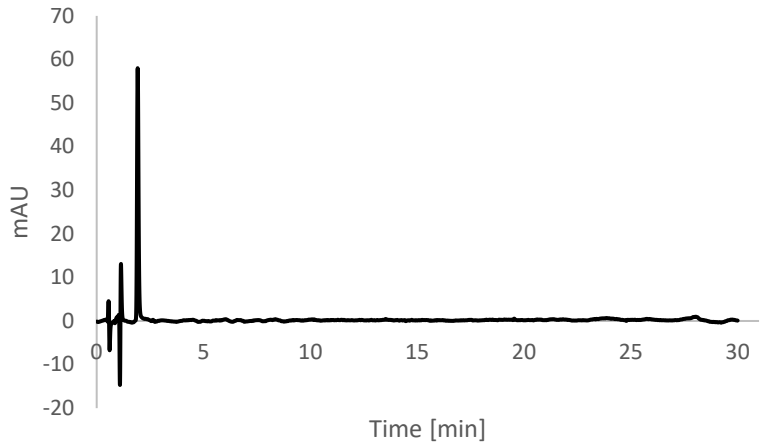

Figure 49: HPLC analysis of peptide **52** at 210 nm.

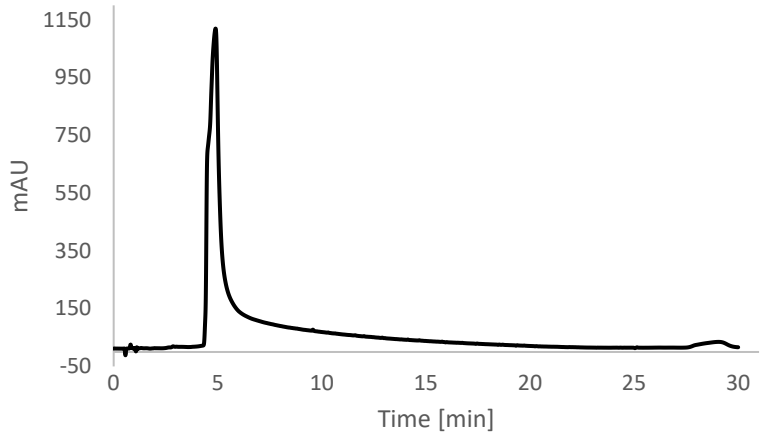

Figure 50: HPLC analysis of peptide **53** at 210 nm.

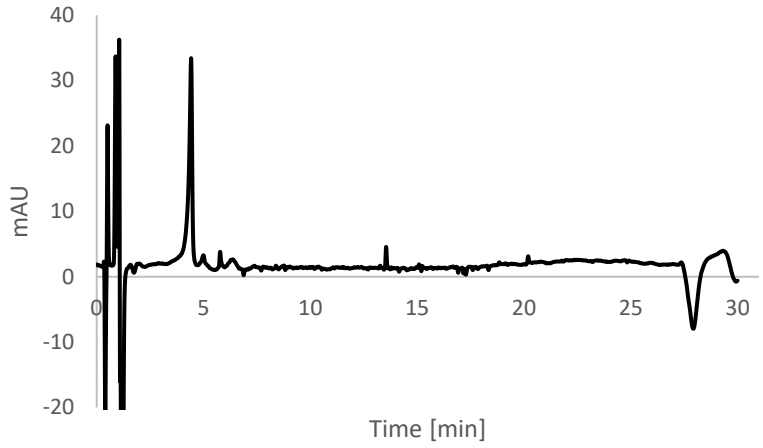

Figure 51: HPLC analysis of peptide **54** at 210 nm.

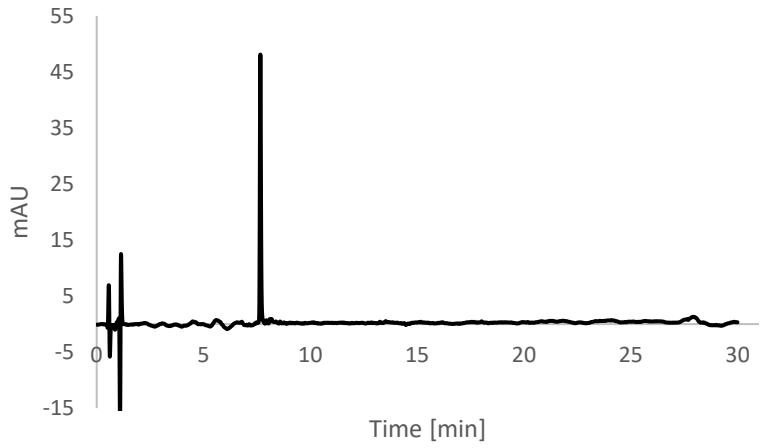

Figure 52: HPLC analysis of peptide **55** at 210 nm.

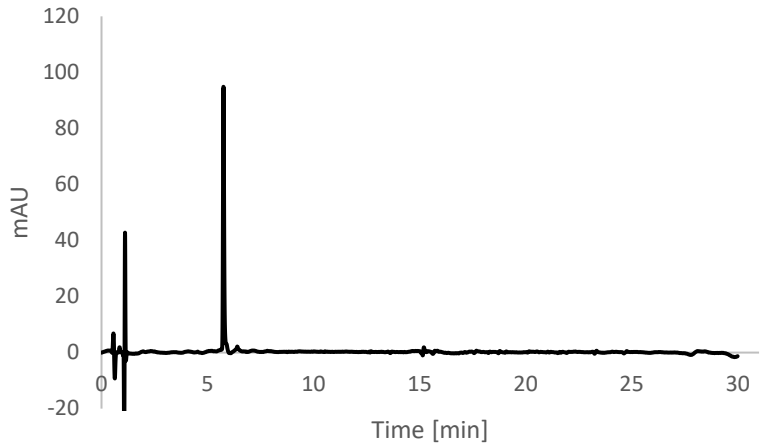

Figure 53: HPLC analysis of peptide **56** at 210 nm.

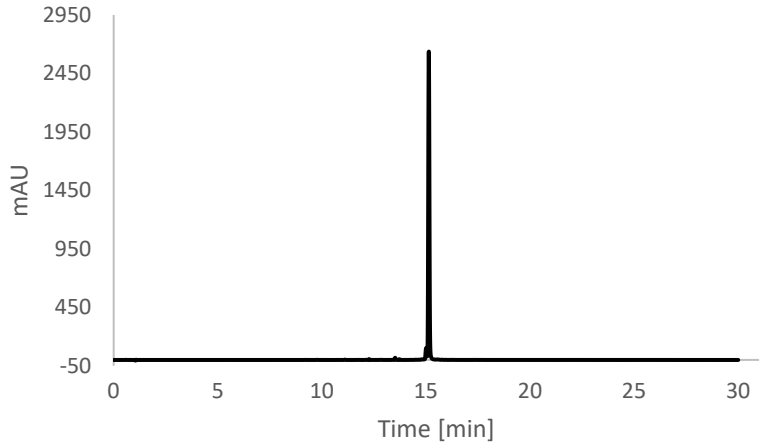

Figure 54: HPLC analysis of peptide **73** at 254 nm.

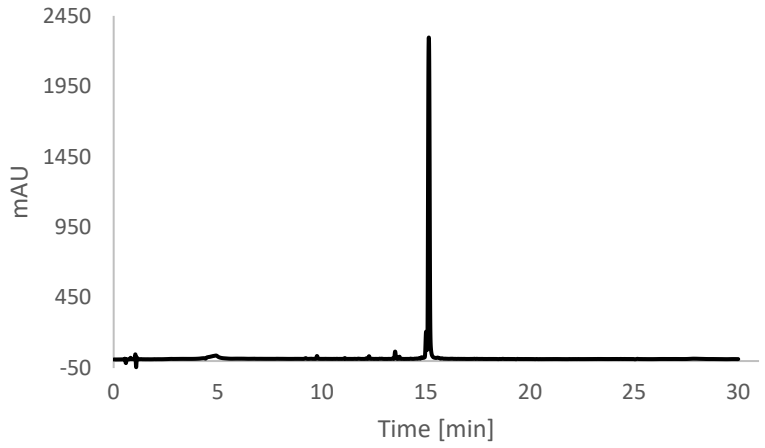

Figure 55: HPLC analysis of peptide **73** at 210 nm.

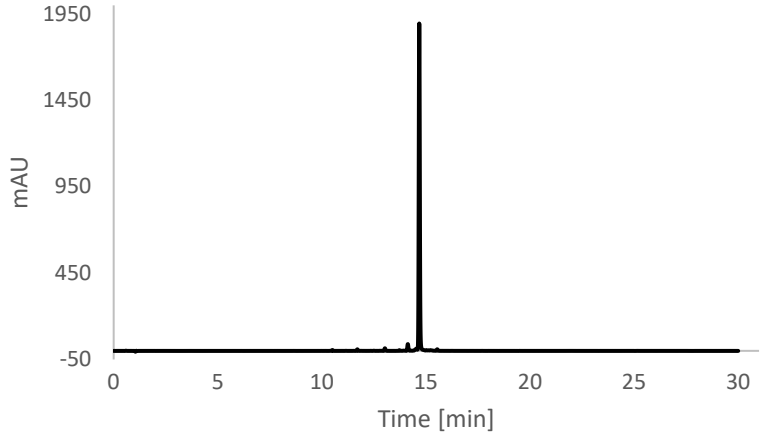

Figure 56: HPLC analysis of peptide **74** at 254 nm.

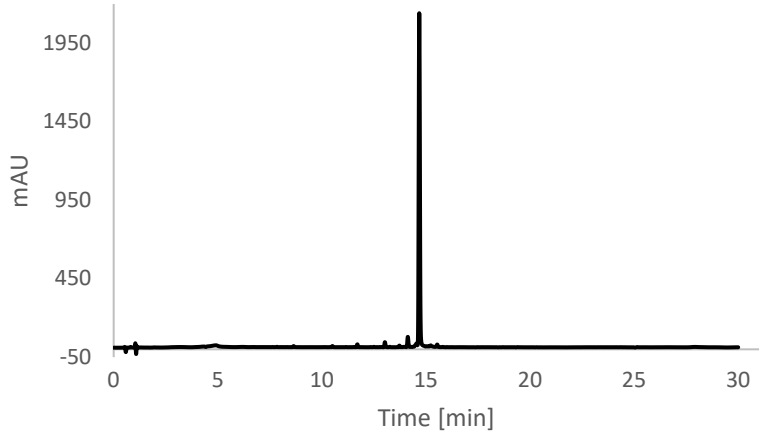

Figure 57: HPLC analysis of peptide **74** at 210 nm.

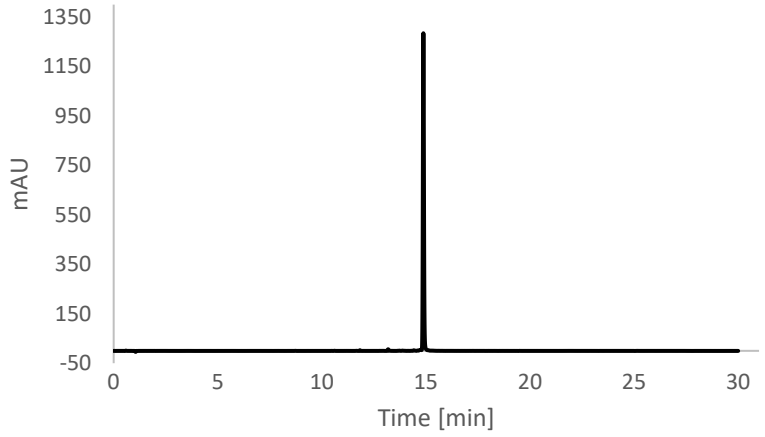

Figure 58: HPLC analysis of peptide **75** at 254 nm.

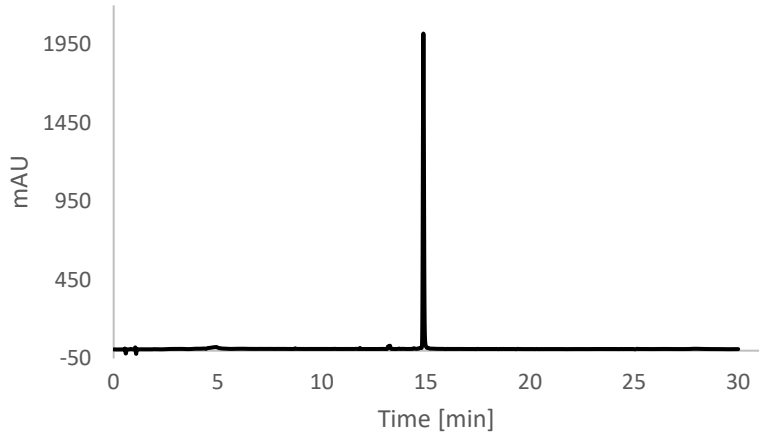

Figure 59: HPLC analysis of peptide **75** at 210 nm.

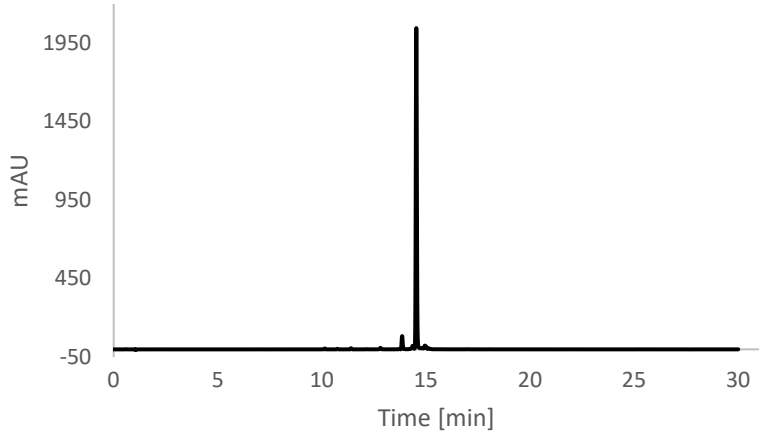

Figure 60: HPLC analysis of peptide **76** at 254 nm.

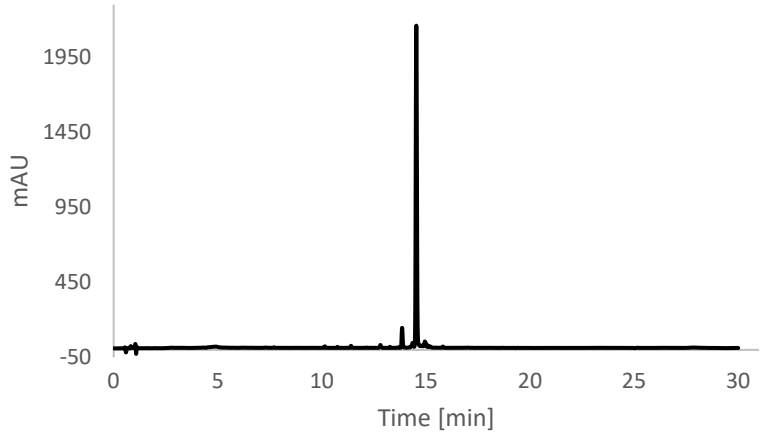

Figure 61: HPLC analysis of peptide **76** at 210 nm.

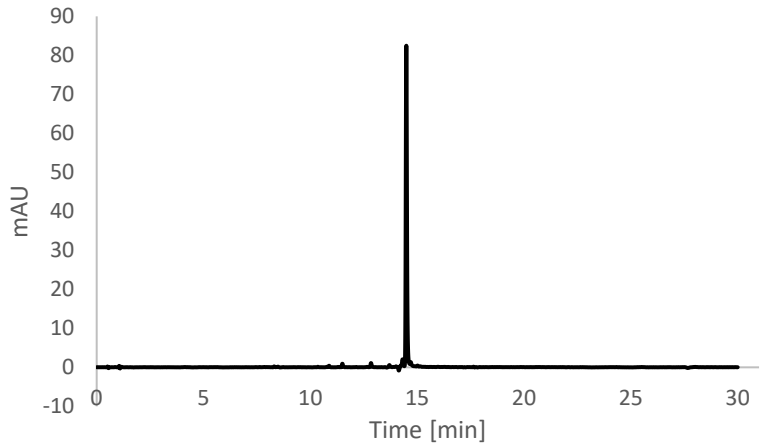

Figure 62: HPLC analysis of peptide **77** at 254 nm.

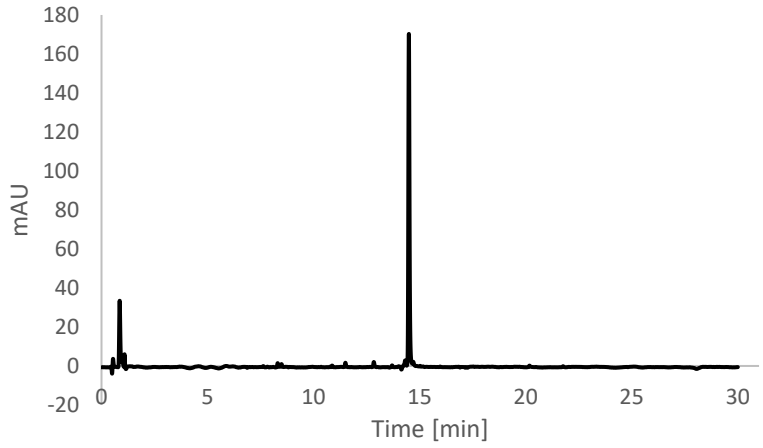

Figure 63: HPLC analysis of peptide **77** at 210 nm.

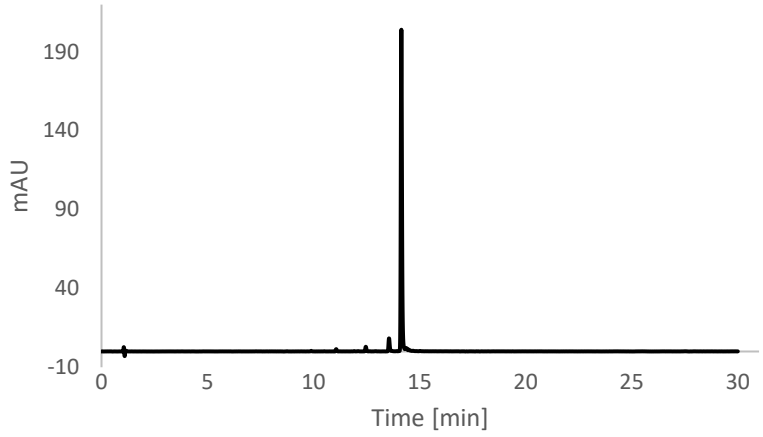

Figure 64: HPLC analysis of peptide **78** at 254 nm.

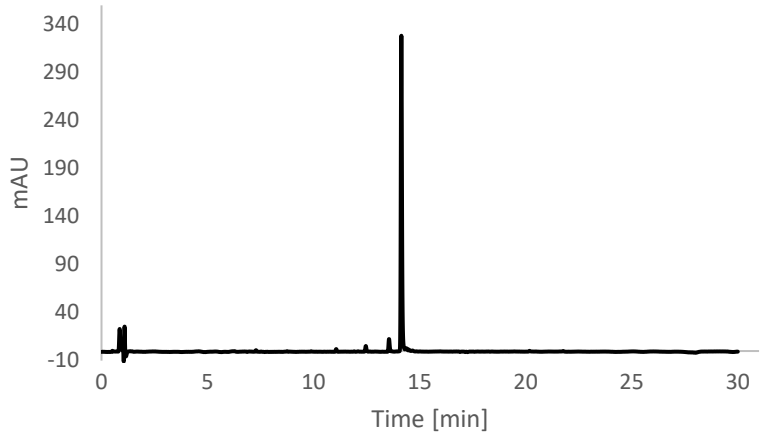

Figure 65: HPLC analysis of peptide **78** at 210 nm.

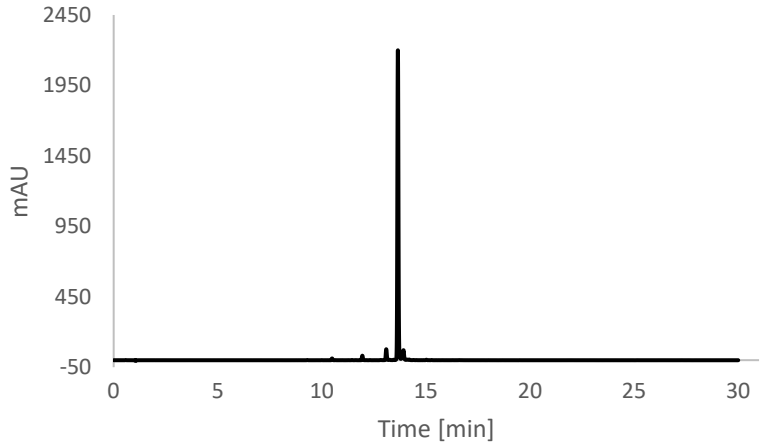

Figure 66: HPLC analysis of peptide **79** at 254 nm.

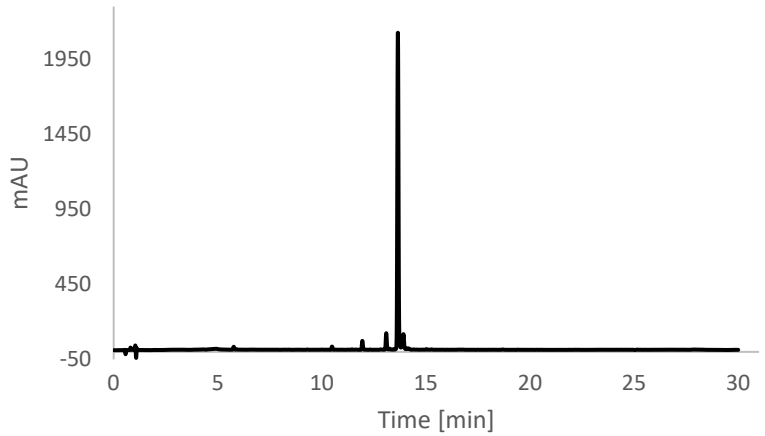

Figure 67: HPLC analysis of peptide **79** at 210 nm.

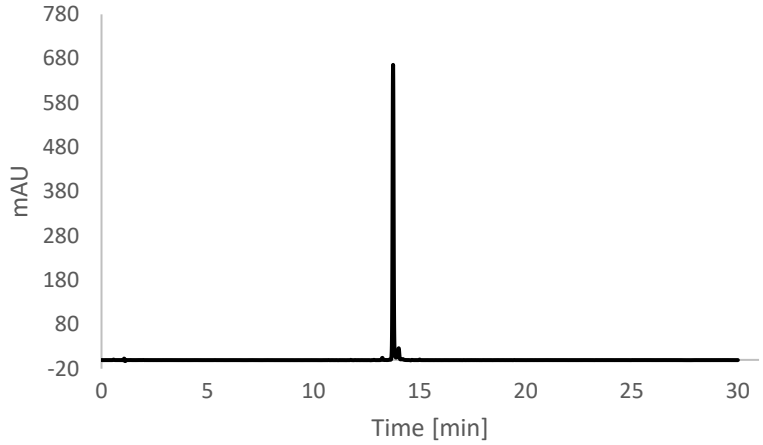

Figure 68: HPLC analysis of peptide **80** at 254 nm.

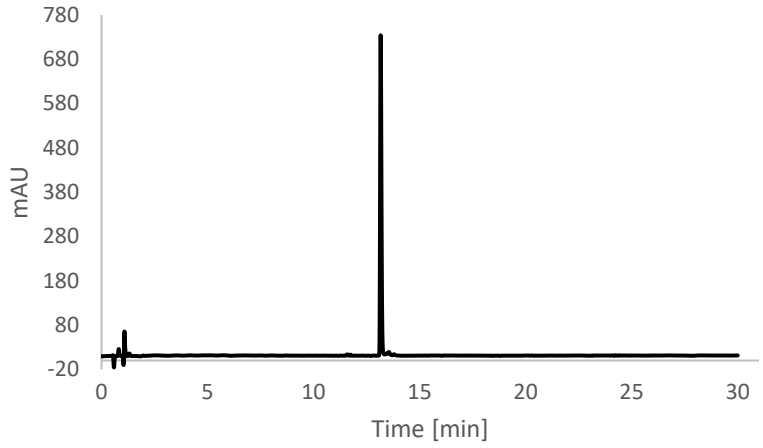

Figure 69: HPLC analysis of peptide **80** at 210 nm.

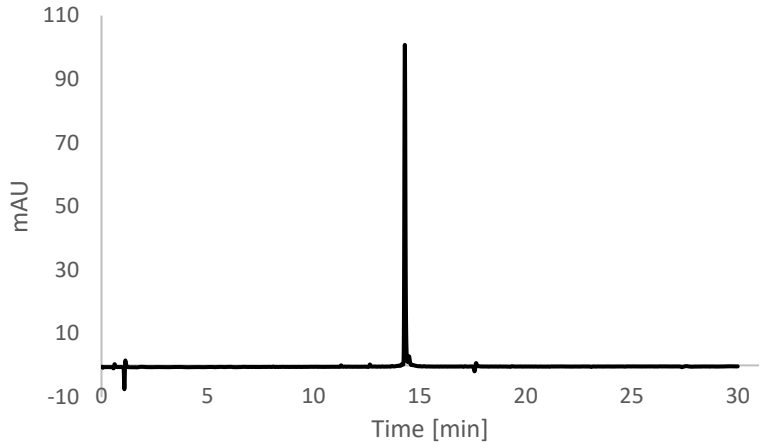

Figure 70: HPLC analysis of peptide **81** at 254 nm.

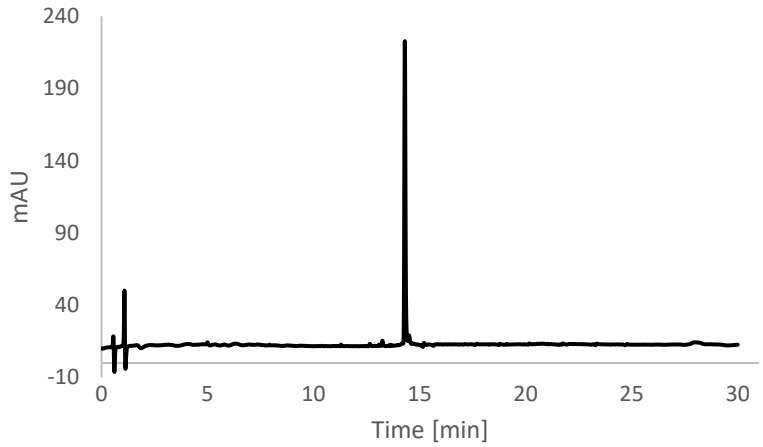

Figure 71: HPLC analysis of peptide **81** at 210 nm.

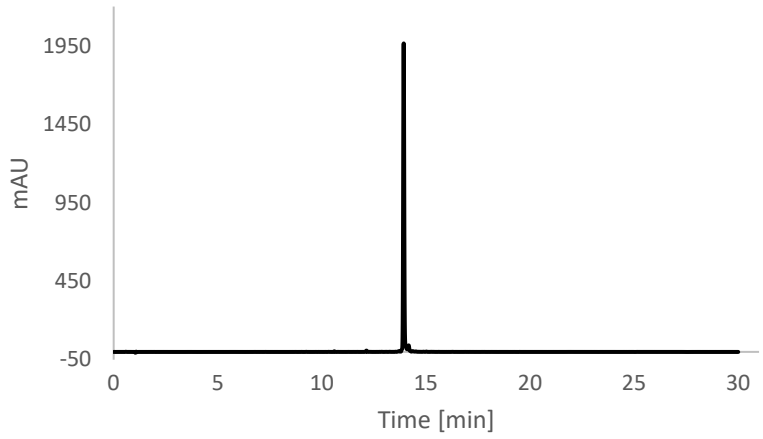

Figure 72: HPLC analysis of peptide **82** at 254 nm.

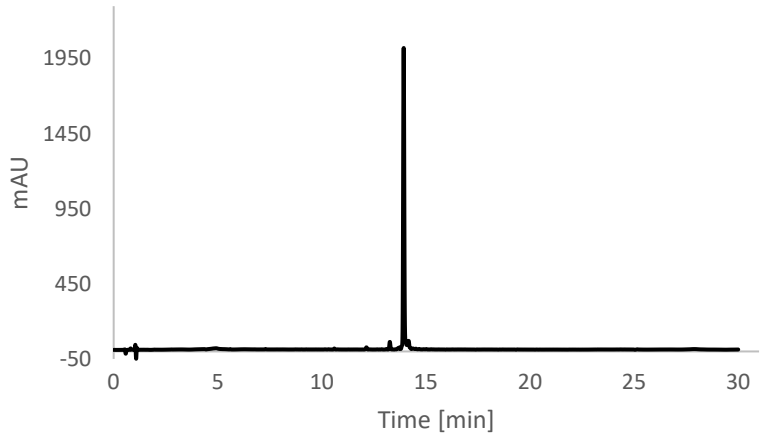

Figure 73: HPLC analysis of peptide **82** at 210 nm.

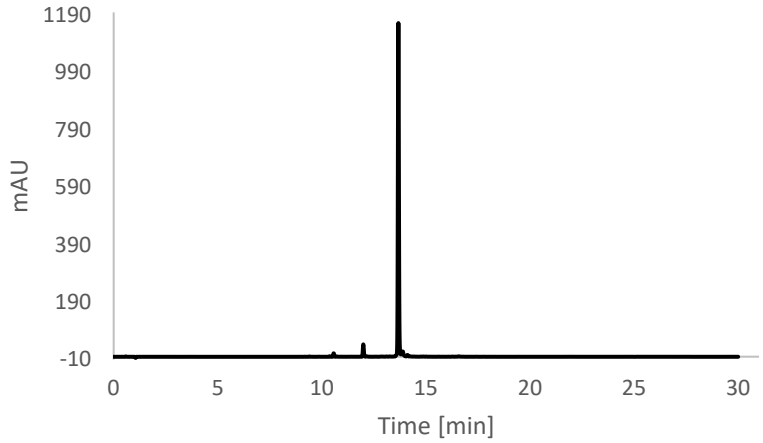

Figure 74: HPLC analysis of peptide **83** at 254 nm.

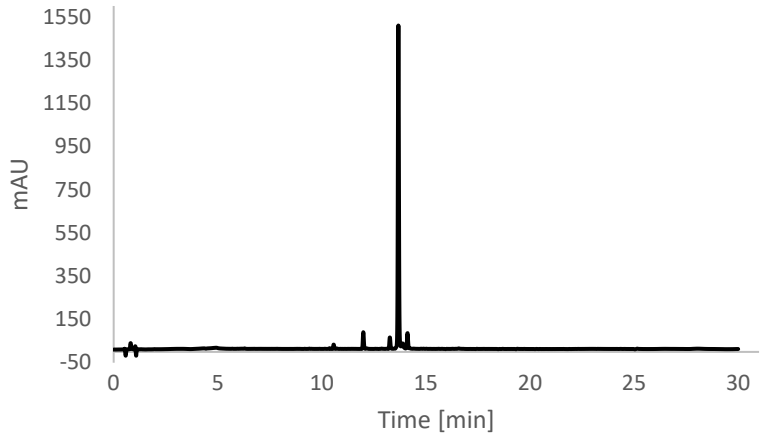

Figure 75: HPLC analysis of peptide **83** at 210 nm.

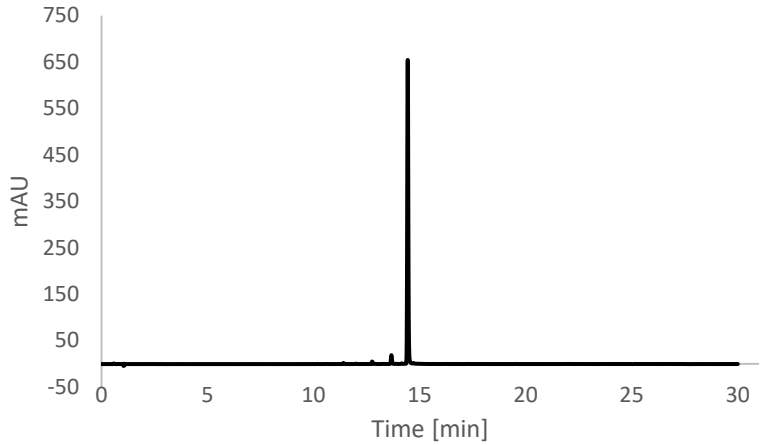

Figure 76: HPLC analysis of peptide **84** at 254 nm.

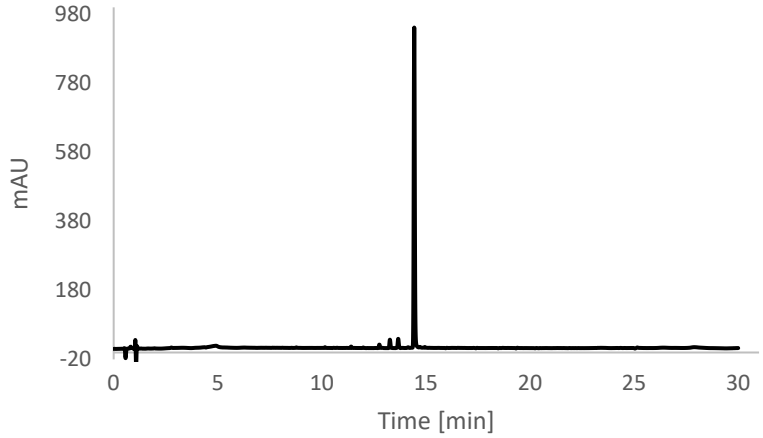

Figure 77: HPLC analysis of peptide **84** at 210 nm.

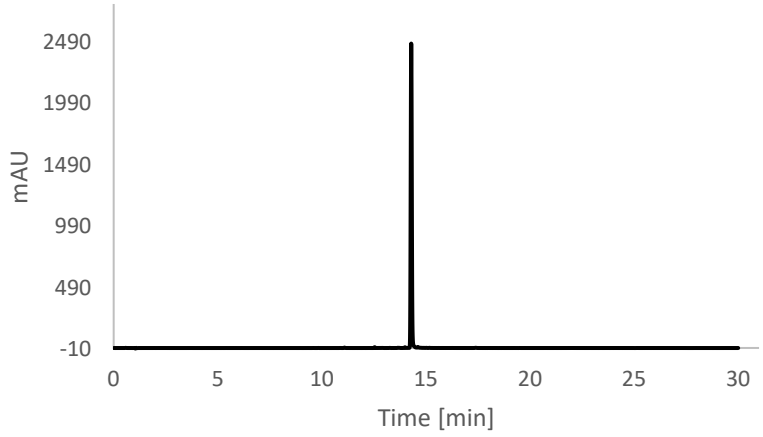

Figure 78: HPLC analysis of peptide **85** at 254 nm.

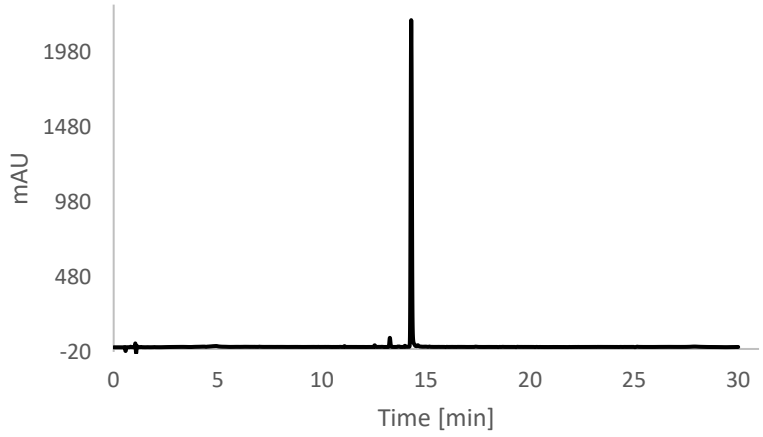

Figure 79: HPLC analysis of peptide **85** at 210 nm.

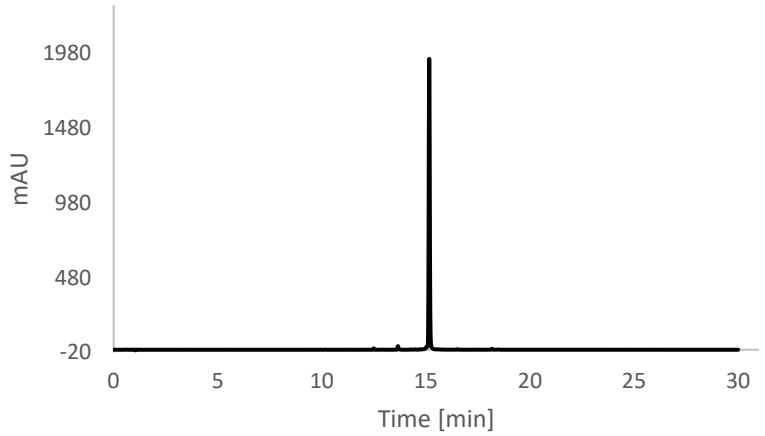

Figure 80: HPLC analysis of peptide **86** at 254 nm.

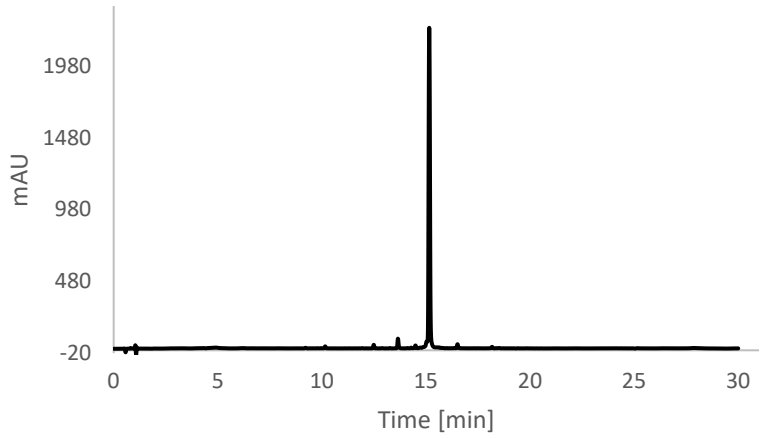

Figure 81: HPLC analysis of peptide **86** at 210 nm.

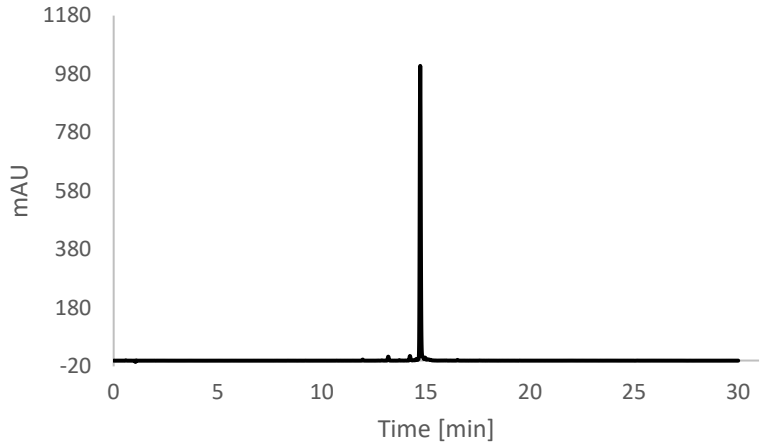

Figure 82: HPLC analysis of peptide **87** at 254 nm.

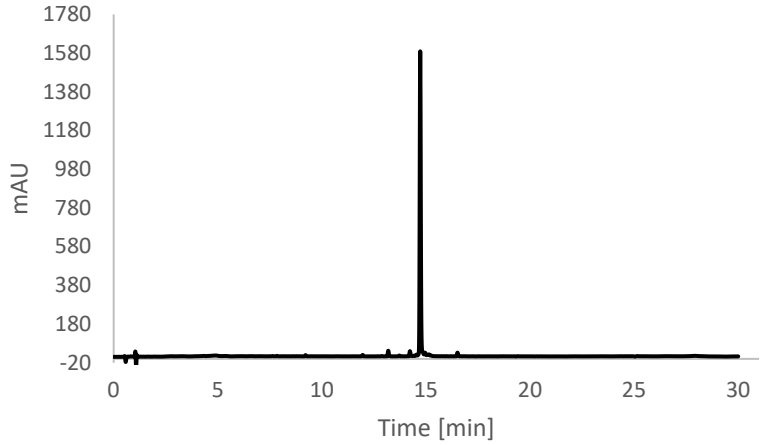

Figure 83: HPLC analysis of peptide **87** at 210 nm.

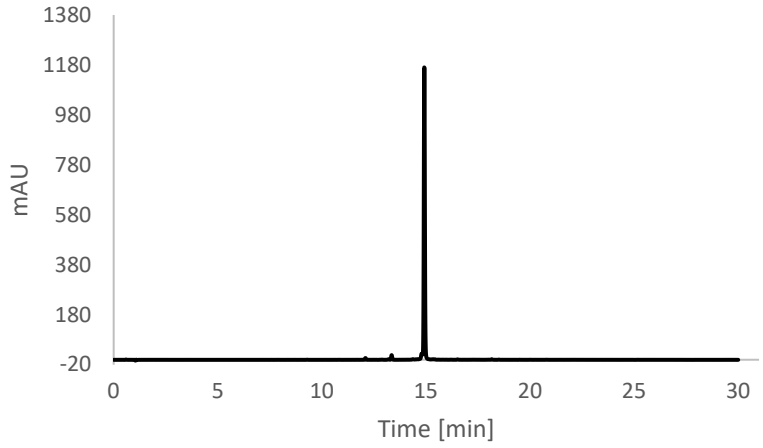

Figure 84: HPLC analysis of peptide **88** at 254 nm.

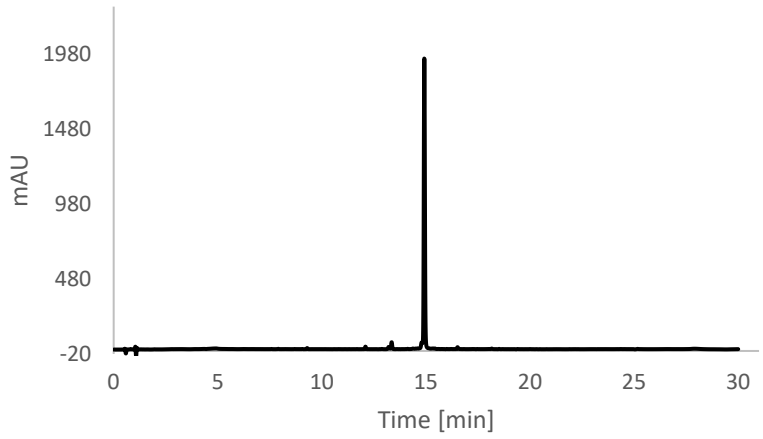

Figure 85: HPLC analysis of peptide **88** at 210 nm.

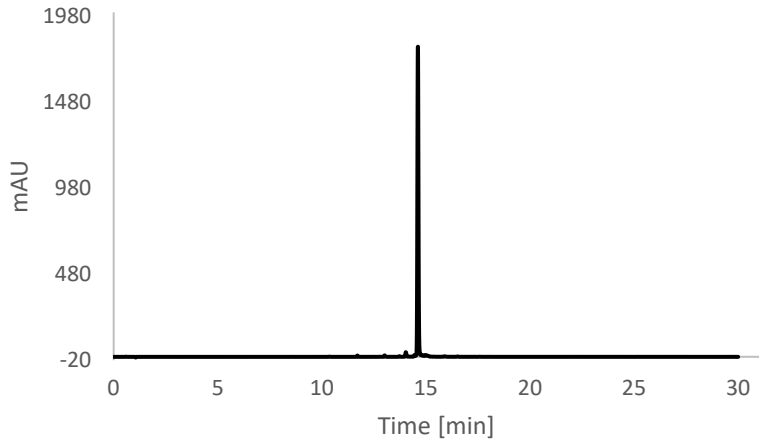

Figure 86: HPLC analysis of peptide **89** at 254 nm.

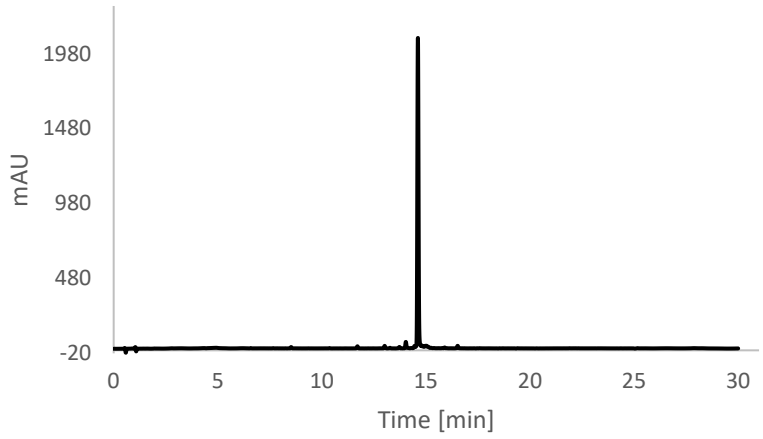

Figure 87: HPLC analysis of peptide **89** at 210 nm.

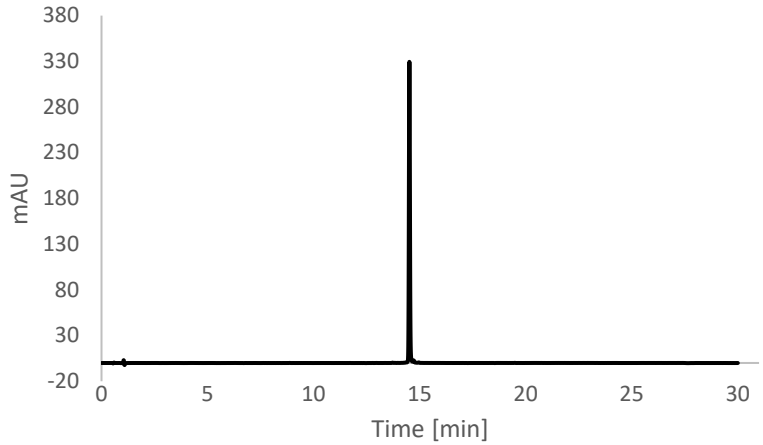

Figure 88: HPLC analysis of peptide **90** at 254 nm.

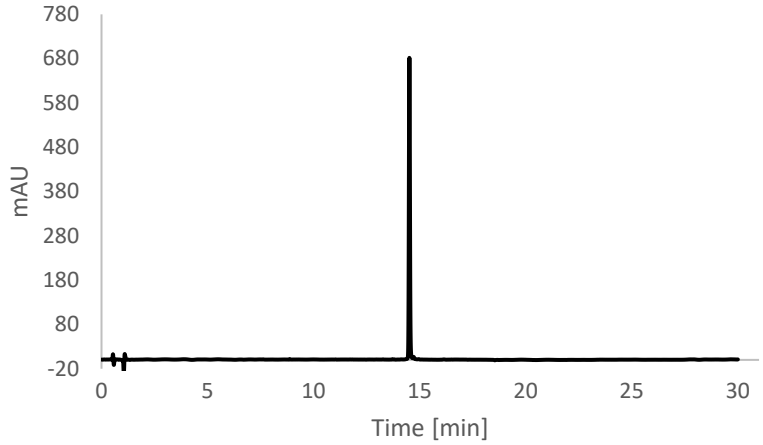

Figure 89: HPLC analysis of peptide **90** at 210 nm.

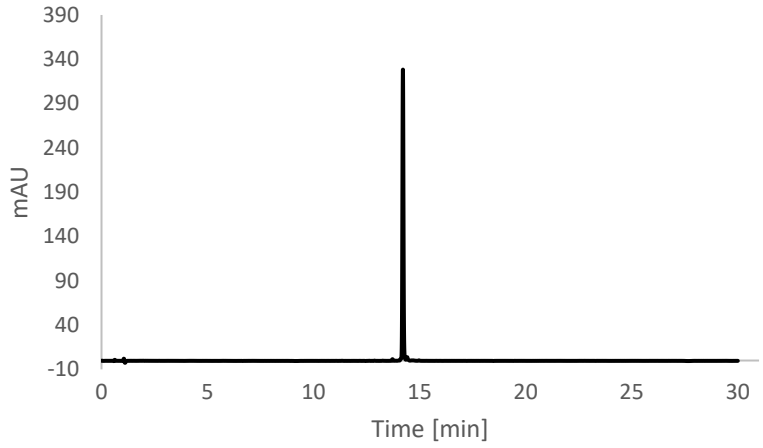

Figure 90: HPLC analysis of peptide **91** at 254 nm.

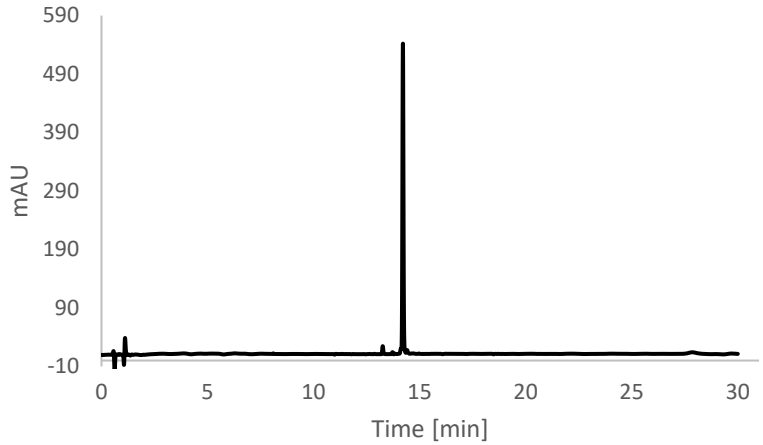

Figure 91: HPLC analysis of peptide **91** at 210 nm.

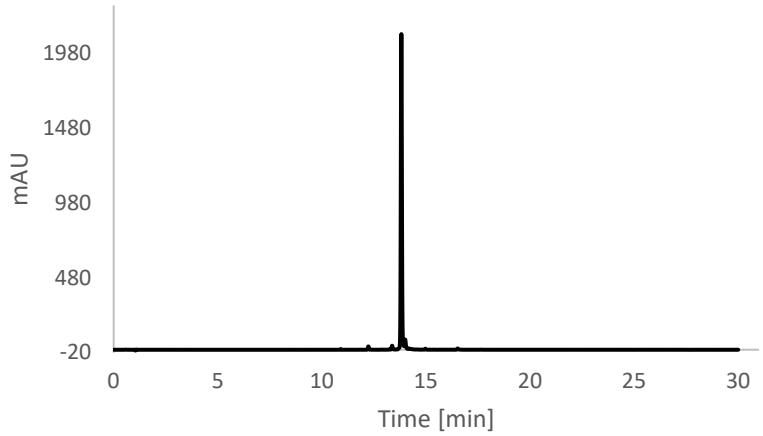

Figure 92: HPLC analysis of peptide **92** at 254 nm.

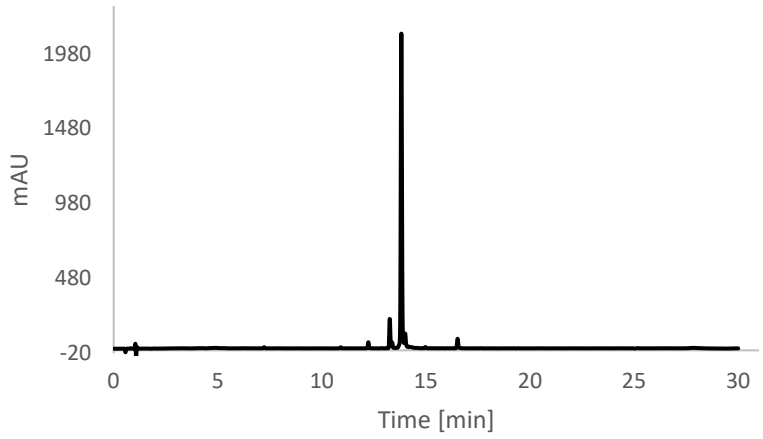

Figure 93: HPLC analysis of peptide **92** at 210 nm.

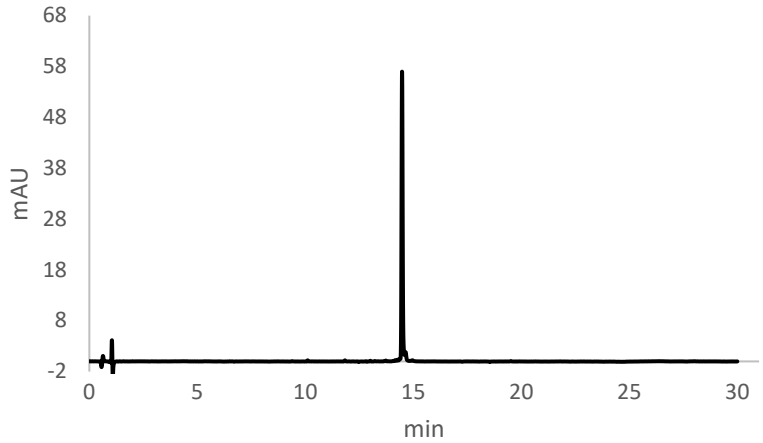

Figure 94: HPLC analysis of peptide **93** at 254 nm.

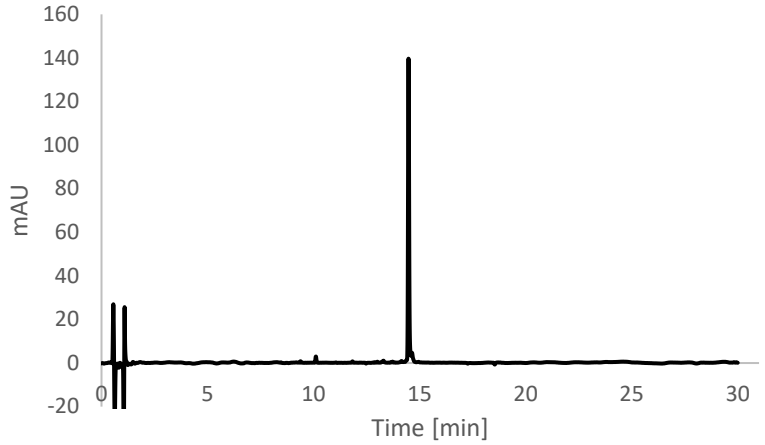

Figure 95: HPLC analysis of peptide **93** at 210 nm.

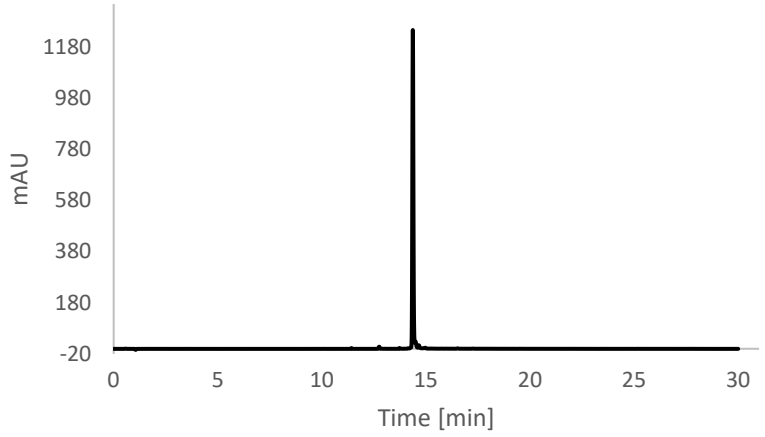

Figure 96: HPLC analysis of peptide **94** at 254 nm.

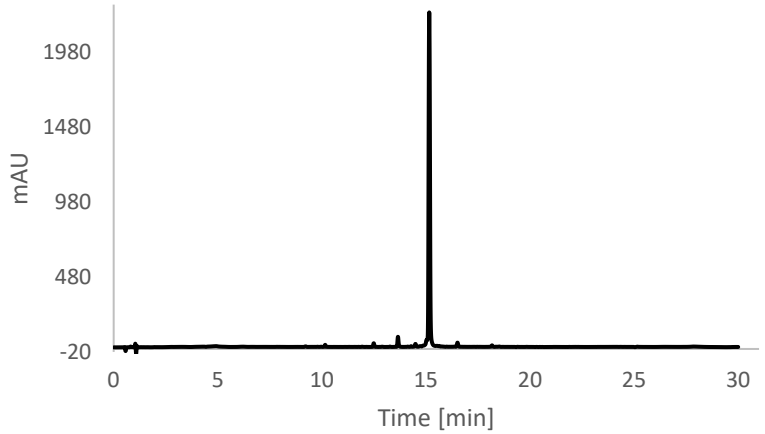

Figure 97: HPLC analysis of peptide **94** at 210 nm.

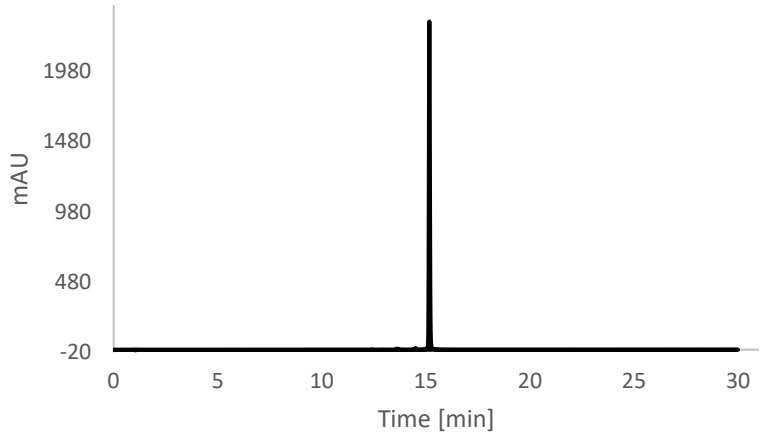

Figure 98: HPLC analysis of peptide **95** at 254 nm.

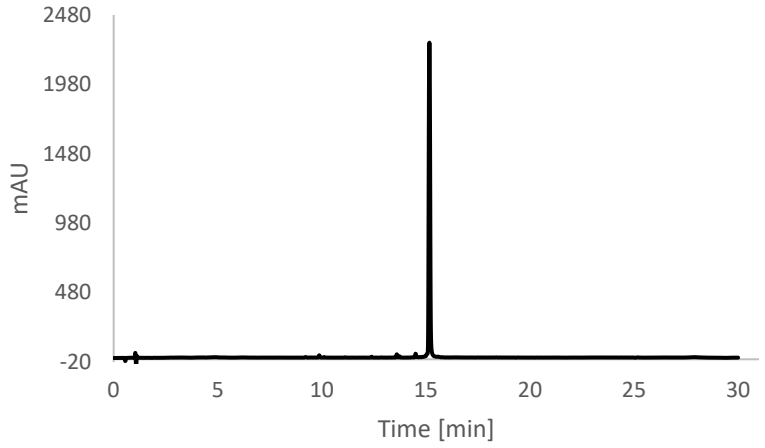

Figure 99: HPLC analysis of peptide **95** at 210 nm.

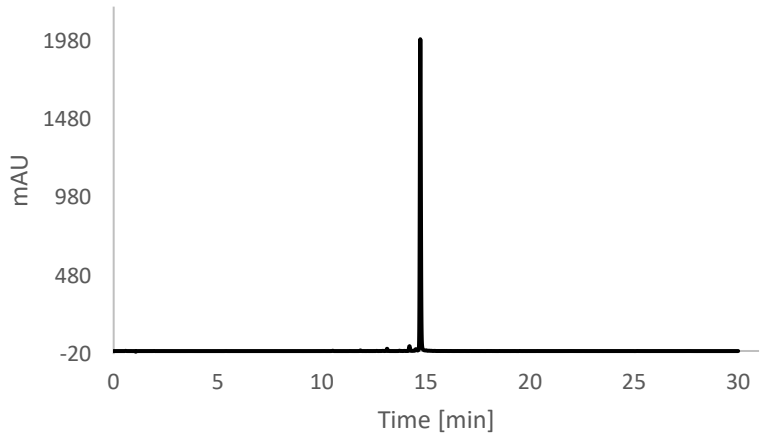

Figure 100: HPLC analysis of peptide **96** at 254 nm.

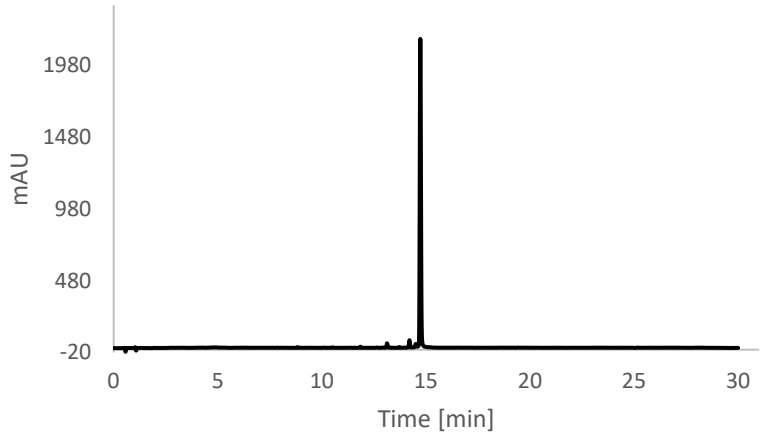

Figure 101: HPLC analysis of peptide **96** at 210 nm.

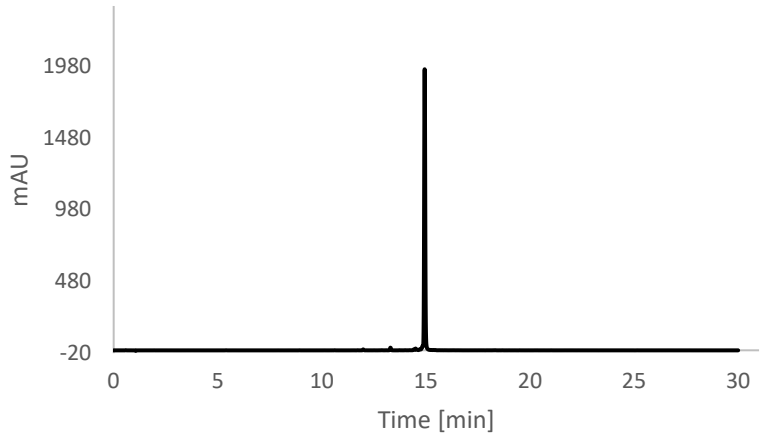

Figure 102: HPLC analysis of peptide **97** at 254 nm.

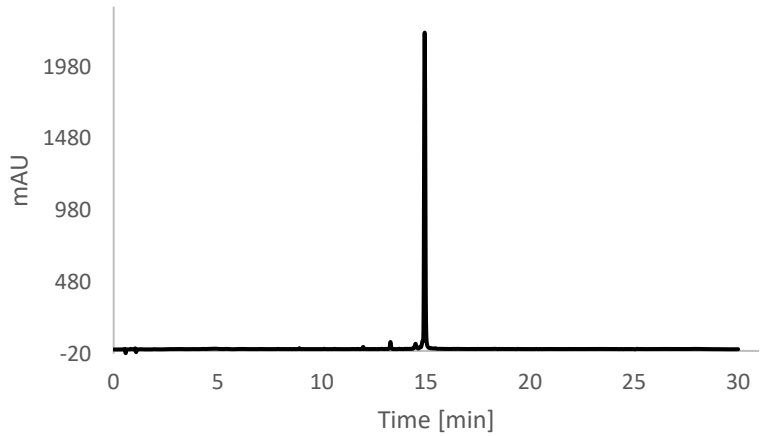

Figure 103: HPLC analysis of peptide **97** at 210 nm.

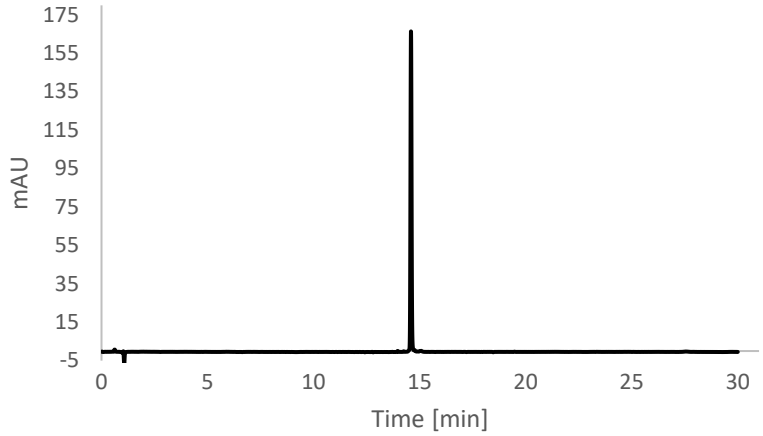

Figure 104: HPLC analysis of peptide **98** at 254 nm.

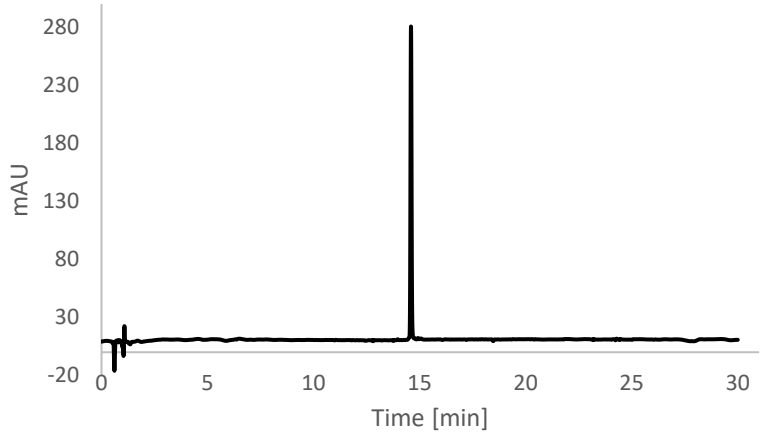

Figure 105: HPLC analysis of peptide **98** at 210 nm.

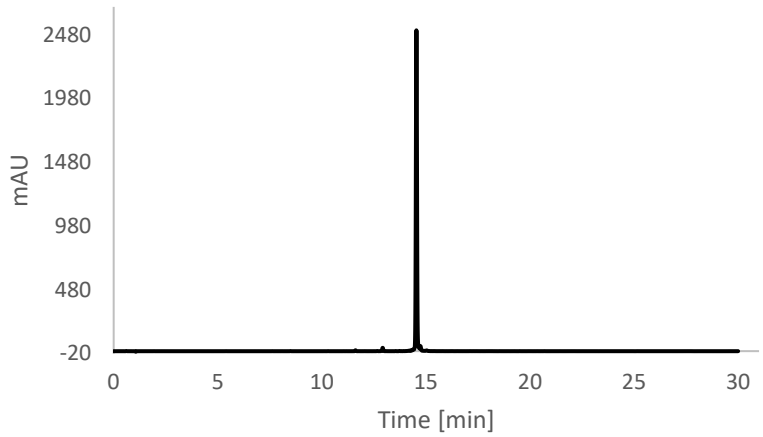

Figure 106: HPLC analysis of peptide **99** at 254 nm.

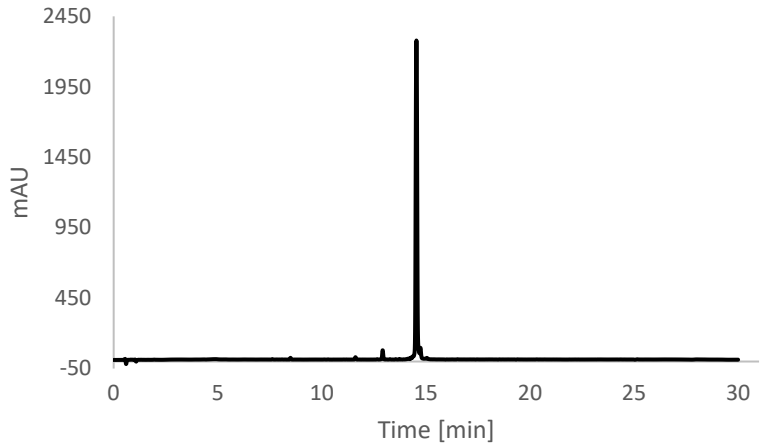

Figure 107: HPLC analysis of peptide **99** at 210 nm.

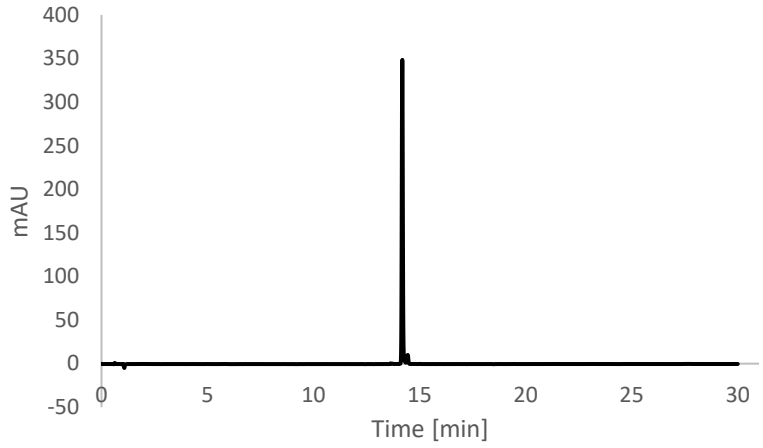

Figure 108: HPLC analysis of peptide **100** at 254 nm.

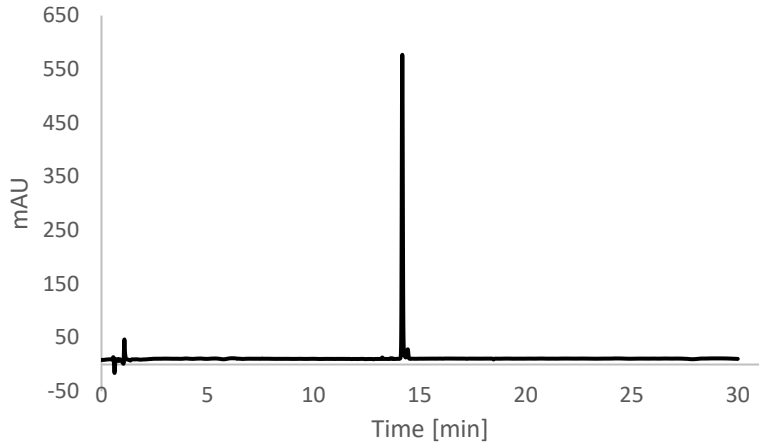

Figure 109: HPLC analysis of peptide **100** at 210 nm.

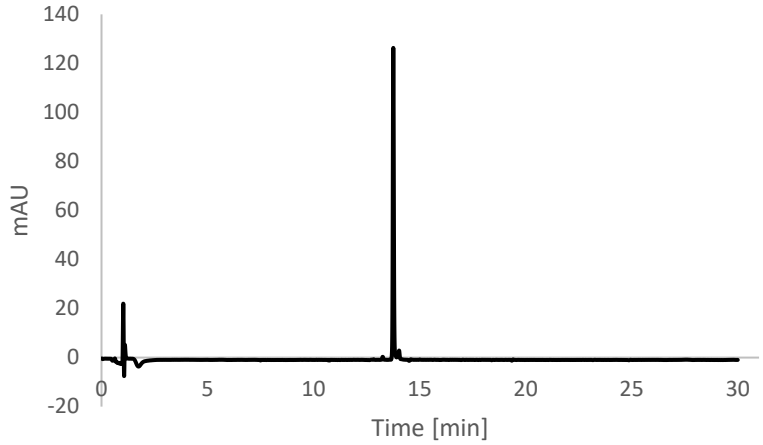

Figure 110: HPLC analysis of peptide **101** at 254 nm.

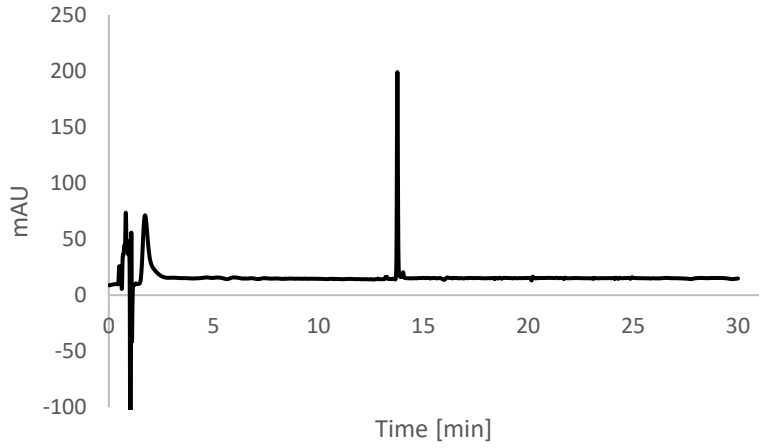

Figure 111: HPLC analysis of peptide **101** at 210 nm.

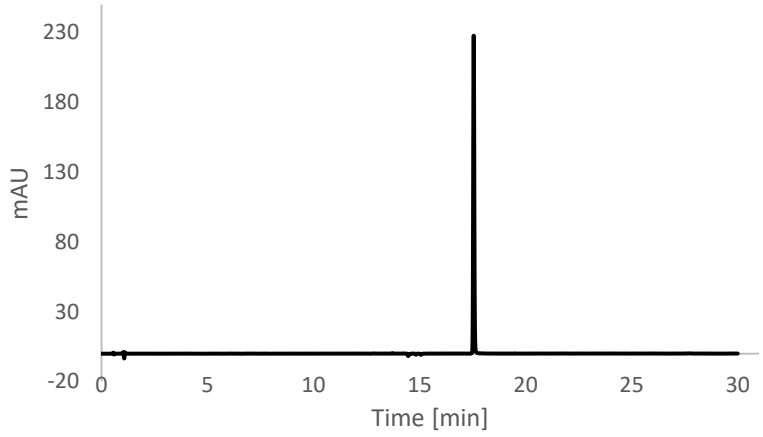

Figure 112: HPLC analysis of peptide **102** at 254 nm.

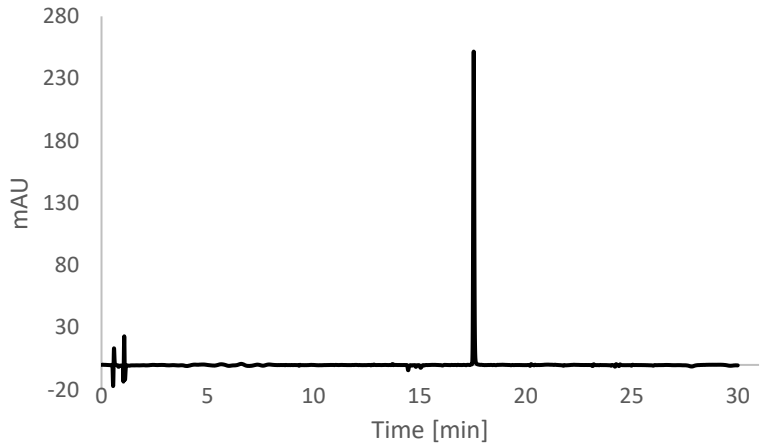

Figure 113: HPLC analysis of peptide **102** at 210 nm.

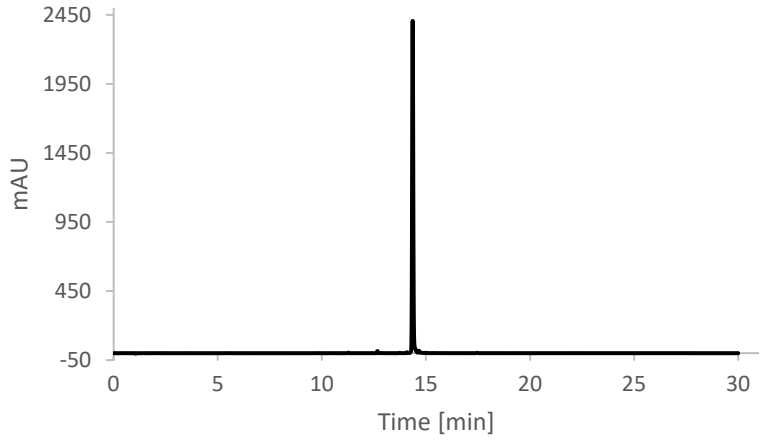

Figure 114: HPLC analysis of peptide **103** at 254 nm.

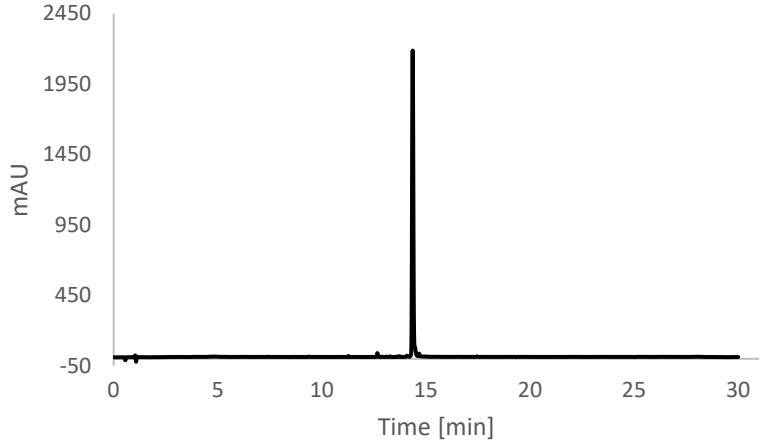

Figure 115: HPLC analysis of peptide **103** at 210 nm.

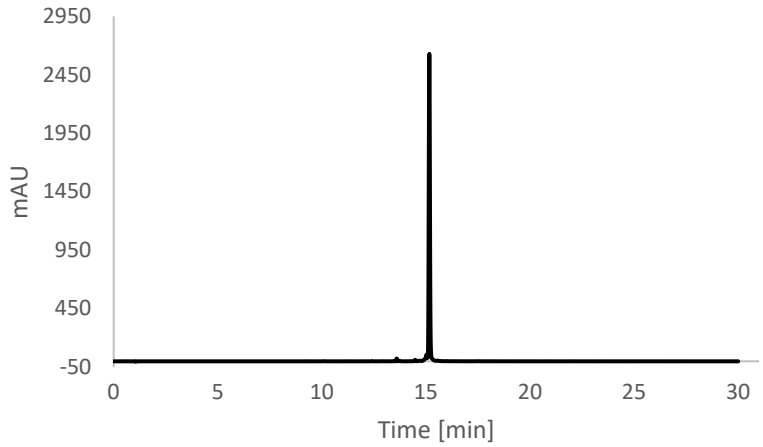

Figure 116: HPLC analysis of peptide **104** at 254 nm.

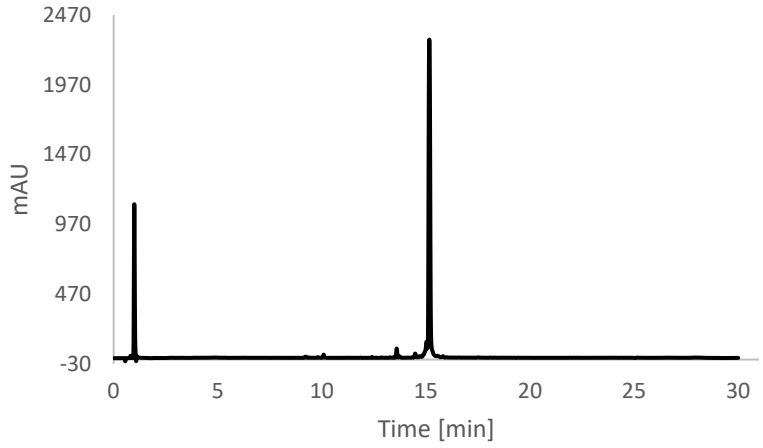

Figure 117: HPLC analysis of peptide **104** at 210 nm.

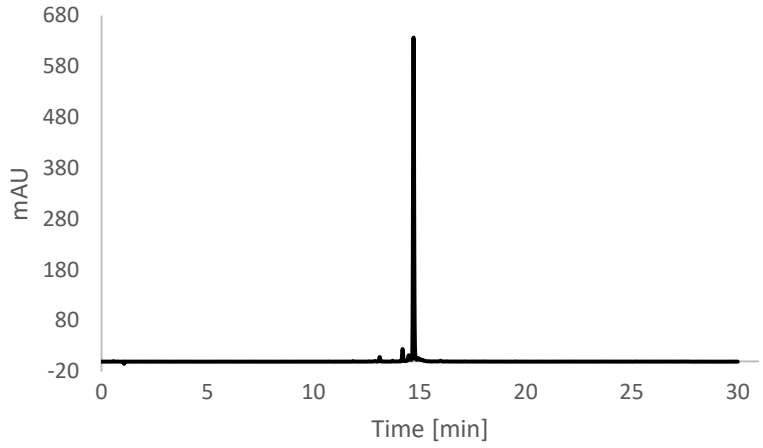

Figure 118: HPLC analysis of peptide **105** at 254 nm.

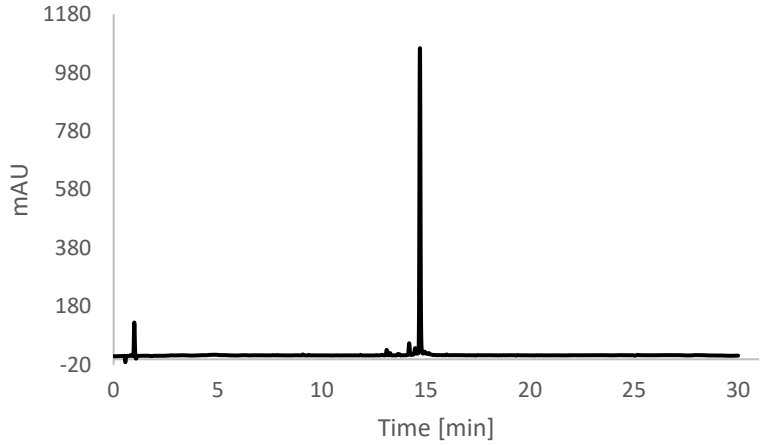

Figure 119: HPLC analysis of peptide **105** at 210 nm.

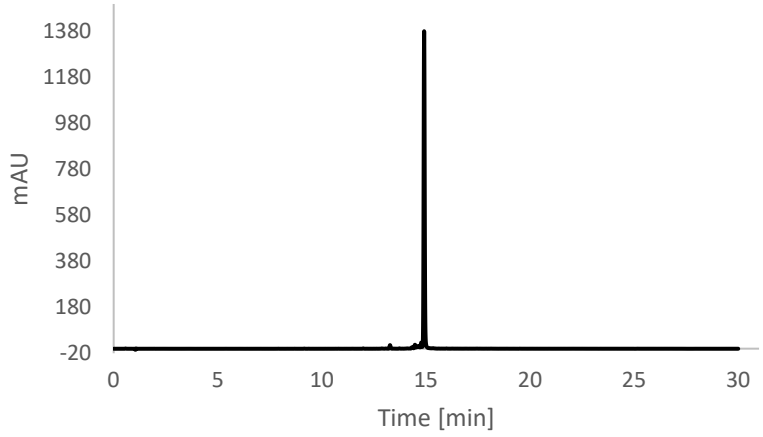

Figure 120: HPLC analysis of peptide **106** at 254 nm.

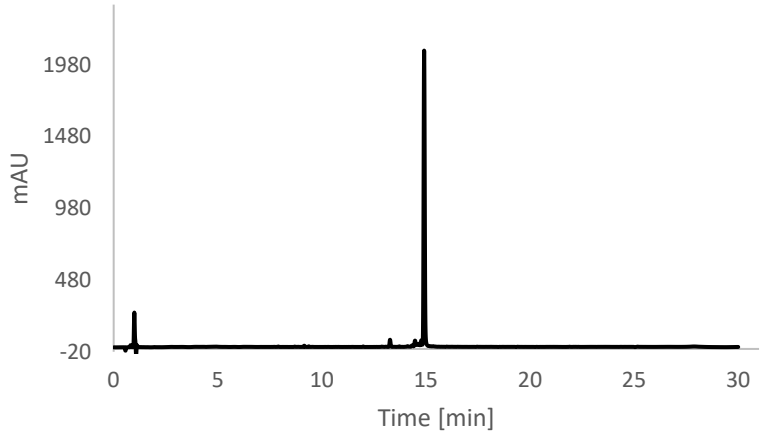

Figure 121: HPLC analysis of peptide **106** at 210 nm.

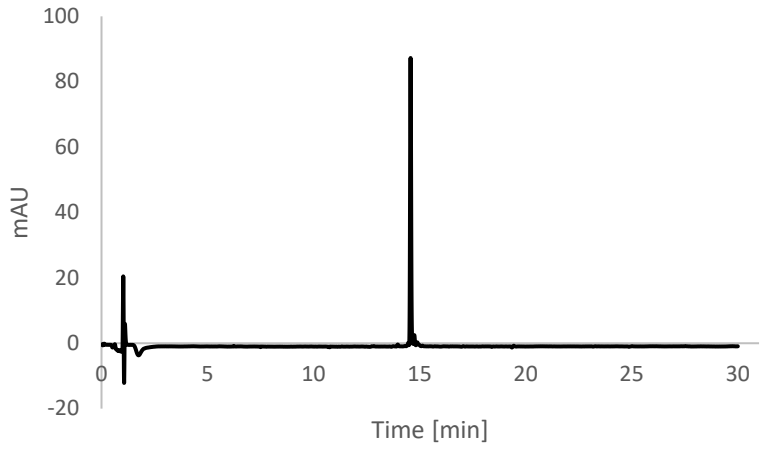

Figure 122: HPLC analysis of peptide **107** at 254 nm.

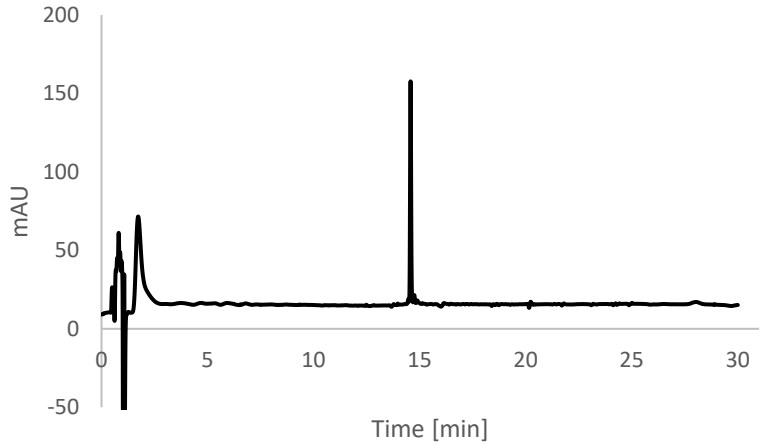

Figure 123: HPLC analysis of peptide **107** at 210 nm.

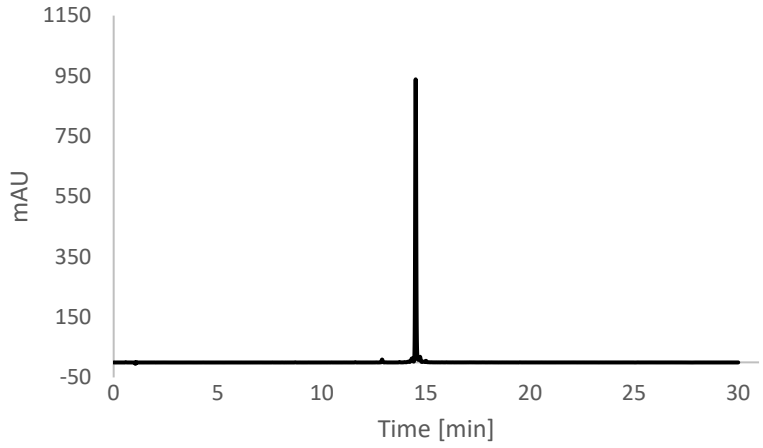

Figure 124: HPLC analysis of peptide **108** at 254 nm.

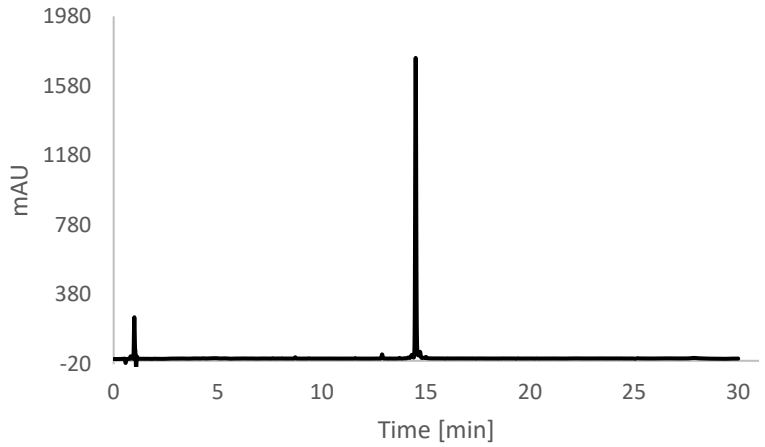

Figure 125: HPLC analysis of peptide **108** at 210 nm.

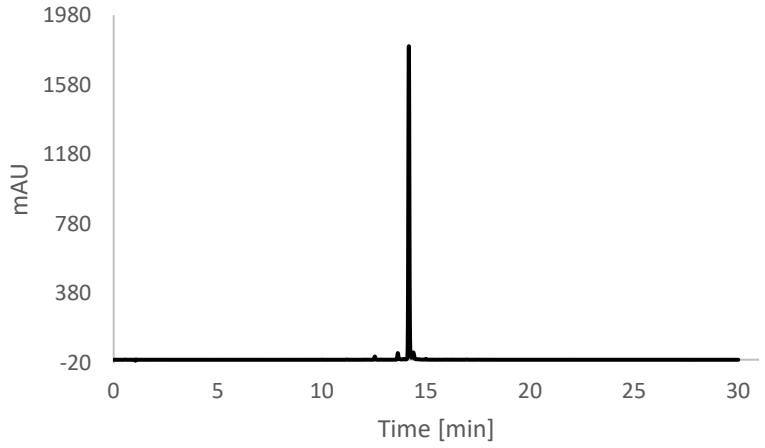

Figure 126: HPLC analysis of peptide **109** at 254 nm.

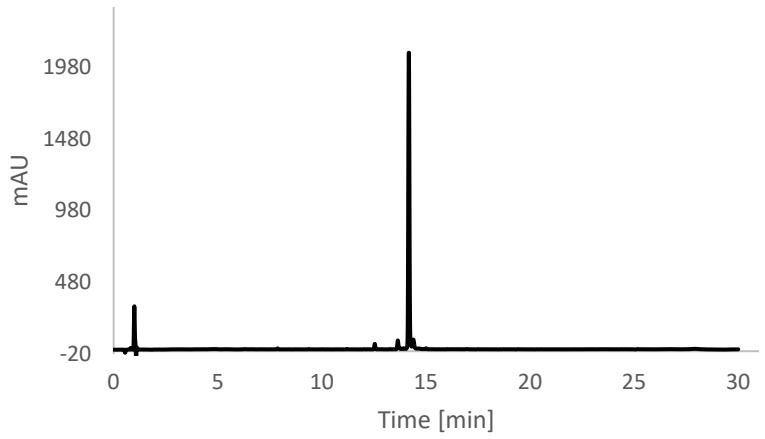

Figure 127: HPLC analysis of peptide **109** at 210 nm.

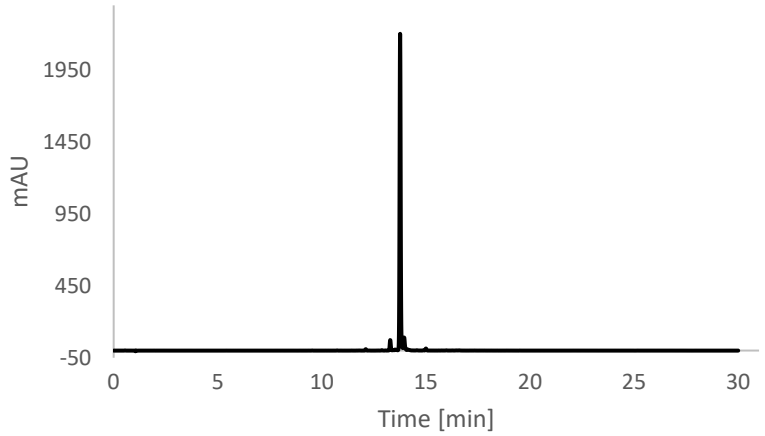

Figure 128: HPLC analysis of peptide **110** at 254 nm.

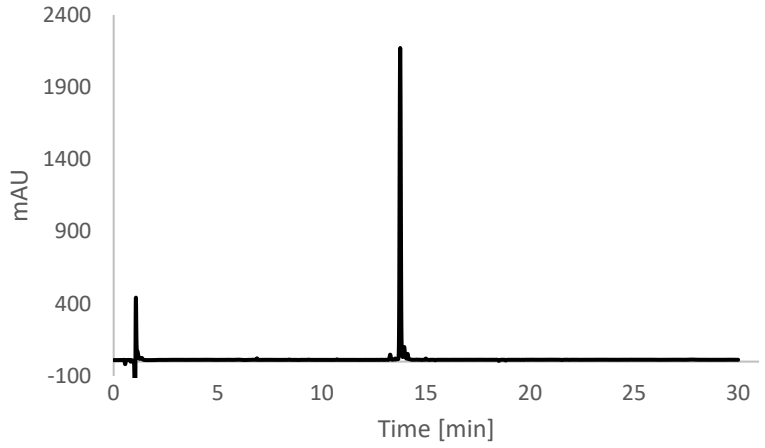

Figure 129: HPLC analysis of peptide **110** at 210 nm.

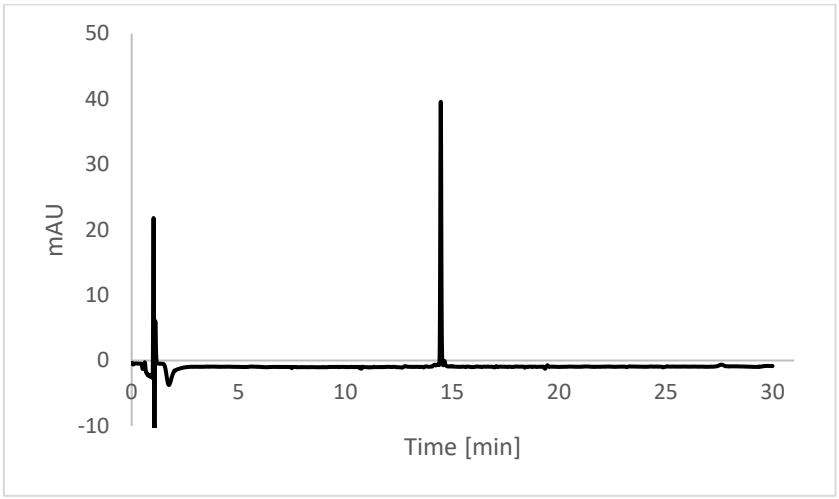

Figure 130: HPLC analysis of peptide **111** at 254 nm.

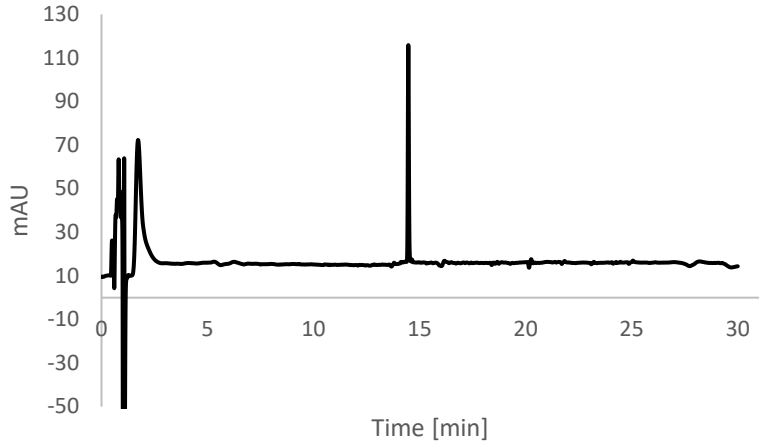

Figure 131: HPLC analysis of peptide **111** at 210 nm.

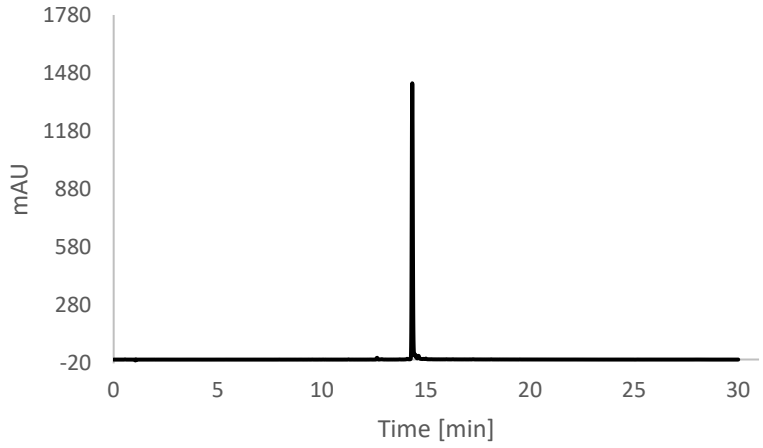

Figure 132: HPLC analysis of peptide **112** at 254 nm.

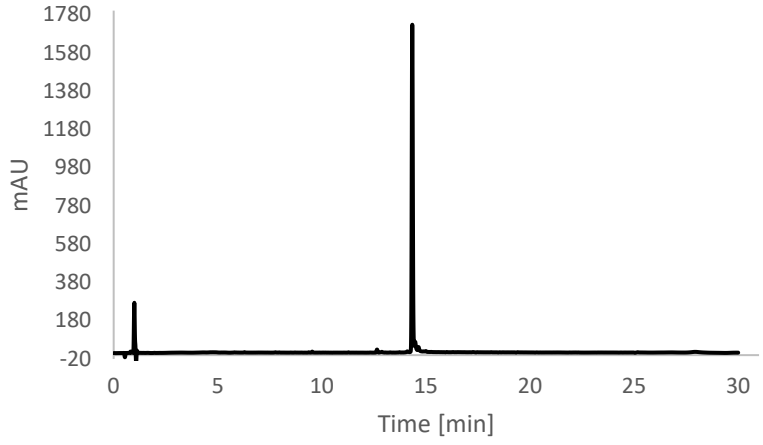

Figure 133: HPLC analysis of peptide **112** at 210 nm.

5.5.3 Lysate Stability Graphs

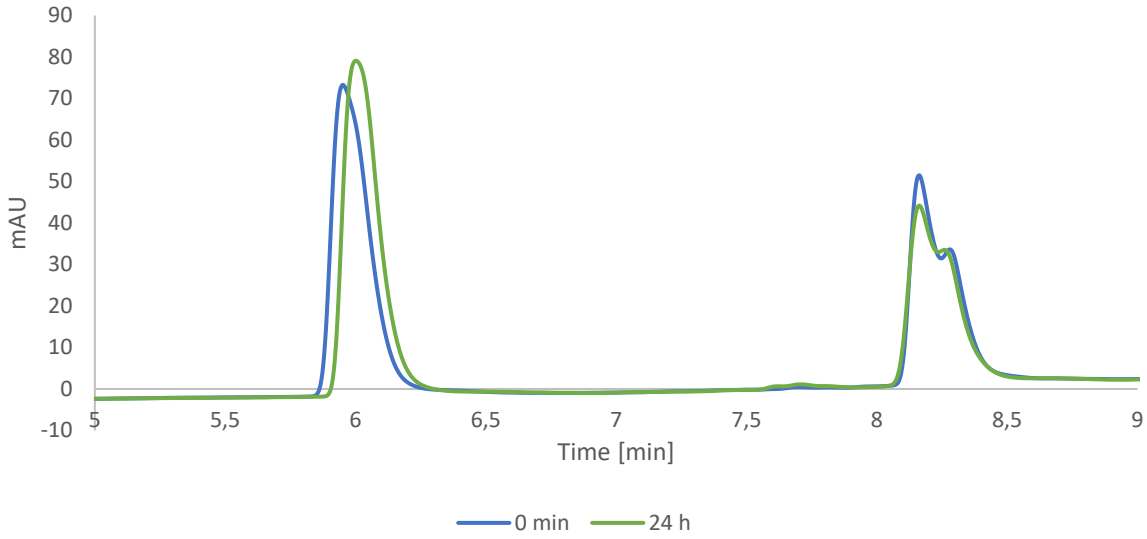

Figure 134: Lysate stability readout of **95**. Measurements were done at t = 0 h (blue) and t = 24 h (green) to evaluate the effect of HELA lysate on the bifunctional probe measured at 254 nm.

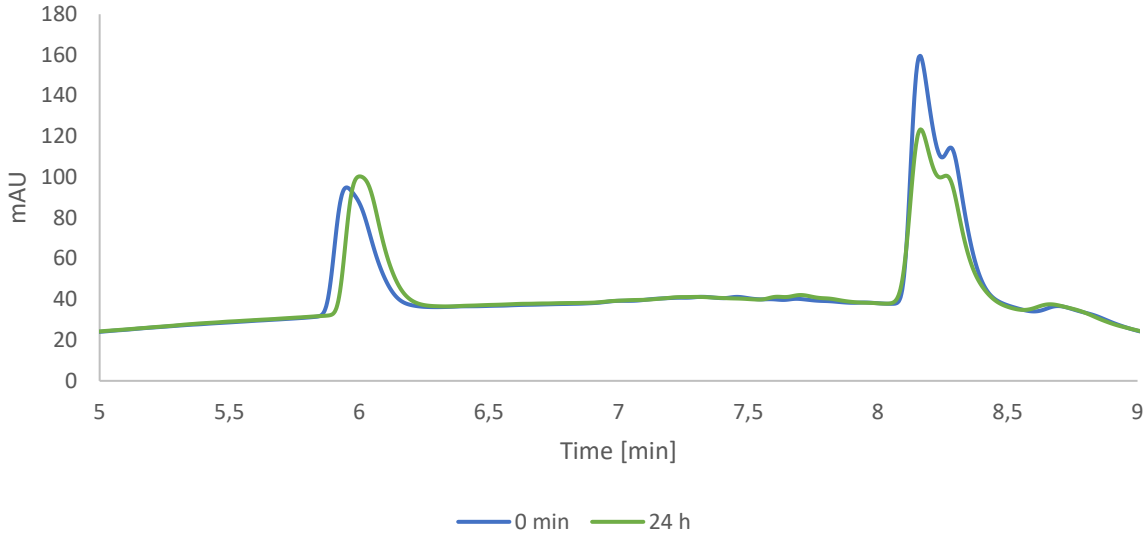

Figure 135: Lysate stability readout of **95**. Measurements were done at t = 0 h (blue) and t = 24 h (green) to evaluate the effect of HELA lysate on the bifunctional probe measured at 210 nm.

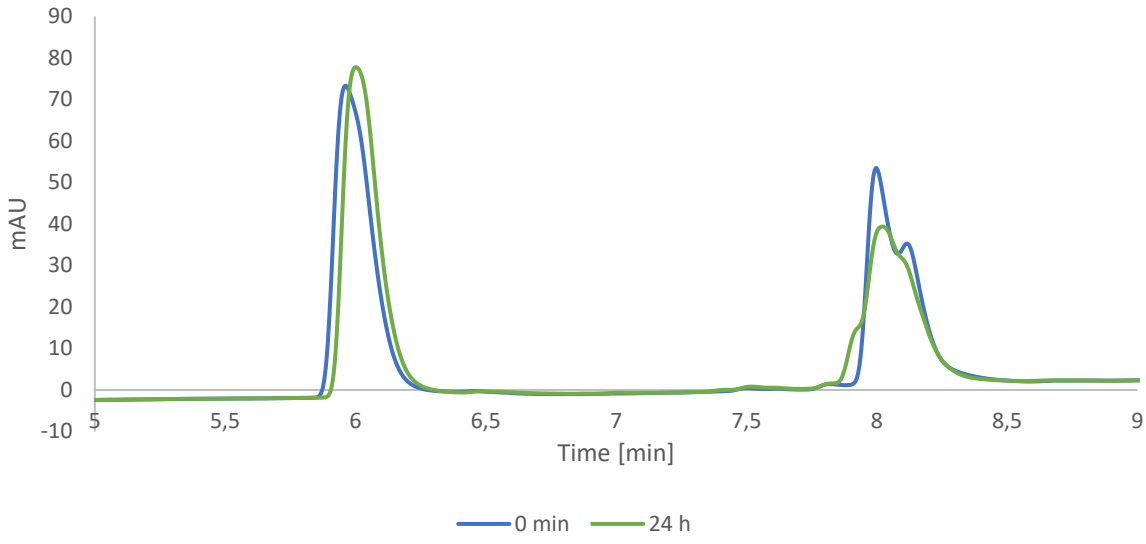

Figure 136: Lysate stability readout of **96**. Measurements were done at t = 0 h (blue) and t = 24 h (green) to evaluate the effect of HELA lysate on the bifunctional probe measured at 254 nm.

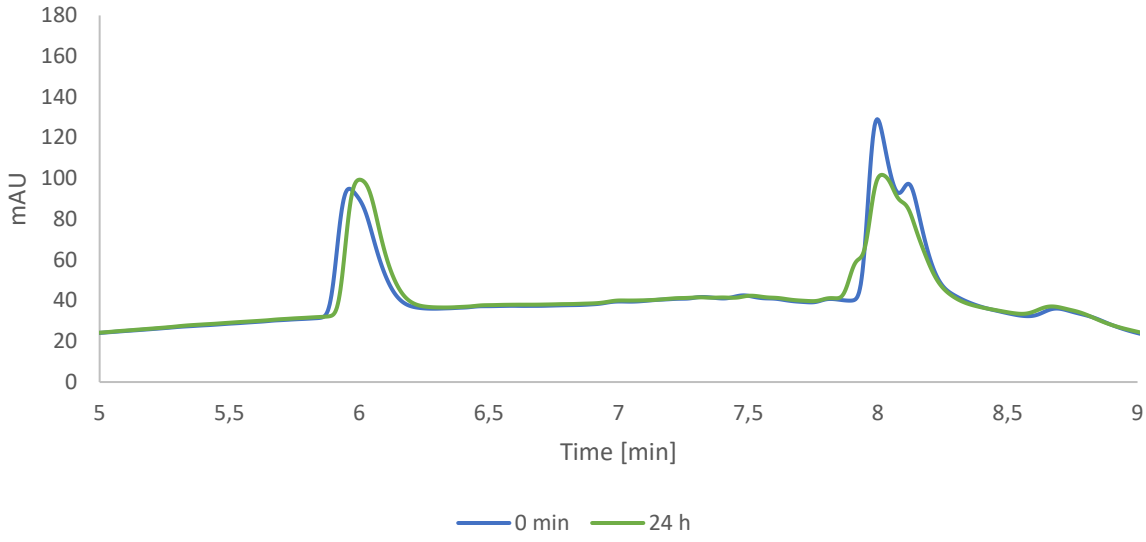

Figure 137: Lysate stability readout of **96**. Measurements were done at t = 0 h (blue) and t = 24 h (green) to evaluate the effect of HELA lysate on the bifunctional probe measured at 210 nm.

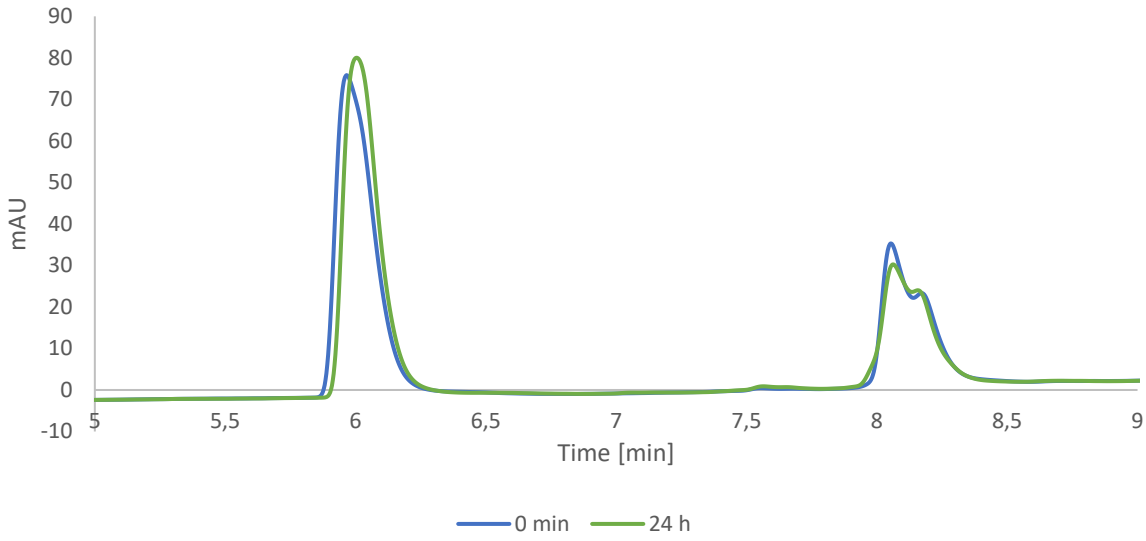

Figure 138: Lysate stability readout of **97**. Measurements were done at t = 0 h (blue) and t = 24 h (green) to evaluate the effect of HELA lysate on the bifunctional probe measured at 254 nm.

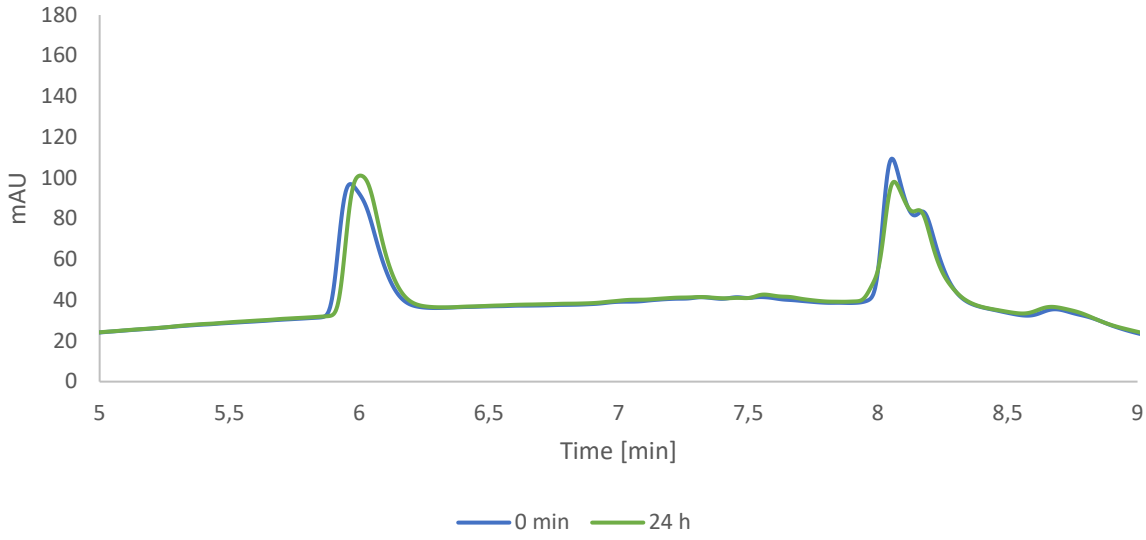

Figure 139: Lysate stability readout of **97**. Measurements were done at t = 0 h (blue) and t = 24 h (green) to evaluate the effect of HELA lysate on the bifunctional probe measured at 210 nm.

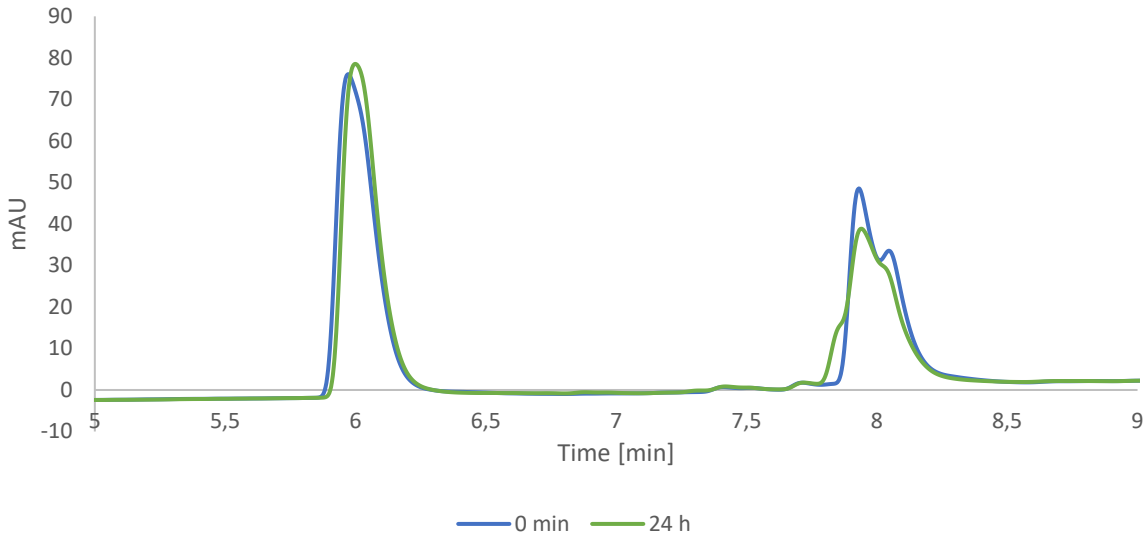

Figure 140: Lysate stability readout of **98**. Measurements were done at t = 0 h (blue) and t = 24 h (green) to evaluate the effect of HELA lysate on the bifunctional probe measured at 254 nm.

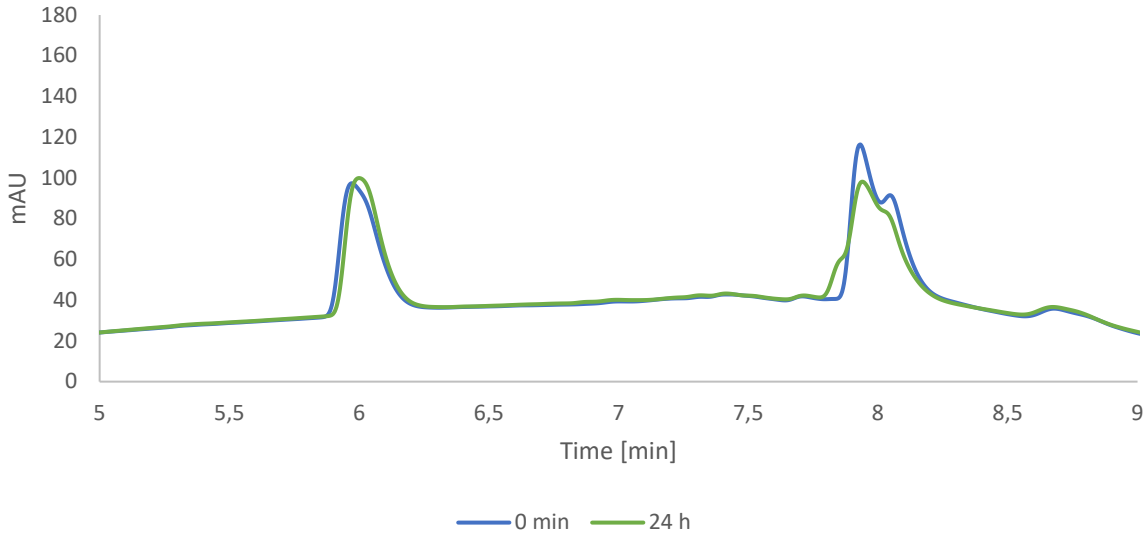

Figure 141: Lysate stability readout of **98**. Measurements were done at t = 0 h (blue) and t = 24 h (green) to evaluate the effect of HELA lysate on the bifunctional probe measured at 210 nm.

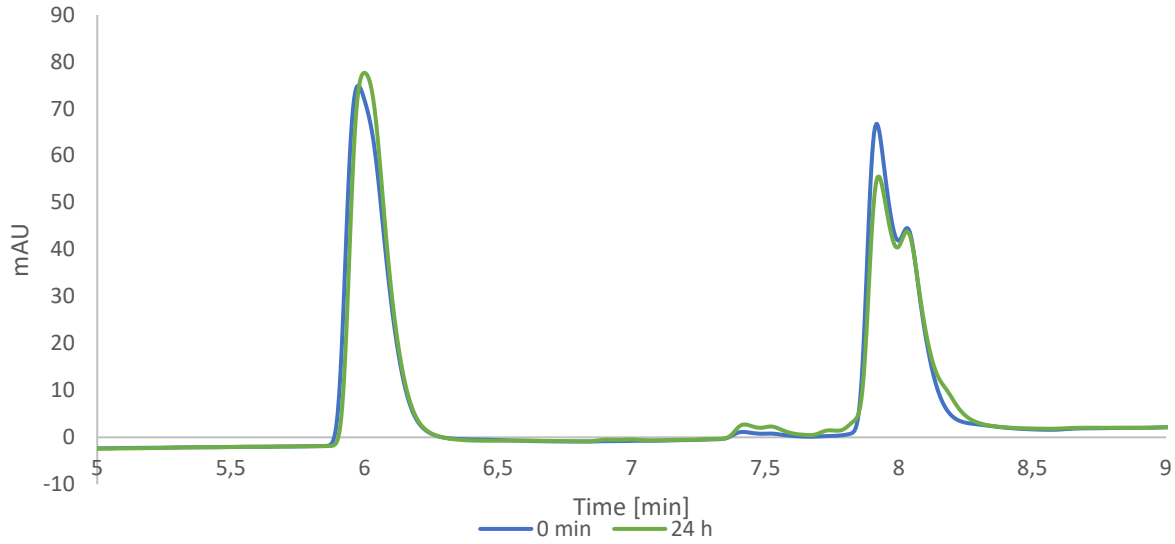

Figure 142: Lysate stability readout of **99**. Measurements were done at t = 0 h (blue) and t = 24 h (green) to evaluate the effect of HELA lysate on the bifunctional probe measured at 254 nm.

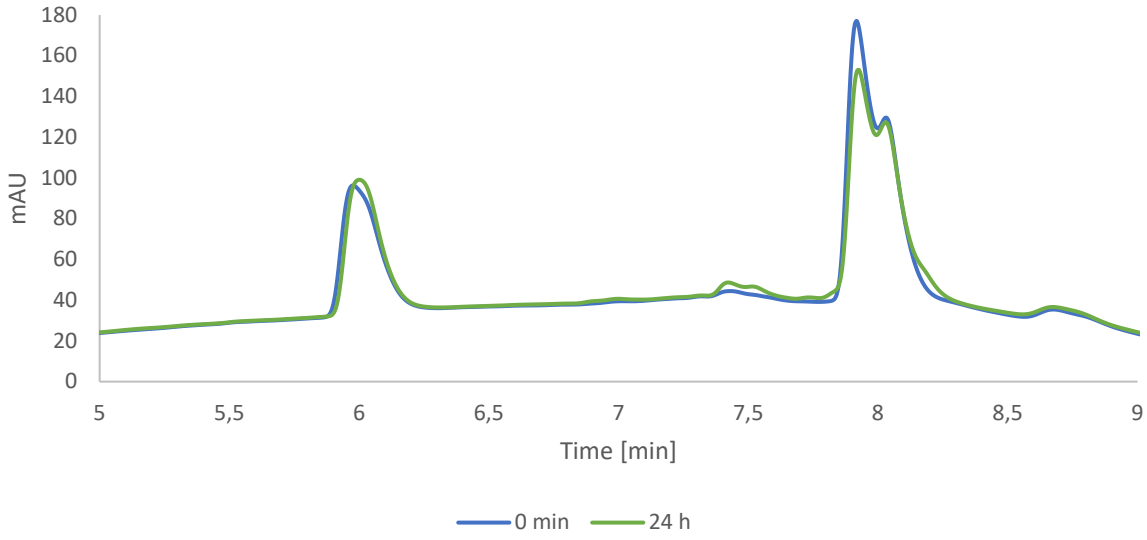

Figure 143: Lysate stability readout of **99**. Measurements were done at t = 0 h (blue) and t = 24 h (green) to evaluate the effect of HELA lysate on the bifunctional probe measured at 210 nm.

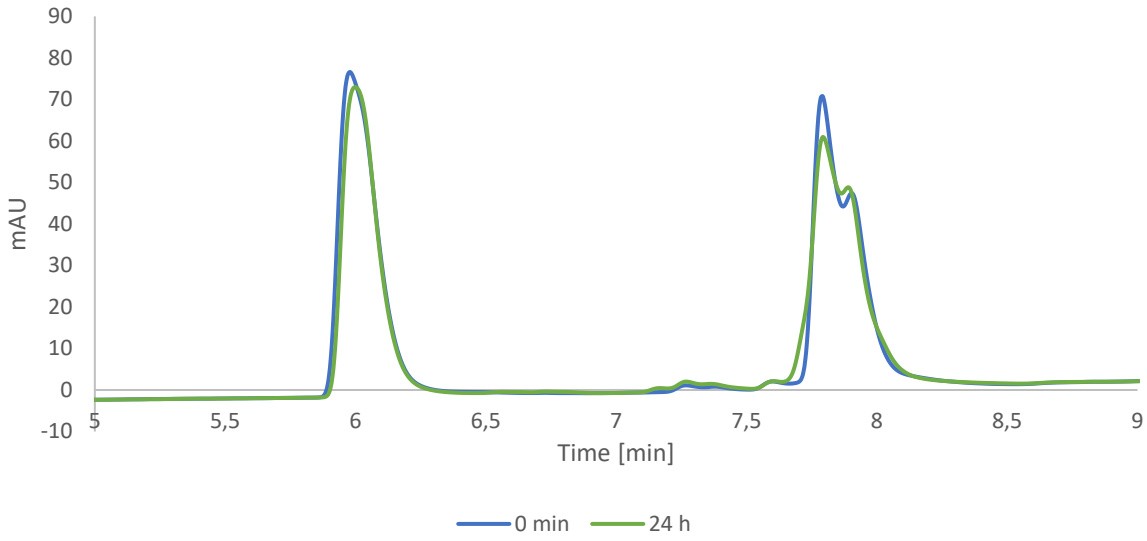

Figure 144: Lysate stability readout of **100**. Measurements were done at t = 0 h (blue) and t = 24 h (green) to evaluate the effect of HELA lysate on the bifunctional probe measured at 254 nm.

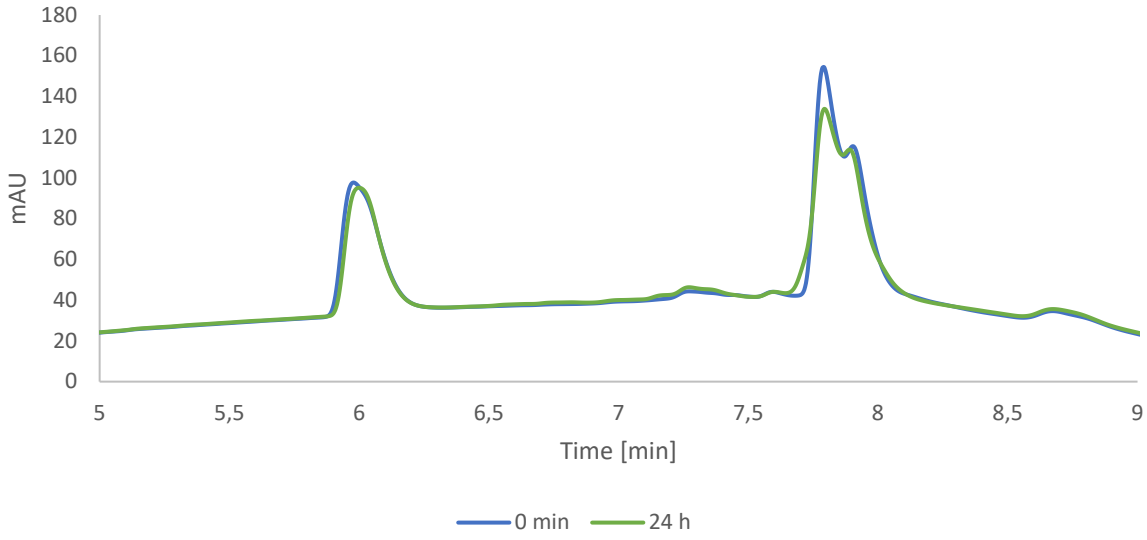

Figure 145: Lysate stability readout of **100**. Measurements were done at t = 0 h (blue) and t = 24 h (green) to evaluate the effect of HELA lysate on the bifunctional probe measured at 210 nm.

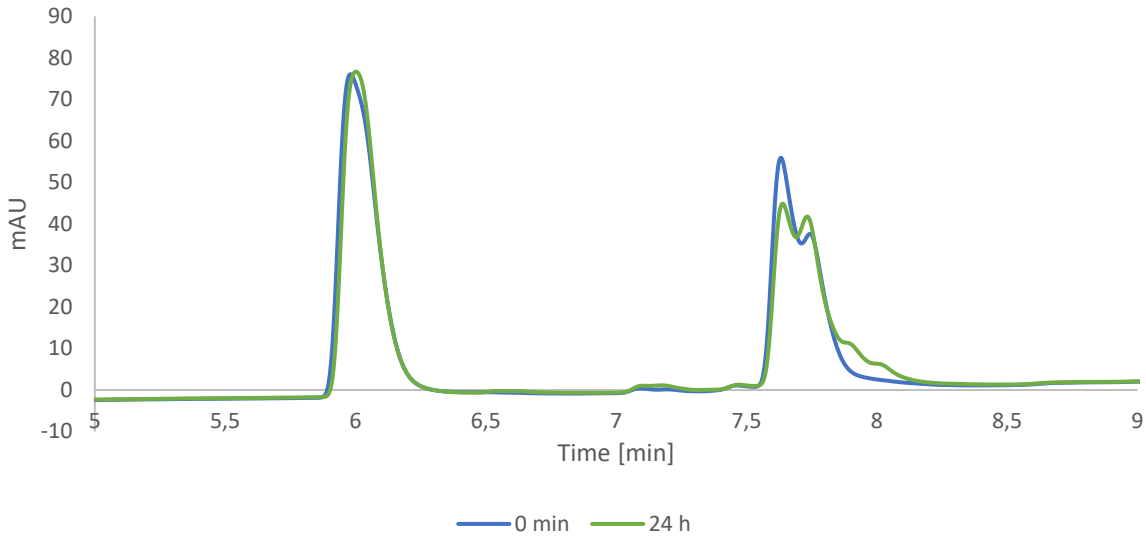

Figure 146: Lysate stability readout of **101**. Measurements were done at t = 0 h (blue) and t = 24 h (green) to evaluate the effect of HELA lysate on the bifunctional probe measured at 254 nm.

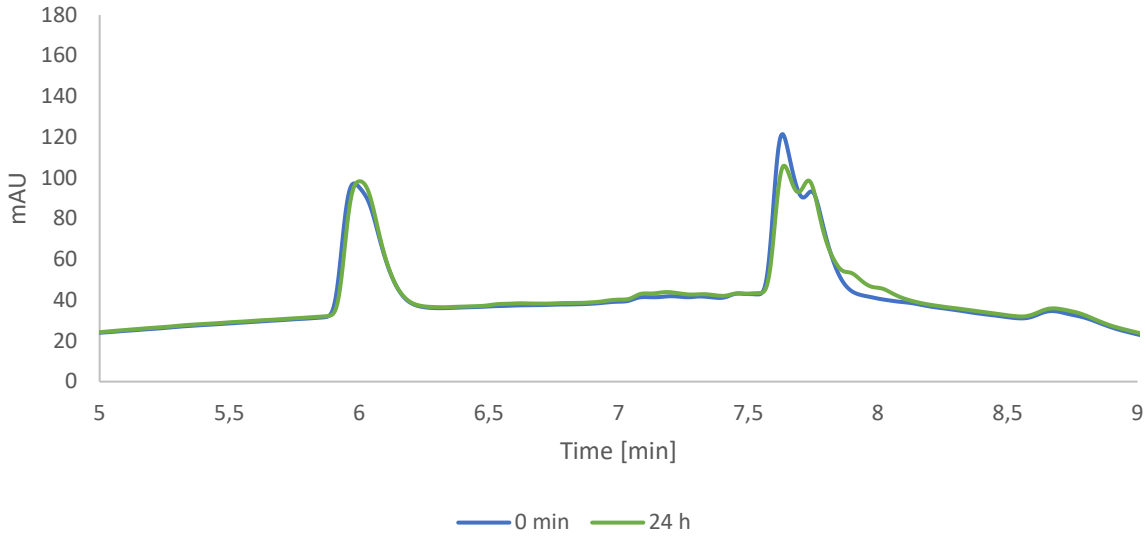

Figure 147: Lysate stability readout of **101**. Measurements were done at t = 0 h (blue) and t = 24 h (green) to evaluate the effect of HELA lysate on the bifunctional probe measured at 210 nm.

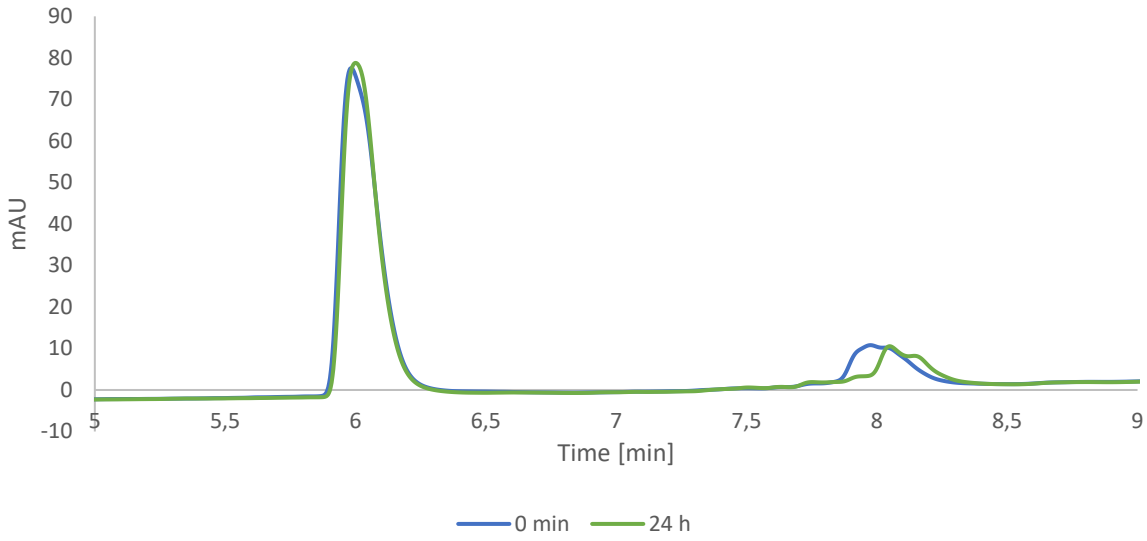

Figure 148: Lysate stability readout of **102**. Measurements were done at t = 0 h (blue) and t = 24 h (green) to evaluate the effect of HELA lysate on the bifunctional probe measured at 254 nm.

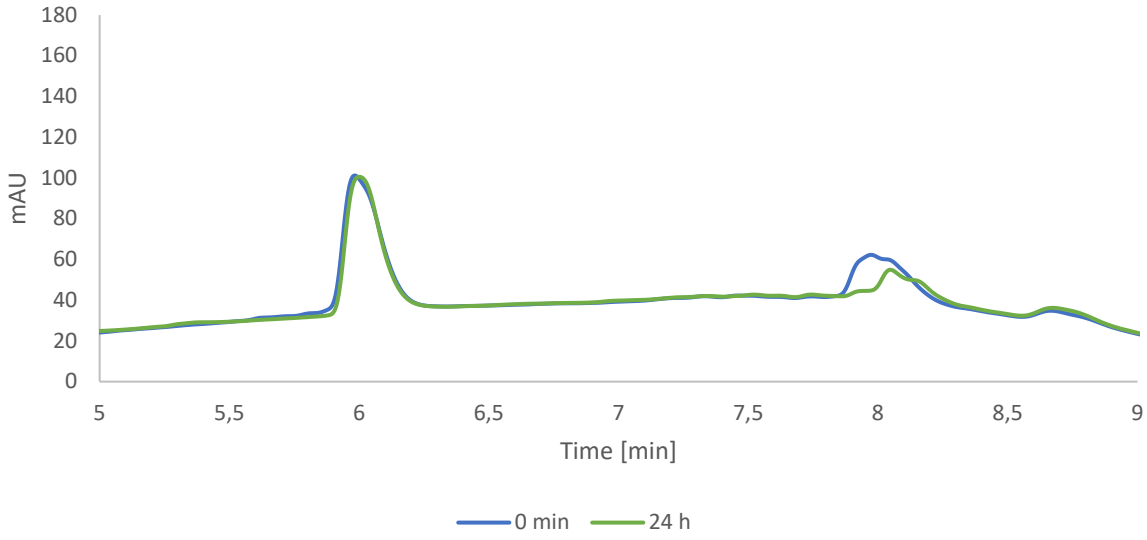

Figure 149: Lysate stability readout of **102**. Measurements were done at t = 0 h (blue) and t = 24 h (green) to evaluate the effect of HELA lysate on the bifunctional probe measured at 210 nm.

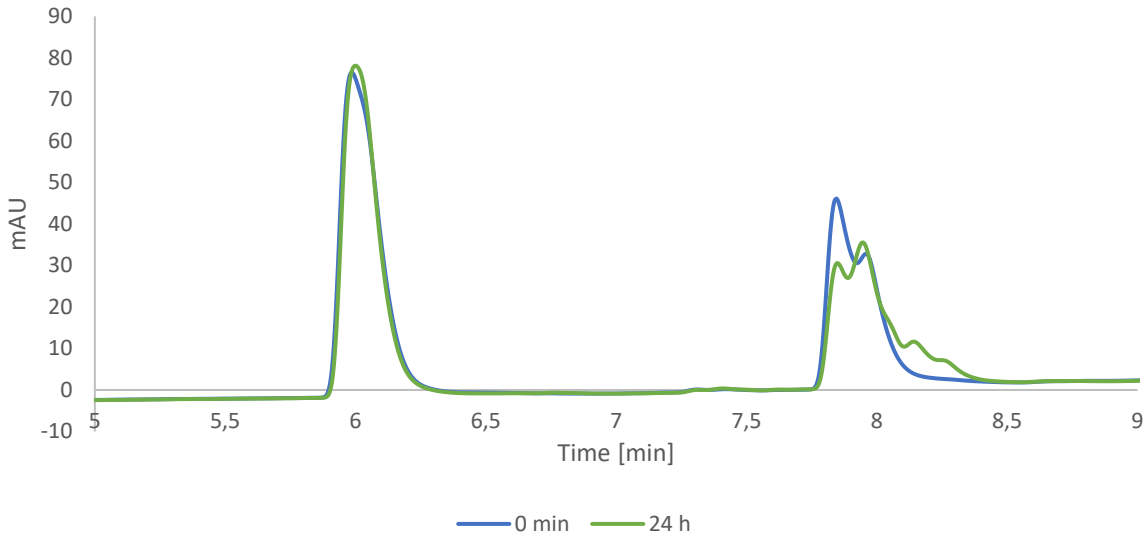

Figure 150: Lysate stability readout of **103**. Measurements were done at t = 0 h (blue) and t = 24 h (green) to evaluate the effect of HELA lysate on the bifunctional probe measured at 254 nm.

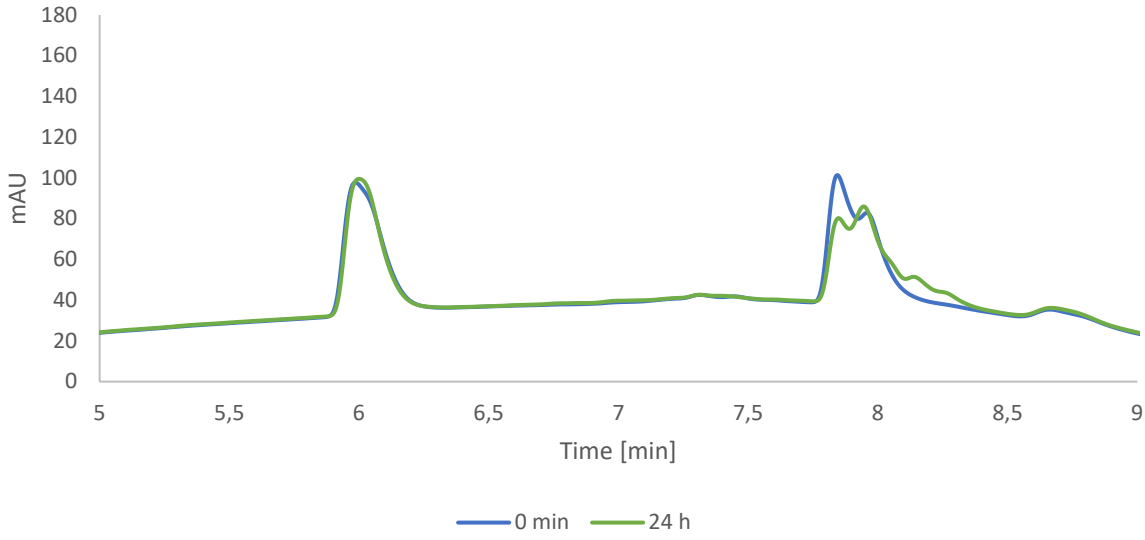

Figure 151: Lysate stability readout of **103**. Measurements were done at t = 0 h (blue) and t = 24 h (green) to evaluate the effect of HELA lysate on the bifunctional probe measured at 210 nm.

6. Literature

[1] A. M. Khalil, J. L. Rinn, *Semin Cell Dev Biol* **2011**, *22*, 359–365.

[2] F. Crick, *Nature* **1970**, *227*, 561–563.

[3] X. Lin, M.-L. Luo, E. Song, *Cell Insight* **2022**, *1*, 100004.

[4] T. Glisovic, J. L. Bachorik, J. Yong, G. Dreyfuss, *FEBS Lett* **2008**, *582*, 1977–1986.

[5] Y. Neelamraju, S. Hashemikhabir, S. C. Janga, *J Proteomics* **2015**, *127*, 61–70.

[6] W. G. Byun, D. Lim, S. B. Park, *Curr Opin Chem Biol* **2022**, *68*, 1–14.

[7] X. Ding, X. Jia, C. Wang, J. Xu, S. J. Gao, C. Lu, *Cell Death Differ* **2019**, *26*, 1750–1765.

[8] H. F. Noller, *Annu Rev Biochem* **1984**, *53*, 119–162.

[9] A. G. Matera, Z. Wang, *Nat Rev Mol Cell Biol* **2014**, *15*, 108–121.

[10] S. M. Elbashir, J. Harborth, W. Lendeckel, A. Yalcin, K. Weber, T. Tuschl, *Nature* **2001**, *411*, 494–498.

[11] H. Dong, J. Lei, L. Ding, Y. Wen, H. Ju, X. Zhang, *Chem Rev* **2013**, *113*, 6207–6233.

[12] C. L. Holley, V. K. Topkara, *Cardiovasc Drugs Ther* **2011**, *25*, 151–159.

[13] J. M. Engreitz, N. Ollikainen, M. Guttman, *Nat Rev Mol Cell Biol* **2016**, *17*, 756–770.

[14] T. Derrien, R. Johnson, G. Bussotti, A. Tanzer, S. Djebali, H. Tilgner, G. Guernec, D. Martin, A. Merkel, D. G. Knowles, J. Lagarde, L. Veeravalli, X. Ruan, Y. Ruan, T. Lassmann, P. Carninci, J. B. Brown, L. Lipovich, J. M. Gonzalez, M. Thomas, C. A. Davis, R. Shiekhattar, T. R. Gingeras, T. J. Hubbard, C. Notredame, J. Harrow, R. Guigó, *Genome Res* **2012**, *22*, 1775–1789.

[15] G. J. Goodall, V. O. Wickramasinghe, *Nat Rev Cancer* **2021**, *21*, 22–36.

[16] A. Zhang, J. C. Zhao, J. Kim, K. wing Fong, Y. A. Yang, D. Chakravarti, Y. Y. Mo, J. Yu, *Cell Rep* **2015**, *13*, 209–221.

[17] S. N. Syed, B. Brüne, *Cancers (Basel)* **2020**, 1–18.

[18] D. P. Bartel, *Cell* **2004**, *11695*, 281–297.

[19] Y. Lee, C. Ahn, J. Han, H. Choi, J. Kim, J. Yim, J. Lee, P. Provost, S. Kim, V. N. Kim, *Nature* **2003**, *425*, 415–419.

[20] V. N. Kim, *Nat Rev Mol Cell Biol* **2005**, *6*, 376–385.

[21] R. Yi, Y. Qin, I. G. Macara, B. R. Cullen, *Genes Dev* **2003**, *17*, 3011–3016.

[22] D. P. Bartel, *Cell* **2009**, *136*, 215–233.

[23] R. Garzon, G. Marcucci, C. M. Croce, *Nat Rev Drug Discov* **2010**, *9*, 775–789.

[24] T. A. Cooper, L. Wan, G. Dreyfuss, *Cell* **2009**, *136*, 777–793.

[25] Y. Nam, C. Chen, R. I. Gregory, J. J. Chou, P. Sliz, *Cell* **2011**, *147*, 1080–1091.

[26] E. Piskounova, S. R. Viswanathan, M. Janas, R. J. LaPierre, G. Q. Daley, P. Sliz, R. I. Gregory, *Journal of Biological Chemistry* **2008**, *283*, 21310–21314.

[27] D. Ustianenko, H. S. Chiu, T. Treiber, S. M. Weyn-Vanhentenryck, N. Treiber, G. Meister, P. Sumazin, C. Zhang, *Mol Cell* **2018**, *71*, 271–283.

[28] S. Roush, F. J. Slack, *Trends Cell Biol* **2008**, *18*, 505–516.

[29] S. J. Kim, P. K. Gregersen, B. Diamond, *J Clin Invest* **2013**, *123*, 823–833.

[30] Y. B. Wei, J. J. Liu, J. C. Villaescusa, E. Åberg, S. Brené, G. Wegener, A. A. Mathé, C. Lavebratt, *Transl Psychiatry* **2016**, *6*, 1–8.

[31] A. Rybak, H. Fuchs, L. Smirnova, C. Brandt, E. E. Pohl, R. Nitsch, F. G. Wulczyn, *Nat Cell Biol* **2008**, *10*, 987–993.

[32] N. R. Genuth, M. Barna, *Mol Cell* **2018**, *71*, 364–374.

[33] B. M. Lunde, C. Moore, G. Varani, *Nat Rev Mol Cell Biol* **2007**, *8*, 479–490.

[34] B. M. Beckmann, A. Castello, J. Medenbach, *Pflugers Arch* **2016**, *468*, 1029–1040.

[35] Chris Oubridge, Nobutoshi Ito, Philip R. Evans, C.-Hiang Teo, Kiyoshi Nagai, *Nature* **1994**, *372*, 432–438.

[36] J. M. Ryter, S. C. Schultz, *EMBO Journal* **1998**, *17*, 7505–7513.

[37] W. E. Walden, A. I. Selezneva, J. Dupuy, A. Volbeda, J. C. Fontecilla-Camps, E. C. Theil, K. Volz, *Science* **2006**, *314*, 1903–1909.

[38] J. Jia, A. Arif, P. S. Ray, P. L. Fox, *Mol Cell* **2008**, *29*, 679–690.

[39] A. T. Phan, V. Kuryavyi, J. C. Darnell, A. Serganov, A. Majumdar, S. Ilin, T. Raslin, A. Polonskaia, C. Chen, D. Clain, R. B. Darnell, D. J. Patel, *Nat Struct Mol Biol* **2011**, *18*, 796–804.

[40] K. Ye, L. Malinina, D. J. Patel, *Nature* **2003**, *426*, 874–878.

[41] L. D. Finger, C. Johansson, B. Rinaldi, P. Bouvet, J. Feigon, *Biochemistry* **2004**, *43*, 6937–6947.

[42] W. E. Walden, A. Selezneva, K. Volz, *FEBS Lett* **2012**, *586*, 32–35.

[43] R. J. Jackson, C. U. T. Hellen, T. v. Pestova, *Nat Rev Mol Cell Biol* **2010**, *11*, 113–127.

[44] M. W. Hentze, A. Castello, T. Schwarzl, T. Preiss, *Nat Rev Mol Cell Biol* **2018**, *19*, 327–341.

[45] S. D. Auweter, F. C. Oberstrass, F. H. T. Allain, *Nucleic Acids Res* **2006**, *34*, 4943–4959.

[46] M. Corley, M. C. Burns, G. W. Yeo, *Mol Cell* **2020**, *78*, 9–29.

[47] S. Gerstberger, M. Hafner, T. Tuschl, *Nat Rev Genet* **2014**, *15*, 829–845.

[48] F. Mayr, A. Schütz, N. Döge, U. Heinemann, *Nucleic Acids Res* **2012**, *40*, 7492–7506.

[49] S. R. Viswanathan, G. Q. Daley, *Cell* **2010**, *140*, 445–449.

[50] J. Balzeau, M. R. Menezes, S. Cao, J. P. Hagan, *Front Genet* **2017**, *8*, 1–16.

[51] R. B. Jaffe, *Obstet Gynecol Surv* **2008**, *63*, 154–155.

[52] V. Ambros, H. R. Horvitz, *Science* **1984**, *226*, 409–416.

[53] S. R. Viswanathan, J. T. Powers, W. Einhorn, Y. Hoshida, T. L. Ng, S. Toffanin, M. O'Sullivan, J. Lu, L. A. Phillips, V. L. Lockhart, S. P. Shah, P. S. Tanwar, C. H. Mermel, R. Beroukhim, M. Azam, J. Teixeira, M. Meyerson, T. P. Hughes, J. M. Llovet, J. Radich, C. G. Mullighan, T. R. Golub, P. H. Sorensen, G. Q. Daley, *Nat Genet* **2009**, *41*, 843–848.

[54] D. Bumcrot, M. Manoharan, V. Koteliansky, D. W. Y. Sah, *Nat Chem Biol* **2006**, *2*, 711–719.

[55] P. M. Cromm, C. M. Crews, *Cell Chem Biol* **2017**, *24*, 1181–1190.

[56] T. Treiber, N. Treiber, U. Plessmann, S. Harlander, J. L. Daiß, N. Eichner, G. Lehmann, K. Schall, H. Urlaub, G. Meister, *Mol Cell* **2017**, *66*, 270-284.

[57] B. Diouf, W. Lin, A. Goktug, C. R. R. Grace, M. B. Waddell, J. Bao, Y. Shao, R. J. Heath, J. J. Zheng, A. A. Shelat, M. v. Relling, T. Chen, W. E. Evans, *SLAS Discovery* **2018**, *23*, 164–173.

[58] X. Wu, G. Gardashova, L. Lan, S. Han, C. Zhong, R. T. Marquez, L. Wei, S. Wood, S. Roy, R. Gowthaman, J. Karanicolas, F. P. Gao, D. A. Dixon, D. R. Welch, L. Li, M. Ji, J. Aubé, L. Xu, *Commun Biol* **2020**, *3*, 193, 1–16.

[59] G. Minuesa, S. K. Albanese, W. Xie, Y. Kazansky, D. Worroll, A. Chow, A. Schurer, S. M. Park, C. Z. Rotsides, J. Taggart, A. Rizzi, L. N. Naden, T. Chou, S. Gourkanti, D. Cappel, M. C. Passarelli, L. Fairchild, C. Adura, J. F. Glickman, J. Schulman, C. Famulare, M. Patel, J. K. Eibl, G. M. Ross, S. Bhattacharya, D. S. Tan, C. S. Leslie, T. Beuming, D. J. Patel, Y. Goldgur, J. D. Chodera, M. G. Kharas, *Nat Commun* **2019**, *10*, 2691, 1–15.

[60] M. E. Bordeleau, A. Mori, M. Oberer, L. Lindqvist, L. S. Chard, T. Higa, G. J. Belsham, G. Wagner, J. Tanaka, J. Pelletier, *Nat Chem Biol* **2006**, *2*, 213–220.

[61] R. Pedram Fatemi, S. Salah-Uddin, F. Modarresi, N. Khoury, C. Wahlestedt, M. A. Faghihi, *J Biomol Screen* **2015**, *20*, 1132–1141.

[62] N. A. Naryshkin, M. Weetall, A. Dakka, J. Narasimhan, X. Zhao, Z. Feng, K. K. Y. Ling, G. M. Karp, H. Qi, M. G. Woll, G. Chen, N. Zhang, V. Gabbeta, P. Vazirani, A. Bhattacharyya, B. Furia, N. Risher, J. Sheedy, R. Kong, J. Ma, A. Turpoff, C.-S. Lee, X. Zhang, Y.-C. Moon, P. Trifillis, E. M. Welch, J. M. Colacino, J. Babiak, N. G. Almstead, S. W. Peltz, L. A. Eng, K. S. Chen, J. L. Mull, M. S. Lynes, L. L. Rubin, P. Fontoura, L. Santarelli, D. Haehnke, K. D. Mccarthy, R. Schmucki, M. Ebeling, M. Sivaramakrishnan, C.-P. Ko, S. v Paushkin, H. Ratni, I. Gerlach, A. Ghosh, F. Metzger, *Science* **2014**, *345*, 688–693.

[63] S. Kiran Naineni, R. Itoua Maïga, R. Cencic, A. A. Putnam, L. A. Amador, A. D. Rodriguez, E. Jankowsky, J. Pelletier, *RNA* **2020**, *26*, 541–549.

[64] M. Toure, C. M. Crews, *Angew Chem -Int Edit* **2016**, *55*, 1966–1973.

[65] A. Ghidini, A. Cléry, F. Halloy, F. H. T. Allain, J. Hall, *Angew Chem -Int Edit* **2021**, *60*, 3163–3169.

[66] D. A. Lorenz, T. Kaur, S. A. Kerk, E. E. Gallagher, J. Sandoval, A. L. Garner, *ACS Med Chem Lett* **2018**, *9*, 517–521.

[67] W. G. Byun, D. Lim, S. B. Park, *ChemBioChem* **2020**, *21*, 818–824.

[68] L. Borgelt, F. Li, P. Hommen, P. Lampe, J. Hwang, G. L. Goebel, S. Sievers, P. Wu, *ACS Med Chem Lett* **2021**, *12*, 893–898.

[69] D. Lim, W. G. Byun, J. Y. Koo, H. Park, S. B. Park, *J Am Chem Soc* **2016**, *138*, 13630–13638.

[70] L. Wang, R. G. Rowe, A. Jaimes, C. Yu, Y. Nam, D. S. Pearson, J. Zhang, X. Xie, W. Marion, G. J. Heffron, G. Q. Daley, P. Sliz, *Cell Rep* **2018**, *23*, 3091–3101.

[71] K. Fosgerau, T. Hoffmann, *Drug Discov Today* **2015**, *20*, 122–128.

[72] A. Henninot, J. C. Collins, J. M. Nuss, *J Med Chem* **2018**, *61*, 1382–1414.

[73] S. M. Guéret, S. Thavam, R. J. Carbajo, M. Potowski, N. Larsson, G. Dahl, A. Dellsén, T. N. Grossmann, A. T. Plowright, E. Valeur, M. Lemurell, H. Waldmann, *J Am Chem Soc* **2020**, *142*, 4904–4915.

[74] C. Wang, W. Shi, L. Cai, L. Lu, Q. Wang, T. Zhang, J. Li, Z. Zhang, K. Wang, L. Xu, X. Jiang, S. Jiang, K. Liu, *J Med Chem* **2013**, *56*, 2527–2539.

[75] E. Valeur, S. M. Guéret, H. Adihou, R. Gopalakrishnan, M. Lemurell, H. Waldmann, T. N. Grossmann, A. T. Plowright, *Angew Chem -Int Edit* **2017**, *56*, 10294–10323.

[76] Y. Tor, *ChemBioChem* **2003**, *4*, 998–1007.

[77] L. Wang, Y. Nam, A. K. Lee, C. Yu, K. Roth, C. Chen, E. M. Ransey, P. Sliz, *Cell Rep* **2017**, *18*, 2664–2675.

[78] M. W. Hentze, A. Castello, T. Schwarzl, T. Preiss, *Nat Rev Mol Cell Biol* **2018**, *19*, 327–341.

[79] C. J. Gerry, S. L. Schreiber, *Nat Chem Biol* **2020**, *16*, 369–378.

[80] Y. Neelamraju, S. Hashemikhabir, S. C. Janga, *J Proteomics* **2015**, *127*, 61–70.

[81] X. Liu, H. S. Haniff, J. L. Childs-Disney, A. Shuster, H. Aikawa, A. Adibekian, M. D. Disney, *J Am Chem Soc* **2020**, *142*, 6970–6982.

[82] S. O. Park, J. Kim, M. Koh, S. B. Park, *J Comb Chem* **2009**, *11*, 315–326.

[83] H. -J Kabbe, A. Widdig, *Angew Chem -Int Edit* **1982**, *21*, 247–256.

[84] W. L. Mock, H. R. Tsou, *Journal of Organic Chemistry* **1981**, *46*, 2557–2561.

[85] J. Sun, Y. Dong, L. Cao, X. Wang, S. Wang, Y. Hu, *Journal of Organic Chemistry* **2004**, *69*, 8932–8934.

[86] J. A. Squella, S. Bollo, L. J. Núñez-Vergara, *Curr Org Chem* **2005**, 9, 565–581.

[87] M. Egbert, A. Whitty, G. M. Keserü, S. Vajda, *J Med Chem* **2019**, *62*, 10005–10025.

[88] G. Mayer, Z. Shpilt, H. Kowalski, E. Y. Tshuva, A. Friedler, *ACS Chem Biol* **2022**, *17*, 1811–1823.

[89] J. M. Tome, A. Ozer, J. M. Pagano, D. Gheba, G. P. Schroth, J. T. Lis, *Nat Methods* **2014**, *11*, 683–688.

[90] P. J. Hajduk, J. R. Huth, S. W. Fesik, *J Med Chem* **2005**, *48*, 2518–2525.

[91] D. M. Krüger, S. Neubacher, T. N. Grossmann, *RNA* **2018**, *24*, 1457–1465.

[92] A. S. Rose, P. W. Hildebrand, *Nucleic Acids Res* **2015**, *43*, W576–W579.

[93] N. R. Voss, M. Gerstein, *J Mol Biol* **2005**, *346*, 477–492.

[94] A. A. Zamyatnin, *Prog Biophys Mol Biol* **1972**, *24*, 107–123.

[95] M. Amblard, J.-A. Fehrentz, J. Martinez, G. Subra, *Mol Biotechnol* **2006**, 239–254.

[96] D. P. Bondeson, B. E. Smith, G. M. Burslem, A. D. Buhimschi, J. Hines, S. Jaime-Figueroa, J. Wang, B. D. Hamman, A. Ishchenko, C. M. Crews, *Cell Chem Biol* **2018**, *25*, 78-87.e5.

[97] A. Miyachi, F. Kondo, M. Kurita, K. Tsuji, K. ichi Harada, *J Biosci Bioeng* **2015**, *119*, 724–728.

[98] "Chromatography on Immobilized Artificial Membrane (IAM) White Paper - Regis Technologies," can be found under

https://www.registech.com/download/chromatography-on-immobilized-artificial-membrane-iam-white-paper/#unlock, **Accessed last 14.12.2022.**

[99] L. S. Povarov, *Russ Chem Rev* **1965**, *34*, 639–656.

[100] M. Fochi, L. Caruana, L. Bernardi, *Synthesis* **2014**, *46*, 135–157.

[101] F. Palacios, C. Alonso, A. Arrieta, F. P. Cossío, J. M. Ezpeleta, M. Fuertes, G. Rubiales, *European J Org Chem* **2010**, 2091–2099.

[102] O. Ghashghaei, C. Masdeu, C. Alonso, F. Palacios, R. Lavilla, *Drug Discov Today Technol* **2018**, *29*, 71–79.

[103] A. Bunescu, Q. Wang, J. Zhu, *Org Lett* **2014**, *16*, 1756–1759.

[104] L. S. Povarov, *Russ Chem Rev* **1967**, *36*, 656–670.

[105] V. V. Kouznetsov, *Tetrahedron* **2009**, *65*, 2721–2750.

[106] H. Ishitani, S. Kobayashi, *Tetrahedron Lett* **1996**, *37*, 7357–7360.

[107] H. Xu, H. Zhang, E. N. Jacobsen, *Nat Protoc* **2014**, *9*, 1860–1866.

[108] G. L. Goebel, L. Hohnen, L. Borgelt, P. Hommen, X. Qiu, *Eur J Med Chem* **2022**, 228, 1–14.

[109] B. Carlo, M. H. Donna, L. Amos, B. Smith, *ChemMedChem* **2013**, *8*, 385–395.

[110] A. Richter, R. Rose, C. Hedberg, H. Waldmann, C. Ottmann, *Chem Eur J* **2012**, *18*, 6520–6527.

[111] E. C. Franklin, F. W. Bergstrom, *J Org Chem* **1936**, *1*, 65–75.

[112] O. Doebner, *Ann* **1887**, 242, 265–289.

[113] Z. Wang, "Doebner Reaction", *Comprehensive Organic Name Reactions and Reagents*, **2010**, 921–923.

[114] M. J. Weiss, C. R. Hauser, *J. Am. Chem. Soc.* **1946**, *68*, 722–723.

[115] G. R. Fulmer, A. J. M. Miller, N. H. Sherden, H. E. Gottlieb, A. Nudelman, B. M. Stoltz, J. E. Bercaw, K. I. Goldberg, *Organometallics* **2010**, *29*, 2176–2179.

[116] M. Chiarucci, R. Mocci, L. D. Syntrivanis, G. Cera, A. Mazzanti, M. Bandini, *Angew Chem -Int Edit* **2013**, *52*, 10850–10853.

[117] M. Tesch, S. Kudruk, M. Letzel, A. Studer, *Chem Eur J* **2017**, *23*, 5915–5919.

[118] K. Pal, A. Sharma, A. L. Koner, *Org Lett* **2018**, *20*, 6425–6429.

[119] J. Václavík, R. Zschoche, I. Klimánková, V. Matoušek, P. Beier, D. Hilvert, A. Togni, *ChemEur J* **2017**, *23*, 6490–6494.

7. Abbreviations

BDNF	brain-derived neurotrophic factor
blimp-1	b lymphocyte-induced maturation protein-1
cat-ELCCA	catalytic enzyme-linked click chemistry assay
Cbz	benzyloxycarbonyl
CCDST	cervical cancer DExH-box helicase 9 suppressive transcript
cdk	cyclin-dependent kinase
CHI	chromatographic hydrophobicity index
c-Myc	cellular Myelocytomatosis
CSD	cold-shock domain
CuAAC	Copper(I)-catalyzed azide-alkyne cycloaddition
DGCR8	DiGeorge syndrome critical region 8
DHX9	DExH-box helicase 9
DNA	deoxyribonucleic acid
EDG	electron-donating group
eIF4A	eukaryotic initiation factor 4A
eIF4E	eukaryotic translation initiation factor 4E
EMSA	electrophoretic mobility shift assay
FOXQ1	Forkhead box Q1
FP	fluorescence polarization
HEK293	human embryonic kidney 293 cells
HIV	human immunodeficiency viruses
HMGA-2	High-mobility group AT-hook 2
HOTAIR	Hox transcript antisense RNA

HTS	High-throughput screen
HuR	Human antigen R
IAM	immobilized artificial membrane
IL-6	interleukin 6
IRE	iron responsive element
IRP1	Iron regulatory protein 1
KH domain	k-homology domain
LA	lewis acid
lncRNA	long non-coding RNA
MCR	multi-component reaction
MDM2	murine double minute 2
miRNA	micro RNA
MOE	methoxyethyl
mRNA	messenger RNA
MSI	microsatellite instability
ncRNAs	non-coding RNA
NEC	negatively charged moiety
NHP2L1	non-histone protein 2 like protein 1
NOE	nuclear overhauser effect
nt	nucleotides
PEG	polyethylene glycol
PPI	Protein-Protein interaction
pre-miRNA	precursor-miRNA
PRI	protein-RNA interaction

pri-miRNA	primary-miRNA
PROTAC	Proteolysis targeting chimeras
PS	Phosphorthioate
Ras	Rat sarcoma virus
(ds)RBD	double-stranded RNA binding domain
RBP	RNA binding Protein
RBD	RNA binding domain
RIBOTAC	ribonuclease targeting chimeras
RISC	RNA-induced silencing complex
RNA	ribonucleic acid
RNase	ribonuclease
RNP	ribonucleoprotein complex
RRM	RNA recognition motif
rRNA	ribosomal RNA
SAR	structure-activity relationship
siRNA	small interfering RNA
SMN2	survival of motor neuron 2
snoRNA	small nucleolar RNA
snRNA	small nuclear RNA
SPPS	solid phase peptide synthesis
SPR	surface plasmon resonance
THQ	tetrahydroquinoline
TR-FRET	time-resolved fluorescence energy transfer
tRNA	transfer RNA

TUTase	3'terminal uridylyl transferase
UHPLC	ultra-high-performance liquid chromatography
VHL	Von-Hippel-Lindau
Zcchc11	zinc finger, CCHC domain containing 11
ZKD	zink-knuckle domain

8. Eidesstaatliche Versicherung (Affidavit)

Eidesstattliche Versicherung (Affidavit)

Hommen, Pascal
Name, Vorname
(Surname, first name)

Matrikel-Nr.
(Enrolment number)

Belehrung:

Wer vorsätzlich gegen eine die Täuschung über Prüfungsleistungen betreffende Regelung einer Hochschulprüfungsordnung verstößt, handelt ordnungswidrig. Die Ordnungswidrigkeit kann mit einer Geldbuße von bis zu 50.000,00 € geahndet werden. Zuständige Verwaltungsbehörde für die Verfolgung und Ahndung von Ordnungswidrigkeiten ist der Kanzler/die Kanzlerin der Technischen Universität Dortmund. Im Falle eines mehrfachen oder sonstigen schwerwiegenden Täuschungsversuches kann der Prüfling zudem exmatrikuliert werden, § 63 Abs. 5 Hochschulgesetz NRW.

Die Abgabe einer falschen Versicherung an Eides statt ist strafbar.

Wer vorsätzlich eine falsche Versicherung an Eides statt abgibt, kann mit einer Freiheitsstrafe bis zu drei Jahren oder mit Geldstrafe bestraft werden, § 156 StGB. Die fahrlässige Abgabe einer falschen Versicherung an Eides statt kann mit einer Freiheitsstrafe bis zu einem Jahr oder Geldstrafe bestraft werden, § 161 StGB.

Die oben stehende Belehrung habe ich zur Kenntnis genommen:

Official notification:

Any person who intentionally breaches any regulation of university examination regulations relating to deception in examination performance is acting improperly. This offence can be punished with a fine of up to EUR 50,000.00. The competent administrative authority for the pursuit and prosecution of offences of this type is the chancellor of the TU Dortmund University. In the case of multiple or other serious attempts at deception, the candidate can also be unenrolled, Section 63, paragraph 5 of the Universities Act of North Rhine-Westphalia.

The submission of a false affidavit is punishable.

Any person who intentionally submits a false affidavit can be punished with a prison sentence of up to three years or a fine, Section 156 of the Criminal Code. The negligent submission of a false affidavit can be punished with a prison sentence of up to one year or a fine, Section 161 of the Criminal Code.

I have taken note of the above official notification.

Dortmund, 16.12.2022
Ort, Datum
(Place, date)

Unterschrift
(Signature)

Titel der Dissertation:
(Title of the thesis):

Design, synthesis, and evaluation of small molecules and associated bifunctional conjugates targeting the Protein–RNA interaction of LIN28 and let-7

Ich versichere hiermit an Eides statt, dass ich die vorliegende Dissertation mit dem Titel selbstständig und ohne unzulässige fremde Hilfe angefertigt habe. Ich habe keine anderen als die angegebenen Quellen und Hilfsmittel benutzt sowie wörtliche und sinngemäße Zitate kenntlich gemacht.
Die Arbeit hat in gegenwärtiger oder in einer anderen Fassung weder der TU Dortmund noch einer anderen Hochschule im Zusammenhang mit einer staatlichen oder akademischen Prüfung vorgelegen.

I hereby swear that I have completed the present dissertation independently and without inadmissible external support. I have not used any sources or tools other than those indicated and have identified literal and analogous quotations.

The thesis in its current version or another version has not been presented to the TU Dortmund University or another university in connection with a state or academic examination.*

*Please be aware that solely the German version of the affidavit ("Eidesstattliche Versicherung") for the PhD thesis is the official and legally binding version.

Dortmund, 16.12.2022
Ort, Datum
(Place, date)

Unterschrift
(Signature)